

**Experimental tools
for quantum networking operations
with single photons and single ions**

Dissertation

zur Erlangung des Grades
des Doktors der Naturwissenschaften
der Naturwissenschaftlich-Technischen Fakultät II
– Physik und Mechatronik –
der Universität des Saarlandes

and at the

Institute of Photonic Sciences (ICFO)
Universitat Politècnica de Catalunya

Jan Huwer

Saarbrücken / Barcelona

2013

Tag des Kolloquiums:

29.01.2014

Dekan:

Prof. Dr. Christian Wagner

Mitglieder des Prüfungsausschusses:

Prof. Dr. Giovanna Morigi
Prof. Dr. Jürgen Eschner
Prof. Dr. Daniel Segal
Prof. Dr. Jonathan Home
Dr. Frank Koppens

Abstract

One promising approach for future quantum networks is the combination of strings of trapped ions as quantum-information processors with entangled photon pairs produced by spontaneous parametric down conversion (SPDC) to establish quantum communication links between distant processing units.

This work reports on experiments using a hybrid quantum-optics set-up, comprising two separate linear ion traps and a resonant SPDC photon-pair source. It demonstrates the controlled interaction of single entangled photon pairs with a single trapped $^{40}\text{Ca}^+$ ion. Preparing the ion as polarization selective absorber in the main polarization bases allows for the reconstruction of the biphoton quantum state, manifesting the photon entanglement in the absorption process.

Beyond that, the thesis documents the implementation of additional experimental tools enabling quantum state transfer experiments from photons to single ions. A dedicated narrow-bandwidth laser system is set up, laser sequences are developed for state discrimination and state rotations of ion qubits, and for the creation and characterization of coherent superposition states, of particular importance for state-transfer schemes. Finally, detection efficiencies of single Raman photons emitted by an ion are characterized with a well controlled single-photon source, and absorption probabilities of single photons are determined with a calibrated laser beam, providing precise values to assess efficiencies for different transfer scenarios.

Zusammenfassung

Ein mögliches System für zukünftige Quantennetzwerke ist die Verknüpfung gefangener Ionen als Quanteninformationsprozessoren mit durch SPDC (Spontaneous Parametric Down Conversion) erzeugten verschränkten Photonenpaaren zum Aufbau von Quantenkommunikationskanälen.

Diese Dissertation behandelt Experimente an einem hybriden Quantenoptikaufbau, bestehend aus zwei separaten linearen Ionenfallen und einer SPDC-Photonenpaarquelle. Sie zeigt die kontrollierte Wechselwirkung einzelner verschränkter Photonenpaare mit einem einzelnen $^{40}\text{Ca}^+$ Ion. Durch Präparation des Ions als polarisationsselektiven Absorber in den drei Hauptpolarisationsbasen, wird der Zwei-Photonen-Quantenzustand rekonstruiert und somit über den Absorptionsprozess die Verschränkung der Photonenpaare nachgewiesen.

Überdies dokumentiert die Arbeit die Einrichtung zusätzlicher Methoden, welche den Zustandstransfer von Photonen auf einzelne Ionen ermöglichen. Ein schmalbandiges Lasersystem wird aufgebaut, Lasersequenzen für Zustandsbestimmung und Zustandsrotationen von Ionen-Qubits und zur Erzeugung und Charakterisierung kohärenter Superpositionszustände werden entwickelt. Ferner werden mit Hilfe einer Einzelphotonenquelle Nachweiseffizienzen für einzelne, von einem Ion erzeugte, Raman-Photonen gemessen und Absorptionseffizienzen einzelner Photonen mit einer kalibrierten Laserquelle charakterisiert. Die ermittelten Werte bilden eine solide Grundlage zur Abschätzung von Erfolgswahrscheinlichkeiten geplanter Transferschemata.

Resumen

Un enfoque prometedor para futuras redes cuánticas es la combinación de iones atrapados con pares de fotones entrelazados que se generan por el proceso SPDC (Spontaneous Parametric Down Conversion). Los iones atrapados se utilizarán como procesadores de información cuántica. Los pares de fotones permitirán el establecimiento de enlaces de comunicación cuántica entre unidades de procesamiento distantes.

En el transcurso de este trabajo, que se sitúa en el marco de la óptica cuántica, se han combinado dos implementaciones experimentales independientes para la realización de un experimento híbrido. Las dos partes del experimento corresponden con dos trampas de iones lineales separadas y con una fuente de pares de fotones resonantes creados por SPDC. En este experimento se demuestra la interacción controlada de pares de fotones individuales entrelazados con un ión atrapado individual de $^{40}\text{Ca}^+$. La preparación del ión como absorbente selectivo de polarización en las bases de polarización principales permite la reconstrucción del estado cuántico de los pares de fotones, manifestando así su entrelazamiento a través del proceso de absorción.

Además, en la tesis presente se documenta la implementación de herramientas experimentales adicionales que permitirán experimentos de transferencia de estados cuánticos de fotones a iones individuales. Así mismo, se describe el montaje de un sistema láser acondicionado con ancho de banda estrecho. Adicionalmente, se desarrollan secuencias de láser para la discriminación y la rotación de estados de qubits de iones y, para la creación y caracterización de estados de superposición coherente, especialmente importantes para varios esquemas de transferencia de estado. Por último, se caracterizan las eficiencias de detección de fotones individuales Raman emitidos por un ión con una fuente de fotones individuales bien controlada, así como también se determinan las probabilidades de absorción de fotones individuales con una fuente láser calibrada. Los valores precisos obtenidos servirán para la evaluación de la eficiencia de diferentes esquemas de transferencia.

Contents

Introduction	1
1. Trapping ions	7
1.1. Paul trap	7
1.2. Interaction of trapped $^{40}\text{Ca}^+$ with EM fields	9
1.2.1. General description of the interaction	9
1.2.2. Doppler cooling	12
1.2.3. Optical quadrupole transition for coherent manipulations	13
1.3. Experimental set-up	15
1.3.1. Laser system	16
1.3.2. Double-trap apparatus	18
1.3.3. Experiment control	20
2. Hybrid quantum network	23
2.1. Spontaneous parametric down conversion	24
2.2. Experimental set-up	25
2.3. Scheme for entanglement transfer	27
2.3.1. Motivation	27
2.3.2. Scheme	28
2.3.3. Remaining prerequisites	31
3. Experiments with single ions and single photons	33
3.1. Interaction of heralded single photons with a single ion	34
3.1.1. Efficient absorption detection with quantum-jump scheme	35
3.1.2. Experimental scheme	37
3.1.3. Absorption-idler correlations	40
3.1.4. Previous experiment: Heralded single-photon absorption by a single ion	41
3.1.5. Coincidence measurements in three polarization bases	43
3.1.6. Photon entanglement detection by a single ion: Quantum tomography	47
3.1.7. Efficiency considerations	49
3.2. Detection efficiency of single emitted 393 nm photon	52
3.2.1. Experimental scheme	53
3.2.2. Characterization of single-photon source	55
3.2.3. Measurement of detection efficiencies	56
3.3. Absorption probability of single 854 nm laser photons in both ion traps	58
3.4. Summary	61

4. Setup of a laser system for coherent manipulations at 729 nm	63
4.1. Theory	64
4.1.1. Optical resonators	64
4.1.2. Laser stabilization	66
4.2. 729 nm laser	68
4.2.1. Set-up for frequency stabilization	68
4.2.2. AOM set-up to ion	72
4.3. High-finesse ULE cavity	74
4.3.1. Temperature stabilization	76
4.3.2. Mode matching	79
4.3.3. Spectral properties	81
4.4. Experiments	82
4.4.1. Sequence	83
4.4.2. Spectroscopy	87
4.4.3. Stability of the laser	90
4.4.4. Electron shelving	96
4.5. Summary	98
5. Ion cooling dynamics	99
5.1. Theoretical background	99
5.1.1. Laser cooling of a trapped multilevel ion	99
5.1.2. Temperature measurements with the 729 nm laser	100
5.2. Optimization of Doppler cooling	102
5.2.1. Calibration of the cooling-laser parameters with spectroscopy	102
5.2.2. Measurement of cooling rate and cooling limit	103
5.2.3. Dependence of cooling performance on 397 nm laser detuning	104
6. Coherent manipulations on the $S_{1/2}$-$D_{5/2}$ transition	107
6.1. Theory	107
6.2. Coherent superposition between $S_{1/2}$ and $D_{5/2}$	110
6.2.1. Ramsey signal	110
6.2.2. Measurement of laser linewidth	112
6.3. Coherent superposition in the $D_{5/2}$ state	114
6.3.1. Coherent dynamics involving an auxiliary $D_{5/2}$ level	114
6.3.2. Generation of coherent superposition in $D_{5/2}$	121
6.3.3. Outlook	123
7. Conclusions	127
7.1. Summary	127
7.2. Outlook	129
A. Appendix	133
A.1. List of Clebsch-Gordan coefficients	133
A.2. Dipole emission and absorption characteristic	134
A.3. Likelihood function for the tomographic reconstruction	135

A.4. Correlation coefficient	136
A.5. Measurement of $D_{5/2}$ population	137
A.6. Decoherence in the presence of periodic magnetic-field noise	138
Bibliography	141

Introduction

Since its foundation and first practical implementation in the first half of the 20th century, classical computation theory became soon one of the most important developments from that time. Until now its main technical application, i.e. the classical computer, has a huge influence both on science and on everyday life. Besides the fact that a completely new branch of communication technologies arose from it, culminating in the realization of a permanent worldwide network of computers, the exponentially growing amount of available computing power at any point of the planet also led to entirely new research areas as for example the study of complex systems known from Biology or the highly computationally intensive field of global climate research. Due to the miniaturization process of the devices that comes with the increase in computational speed, the hardware used in classical computers for the implementation of logic gates and memories will soon be at the quantum limit, when the classical regime does not hold anymore and quantum mechanical effects gain influence on the systems.

At the end of the 20th century people started to think about how to use fundamental quantum-mechanical phenomena to process information [1, 2]. Initially, these visions were still far away from any implementation because this would have required the isolation and control of single quantum systems. Nevertheless, such systems became available with the first trapping and cooling of a single atomic ion [3] and with the control over individual photons in cavity QED [4]. Soon, a complete new combined experimental and theoretical research area called *quantum information* started to evolve. Analogous to its classical counterpart it is nowadays subdivided into *quantum computation* and *quantum communication*.

Different to the developed classical digital communication technologies, basic quantum communication does not necessarily require a quantum computer to establish a communication link. As a consequence, both fields of quantum computation and quantum communication have since the beginning evolved independently. In the recent years, big progress has been made in both research areas, resulting in the experimental demonstration of first quantum processors and even already commercial applications for quantum key distribution over quantum communication links, to secure classical communication channels. Although both areas are still at the beginning, future limitations become already present. To provide the scalability of quantum processors for the execution of complex quantum algorithms, many individual processing units must be linked via quantum communication channels which allow for an exchange of quantum information between them. On the other hand, the long-distance quantum communication channels demonstrated so far are typically implemented with photonic carriers of quantum information, suffering from photon losses just as classical optical communication channels. Long-distance quantum communication will be possible if the channel is sub-divided in several short-distance links with quantum processors at the breaking points, allowing for the implementation of so-called *quantum-repeater* schemes. The strong need for interfaces between quantum processing units and communication channels and the efficient link between distant processing units gave rise to a third important research field in the context of quantum

information. This is the research area of *quantum networks*.

The motivation for this thesis is to establish the last missing experimental tools in an existing experimental set-up which is intended for a general study of different quantum-network scenarios with ion-trap quantum processors. In the following, this introduction will give a very short overview over the state-of-the-art in the mentioned three principal research branches of quantum information to provide the necessary context.

Quantum information processing

Several quantum algorithms were proposed that promise to be much more efficient than their classical counterparts for the solution of certain classical problems. The most prominent examples are one by Grover [5] for the search of data bases, and Shor's algorithm for the factorization of large numbers [6]. The great potential in quantum information processing comes from the fact that its fundamental information unit called *qubit* does not only allow two discrete logic states 0 and 1 but also arbitrary superpositions of these, which means that several possible input states can be computed in a single operation (*quantum parallelism*). Arbitrary quantum logic gates are then usually composed from a universal set of two- or multi-qubit entanglement operations and single-qubit manipulations [7, 8, 9]. Apart from the prospect of a device for universal quantum-information processing tasks that would outperform any classical computer when solving classical problems, great hope lies in the development of a so-called quantum simulator, a special purpose quantum computer. This could be, for example, a quantum mechanical many-body system whose dynamics are engineered such that they mimic the dynamics of other quantum-mechanical many body systems, enabling the study of all sorts of phase transitions. As the simulation of these strongly coupled many-body systems is far beyond the possibilities of today's computing capabilities, striking results and important theoretical insights are expected from large-scale quantum simulators. Prominent physical phenomena to study are for example magnetism and superconductivity.

There exists a huge variety of different physical systems which are promising candidates for the realization of a quantum processor. Just to name a few, the investigated candidates range from very small quantum-optical systems as single atoms [10] and ions [11] to solid-state or molecular systems using nuclear spins [12, 13], superconducting Josephson junctions [14], and quantum dots [15]. Also, purely photonic schemes exist to carry out quantum-logic operations [16].

To date, one of the most developed devices is based on strings of laser-cooled atomic ions confined in Paul traps. The potential of these systems lies in very high fidelities for multi-qubit operations [17, 18] and practically unity efficiency for the measurement of qubit states [19]. Depending on the ion species that is used and on the electronic states that are chosen for the implementation of a qubit, long coherence times are achievable [20, 21], allowing the storage of quantum information, which is an essential requirement when operating in a quantum network structure. First quantum algorithms as the Deutsch-Jozscha algorithm [22], quantum teleportation [23, 24], quantum error correction [25, 26], and the operation of a universal quantum processor [27] were already experimentally demonstrated. Also, the quantum Fourier transform, which plays a key role in the implementation of Shor's factoring algorithm, has been successfully implemented [28, 9]. Ion-trap quantum processors are also perfectly suited

for the field of quantum simulation. A large number of simulations covering a broad field in physics has been experimentally demonstrated so far. Plenty of examples are available in [29] and references therein.

Quantum communication

While quantum computers may threaten the security of today's communication by the efficient factorization of large prime numbers, there exist communication protocols using flying qubits (e.g. single photons or entangled photon pairs) for the transmission of a classical encryption key, which are absolutely tap-proof [30]. This technology of quantum cryptography relies on the existence of entanglement in a quantum system and/or on the fact that a quantum-mechanical measurement always projects the system into the eigenstate corresponding to the measurement result.

Apart from this first practical application of quantum communication, the reliable transmission of quantum information is one fundamental ingredient for the realization of quantum networks by the interconnection of several qubits or small quantum processors. Using photons as carriers of quantum information seems to be the most practical approach as they have suitable properties in terms of coherence and propagation. Nevertheless, due to photon loss, the transmission of quantum information is nowadays limited to distances of about one hundred kilometers. To be able to still work with high efficiency over such lossy quantum channels, the general strategy is to use photons only to distribute entanglement between the two ends of a communication channel and to use this entanglement then as a resource for the transmission of quantum information with a teleportation scheme, as proposed in [31]. Entangled photon-pair sources based on spontaneous parametric down conversion (SPDC) play a very prominent role in the field of quantum communication, as they provide a robust way of creating entangled photons at high rates. When placed in the middle of a quantum channel and sending each photon of a pair to opposite ends to carry out a teleportation scheme, this configuration makes it in principle possible to double the maximal length of the channel. Enabling even higher communication distances requires already a quantum-network structure which offers the possibility for the temporal storage of entanglement in quantum memories or processors at the ends of several short-distance channels. By local operations in these intermediate nodes, the entanglement can then be extended to the outermost ends of a long-distance communication channel consisting of several subsequent short-distance links by using a quantum-repeater scheme, as proposed in [32].

The field of quantum cryptography is nowadays already so far evolved that commercial solutions for quantum key distribution (to secure classical communication channels) are available by a growing number of companies. Experiments in quantum communication using entangled photon pairs have demonstrated the teleportation of quantum states over the distance of 55 m by using a 2 km long optical fiber link [33]. Teleportation over distances of up to 143 km was demonstrated by transmitting the photons over free space [34]. The successful operation of a quantum repeater has not been documented yet.

Quantum networks

The research area in quantum information comprising the biggest experimental challenges is the field of quantum networks [35]. The main task here is to develop efficient interfaces to transfer quantum information between the nodes of a network that are established with quantum processors, and the quantum channels that we just discussed. To realize a quantum channel with teleportation protocols, distant entanglement between two nodes of the network is required as a resource. One can distinguish two classes of entanglement schemes. The first class relies on the entanglement of each node with an *emitted* photon [36]. Letting the photons from two distant nodes interfere on a beam splitter and performing a coincidence measurement enables then the projection of the two emitters into an entangled state. This was proposed for two-photon interference [37, 38, 39] as well as for single-photon interference [40]. The second class of entanglement schemes is not based on the entanglement transfer via photon emission but via photon *absorption*. The idea is to generate an entangled photon pair independently of the state of the two nodes (this is conveniently achieved with SPDC) and to let the distant nodes absorb the two photons in such a way, that their entanglement gets transferred [41]. Once that distant entanglement is established, this will not only allow the exchange of quantum information between two distant quantum processors but also enable the execution of remote quantum gates between distant network sites. This procedure will facilitate to implement algorithms that require higher numbers of qubits than contained in a single processing unit without the need to scale up the individual processors.

Concerning the network interfaces, different strategies are pursued to efficiently couple single atomic qubits to photons. The most efficient approach is to place single atoms or ions inside an optical cavity [42, 43, 44]. Systems without optical cavities usually make use of sophisticated high numerical-aperture objectives [45, 46]. Recent progress in the production of good quality high numerical-aperture aspheric lenses significantly simplifies this approach [47]. Another possibility is to place the atoms close to mirrors, covering a significant portion of the whole solid angle [48, 49]. As photons are conveniently transmitted over optical fibers, it seems natural to develop interfaces that directly couple the mode of a fiber with a single atom. This is achieved by simply bringing the atoms very close to a fiber end [50, 51] or by placing an atom in between two facing ends of optical fibers with specially engineered surfaces, forming a cavity [52, 53]. Another approach uses the evanescent coupling between atoms and a tapered fiber [54] in the vicinity of the fiber surface.

The successful operation of a quantum network, especially the execution of deterministic remote quantum information processing between macroscopically separated matter qubits has not fully been demonstrated yet. But in the few worldwide existing experimental set-ups that would theoretically offer the possibility for such a demonstration, important preliminary steps have already been achieved: Atom-photon entanglement via the emission of single photons [55, 43, 44], distant entanglement between two atomic systems using projective measurements after two-photon interference [56, 57] and single-photon interference [58], and the generation of distant entanglement via direct photon transmission [59]. Finally, proof-of-principle experiments for the teleportation between distant matter qubits were performed [60, 61].

All of the mentioned experiments have in common that they make use of a single species of quantum system, i.e. single atoms or ions. But in the context of quantum networks it is most likely that the unique properties from different quantum systems have to be combined

to develop efficient network infrastructures. In the recent years this gave rise to another research field, called *hybrid quantum systems*, which is aiming at the interconnection of different quantum systems. The variety of investigated combinations is too large to provide a representative list here. The most prominent candidate system is certainly the combination of SPDC photon-pair sources (as the most adequate system for quantum communication) with quantum processors based on trapped ions (as the most developed system for quantum information processing). Additionally, systems aiming at the interconversion of photons from the visible (resonant with the employed atomic species) to the well established telecommunication bands [62, 63] and vice versa [64] will make it possible to use the already existing infrastructure for classical optical communication and will play a key role in the further development of quantum networks.

This work

The presented thesis project was carried out on an experimental set-up which is intended to study general principles of operation of a small-scale quantum network. Its main components are two separate linear ion traps, high numerical-aperture optics for efficient atom-photon coupling, and an entangled photon-pair source which is operated on resonance with an optical transition in the utilized ion species. This thesis contributes the ability for coherent manipulations and state detection of qubits in both ion traps. Specifically, it documents the setup of a laser system which allows for the required coherent control of single ions in the experiment (Chapters 4–6), paving the way for entanglement transfer from photon pairs to ionic qubits. Concerning the operation of a hybrid quantum system, the thesis presents experiments which show for the first time the heralded interaction of single *entangled* SPDC photons with a single trapped ion (Chapter 3). The same chapter documents further experiments at the single-photon level that were performed for a detailed characterization of the maximally achievable coupling efficiencies between single photons and single ions with the set-up. Chapters 1 and 2 introduce the general theoretical concepts and set-up for the ion-trap apparatus and the photon-pair source.

It should be emphasized, however, that joining the laboratory in Spain after the general experimental set-up had been just finished gave me the great opportunity to participate in a series of demanding experiments right from the beginning. These results are not detailed here but have been reported in earlier theses [65, 66, 67, 68] and in publications: In an experiment with atomic single-photon sources we observed the pulsed interference of single Raman-scattered photons emitted by a single ion in each trap [69]. A second experiment was carried out to investigate the polarization correlation between successively emitted fluorescence photons on a short-lived atomic transition [70]. With the hybrid set-up of the SPDC photon-pair source and a single ion trap we first demonstrated the basic interaction between the two systems by essentially doing spectroscopy of an atomic transition with the down-conversion photons [71]. In the following mile-stone experiment we showed the heralded interaction of single down-conversion photons with a single trapped ion [72].

Further remarks

A major burden and, at the same time, opportunity of this thesis project was the fact that the lab was moved from Spain to Germany at about half time. I was the main person to transfer the know-how of the ion-trap experiment and was therefore heavily involved in the coordination and execution of the move. The rebuilding of the apparatus in Saarbrücken, while delaying notably the progress of the work, also enabled the renovation of important parts of the set-up with the help of a new team of PhD students who joined the efforts and, in the course of the reconstruction, learned operating the lab.

1. Trapping ions

Single trapped earth alkaline ions are text-book examples of quantum mechanical systems, and with the invention of laser cooling [73, 74] and radio-frequency (Paul) traps [75] they soon became preferred study objects in the fast evolving area of quantum optics [76, 77]. Compared to the beginning, when the main purpose of the experiments was to study the properties of the trapped ions themselves, nowadays the systems are more and more used as well established tools to tackle more abstract theoretical questions in physics (with quantum simulators) [29] or to develop a new generation of frequency standards (optical clocks) [78].

Even though being reduced to just a tool that has to be used to address a certain technological or physical problem, ion-trap experiments are still a complex piece of technology on their own, combining technologies and the corresponding best available technical devices from a very broad field of physics. The three main components are almost always the ion-trap apparatus including optics and detectors to measure scattered photons, a laser system for cooling and manipulating the ions, and a dedicated electronic device to connect all of the individual components and to control the whole experiment.

The purpose of this chapter is to shortly introduce the main theoretical concepts and explain the experimental details that are important to understand the operation of the ion-trap experiment that has been worked with during the thesis. Section 1.1 will give a quick overview of the physics of the specific ion trap and Section 1.2 will focus on the theoretical description of the interaction of a single ion with laser light. Section 1.3 is devoted to the details of the experimental set-up, including the laser system, the traps, and the control electronics.

1.1. Paul trap

The central workhorse in most of today's experiments with atomic ions is a radio frequency (RF) trap based on the principle that was invented by W. Paul [75], which makes it possible to confine charged particles in free space over very long times [3]. Being placed in an ultra-high vacuum system, the ions are at the same time well isolated from the environment, providing a unique tool for high-precision spectroscopy and for the study of single quantum systems. The quantized motion of a single or string of several ions confined in a linear Paul trap has furthermore led to the first experimental demonstration of fundamental quantum-logic operations [79, 80] and later to the implementation of a quantum simulator [29]. In the following only the basic principle of the Paul trap will be explained, more detailed descriptions are for example available in [81, 82, 65].

To spatially confine a charged particle in a linear Paul trap, one uses a combination of an oscillating electric field U_{rf} to achieve a radial confinement and a static electric field U_{tip} to establish an axial enclosure of the particle's motion. Owing to the Laplace equation, the generation of a three-dimensional trapping potential by using only static electric fields is impossible. Figure 1.1 shows the typical configuration of a linear Paul trap as it is used in the experiment.

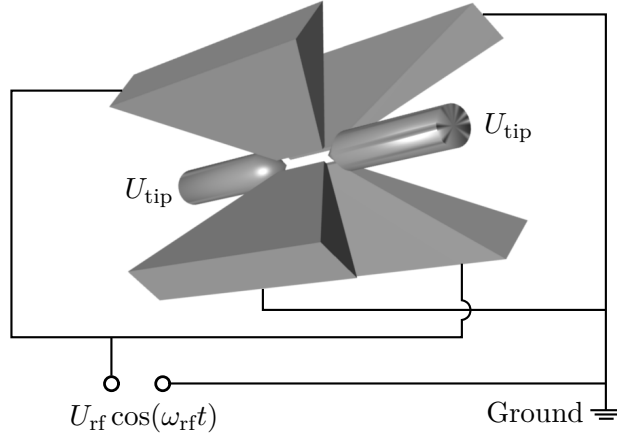


Figure 1.1.: Linear Paul trap consisting of four blades for the radial confinement and two end-tips for axial confinement.

For an orientation of the trap axis along the z -direction, the generated instantaneous potential in the vicinity of the trap center has the form

$$\phi(x, y, z, t) = \frac{\alpha U_{\text{tip}}}{2l_0^2}(-x^2 - y^2 + 2z^2) + \frac{U_{\text{rf}}}{2r_0^2} \cos(\omega_{\text{rf}} t)(x^2 - y^2) \quad (1.1)$$

where r_0 and l_0 are the respective minimal distances from the blades and the end-tips to the trap center. α is a geometry factor that accounts for the penetration of the end-tip field on the trap axis for a certain applied voltage U_{tip} .

The equations of motion for a particle with mass m and charge e in this potential are described by the Mathieu differential equations

$$\frac{d^2 r_i}{d\zeta^2} + [a_i - 2q_i \cos(2\zeta)] r_i = 0 \quad (1.2)$$

with $r_i = x, y, z$ and after substituting $\zeta = \omega_{\text{rf}} t / 2$. The coefficients a_i and q_i are defined as

$$a_x = a_y = -\frac{1}{2}a_z = -\frac{4e\alpha U_{\text{tip}}}{ml_0^2 \omega_{\text{rf}}^2}, \quad q_x = -q_y = -\frac{2eU_{\text{rf}}}{mr_0^2 \omega_{\text{rf}}^2}, \quad q_z = 0. \quad (1.3)$$

The trap size, voltage, and RF frequency are chosen such that these so-called stability parameters lead to stable solutions of (1.2), which is typically the case for $|a_i|, q_i^2 \ll 1$. In this limit, the motion of a trapped particle is approximated by

$$r_i(t) \propto \cos(\omega_i t) \left(1 - \frac{q_i}{2} \cos(\omega_{\text{rf}} t) \right) \quad (1.4)$$

which is the superposition of a low frequency oscillation with ω_i (*secular* motion) and a less pronounced fast oscillation at the RF-drive frequency ω_{rf} (*micro motion*). After neglecting the micro-motion part, the motion is well described by a three-dimensional harmonic oscillator with the eigenfrequencies

$$\omega_i = \frac{\omega_{\text{rf}}}{2} \sqrt{a_i + \frac{1}{2}q_i^2}, \quad (1.5)$$

as it is extensively studied in many standard quantum-mechanics text books. The axial motion is thereby quantized in units of

$$\omega_z = \sqrt{\frac{2e\alpha U_{\text{tip}}}{ml_0^2}} \quad (1.6)$$

and is independent on the dynamic part of the trapping potential in the radial direction. In contrast to that, the radial oscillator modes depend on the axial confinement and are quantized as

$$\omega_{x,y} = \sqrt{\omega_{(x,y)0}^2 - \frac{1}{2}\omega_z^2} \quad (1.7)$$

with the pure radial frequencies $\omega_{(x,y)0} = q_{x,y}\omega_{\text{rf}}/2\sqrt{2}$, corresponding to $U_{\text{tip}} = 0$.

Depending on the mass of a trapped particle, a Paul trap can confine single ions from a few minutes up to several days. The achievable trapping times are limited by collisions and chemical reactions with the background gas, which makes ultra-high vacuum conditions an additional crucial ingredient to achieve a good trap performance. For light earth-alkaline atoms like ^{40}Ca it is therefore absolutely necessary to additionally laser cool the ions in the Paul trap to prevent their loss from the trap over the time of one experimental day. Details about the ion traps in our experimental set-up will follow in Section 1.3.2.

1.2. Interaction of trapped $^{40}\text{Ca}^+$ with EM fields

In the following section, the basic principles of the ion-laser interaction will be explained. Figure 1.2 shows a level scheme of $^{40}\text{Ca}^+$ with all optical transitions that can be addressed with lasers in the experiment.

Lasers are used to localize the ion in the trap potential by laser cooling its quantized motion. The resulting strong local confinement allows an efficient coupling of the ion's fluorescence to single optical modes that are defined by optical fibers outside of the vacuum chamber and, vice versa, of laser beams to the ion. The cooling is ideally applied on a transition which provides a high scattering rate of photons. For $^{40}\text{Ca}^+$, this is usually achieved with two lasers at 397 nm and 866 nm, where the red laser is only needed as a repumper, preventing the population from ending up in the metastable $D_{3/2}$ state.

For coherent manipulations, state discrimination, and sideband cooling an optical transition with a narrow natural linewidth significantly below the typical trap frequencies is required. This is done on the optical quadrupole transition at 729 nm.

In Section 1.2.1, the basic description for the ion-laser interaction will be shortly summarized. Section 1.2.2 will then focus on the mechanism of Doppler cooling of the ion motion in the trap. The last section (1.2.3) will finally explain the most important properties of the optical quadrupole transition.

1.2.1. General description of the interaction

A two-level atom with the two electronic states $|g\rangle$ and $|e\rangle$ separated by the resonance frequency ω_0 , trapped in a harmonic potential with trap frequency ω_T along the z -axis, and interacting

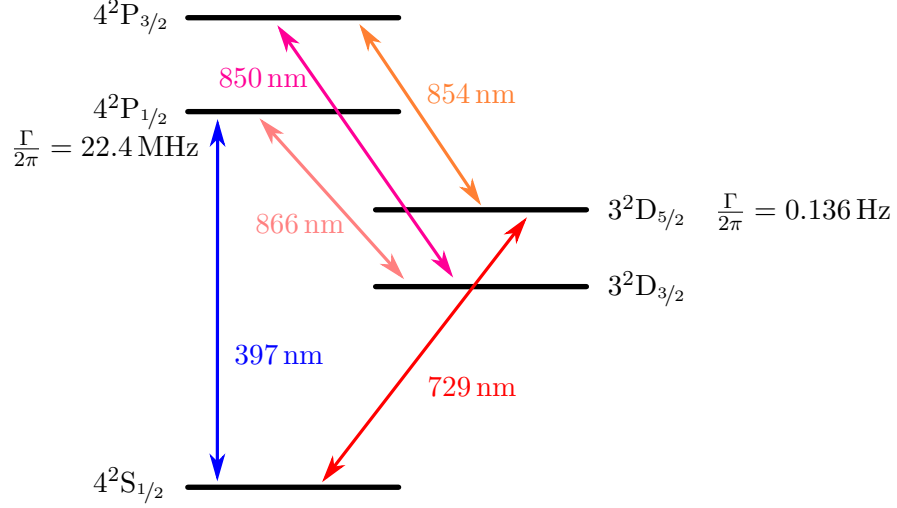


Figure 1.2.: Level scheme of $^{40}\text{Ca}^+$ with all optical transitions that are experimentally accessible with lasers in the current set-up. The indicated decay rates Γ of the $\text{P}_{1/2}$ and $\text{D}_{5/2}$ state are taken from [83, 84].

with a laser at the frequency ω_L is described by the Hamiltonian¹ [85]

$$H = \hbar\omega_T \left(a^\dagger a + \frac{1}{2} \right) + \frac{\hbar\omega_0}{2} (|e\rangle\langle e| - |g\rangle\langle g|) + \underbrace{\frac{\hbar\Omega}{2} (|e\rangle\langle g| + |g\rangle\langle e|)}_{H^{(i)}} \left(e^{i(\mathbf{k}\cdot\mathbf{z} - \omega_L t + \phi)} + \text{h.c.} \right). \quad (1.8)$$

Here, a and a^\dagger are the annihilation and creation operators of single quanta of the vibrational energy $\hbar\omega_T$, Ω is the Rabi frequency describing the coupling strength of the ion-laser interaction, \mathbf{k} and \mathbf{z} are the wave vector of the laser field and the position of the ion in the trap potential along the z -direction, and ϕ is the relative phase of the laser field with respect to the atomic (dipole or quadrupole) moment. In the interaction picture, the part $H^{(i)}$, describing the interaction with the laser field and the coupling to different motional states $|n\rangle$ of the harmonic trap potential, is written as²

$$H_{\text{int}}^{(i)} = \frac{\hbar\Omega}{2} |e\rangle\langle g| e^{i\eta(a_{\text{int}} + a_{\text{int}}^\dagger)} e^{i(\phi - \Delta t)} + \text{h.c.} . \quad (1.9)$$

$a_{\text{int}} = a e^{-i\omega_T t}$ and a_{int}^\dagger are the corresponding ladder operators in the interaction picture and $\Delta = \omega_L - \omega_0$ is the detuning of the laser from the atomic resonance. The quantity

$$\eta = k \cos(\beta) \sqrt{\hbar/2M\omega_T} \quad (1.10)$$

¹We are only considering the case of a one dimensional trap potential. The generalization for a three dimensional trap potential is straightforward.

²The *rotating-wave approximation* has been applied, neglecting terms oscillating at frequencies $\omega_L + \omega_0$.

is the Lamb-Dicke parameter, corresponding to the ratio of the extension of the atomic wave function for the lowest motional state in the trap potential, $\langle 0|\mathbf{z}^2|0\rangle^{\frac{1}{2}}$, to the wavelength of the exciting radiation. The angular dependence on β accounts for the relative orientation between the laser beam and the oscillation axis of the ion's motion [86].

The interaction Hamiltonian (1.9) describes the coupling of the initial state $|g, n\rangle$ to the manifold of excited states $|e, n'\rangle$, depending on the laser detuning. For the case that $\Delta = s \omega_{\text{T}}$ ($s = \text{integer}$), the Rabi frequency for the so-called motional sideband excitation is given by the motional transition matrix element [87]

$$\Omega_{n, n+s} = \Omega \left| \langle n+s | e^{i\eta(a+a^\dagger)} | n \rangle \right| = \Omega e^{-\frac{\eta^2}{2}} \eta^{|s|} \sqrt{\frac{n_{<}!}{n_{>}!}} L_{n_{<}}^{|s|}(\eta^2) \quad (1.11)$$

with $n_{<}$ ($n_{>}$) being the lesser (greater) of $n+s$ and n , and $L_n^{|s|}(\eta^2)$ being the generalized Laguerre polynomials.

In the Lamb-Dicke regime

$$\eta^2 \langle (a+a^\dagger)^2 \rangle = \eta^2 (2n+1) \ll 1, \quad (1.12)$$

the exponential term in (1.9) containing the motional coupling is expanded up to the first order in η , leading to

$$H_{\text{int}}^{(i)} = \hbar \frac{\Omega}{2} \left(|e\rangle \langle g| e^{i(\phi-\Delta)t} + |g\rangle \langle e| e^{-i(\phi-\Delta)t} \right) \quad (1.13)$$

$$+ i\hbar \frac{\Omega}{2} \eta \left(|e\rangle \langle g| a e^{i(\phi-(\Delta+\omega_{\text{T}})t)} - |g\rangle \langle e| a^\dagger e^{-i(\phi-(\Delta+\omega_{\text{T}})t)} \right) \quad (1.14)$$

$$+ i\hbar \frac{\Omega}{2} \eta \left(|e\rangle \langle g| a^\dagger e^{i(\phi-(\Delta-\omega_{\text{T}})t)} - |g\rangle \langle e| a e^{-i(\phi-(\Delta-\omega_{\text{T}})t)} \right). \quad (1.15)$$

(1.13) describes a coupling without any change of the ion's motion for $\Delta = 0$ with the Rabi frequency Ω . This is a so-called carrier transition. (1.14) contains a coupling to the first lower motional sideband ("red sideband") for a laser detuning of $\Delta = -\omega_{\text{T}}$. Compared to the carrier, the effective Rabi frequency $\Omega_{n-1, n} = \eta\sqrt{n} \Omega$ is reduced and depends on the motional state $|n\rangle$ of the ion. Correspondingly, (1.15) describes a coupling to the first higher motional state ("blue sideband") for $\Delta = +\omega_{\text{T}}$ with the Rabi frequency $\Omega_{n+1, n} = \eta\sqrt{n+1} \Omega$.

Experimental situation

For all experiments in this thesis, the cooling beam at 397 nm had an angle of approximately $\beta = 22.5^\circ$ with respect to the trap axis, into which direction the lowest trap frequency is oriented. This results in a maximum value for the Lamb-Dicke parameter of $\eta_{397} = 0.15$. For the beam at 729 nm ($\beta \approx 45^\circ$), the Lamb-Dicke parameter is expected to be $\eta_{729} = 0.06$. This legitimates the above approximation even for high motional states ($n \approx 70$) on the 729 transition. For the cooling transition that has a much shorter wavelength, the Lamb-Dicke regime is only sufficiently fulfilled for low motional states of the ion ($n \leq 10$).

1.2.2. Doppler cooling

When loading ions into a radio-frequency trap, their initial energy is typically very high, depending on the depth of the trapping potential on the order of several hundreds of Kelvin. For quantum-optics experiments with single ions it is crucial to cool the ions to low motional states in the trapping potential. This prevents the atomic particles, on the one hand, from being lost out of the trap potential due to collisions with background gas or due to heating from the trap drive. On the other hand, a low ion temperature eliminates spectral broadening caused by Doppler shifts and ensures a strong local confinement, important for the effective coupling of a single ion with a single optical mode. The ion's motion is therefore usually Doppler cooled with laser light to temperatures below 1 mK. A detailed review of laser cooling of free and bound atoms is found in [88]. In the following, a simple classical explanation for the cooling process of a trapped two-level atom will be given as it is used in [85]. However, in the experiment we are not dealing with a classically cooled particle, nor is the atomic level scheme a simple two-level system, which leads to some deviations from the description given in this section. Experiments investigating the cooling dynamics of the Doppler-cooling process in the real situation and a corresponding theoretical description will be treated in Chapter 5.

We first assume a two-level atom with the radiative decay rate Γ , the resonance frequency ω_0 , and the excited-state probability $\rho_{ee} = \langle e|\rho|e \rangle$. We further assume that the atom is only weakly bound ($\Gamma \gg \omega_{\text{trap}}$)³ in a trapping potential with trap frequency ω_{trap} . The atom is illuminated by a laser beam with wave vector \mathbf{k} and frequency ω_L and will therefore experience the radiative force

$$F_a = \hbar k \Gamma \rho_{ee} \quad (1.16)$$

through the absorption processes, given by the product of the single-photon momentum and the photon scattering rate $\Gamma \rho_{ee}$. From the optical Bloch equations it follows that [89]

$$\rho_{ee} = \frac{\Omega^2/4}{\delta^2 + \Omega^2/2 + \Gamma^2/4} \quad (1.17)$$

with $\delta = \omega_L - \omega_0 + \mathbf{k} \cdot \mathbf{v}$ for the effective detuning between laser and atomic resonance, including the Doppler shift due to the instantaneous velocity \mathbf{v} of the atom. If substantial cooling has already taken place, (1.16) can be approximated around $v = 0$ by

$$F_a \approx F_0 + f_1 v \quad (1.18)$$

with

$$F_0 = \hbar k \Gamma \frac{\Omega^2/4}{\Delta^2 + \Omega^2/2 + \Gamma^2/4} \quad (1.19)$$

and

$$f_1 = F_0 \frac{2k\Delta}{\Delta^2 + \Omega^2/2 + \Gamma^2/4}, \quad (1.20)$$

which leads to a velocity dependent friction force that results in a cooling effect for negative detunings $\Delta = \omega_L - \omega_0$ of the laser from the atomic resonance.

³A full QM treatment of the cooling process for a harmonically trapped atom in [87] shows that the main results are the same as the ones for a free atom in the limiting case $\Gamma \gg \omega_{\text{trap}}$.

The cooling rate \dot{E}_c due to photon absorptions is given by

$$\dot{E}_c = \langle F_a v \rangle = f_1 \langle v^2 \rangle = 4\hbar k^2 \frac{s\Delta/\Gamma}{\left(1 + s + \frac{4\Delta^2}{\Gamma^2}\right)^2} \langle v^2 \rangle, \quad (1.21)$$

where we have introduced the saturation parameter $s = 2\Omega^2/\Gamma^2 = I/I_{\text{sat}}$. Heating occurs due to the random emission directions of the spontaneously scattered photons and the random times at which the absorptions happen, leading to the heating rate

$$\dot{E}_h = \frac{1}{2M} \frac{d}{dt} \langle p^2 \rangle \approx \frac{1}{2M} (\hbar k)^2 \Gamma \rho_{ee}(v=0) (1 + \xi) = \frac{(\hbar k)^2}{4M} (1 + \xi) \frac{s\Gamma}{1 + s + \frac{4\Delta^2}{\Gamma^2}}, \quad (1.22)$$

where the factor ξ accounts for the directional anisotropy between the heating and cooling forces on a dipole transition. For the cooling transition that is used in our experiment, $\xi = \frac{1}{3}$, which corresponds to a fully isotropic distribution of the spontaneously scattered photons [88].

The Doppler-cooling limit T_{min} is reached, when the heating and cooling processes are compensating each other ($\dot{E}_c = \dot{E}_h$)

$$T_{\text{min}}(\Delta) = \frac{m \langle v^2 \rangle}{k_B} = \frac{\hbar \Gamma}{8k_B} (1 + \xi) \left((1 + s) \frac{\Gamma}{2\Delta} + \frac{2\Delta}{\Gamma} \right), \quad (1.23)$$

with k_B the Boltzmann constant. The minimum value of T_{min} is reached for a laser detuning of

$$\Delta = \frac{\Gamma}{2} \sqrt{1 + s}, \quad (1.24)$$

which results in the general rule of thumb for the detuning of just half the natural linewidth when far below saturation ($s \ll 1$). From (1.23) it follows that being well below saturation is in addition the necessary condition to reach the absolute minimum temperature ($T_{\text{min}} = \frac{\hbar \Gamma}{3k_B}$) with standard Doppler cooling. On the other hand, low photon scattering rates imply a low overall rate at which the cooling process happens.

1.2.3. Optical quadrupole transition for coherent manipulations

Several mile-stone experiments (as for example [80]) have proven, that the allowed quadrupole transition between the $S_{1/2}$ and $D_{5/2}$ state at 729 nm in $^{40}\text{Ca}^+$ is the ultimate tool for coherent manipulations and quantum logic operations in an ion-trap system. A good theoretical description is given in [86] and [82]; a short summary of the most relevant details for this thesis will be given in the following.

For a coupling of the ground state $|S\rangle$ to the excited state $|D\rangle$, the interaction Hamiltonian contained in (1.8) takes the form

$$H^{(i)} = e\hat{Q}\nabla\mathbf{E}(t) \quad (1.25)$$

where e is the electron charge, \hat{Q} the quadrupole tensor, and $\mathbf{E}(t)$ the electric field of the laser. The Rabi frequency Ω in (1.8) is then defined as [90]

$$\Omega = \left| \frac{eE_0}{2\hbar} \langle S, m | (\boldsymbol{\epsilon} \cdot \mathbf{r}) (\mathbf{k} \cdot \mathbf{r}) | D, m' \rangle \right| \quad (1.26)$$

with E_0 for the electric field amplitude, $\boldsymbol{\epsilon}$ the polarization vector, and \mathbf{r} the position operator. m and m' indicate the initial and final magnetic quantum number m_j of the total angular momentum of the valence electron. Rewriting the matrix element as shown in [90] and introducing the Clebsch-Gordan coefficients $\Lambda_{m,m'}^4$ after application of the Wigner-Eckart theorem, (1.26) is expressed as [82]

$$\Omega = \frac{eE_0}{2\hbar} \sqrt{\frac{15A}{c\alpha k^3}} \Lambda_{m,m'}^{(\Delta m)} \boldsymbol{\epsilon}_i n_j \quad (1.27)$$

where A is the Einstein coefficient for the total spontaneous decay rate from any of the $D_{5/2}$ levels to all of the $S_{1/2}$ levels. α is the fine-structure constant and \mathbf{n} is the unit vector pointing in the direction of \mathbf{k} . The geometrical dependence of the quadrupole transition contained in the term

$$g^{(\Delta m)} = c_{ij}^{(\Delta m)} \boldsymbol{\epsilon}_i n_j \quad (1.28)$$

is determined by the Racah tensors $c_{ij}^{(q)}$ that are listed in [90]. Following the convention from [86], the geometry of the interaction is described by the angle φ between \mathbf{k} and the magnetic field \mathbf{B} , and the angle γ between the linear laser polarization $\boldsymbol{\epsilon}$ and the direction of \mathbf{B} , projected into the plane of incidence. Defining the coordinate system such that $\mathbf{B} = B(0, 0, 1)$, this leads with $\mathbf{n} = (\sin \varphi, 0, \cos \varphi)$ and $\boldsymbol{\epsilon} = (\cos \gamma \cos \varphi, \sin \gamma, -\cos \gamma \sin \varphi)$ to the explicit dependencies

$$g^{(0)} = \frac{1}{2} |\cos \gamma \sin(2\varphi)| \quad (1.29)$$

$$g^{(\pm 1)} = \frac{1}{\sqrt{6}} |\cos \gamma \cos(2\varphi) + i \sin \gamma \cos \varphi| \quad (1.30)$$

$$g^{(\pm 2)} = \frac{1}{\sqrt{6}} |\frac{1}{2} \cos \gamma \sin(2\varphi) + i \sin \gamma \sin \varphi|, \quad (1.31)$$

that are plotted in Figure 1.3. Of particular interest is the configuration with $\varphi = \gamma = 45^\circ$, making an excitation of all allowed transitions possible and thereby providing the highest flexibility for quantum-state engineering and the creation of coherent superpositions in the $D_{5/2}$ state with a single laser beam.

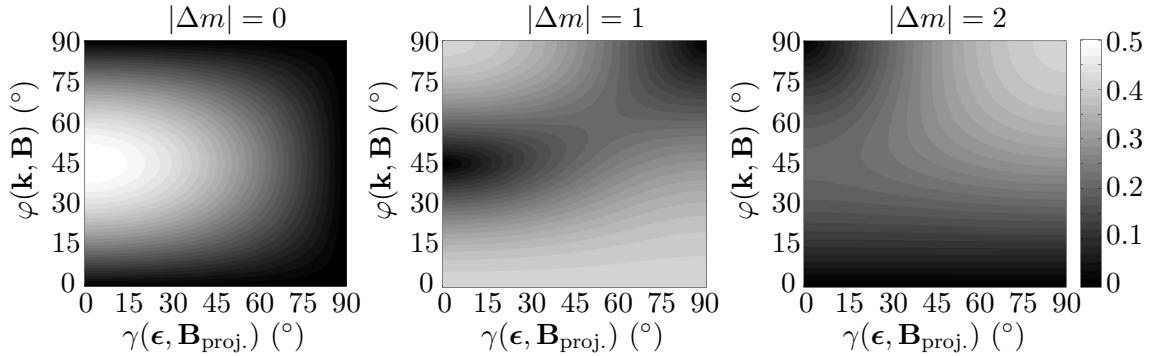


Figure 1.3.: Geometrical dependence of the relative coupling strength for all allowed transitions between sub-levels of the $S_{1/2}$ and $D_{5/2}$ state.

In the presence of a magnetic field, the Zeeman levels of S and D are shifted in frequency by $\delta\nu = g_j m \frac{\mu_B}{\hbar} B$ where g_j is the Landé factor for the respective atomic state and μ_B the Bohr

⁴For completeness, the Clebsch-Gordan coefficients are listed in Appendix A.1.

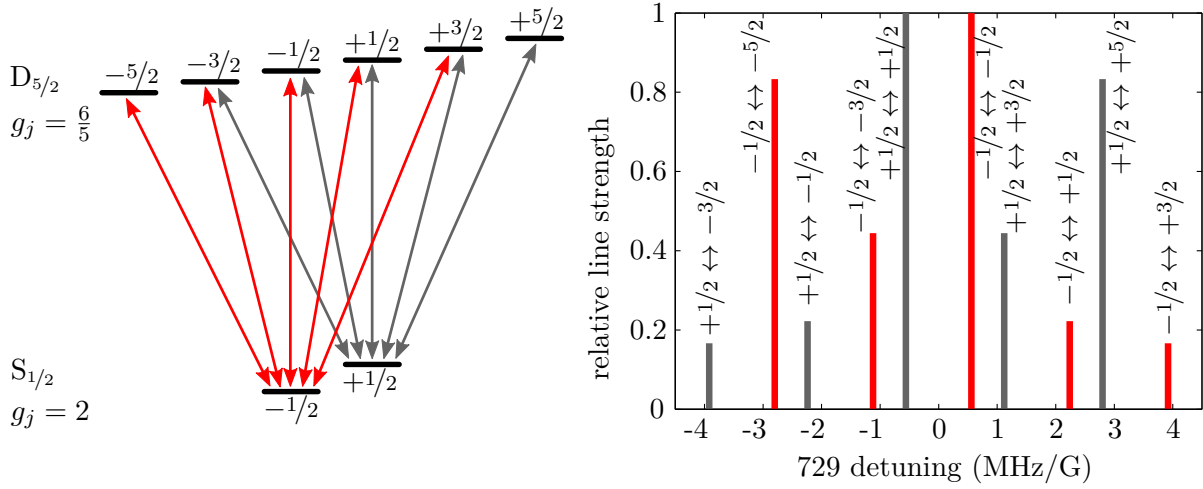


Figure 1.4.: Allowed transitions between the Zeeman levels of the $S_{1/2}$ and $D_{5/2}$ state. The line strengths ($\propto (\Lambda_{m,m'} g^{(\Delta m)})^2$) are calculated for a linearly polarized laser beam with $\varphi = \gamma = 45^\circ$ and are normalized to the strongest spectral component.

magneton. For a transition between the states $|S, m\rangle$ and $|D, m'\rangle$, this leads to a total shift in the transition frequency of

$$\delta\nu = \left(\frac{6}{5}m' - 2m\right) \frac{\mu_B}{h} B. \quad (1.32)$$

Figure 1.4 shows the resulting structure of all possible carrier transitions on the quadrupole transition, calculated for the geometry that has been used for all experiments in this thesis. An experimental spectrum is shown in Section 4.4.2, which compares very well with the expected distribution of coupling strengths.

1.3. Experimental set-up

The main motivation for the experiment is to study quantum interfaces between static and flying qubits as an essential building block for a quantum network and to demonstrate the operation of a macroscopic version of such a network on a small scale (two nodes connected by one channel). To this purpose an experiment was set up originally (at *ICFO* in Barcelona) which consists of two identical ion traps contained in individual vacuum chambers that are mounted at a distance of ~ 1 m on the same optical table. Details about different aspects of the early experimental set-up are well documented in [65, 66, 67] and will only shortly be summarized in this thesis. For historical reasons one ion trap will be referred to as the *Dark Trap* and the other ion trap as the *Bright Trap*. Almost all experiments that are presented in this thesis were carried out in the Bright Trap.

Two years after starting the thesis the whole experiment was unmounted and set up again after moving it to the *Universität des Saarlandes* in Germany. At the same time, the complete laser system was replaced by newer models with improved performance compared to the original devices. In addition, essentially the whole laser set-up including all components for frequency detuning and amplitude switching and the beams directed into the vacuum chambers was

changed to enable a completely independent operation of both ion traps. In the following sections, the experimental set-up will be explained in its final configuration after rebuilding it in Germany. All experiments presented in this thesis apart from the ones discussed in Section 3.1 were performed after the relocation of the experiment.

Section 1.3.1 gives a summary about the different laser sources available at the experiment and their stabilization. In Section 1.3.2, the most important characteristics of the ion traps including fluorescence collection and detection will be described. Section 1.3.3 will shortly summarize the properties of the pulse sequencer that is used to control the experiment.

1.3.1. Laser system

To be able to access all relevant electronic levels of $^{40}\text{Ca}^+$ (see Figure 1.2), to ionize single Calcium atoms, and to stabilize the frequency of most of the required laser sources, diode lasers at seven different wavelengths with different spectral linewidths $\Delta\nu$ are used in the experiment:

846 nm: First photoionization step of neutral ^{40}Ca atoms; free running, $\Delta\nu < 2\text{ MHz}$.

397 nm: Doppler cooling, optical pumping, and state detection; frequency stabilized with transfer lock, $\Delta\nu < 300\text{ kHz}$.

866 nm: Repumper when working with the 397 nm laser; frequency stabilized with transfer lock, $\Delta\nu < 300\text{ kHz}$.

850 nm: Excitation of $\text{D}_{3/2}\text{-P}_{3/2}$ transition; frequency stabilized with transfer lock, $\Delta\nu < 300\text{ kHz}$.

854 nm: Excitation of $\text{D}_{5/2}\text{-P}_{3/2}$ transition, optical pumping, and master laser of the entangled-photon pair source; frequency stabilized with transfer lock, $\Delta\nu < 300\text{ kHz}$.

852 nm: Reference laser for the transfer lock; stabilized to Cs vapor cell, $\Delta\nu < 300\text{ kHz}$.

729 nm: Coherent manipulations; stabilized to ultra-stable reference cavity, $\Delta\nu < 1\text{ kHz}$.

The frequency, phase, and amplitude of all laser beams is controlled by using acousto-optic modulators (AOMs). A small fraction of light of every laser is sent to a wavemeter (HighFinesse, WS7) to monitor its precise wavelength.

Photoionization

A very detailed description of the photoionization set-up including a review of several other possible schemes is found in [65].

The basic principle is to excite neutral ^{40}Ca atoms, coming out of an oven, first with a resonant two-photon excitation to a high lying Rydberg state. Due to the strong electric fields that the atoms experience in the Paul trap they are then subsequently ionized by the release of a singly excited valence electron to the continuum.

The first excitation step is done on the $4s^2\ ^1\text{S}_0 - 4s4p\ ^1\text{P}_0$ transition of Ca at 423 nm. The laser light is produced by second harmonic generation in single passage in a PPKTP crystal that is pumped with a high power ($\sim 130\text{ mW}$) commercial grating-stabilized diode laser at 846 nm

(Toptica, DL 100). The laser is not frequency stabilized; while monitoring the wavelength on the wavemeter, it is usually just tuned by hand to the known atomic resonance. The second excitation step from $4s4p\ ^1P_0$ to high lying Rydberg states ($n \geq 40$) at a wavelength of 390 nm is then achieved with a UV LED (Nichia, NCCU001) with an emission spectrum centered around 380 nm and a bandwidth (FWHM) of around 30 nm. For each vacuum chamber, both light sources are spatially overlapped in a multimode fiber and focused to the trap center. The typical time scale for trapping a single ion in each trap is about 5 min.

397 nm, 866 nm, 850 nm, and 854 nm

The laser light for Doppler cooling at 397 nm is generated by second harmonic generation of light at 794 nm that is coming from an amplified grating-stabilized diode laser (Toptica, TA-SHG pro). Three AOMs (Brimrose, TEF-125-100-400) set up in double-passage configuration are utilized to control three individual beams that are required for laser cooling and state discrimination in the Dark Trap, and laser cooling, state discrimination and optical pumping in the Bright Trap.

The laser beams for repumping during cooling (866 nm) and for optical pumping to the other levels (850 nm, 854 nm) are all grating-stabilized diode lasers (Toptica, DL pro). For 866 nm and 850 nm, two AOMs per wavelength (Brimrose, TEF-125-100-798, TEF-150-100-860) in double-passage configuration are used to provide independent control of the beams for the two traps. The laser at 854 nm is mainly used as a master laser for the entangled photon-pair source that will be explained in Chapter 2. A small portion of its amplified power is split off and sent to the ion-trap table. Two double-passage AOMs (Intraaction, ATM-2001A2; Brimrose, TEM-200-50-860) are utilized to control two individual beams, allowing for excitation or optical pumping from two different directions in the Bright Trap or from a single direction in the Bright and the Dark Trap. Due to the construction of the photon-pair source, the master laser runs on resonance with the atomic transition. This requires to introduce an additional frequency shifter (Intraaction, ATM-2001A2) which compensates the shifts induced by the just mentioned AOMs.

All beams are sent through polarization maintaining single-mode fibers to the vacuum chambers. There they are typically collimated with a fiber coupler (Schäfter + Kirchhoff, 60FC-4-M12) and focused with a plano convex lens of focal length $f = 250$ mm to the trap center. This results in focal spot sizes of maximally $130\ \mu\text{m}$ ($1/e^2$), depending on the wavelength.

All lasers are frequency stabilized using a transfer-locking scheme that will be explained in the next section. From spectroscopy experiments as the ones that will be shown in Section 5.2.1, we infer a spectral linewidth of the lasers which is around $\Delta\nu \approx 130$ kHz.

Transfer lock

The overall scheme for the transfer lock and its characterization are explained in detail in [66, 91]. The required electronics for the lock are described in [67].

The main idea behind the transfer-locking scheme is to achieve, on the one-hand side, narrow laser linewidths through a Pound-Drever-Hall lock⁵ to low-finesse Fabry-Pérot cavities ($\Delta\nu =$

⁵A short explanation with all relevant references for the Pound-Drever-Hall technique will be given in Section 4.1.2.

1.9 MHz) and to reach, on the other-hand side, long-time stability by locking these cavities (the so-called *transfer cavities*) to an atomic reference.

The core of the locking chain is a grating-stabilized diode laser at 852 nm (Toptica, DL 100) which is frequency stabilized to the D2 line in Cs by a combination of frequency-modulation spectroscopy and Doppler-free absorption spectroscopy in a Cs vapor cell at room temperature. The stability of this reference laser is then transferred to the transfer cavities by stabilizing their length with a Pound-Drever-Hall lock which is implemented by home-built electronics called *cavity lockers* [67]. The lasers that need to be stabilized are then locked with (again) the Pound-Drever-Hall method to the transfer cavities. The different transfer-cavity lengths are tuned such that the resonance condition for each laser is achieved at the exact frequency of the corresponding transition in $^{40}\text{Ca}^+$.

Even though the scheme requires sophisticated self-built electronics, it is highly modular and allows a completely decentralized stabilization of many lasers. In addition, all components operate under atmospheric pressure at room temperature and no vacuum chamber and cavity spacer made from ultra-low expansion material are needed. However, working under atmospheric pressure makes the system sensitive to changes of the barometric pressure inside the lab which are directly correlated with the general weather situation. Changes of the air pressure are changing the refractive index inside of the air-filled transfer cavities, causing slow drifts of the lasers on the time scale of several days. Therefore it is unavoidable to precisely calibrate critical laser frequencies (as the ones for Doppler cooling) every morning by doing spectroscopy with an ion.

Qubit laser at 729 nm

As part of this thesis, an ultra-stable laser at 729 nm has been set up to address the optical quadrupole transition in $^{40}\text{Ca}^+$ for coherent manipulations. A detailed description of the set-up and a characterization is found in Chapter 4.

The laser system is a grating-stabilized and amplified diode laser (Toptica, TA pro), delivering up to 500 mW of power at 729 nm. To achieve a long coherence time, it is stabilized to an ultra-stable high-finesse cavity ($\Delta\nu = 4$ kHz) made from ultra-low expansion glass, employing a very fast feedback loop with the already mentioned Pound-Drever-Hall technique. Measurements discussed in Section 6.2.2 show that the laser has a spectral linewidth below 32 Hz. For the switching and detuning of the laser beams going to both vacuum chambers, a slightly more sophisticated AOM set-up is used than for the other lasers in the experiment, details will follow in Section 4.2.2.

1.3.2. Double-trap apparatus

The ion traps were mainly set up by F. Rohde, C. Schuck, M. Almendros, and M. Hennrich, a detailed documentation is found in the PhD theses [65] and [66].

Paul traps

The linear Paul traps that are used in the experiment were originally designed in the group of Prof. R. Blatt at the University of Innsbruck where they were also manufactured in the mechanical workshop. The dimensions of the trapping region are $r_0 = 0.8$ mm for the blade

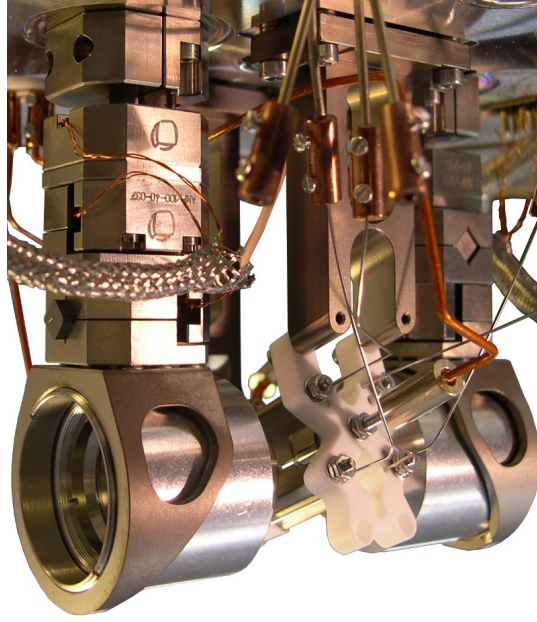


Figure 1.5.: Picture of one ion trap surrounded by two HALOs that are mounted on xyz -translation stages.

distance to the trap center and $l_0 = 2.5$ mm for the distance of the endtips to the center. The Dark Trap is running at a radio frequency of 25.890 MHz with 8.5 W power and the Bright Trap at 26.135 MHz with 9 W power. The endtips are usually operated at a voltage of $U_{\text{tip}} = 400$ V, resulting in axial trap frequencies of 1.195 MHz for the Bright Trap and 1.166 MHz for the Dark Trap.

HALOs

As shown in Figure 1.5, each ion trap is surrounded by two High numerical Aperture Laser Objectives (HALO) that are hanging on xyz -translation stages (Attocube). Details about this part of the set-up are found in [65]. The most important features of these objectives are a numerical aperture $\text{NA} = 0.4$ at a working distance ranging from 11.8 mm (397 nm) to 13.2 mm (866 nm) and diffraction limitation over the whole range of required wavelengths, leading to focal spot sizes of $1.2 \mu\text{m}$ for 397 nm and $2.6 \mu\text{m}$ for 866 nm. Corresponding to the high numerical aperture, it is possible to cover 4.17 % of the whole solid angle with each HALO. For each trap, one HALO is aligned for optimal coupling to a single ion at 854 nm and the second one for 397 nm.

Fluorescence detection

The fluorescence light from each trap at 397 nm is coupled to a multi-mode fiber and detected with a PMT (Hamamatsu, H7422P-40 SEL). A typical value for the overall detection efficiency of single photons at 397 nm that are emitted by a single ion is around 0.7 % when using only one HALO for the collection. As an alternative way there is the option to send the fluorescence

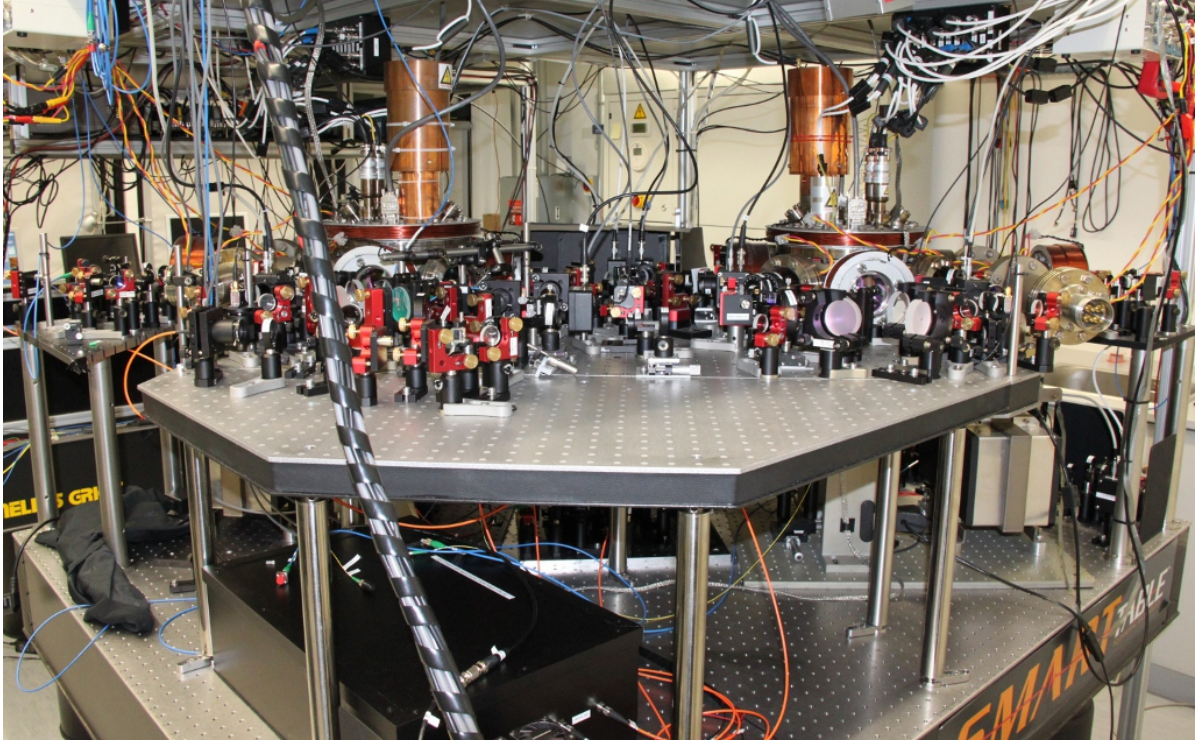


Figure 1.6.: Picture of the optical table containing the double-trap set-up in the new lab at the Universität des Saarlandes.

light from both traps to an EMCCD camera (Andor, DV887DCS-BV), which is usually used during the trapping of single ions.

Magnetic field control

Each trap is mounted in a separate vacuum chamber under ultra-high vacuum conditions. Figure 1.6 shows a picture of the double-trap apparatus. Magnetic coils positioned at right angles around each trap center (on the outside of the vacuum chambers) are used to apply a magnetic field on a chosen quantization axis and to precisely compensate static stray fields. The coil currents are controlled with home-built electronics, providing a current stability of $100 \mu\text{A}$.

1.3.3. Experiment control

Already basic quantum-optics experiments with single ions require a high degree of control over the individual laser sources in terms of frequency and amplitude tuning, and a system to record the fluorescence photons that are emitted by the ions. More sophisticated experiments make use of complex pulse sequences, including the precise timing and phase control of laser pulses and the ability to determine and react to the quantum state of an ion in real time. The laser beams are usually switched with AOMs which makes it necessary to achieve the above mentioned requirements in the RF regime.

M. Almendros developed during his PhD a highly versatile pulse sequencer called *HYDRA*, which fulfills all of the necessary requirements for state-of-the-art quantum-optics experiments with the set-up. A detailed description is found in his thesis [67].

HYDRA is a backplane-based bus system of parallel synchronized RF signal generators that is controlled by a digital signal processor (DSP). This makes a completely autonomous and fast operation of the system possible. A connected PC is only needed to load and initialize a sequence and to record the collected data. The individual RF modules connected to the backplane consist basically of a direct digital synthesizer (DDS) and a digital to analog converter (DAC), enabling the generation of RF output signals with variable frequency and amplitude. Each module is independently controlled by a field programmable gate array (FPGA), which makes it possible to drive very fast and complex pulse forms or sequences on several modules independently. Some of the modules feature additionally an analog input channel and an implemented (digital) PID to give a feedback to the amplitude of the output signal. This enables the stabilization of the intensity of a laser beam by feeding an amplitude signal from a photodiode to the analog input. The system further features plenty of digital inputs and outputs and 8 counters that are used for counting fluorescence photons. The most important specifications of the system are

- 80 MHz of maximum update rate.
- RF output ranging from 4.5 to 300 MHz.
- Maximum RF output attenuation below -80 dB.
- Conditional jumps to different parts of a sequence depending on different input variables.

The sequencer is controlled by a computer program written in C++, which is also the language that is used to program individual sequences. Sequence programs consist of sequential instructions in the form of packages that are executed at certain triggers by the FPGAs in the individual output modules and the DSP. Due to the highly parallel design of the device, the programming of sophisticated sequences with conditional jumps and loops is quite a challenge, but feasible with a profound hands-on practice with the system.

The 80 MHz clock speed of the system limits the maximum timing precision of the counter modules. The shortest counter interval is therefore given by 12.5 ns, which is not sufficiently fast for experiments that rely on very fast correlations as the ones discussed in Chapter 3. Therefore a time-tag mode which records the time stamps of individual photon detection times is not implemented in HYDRA. The photon counts recorded in a certain acquisition time are either stored directly in the connected PC (as for normal spectroscopy) or stored temporarily in a variable inside HYDRA to determine the quantum state of an ion in real time (see Section 4.4.1). For the experiments described in Chapter 3, which require high temporal resolution, data acquisition is usually carried out with a time-correlated single-photon counting system (PicoQuant, PicoHarp 300), offering a maximum timing resolution of 4 ps.

2. Hybrid quantum network

The ion-trap set-up introduced in the previous chapter contains already all necessary components that are required for an extensive study of different quantum-network scenarios as proposed in [38, 40, 92]. However, those schemes focus on the generation of entanglement between two distant nodes of the network, which is already a complex task and often requires the combination of several fundamental building blocks. One fundamental operation in a quantum network being of general interest is to perform the state mapping from a photon, that is entangled with a second quantum system, to a single atom. To study this type of atom-photon interaction, it is possible to generate single photons, that are entangled with their atomic emitter (as for example demonstrated in [55]), but this is a demanding experiment on its own and therefore not convenient for detailed studies of only the absorption process.

A much more robust way to generate photons that are entangled with another quantum system is by spontaneous parametric down conversion (SPDC) [93, 94], which enables the generation of entangled photon pairs at high rates. Hong and Mandel [95] demonstrated that the detection of the so-called *signal* photon of a pair heralds the presence of the strongly time correlated second photon of the pair – called *idler* – and that the photon-pair source is thereby converted into a so-called *heralded single-photon source*. This type of single-photon source is technologically very simple (compared to a single-atom experiment) and represents therefore a convenient tool to study schemes for the state mapping from photons onto ions at the single-particle level.

Another motivation for the operation of an entangled photon-pair source in combination with an ion-trap set-up is the very prominent role of SPDC based photon-pair sources in the nowadays already far developed field of quantum communication [30]. Apart from the systems for quantum key distribution that are already commercially available, several milestone experiments as long-distance teleportation of quantum states through an optical fiber [33] or even over free space [34], have proven that SPDC photon-pair sources provide an excellent and easy to operate resource of entanglement for realistic quantum-network scenarios.

But pure quantum communication is not the only application of photon-pair sources. Following the proposal for universal quantum computation with linear optics [16] or the promising scheme for one-way quantum computation with entangled cluster states [96], photon pairs have also proven to be an excellent candidate system for quantum logical tasks, as for example demonstrated in [97, 98]. Even though deterministic operations are in principle possible with those schemes [99], the preparation of the input qubits is usually still probabilistic [100], lowering the efficiency of the computations and thereby the scalability of the systems. But nevertheless, this field is still quickly advancing and there is no doubt, that entangled photon-pair sources will be the future universal work horses for real-world implementations of long-range quantum networks.

On the other hand, quantum processors based on strings of trapped ions are, to date, the furthest developed tool to carry out deterministic universal quantum-computational tasks with

highest fidelities, that are not reached by any other quantum system. It is therefore of fundamental interest to experimentally study the operation of a hybrid quantum system, which arises by interfacing an ion-trap quantum processor with entangled photon pairs produced by SPDC.

For this purpose, N. Piro has set up an entangled photon-pair source during his PhD, which is resonant with the $D_{5/2} - P_{3/2}$ transition in $^{40}\text{Ca}^+$ at 854 nm. A detailed description is found in his thesis [68] and in references [101, 102]. Since this photon-pair source is a small experiment on its own and governed by a completely different field of physics, it is described here in a separate chapter. Nevertheless, it has to be considered as just a highly specialized component of the overall ion-trap experiment, which makes the set-up so far unique in the ion-trapping community.

In Section 2.1, the physical principle of SPDC will be summarized and Section 2.2 will give an overview of the experimental set-up of the photon-pair source. Section 2.3 will focus on one possible scheme to study the transfer of entanglement from a photon pair to a single ion, which is the main motivation for all experiments presented in this thesis.

2.1. Spontaneous parametric down conversion

Spontaneous parametric down conversion is a phenomenon described in nonlinear optics that occurs when a strong light field \mathcal{E} is incident on an optical medium that exhibits a second order non-linearity in its polarizability P .

$$P = \epsilon_0 \chi^{(1)} \mathcal{E} + \epsilon_0 \chi^{(2)} \mathcal{E}^2 + \dots, \quad (2.1)$$

where ϵ_0 is the permittivity of free space and $\chi^{(n)}$ the n th-order electric susceptibility of the medium. In the resulting three-wave mixing process it is possible to transform a single incident photon from a *pump* beam at frequency ω_p to two single photons at frequencies ω_s (signal) and ω_i (idler). Since this is a spontaneous process, stimulated by fluctuations of the vacuum field, the efficiency in a normal bulk crystal is usually very low ($\sim 10^{-10}$ photon-pair production rate per pump photon [103]). Assuming that no momentum or energy is transferred to the medium results in the so-called phase-matching conditions

$$\omega_p = \omega_s + \omega_i \quad (2.2)$$

$$\mathbf{k}_p = \mathbf{k}_s + \mathbf{k}_i, \quad (2.3)$$

where $\mathbf{k}_{p,s,i}$ are the wave vectors for pump, signal, and idler in the medium.

The nonlinear medium that is used in the photon-pair source is KTiOPO_4 (KTP); details about the geometric and nonlinear properties of this material are found in [68]. The crystal is designed for *collinear* generation of signal and idler photons at the same frequency $\omega_s = \omega_i = \omega_p/2$, which means that they are generated in the same spatial mode, with their propagation direction parallel to the pump.

The system is further designed to generate signal and idler photon with opposite linear polarizations, of which one is identical with the polarization of the pump. This configuration is termed as *Type-II* phase matching in the literature.

Birefringence in the crystal causes then a different refractive index for the propagation of signal and idler which results in a phase mismatch of both waves and a wave-vector mismatch

$\Delta\mathbf{k}$. Due to this additional term, (2.3) is usually not exactly fulfilled, thereby strongly reducing the overall conversion efficiency. A convenient method to overcome this deficiency is to periodically reverse the phase by equipping the crystal with a periodically inverted nonlinear coefficient along the propagation axis. This may be achieved by exposing the crystal in the production process to an electrical field with periodically inverted polarity, which gives this process the name *poling*. By adjusting the poling period Λ to the phase mismatch $\Delta\mathbf{k}$ by [104]

$$\Lambda = \frac{2\pi}{\Delta k}, \quad (2.4)$$

it is possible to optimize the down-conversion process for a specific wavelength. This technique of periodic poling (PP) is called *quasi-phase matching*.

To summarize, the entangled photon-pair source in the lab generates polarization-entangled photon pairs by type-II collinear SPDC in a PPKTP crystal. The photon pairs which it produces are found in the maximally entangled $|\Psi^-\rangle$ Bell singlet state with respect to the polarization basis of horizontal and vertical polarization $\{|H\rangle, |V\rangle\}$ [101, 102]:

$$|\Psi^-\rangle = \frac{1}{\sqrt{2}}(|H\rangle_i|V\rangle_s - |V\rangle_i|H\rangle_s). \quad (2.5)$$

2.2. Experimental set-up

The experimental set-up is described in detail in [102, 68], this section is only meant to give an overview about the main features that are important for its operation and a better understanding of the experiments that are presented in this thesis. Figure 2.1 gives an overview of the main components.

The most important device is the before-mentioned master laser of the source, running at 854 nm. This diode laser is first amplified (not displayed in the figure) and then frequency doubled within the same commercial system (Toptica, TA-SHG 110¹), delivering typically around 60 mW of power at 427 nm after a short single-mode fiber, right before the PPKTP crystal. The laser is frequency stabilized using the transfer-locking scheme as described in Section 1.3.1. Compared to the other lasers on the ion-trap set-up, frequency tuning of the master laser is not achieved by sending it through an AOM since the resulting losses due to limited diffraction efficiencies would be too high. Tunability is obtained by detuning the 852 nm laser that is used to lock the transfer cavity of the system with an AOM and thereby effectively changing the setpoint for the frequency of the 854.

As described in the previous section, entangled photon pairs at 854 nm are then produced by spontaneous parametric down conversion in a PPKTP crystal, which is coupled in free space using lenses. The photon pairs are then split with a beam splitter and one arm is directly coupled into a single-mode fiber which is connected with the ion-trap experiment. The second arm is first sent through a polarization analyzing unit comprising a half-wave plate (HWP), a quarter-wave plate (QWP), and a polarizing beam splitter (PBS), before it is coupled to a polarization maintaining single-mode fiber.

The output of this fiber is coupled to a narrow-band spectral filter which consists of two cascaded and actively stabilized Fabry-Pérot cavities. Throughout the thesis, this part of the

¹During the move of the experiment the system got replaced by the model *TA-SHG pro* which has essentially the same specifications but offers a much better long-term stability.

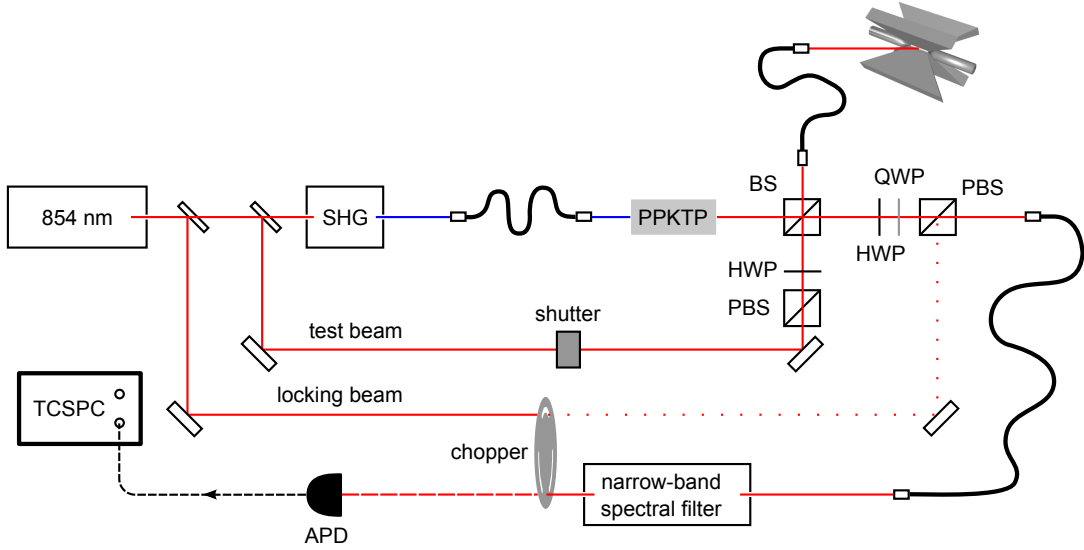


Figure 2.1.: Schematic representation of the narrow-band entangled photon-pair source when operated as a heralded single-photon source. Lenses and passive spectral filters are omitted in the drawing. The used acronyms are as follows: TCSPC: Time Correlated Single Photon Counter, SHG: Second Harmonic Generation, QWP: Quarter Wave Plate, HWP: Half Wave Plate, BS: non-polarizing Beam Splitter, PBS: Polarizing Beam Splitter.

source will be called the *filter arm* and down-conversion photons passing through it will be called *filtered photons*. The spectral filtering unit cuts out a 22 MHz bandwidth of the 200 GHz broad emission spectrum from the down-conversion process. A small portion of light from the master laser is split off and sent through a chopper to the cavity filters that are then stabilized with a Pound-Drever-Hall lock to the master-laser frequency. The filtered photons are detected with an avalanche photo diode (APD) that is connected to the counting electronics mentioned in Section 1.3.3. To protect the APD from the locking beam, the filtered photons pass through the same anti-correlated chopper always when the locking beam is blocked on the filter input side. Due to its slot ratio of 85:15 (filtered photons:locking beam), the chopper limits the maximum possible duty cycle of experiments with the photon-pair source to 85%. The rotation speed is usually adjusted around 10 Hz.

The cavity-filter bandwidth is chosen to correspond to the atomic transition linewidth in $^{40}\text{Ca}^+$ and is centered at the frequency of the master laser. Owing to the frequency correlation between signal and idler defined in (2.2), a frequency mismatch between a detected signal photon in the filter arm and the master laser $\Delta\omega_s$ always corresponds to an opposite detuning of the correlated partner photon in the unfiltered arm of the source

$$\Delta\omega_s = -\Delta\omega_i . \quad (2.6)$$

Within the filtering bandwidth, both photons of a pair are therefore considered to be degenerate in their frequency. When tuning the master laser onto the atomic resonance, the filter perfectly mimics the absorption bandwidth of the ion and thereby selects signal photons with partners

that are resonant with the atomic transition. This enables one to observe coincidences between single-photon clicks in the filter arm and single-photon absorptions by a single ion.

A small fraction of light from the master laser is used as a test beam and is directly coupled to the single-mode fiber, connecting the source with the ion experiment. This beam can be switched on and off with a shutter and is usually used to optimize the coupling of the fiber output mode to a single trapped ion. For the experiments discussed in Section 3.1.5, it is important to preserve arbitrary polarization states of the photons that are sent to the ion. The test beam is then (together with the PBS and HWP) used to provide a polarization reference which is needed to check and adjust the neutrality of the non-polarization-maintaining fiber.

2.3. Scheme for entanglement transfer

The most obvious application for a hybrid quantum network consisting of strings of trapped ions and entangled photon-pair sources is to study the controlled transfer of entanglement from flying qubits onto the nodes of the network. This would essentially facilitate the direct loading of a qubit into a quantum processor, after it has been transmitted over a network. Performing the simultaneous entanglement transfer from a photon pair to two distant ions would further enable the generation of entangled pairs of ions between different nodes of the network. Following the generic scheme for a quantum repeater as proposed by Briegel *et. al* [32], the entanglement could then be *swapped* to more distant nodes of the network by local ion-ion entanglement operations (as for example in [18]) between two ions from different pairs.

2.3.1. Motivation

In more general terms, the proposal for a quantum repeater [32] requires as a prerequisite the simultaneous existence of many pairs of entangled particles at different network sites, which could also be achieved by only using photons. But in the case of a purely photonic network, these so-called elementary links would have to be generated all at the same time, resulting in a very low success probability for a long-distance implementation of a quantum repeater. Therefore, the general agreement exists that the use of quantum memories in the nodes is essential for the scalable operation of a quantum repeater since it enables the preparation of the subsystems with probabilistic entanglement schemes and performing the deterministic swapping operations only as soon as all of the elementary links are ready.

This implies that trapped ions are not necessarily appropriate as intermediate nodes for a quantum repeater since the efficient coupling of single atoms with single photons is still a major challenge. But there exists a variety of other candidate systems to implement quantum memories which offer much better coupling efficiencies. The most promising memories to date offering very high write and read-out fidelities are based on atomic ensembles in vapor [105] or rare-earth doped crystals, as for example demonstrated in [106]. However, at the moment those systems are not yet significantly less demanding than an ion-trap experiment, which makes their scalability still problematic. In addition, entanglement swapping has to be implemented by first mapping the memory state back onto photons and then performing the necessary operations using linear optics [107]. This makes those quantum-repeater implementations vulnerable to detector dark counts and limited photon detection efficiencies, which significantly influences

the fidelity of the swapping process compared to the almost 100 % fidelity [18] that is achieved in a linear ion trap.

Even if the intermediate links of a quantum-repeater assisted quantum network may be implemented with other physical systems (that might be more suitable than strings of trapped ions), the resulting quantum channel will at some point have to be connected to a quantum processor. Judging from the current state of research in quantum information processing, this quantum processor is most likely to be implemented by trapped ions in a dedicated trap architecture.

One approach to link the quantum processor to the network is to use a teleportation protocol following the proposal by Bennett *et al.* [31]. This would require to entangle first a single ion from the processor with an emitted photon and to perform then a Bell-state measurement of this photon together with the flying qubit coming from the network channel. The process therefore requires a high degree of control over the temporal overlap of both photon wave packets in the Bell-state measurement. The second possible approach is to perform a controlled single-photon absorption of the flying qubit by a single trapped ion in such a way, that the quantum state is transferred to and permanently stored in the atomic level structure. This has not been demonstrated yet and is the main motivation for all experiments and results presented in this thesis. At first sight, the absorption scheme seems to be conceptually much simpler than the teleportation scenario, but a closer look at the necessary steps that will be outlined in the following section reveals that the main difficulties are essentially the same.

The biggest challenge in quantum-repeater architectures and more general quantum networks is that almost all fundamental operations rely on either the absorption, emission, or detection of single photons. Concerning detector efficiencies, only small improvements were obtained during the past years and no fundamental technological breakthrough is expected for the near future². The only process that could be greatly enhanced is to gain a better control over the single-photon absorption and emission of atomic systems.

The most popular approach is to place single atoms in optical cavities which greatly enhances the coupling efficiency for both, the emission and the absorption of single photons as demonstrated in [59]. Even though these complex systems achieve impressive coupling efficiencies in the few-10 % range, the overall success probabilities are still far from unity. To improve the absorption process, a second possible strategy is to design the interaction process such that a heralding event is generated which announces the success of a single-photon absorption. This scenario is particularly attractive since it is independent of optimizing the absorption itself. Control over the whole process is simply gained by making the very rare absorption events visible with very high probability. Such heralded absorption is pursued here.

2.3.2. Scheme

The level scheme of $^{40}\text{Ca}^+$ offers perfect conditions for studying the heralded absorption of photons at 854 nm. There exists a large variety of possible scenarios to perform the state mapping from a single absorbed photon onto the atomic ground state; an overview and detailed discussion will be available in [108, 109]. In the following we will focus on one possible scheme which is conceptually clear and serves to explain the main technical steps that are necessary for

²At least what concerns a gain of quantum efficiency at a constantly high temporal resolution in the visible, which is usually necessary for the work with atomic systems.

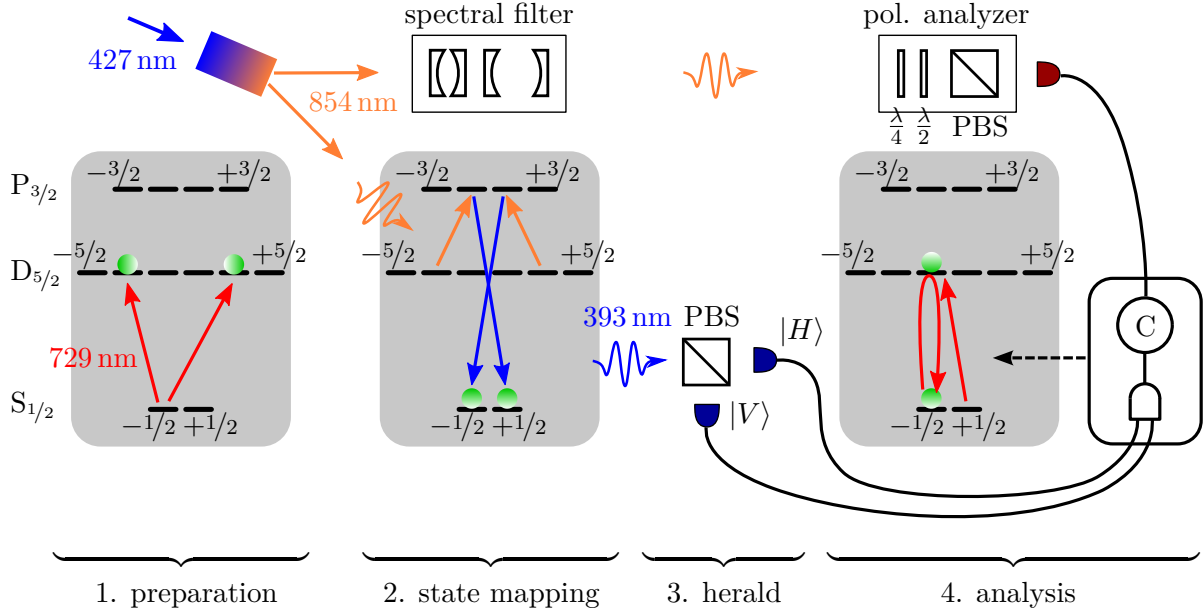


Figure 2.2.: Scheme for entanglement transfer from an entangled photon pair onto a single ion and a single photon. The upper part represents the essential components from the source, the lower part the corresponding steps for the ion-trap experiment (only the outermost magnetic quantum numbers are labeled in the level scheme). The main B-field at the ion must be oriented in parallel to the wave vectors of the absorbed and Raman scattered photon ($\mathbf{B} \parallel \mathbf{k}_{854} \parallel \mathbf{k}_{393}$). Note that for conceptual reasons the order of spectral filter and polarization analyzer is reversed in the filter arm of the source. A stepwise explanation of the scheme is given in the text.

an implementation of most of the other schemes. Additionally, this scheme fulfills the geometric requirements imposed by the present experimental set-up and is therefore a candidate for an experimental implementation.

Figure 2.2 gives an overview of the scheme to perform and verify the transfer of the entanglement from a photon pair to a single ion and a remaining photon. It is obvious that the scheme also serves to map arbitrary polarization-qubit states of single photons onto a single ion and to transfer photonic entanglement to remote entanglement of two ions. The four essential steps are identified as the preparation of the ion, the state transfer via a spontaneous Raman transition, the detection of a single heralding photon, and the analysis of the final qubit states.

1. Preparation

As explained in Section 2.1, the entangled photon-pair source generates pairs at 854 nm in the maximally entangled singlet state

$$|\Psi^-\rangle_{\text{photon}} = \frac{1}{\sqrt{2}}(|H\rangle_i |V\rangle_s - |V\rangle_i |H\rangle_s), \quad (2.7)$$

where the indices s and i indicate the state of signal and idler.

The ion is prepared in a coherent superposition in the metastable $D_{5/2}$ state ($\tau \approx 1.17$ s) between the magnetic sub-levels with $m = -3/2$ and $m = +3/2$

$$|\Psi\rangle_{\text{ion}} = \frac{1}{\sqrt{2}}(|D_{5/2}, -3/2\rangle + |D_{5/2}, +3/2\rangle) . \quad (2.8)$$

This will be attained by coherent manipulations with the laser at 729 nm.

2. State mapping

One photon of a pair (the signal) will be sent through the spectral filter in the source, mimicking the absorption bandwidth of the ion. Due to the degeneracy of the photon pairs, this will select the bandwidth of the corresponding idler photon which is then potentially absorbed by the ion.

The idler will be sent to the ion with its wave vector \mathbf{k}_{854} parallel to the main magnetic field \mathbf{B} , defining the quantization axis for the ion. It is therefore more convenient to describe the two-photon state right before the absorption in a circular polarization basis in the reference frame of the ion

$$|\Psi^-\rangle_{\text{photon}} = \frac{1}{\sqrt{2}}(|\sigma^+\rangle_{\text{i}}|\sigma^-\rangle_{\text{s}} - |\sigma^-\rangle_{\text{i}}|\sigma^+\rangle_{\text{s}}) , \quad (2.9)$$

with σ^\pm being the circular polarizations that excite dipole transitions with $\Delta m = \pm 1$.

During the absorption, the ion will be excited to the $P_{3/2}$ state which decays with 93.5 % probability [110] to the $S_{1/2}$ groundstate. In this Raman process, a single UV photon at 393 nm will be generated, providing an excellent herald for the single photon absorption. When observing the emission of the herald at the time t_{h} along the quantization axis ($\mathbf{B} \parallel \mathbf{k}_{393}$) and in the circular polarization basis, the resulting wave function of the remaining signal, herald, and ion is described by the entangled state

$$|\Psi\rangle = \frac{1}{\sqrt{2}}(|S_{1/2}, +1/2\rangle|\sigma^+\rangle_{\text{h}}|\sigma^-\rangle_{\text{s}} - e^{i\omega\Delta t}|S_{1/2}, -1/2\rangle|\sigma^-\rangle_{\text{h}}|\sigma^+\rangle_{\text{s}}) , \quad (2.10)$$

where the index h denotes the polarization state of the herald. The phase factor accounts for the accumulated phase of the state due to the random delay $\Delta t = t_{\text{h}} - t_0$ between the absorption at t_{h} and the preparation of the superposition in $D_{5/2}$ at t_0 . In the reference frame rotating at the frequency splitting of the final superposition in $S_{1/2}$, the frequency ω of this phase evolution is given by the energy difference to the superposition in $D_{5/2}$.

3. Detection of herald

One important detail about this scheme is that depending on the direction of observation, the polarization of the herald will be entangled with the internal state of the ion. Therefore this information has to be erased before measuring the presence of a herald by projecting its polarization state to the $|H\rangle$ - $|V\rangle$ basis with the aid of a polarizing beam splitter (PBS), when observing the photons along the quantization axis. Each herald will then be randomly projected to either $|H\rangle_{\text{h}} := \frac{1}{\sqrt{2}}(|\sigma^+\rangle_{\text{h}} + |\sigma^-\rangle_{\text{h}})$ or $|V\rangle_{\text{h}} := \frac{1}{\sqrt{2}}(|\sigma^+\rangle_{\text{h}} - |\sigma^-\rangle_{\text{h}})$. Depending on which detector is measuring a photon on the two output ports of the PBS, this results then in the two possible final states of ion and signal photon

$$|H\rangle_{\text{h}} : \quad |\Psi\rangle = \frac{1}{\sqrt{2}}(|S_{1/2}, +1/2\rangle|\sigma^-\rangle_{\text{s}} - e^{i\omega\Delta t}|S_{1/2}, -1/2\rangle|\sigma^+\rangle_{\text{s}}) \quad (2.11)$$

$$|V\rangle_{\text{h}} : \quad |\Psi\rangle = \frac{1}{\sqrt{2}}(|S_{1/2}, +1/2\rangle|\sigma^-\rangle_{\text{s}} + e^{i\omega\Delta t}|S_{1/2}, -1/2\rangle|\sigma^+\rangle_{\text{s}}) . \quad (2.12)$$

Apparently there exists also the possibility to generate a spontaneous Raman photon on the two accessible π transitions ($\Delta m = 0$) from $P_{3/2}$ to $S_{1/2}$. Due to the dipole emission characteristics (see Appendix A.2), those photons are not emitted along the quantization axis and do therefore not disturb the discussed scheme. They could of course be used as herald in a different transfer scheme with a different geometry ($\mathbf{B} \parallel \mathbf{k}_{854} \perp \mathbf{k}_{393}$).

A second detection event is obtained by the signal photon at the end of the filter arm in the source. The correlation of this event with the coincident detection of the herald of the ion serves as an overall trigger, which indicates the successful transfer of the entanglement with the subsequent measurement of the signal photon in a certain polarization basis.

4. Analysis

The analysis of the polarization state of the signal photon in a certain basis is trivial, it is achieved by sending it through a standard polarization analyzing unit as depicted in the figure.

The state detection in a certain basis on the ion is a more complex task. First, the detected random phase flip of π of the state due to the projection of the herald with the PBS as described in step 3 has to be taken into account for the later choice of the measurement basis. Second, the phase accumulated due to the random time at which the absorption happened has to be determined. This is achieved by precisely measuring Δt via the detection of the herald. Taking this second phase contribution to the final state additionally into account and utilizing the 729 laser, the superposition in the ground state is then mapped to a superposition between $S_{1/2}$ and $D_{5/2}$ with subsequent coherent manipulations [111] to choose the measurement basis. The state of the qubit is finally determined with an electron shelving technique [85].

In a more advanced quantum-network scenario which might include further quantum information processing with the transferred qubit, the obtained information about the accumulated phase of the superposition in the ground state could be used to rotate the qubit state to a well defined basis, utilizing again coherent manipulations with the 729 laser.

2.3.3. Remaining prerequisites

When joining the group in 2008, the two main components for the implementation of such an entanglement-transfer scheme were already operative as independent devices: the photon-pair source and the ion-trap apparatus. In the following year, we could primarily demonstrate a first interaction of photons from the down-conversion source with a single ion and later also that the heralding of this process via the detection of the signal photon in the filter arm is possible [68, 71, 72]. However, those experiments employed the polarization correlation of the photon pairs for the interaction only in a classical way. Furthermore, there was no laser system available to implement coherent manipulations for the preparation of atomic coherent superpositions and state detection. In addition, single-photon coupling and detection efficiencies in the set-up were only preliminary estimates, which made calculations for expected success probabilities of certain transfer schemes rather speculative. To advance the overall experimental set-up to a state that would finally enable the implementation of the previously presented transfer scheme, the following tasks were carried out during this thesis:

- 1) Demonstration of entanglement-dependent interaction between photon pairs and a single ion.
- 2) Precise measurement of the absorption probability of single 854 nm photons.
- 3) Precise measurement of the detection efficiency of single Raman-scattered photons at 393 nm.
- 4) Setup of an ultra-stable laser system at 729 nm for coherent state manipulations.
- 5) State discrimination via electron shelving with the 729 nm laser.
- 6) Coherent manipulations for qubit rotations with the 729 nm laser.
- 7) Preparation of coherent superpositions in the $D_{5/2}$ state.

The items 1)–3) are addressed in the following Chapter 3. Points 4) and 5) are documented in Chapter 4, and Chapter 6 will show experimental demonstrations for the items 6) and 7).

3. Experiments with single ions and single photons

Apart from its technological importance for quantum networks, control of the interaction between light and matter at the single-particle level has been a dream in quantum optics for a long time. The experimental set-up with which the work described in this thesis has been carried out is one of the few existing apparatus that is sufficiently equipped to advance into that unique research field.

The emission of single photons by a single atom or ion with an appropriate level scheme is rather easy to control via the excitation with a pulsed laser sequence. This has extensively been studied and used in several experiments employing neutral atoms in free space [112], neutral atoms in cavities [113, 114], trapped ions in cavities [115, 116], trapped ions in free space [55, 69], single molecules [117], or quantum dots [118], just to name a few popular quantum systems. In contrast to that, the demonstration of the controlled coupling of single photons to a single absorber has so far only been demonstrated with a neutral atom in a cavity [59]. This is not surprising, since the experiments tackling the single-photon absorption require already as a precondition the fully controlled operation of a single-photon source.

In our experiment, the single-photon absorption is studied with a hybrid-system approach, consisting of a heralded single-photon source based on SPDC (see Section 2.2) and a single trapped ion, which is coupled in free space to the photons, using high numerical aperture optics (see Section 1.3.2). Previous experiments with the set-up [71, 72] have shown, that the operation of such a hybrid quantum system is feasible. Experiments with atoms in cavities [59] generally provide an overall high success probability for the absorption but lack any mechanism to see if a single absorption has actually succeeded. In contrast to that, the absorption in free space allows the generation of a heralding event which precisely signals the moment of absorption (see Section 2.3.2). This dramatically increases the visibility of the process, given the intrinsically low coupling efficiencies without the use of a cavity.

The experiments that were previously done with the set-up made use of the temporal and frequency correlation of the photon pairs that are emitted by the SPDC source. The polarization dependence of the absorption was further demonstrated, but the photon-pair source was not operated as an entangled photon-pair source since the pairs were split with a polarizing beam splitter, removing any polarization entanglement.

Section 3.1 will demonstrate experiments which show for the first time the interaction of entangled photon pairs with a trapped ion at the single particle level. The polarization entanglement is manifested in the absorption process. This is verified by performing a full tomography of the photon state with the ion as a polarization-selective single-photon detector. The section will also summarize the main results of preceding measurements which the new results are based on and which they extend significantly. Sections 3.2 and 3.3 will then focus on experiments which characterize the detection efficiency of a single Raman-scattered pho-

ton at 393 nm and the single-photon absorption efficiency at 854 nm. The results show that the achieved coupling efficiencies are compatible with earlier preliminary estimates in [68], which makes a future implementation of entanglement transfer schemes of the type described in Section 2.3.2 feasible.

3.1. Interaction of heralded single photons with a single ion

Several preliminary experiments (recording for several weeks quantum jumps with painfully low rates of 0.5 jumps/min [71]) allowed a first observation of the absorption of down-conversion photons by a single ion. In those experiments, the photon-pair source was operated at a wavelength of 850 nm, resonant with the $D_{3/2}$ - $P_{3/2}$ transition; details are found in [65, 68]. To summarize, the results showed a clear signature for the interaction of the photons with a single ion, but the interaction was effectively the one with a classical light field¹, as the SPDC source was not operated as heralded single photon source. The quantum character of the interacting photons was *a posteriori* projected into a single-photon state since the used quantum-jump scheme on the ion is sensitive to single-photon absorptions.

The second series of experiments that have been carried out employed a different interaction scheme by changing the photon-pair wavelength to 854 nm, thereby addressing the $D_{5/2}$ - $P_{3/2}$ transition. Due to a higher oscillator strength and a more favorable branching ratio for spontaneous decay from $P_{3/2}$ to $S_{1/2}$ after photon absorption (triggering the absorption detection), the choice of this atomic transition lead to a significantly higher absorption and detection probability for the interaction of single SPDC photons with a single ion. In addition, the source was operated in a heralded single-photon source mode by detecting the signal photons in the filter arm. The correlation of these events with the observed single-photon absorptions by the ion allowed then a post-selection of the events where the ion effectively interacted with a light field in the single-photon state $\langle n \rangle = 1$. Those experiments demonstrated for the first time the controlled interaction of single photons from a down-conversion source with a single atomic system. A detailed documentation is available in [68] and [72].

The third series of experiments, that are reported in this thesis, is based on the same techniques to detect the single-photon absorptions and correlate the events with the herald of the single-photon source. But this time, the photon polarization entanglement is preserved until the absorption of one photon by the ion and the absorption is shown to depend on it. The experiments therefore represent the first demonstration of controlled interaction of *entangled* individual photon pairs with a single trapped ion. The polarization entanglement is probed by letting the ion act as a polarization-selective absorber in different polarization bases, using optical pumping. The experiments represent the last necessary step before moving on to future experiments which aim at the storage of the polarization state of the absorbed photon and thereby enable an entanglement transfer as discussed in the previous chapter.

Section 3.1.1 will explain the quantum-jump scheme that is used to detect single-photon absorptions by a single ion with high probability. Section 3.1.2 will introduce the experimental set-up and Section 3.1.3 focuses on the evaluation of the observable correlation for the heralded

¹As for a long time theoretically discussed and finally in [119] experimentally demonstrated, SPDC pairs produced by continuous pumping of the nonlinear medium show thermal statistics of the pair detection times.

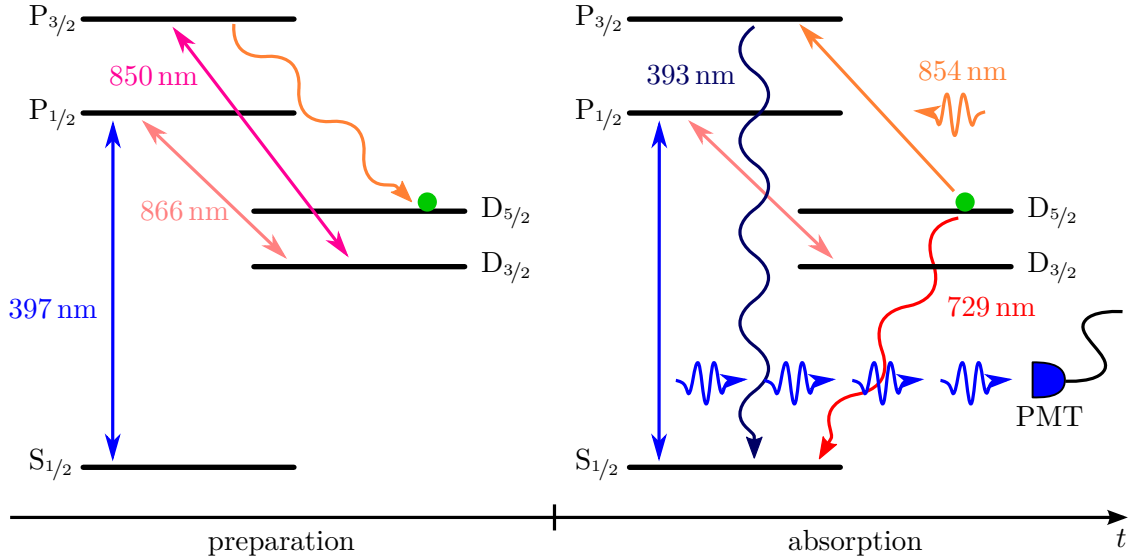


Figure 3.1.: Scheme for the detection of single-photon absorptions by a single ion at 854 nm. During the preparation, the population (green circle) is prepared in the metastable $D_{5/2}$ state by excitation with 397 nm, 866 nm, and 850 nm. The absorption of a single 854 nm photon transfers the population back to the ground state via the emission of a single Raman-scattered photon at 393 nm. The cooling lasers then lead to the emission of steady fluorescence at 397 nm which is detected with a PMT.

single-photon absorption. This is the main experimental quantity to characterize the ion-photon interaction. Section 3.1.4 will give a short summary about the main results of the previous experiments, the new results are then discussed in the Sections 3.1.5 – 3.1.7.

3.1.1. Efficient absorption detection with quantum-jump scheme

The scheme proposed in Section 2.3.2 to herald a single-photon absorption relies on the detection of a single Raman-scattered photon at 393 nm. Using high numerical-aperture optics to collect this photon, the overall detection efficiency is on the order of $\sim 10^{-2}$. A detailed characterization will follow in Section 3.2. Given the fact that the single-photon absorption is with a probability of $\sim 10^{-4}$ rather unlikely (more details in Section 3.3) and taking an estimated maximal rate of 5×10^3 fiber-coupled resonant photons from the source into account, this results in an expected rate of $\sim 0.3 \text{ min}^{-1}$ detected absorptions. In experiments which are aiming at the observation of coincidences between filtered-photon detections in the source ($\sim 7\%$ probability [68]) and absorption heralds at the ion, with the present source brightness this would result in measurement times of several months to attain the required statistics for basic studies of the interaction. To shorten this process in a first step, the original scheme got slightly modified to a variation of the *shelved electron amplifier scheme* as first demonstrated by Dehmelt *et al.* [120], which overcomes the low detection efficiency of the herald and allows a highly efficient absorption detection on the ion. Figure 3.1 gives an illustration of the general principle.

After preparing the ion in the $D_{5/2}$ state, the 850 nm laser is switched off and the cooling

laser (397 nm) and repumper (866 nm) remain on. Being in the metastable state, the ion is not interacting with the lasers anymore and remains dark. This way, the ion reenters the cooling cycle right after the absorption of a single 854 nm photon and subsequent emission of a single 393 nm photon². This leads to a sudden start of the emission of a constant stream of fluorescence photons (a quantum jump). These photons are easy to detect and permit, similar to the electron-shelving technique discussed in Section 4.4.4, a discrimination whether the ion is in the $D_{5/2}$ state or has left it with practically 100 % efficiency. Any quantum state that might be encoded in a superposition between the two Zeeman sub-levels of the ground state will be destroyed immediately due to the presence of the 397 nm laser. The scheme is therefore not applicable to any scenario where a photonic qubit state is supposed to be permanently stored in the ground state, but it serves to carry out proof-of-principle experiments on the heralded absorption process with high efficiency.

The population in the $D_{5/2}$ state might also spontaneously decay to the ground state via the emission of a single photon at 729 nm. This event would then also lead to the onset of fluorescence and cause a false absorption detection. The scheme thereby suffers from a constant background rate, given by the inverse of the natural lifetime $\tau = 1.17$ s of the $D_{5/2}$ state.

Even though this scheme has a very high efficiency in detecting single-photon absorptions (mainly limited by the branching ratio of 94.1 % from $P_{3/2}$ to the sum of $S_{1/2}$ and $D_{3/2}$ [110]), it requires some effort to obtain a good precision for the time at which an absorption happened. As discussed in [68], this is of essential importance for a good signal to noise ratio when working with the heralded single-photon source. The most precise information that one can get from the measurement is the arrival time of the very first detected fluorescence photon, which follows an exponential probability density as a function of the time after the absorption event. Since the overall photon collection and detection efficiency is fixed, the resulting standard deviation δt for the absorption time is determined by the inverse of the rate r of detected fluorescence photons, $\delta t = 1/r$. The best precision is therefore achieved with the highest possible scattering rate r of the ion when it is driven by 397 nm and 866 nm. Typical high detection rates that still provide stable cooling conditions for the ion are around $r = 5 \times 10^5$ s⁻¹, leading to an uncertainty of $\delta t = 2$ μ s.

The timing precision of the fluorescence detection is limited by the transit-time spread of the PMTs, being around $\tau_{\text{tts}} \approx 280$ ps with our apparatus (Hamamatsu, H7422P-40 SEL; PicoQuant, PAM 102-P). Time stamps of single-photon clicks are stored with a TCSPC unit (PicoQuant, PicoHarp 300), having a maximum timing resolution of 4 ps. The detection time of the very first measured fluorescence photon for each observed absorption is extracted from the recorded fluorescence trace with a dedicated program written in C. The program first analyzes the fluorescence trace by applying a moving average filter and comparing the result with a set threshold. This enables the detection of the coarse times for sudden changes in the fluorescence rate. The program then identifies the time t_m of the first detection event after the onset of fluorescence by comparing the time intervals $\Delta t_m = t_m - t_{m-1}$ between always three subsequent single-photon detection events with a set threshold τ_{th} : $\Delta t_{m-1} > \tau_{\text{th}} \wedge \Delta t_m < \tau_{\text{th}}$. Further details about the method including theoretical considerations for an optimal setting of the thresholds are documented in [68].

²The absorption may also cause the emission of a photon at 850 nm when the decay happens to $D_{3/2}$ (~ 0.5 % [110]). Since the repumper is switched on, this event also leads back to the cooling cycle.

3.1.2. Experimental scheme

A drawing of the experimental set-up as it is used for the experiments is shown in Figure 3.2. Details particularly relevant for either the previous or current experiments will be discussed in the respective sections. In this section only the general components and working principle will be explained.

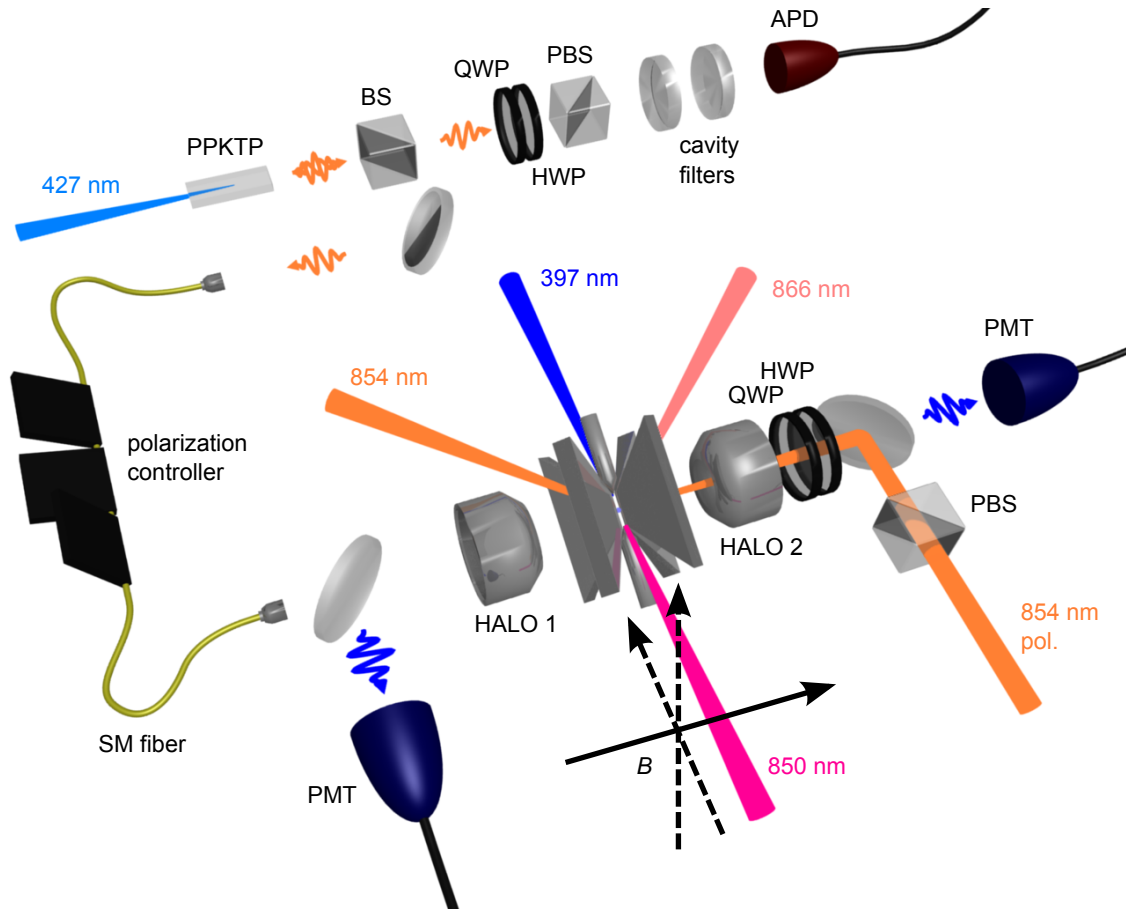


Figure 3.2.: Experimental set-up that is used to measure the interaction of heralded single photons with a single ion. The upper part represents the relevant components from the source, being the non-linear crystal (PPKTP), the beam splitter (BS) to split the photon pairs, the polarization analyzing unit (QWP, HWP, PBS), the frequency filter, and the APD. The lower part depicts the ion-trap experiment. HALO 1 is used to couple the down-conversion photons to a single ion. The ion's fluorescence is collected with both HALOs and separated from the incident down-conversion photons and the pumping beam at 854 nm by dichroic mirrors. The photons are then detected by two separate PMTs, whose signals are combined and recorded as a single fluorescence trace.

Set-up

A single $^{40}\text{Ca}^+$ ion is confined and laser cooled in a linear Paul trap which is placed between two high-numerical aperture laser objectives (HALOs) (see Section 1.3.2). The ion is addressed by various laser beams for cooling and optical pumping. The HALOs serve to efficiently collect the ion's laser-excited fluorescence on two photomultipliers (PMT) and to couple the ion with single photons in a single optical mode. Magnetic-field coils (not shown in Figure 3.2) permit to apply magnetic fields on the optical axis of the HALOs and on the two perpendicular directions, horizontal and vertical with respect to the optical table as indicated. They are used to generate a main magnetic field on a well defined axis, while compensating for stray fields on the two other axes. The photon pairs in the source are split by a beam splitter (BS) and one output mode is sent through a frequency filter (see Section 2.2), matching the atomic transition in center frequency and bandwidth (22 MHz). Before the filtering stage, the photons pass through a polarization analyzing unit, comprising a quarter wave plate (QWP), a half wave plate (HWP) and a polarizing beam splitter (PBS). Photons that pass through the filter are detected by an avalanche photodiode (APD). Since they herald the presence of their partner photon in the second output mode of the BS, they will be referred to as *trigger photons*. The photons in this second unfiltered output mode of the BS are coupled to the ion through one of the HALOs, after passing through a 16 m long single-mode fiber, connecting the two set-ups.

Laser sequence

As explained in Section 3.1.1, the controlled absorption of single photons with the quantum-jump scheme requires a sequential preparation of the ion. This is optimally done with a pulsed laser sequence that periodically prepares the ion for the absorption and cools the ion's motion.

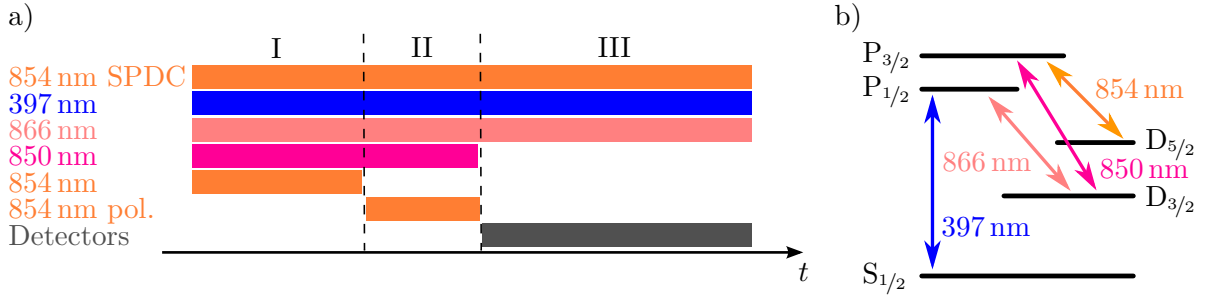


Figure 3.3.: a) Laser sequence that is used to measure the absorption of single photons coming from the SPDC source. The three sequence parts are explained in the text. b) Level scheme of $^{40}\text{Ca}^+$ with all relevant transitions for the pulsed absorption.

Figure 3.3 shows the laser sequence that is used in the experiments. The start of the sequence is synchronized with the chopper in the source, sending the locking beam to the filter arm to stabilize the two cavity filters. The chopper is usually running at a speed of 10 Hz. In the ion trap, each period starts with Doppler cooling for 5 ms with laser light at 397 nm and 866 nm (part I). Additional laser beams at 850 nm and 854 nm ensure that populations remaining in other states from the previous sequence cycle are emptied.

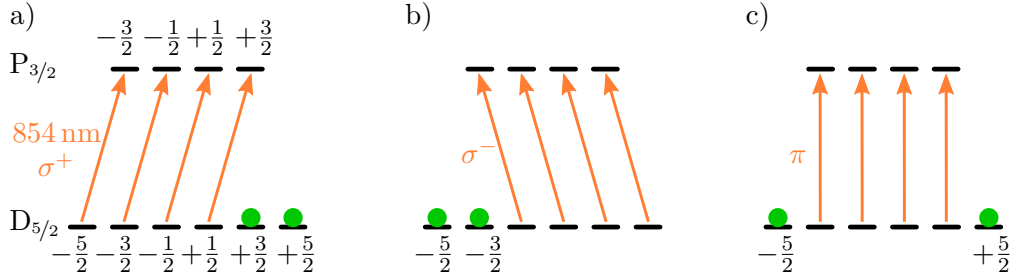


Figure 3.4.: Preparation of the ion for polarization-sensitive absorption with an optical pumping beam at 854 nm for the case of a) σ^+ , b) σ^- , and c) π polarized light.

Thereafter (part II), the internal state of the ion is prepared for the next 10 ms for polarization-sensitive absorption of SPDC photons: laser light at 850 nm populates the $D_{5/2}$ level while at the same time, laser light at 854 nm optically pumps the ion into specific Zeeman sub-levels of that manifold. The prepared state is controlled by the polarization \mathbf{E}_p and propagation direction \mathbf{k}_p of the 854 nm pumping light with respect to the orientation of the magnetic field \mathbf{B} that sets the quantization axis. A clean polarization of the pumping beam is set by using a PBS, a QWP, and a HWP as indicated in Figure 3.2. With σ -polarized light on axis with the magnetic field ($\mathbf{k}_p \parallel \mathbf{B}$), an incoherent mixture of the states either with magnetic moments $m = \{+3/2, +5/2\}$, or with $m = \{-3/2, -5/2\}$ is prepared (Figure 3.4 a) and b)). With π -polarized light propagating perpendicular to the magnetic field orientation ($\mathbf{k}_p \perp \mathbf{E}_p \parallel \mathbf{B}$), an incoherent mixture of the states with $m = \{-5/2, +5/2\}$ is prepared (Figure 3.4 c)). In all cases, after preparation, an SPDC photon with the same polarization as the preparing light cannot be absorbed, while the orthogonal polarization leads to maximum absorption, making the ion act as a polarization-selective absorber in the chosen polarization basis.

Finally, in the 85 ms long detection phase in part III of the sequence, the PMT photodetectors are activated while the ion is exposed to the unfiltered SPDC photons, which are continuously sent during the whole sequence. In the filter arm of the source, the chopper is now transmitting photons from the down-conversion crystal which are detected by the APD, that is constantly on.

When starting with the cooling in part I of the sequence again, an additional laser beam at 854 nm is switched on that is incident under an angle of 45° respective to the optical axis. The linear polarization of this beam is oriented such that it corresponds (for all magnetic field orientations that are used in the experiment) to a superposition of σ^+ and σ^- in the reference frame of the ion. This ensures that remaining population in the $D_{5/2}$ state is always emptied if no absorption or decay happened during the detection phase and that the ion always enters the cooling cycle.

Stability of the alignment

The most difficult and sensitive part of the experiments is the coupling of the ion to the single mode of the fiber, carrying the photons from the down-conversion set-up. The alignment is done by using the methods described in [68]. In all measurements the single-mode coupling was found to be drifting on a time-scale of about half an hour, being mainly caused by (small)

temperature drifts of the lab and acoustic noise³. Thus, the alignment was in all experiments checked and optimized every half an hour.

3.1.3. Absorption-idler correlations

The evaluation of the interaction of the heralded single-photon source with a single ion is done by calculating a histogram of the time delays between the identified absorption events and the single-photon clicks of trigger photons recorded in the filter arm of the source. Apart from normalization, this is equivalent to a calculation of the second-order correlation function

$$g^{(2)}(\tau) = \frac{\langle n_1(t)n_2(t+\tau) \rangle}{\langle n_1(t) \rangle \langle n_2(t+\tau) \rangle}, \quad (3.1)$$

where $n_{1,2}(t)$ are the numbers of measured events at the time t at the ion and in the filter arm on a time grid with bin size $\Delta\tau$. The photon pairs are known to be time correlated down to a time scale below 100 ps [121]. For negligible time delays arising by different path lengths of photons sent through the filter arm and photons sent to the ion, one would therefore expect a strong peak only at $\tau = 0$ in the $g^{(2)}$ function. Due to the frequency filters in the filtering arm, the detection-time distribution of trigger photons relative to the absorption times of their unfiltered partners follows an exponential distribution with an $1/e$ time of 7.2 ns, compatible with the filtering bandwidth. This is negligible compared to the spread of detection times for the absorptions, with an $1/e$ time of $\frac{1}{r}$ being typically in the micro-second regime (see Section 3.1.1). To compress all observed coincidences into the central bin at $\tau = 0$ in the correlation function, the bin size is usually chosen as $\Delta\tau = \frac{3}{r}$, leading to 95 % of all coincident events in a single bin.

Figure 3.5 shows an example for an experimental correlation function obtained in these measurements. Compared to the earlier experiments that first demonstrated the heralded single-photon absorption, a reduced detected fluorescence rate from the ion of $3 \times 10^5 \text{ s}^{-1}$ had to be used, resulting in the optimal bin size of $\Delta\tau = 10 \mu\text{s}$. The reason for this was a changed geometry of the repumping laser beam at 866 nm for the cooling, a broken PMT⁴, and changes in the set-up for the fiber coupling of the fluorescence light. The number of coincidences $N_{\tau=0}$ in the peak at $\tau = 0$ together with the estimated background N_{bg} , calculated as the mean of the whole $g^{(2)}$ function, are the main experimental quantities that are evaluated in all of the following experiments. The net number of coincidences N_c is obtained by simply subtracting the background $N_c = N_{\tau=0} - N_{\text{bg}}$. Assuming poissonian statistics for both, the occurrences of the correlation events and the background events, the standard deviation for this value is given by $\sqrt{N_{\tau=0}}$.

The background arises due to random correlations between events from different pairs, false absorption events due to spontaneous decay of the $D_{5/2}$ state, and dark counts and other

³After re-setting up the experiment in the new labs, it was additionally found that the xyz -translation stages supporting the HALOs had severe problems with catch-up of RF noise from the trap drive in the cables outside of the vacuum chambers. This caused charging effects on the piezos which resulted in a slow drift of the HALO positions. The problem got solved by adding low-pass filters right on the outside of the feedthroughs, which led to a significantly improved long-term stability. This problem might have been also present in the here reported experiments, but in a much less pronounced way.

⁴One of the two PMTs that are used for the fluorescence detection had to be replaced by an older model (Hamamatsu, H7360-02), which has only $\sim 70\%$ of the quantum efficiency of the normally used detectors.

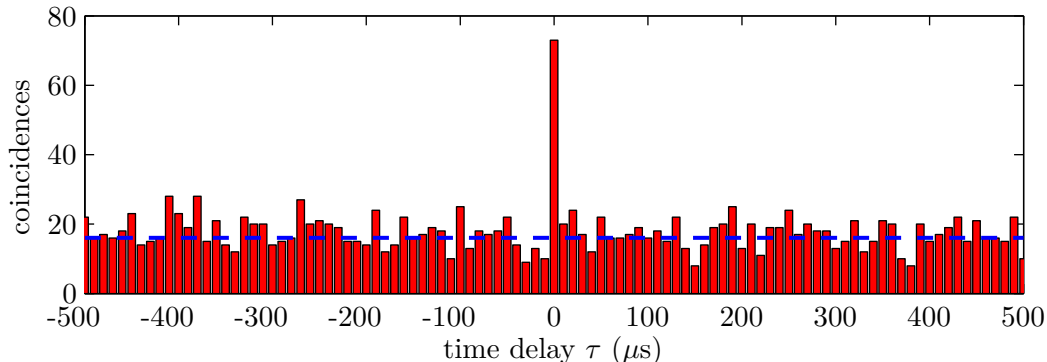


Figure 3.5.: Experimental correlation function between single-photon absorptions by the ion and trigger-photon detections in the filter arm of the source. The data is plotted with a bin size of $10 \mu\text{s}$, the total acquisition time is 60 min. The central peak corresponds to $73(9)$ coincidences, the overall background is $16.06(3)$, determined by the mean of the whole correlation function (1.6×10^4 bins in total) and indicated by the blue dotted line.

background events in all involved detectors. A more quantitative analysis will follow in Section 3.1.7.

3.1.4. Previous experiment: Heralded single-photon absorption by a single ion

The experiments performed earlier for the heralded interaction of single down-conversion photons with a single ion in a pulsed interaction scheme are reported in another PhD thesis [68], the results are further published in [72]. This section serves to highlight in which way the experiments that will be discussed in the following sections go beyond the previous ones by summarizing the earlier achieved degree of control over the interaction.

The first demonstration of the controlled absorption of single photons by a single ion has been achieved with a heralded single-photon source. In contrast to the representation in Figure 3.2, the photon pairs coming out of the PPKTP crystal in the source were split with a polarizing beam splitter (PBS), destroying any polarization entanglement between the photons and delivering a well defined linear polarization state in the two output modes of the PBS. The polarization analyzing unit in the filtering arm was therefore removed. For convenience, the 16 m long fiber carrying the photons to the ion lab was a polarization maintaining fiber, providing a high degree of stability even in the presence of strong temperature fluctuations and mechanical stress over the period of several months for the preparation and final measurements. To transform the polarization of down-conversion photons that are interacting with the ion to a circular basis, a QWP was introduced right in front of HALO 1 in Figure 3.2. The ion was prepared by optical pumping with circularly polarized light, following the scheme illustrated in Figure 3.4 a) and resulting in the mixed state $|D_{5/2}, m = \{+3/2, +5/2\}\rangle$. In all measurements, the main magnetic field was applied on the optical axis of the HALOs.

When setting the photon polarization such that it was opposite (perpendicular) to the polarization of the pumping beam, the absorption probability was maximized and maximum rates

of $5.2(4) \text{ min}^{-1}$ coincidences were observed, after the subtraction of background.

It was then verified, that the absorption probability of photons is depending on the polarization of the incident photons. This is of course obvious when preparing the ion with optical pumping as explained, the novelty was that this could be verified at the single-photon level due to the use of the heralded single-photon source. When changing the polarization of the incident photons with the wave plate to the identical circular polarization as the pumping beam, a full suppression of the number of observed coincidences to the background level was observed. Since the overall absorption probability of all photons coming from the down-conversion source got modulated in these measurements, a corresponding clear dependence of the background in the evaluated $g^{(2)}$ functions was observable as well.

With this important information that the polarization-selective single-photon absorption is controllable, another set of measurements has been done. The degeneracy of the photon pairs at the frequency of the pump laser together with the tunable filter arm permitted the demonstration of a remote spectroscopy of the addressed atomic transition. Therefore the ion was prepared as in the just discussed measurement and the photon polarization was adjusted to maximum absorption probability. Coincidences were then measured for different detunings of the master laser of the source (and consequently corresponding detunings of the frequency filters for the trigger photons). The observed dependence of correlation showed the expected lorentzian shape, with a linewidth compatible with the convolution of the atomic transition linewidth and the bandwidth of the filtering cavities. The mind-twisting specialty about these experiments was that the absorption rate of photons by the ion was independent of the frequency setting of the master laser due to the very broad spectrum of unfiltered photons reaching the ion. Only the frequency filtering in the filter arm of the source made it possible to just look at the correlations that were caused by photons which were in the set frequency window. Further measurements were done with an inverted magnetic field direction on the ion, leading to the preparation of the mixed state $|D_{5/2}, \{-3/2, -5/2\}\rangle$ (corresponding to scheme b) in Figure 3.4). This allowed us to repeat the spectroscopy, but now probing the other end of the $D_{5/2}$ - $P_{3/2}$ transition. The observed shift of the spectrum, compatible with the expected Zeeman splitting of the involved atomic states, further confirmed the reliability of this type of spectroscopy.

To summarize, the experiments demonstrated the controlled interaction of single down-conversion photons with a single ion, using the strong time correlation that the photon pairs share. The polarization selectivity of the absorption process was evidenced in a circular polarization basis. The intrinsic frequency correlation between the photons in a pair finally enabled the performance of a remote spectroscopy of the atomic transition without effectively detuning the light interacting with the ion. In the following sections, a similar way to remotely project the state of photons interacting with the ion by the application of certain measurements to the trigger photons will be extensively utilized to demonstrate the non-classical polarization correlation of the photon pairs.

3.1.5. Coincidence measurements in three polarization bases

To measure the interaction of an *entangled*⁵ heralded single-photon source with a single ion, several changes were implemented on the set-up compared to the earlier experiments.

Most importantly, the photons are now split with a non-polarizing 50/50 beam splitter (BS) as depicted in Figure 3.2, delivering the maximally entangled $|\Psi^-\rangle$ state (2.5) between its two output modes. The replacement of a PBS by a BS sounds rather trivial, but this single component is the most crucial part of the set-up. Since the rate of generated photon pairs is far below something that could be monitored on an IR card, the efficient coupling of the two output modes of the BS is a major challenge. Another complication when splitting the photon pairs with a BS and working with an ion as absorber is stray light from the locking beam of the cavity filters that is coupled into the fiber to the ion and deteriorates the preparation of the ion for absorption. This happens after multiple back reflections on optical components in the source and is difficult to suppress. The effect is much less pronounced when splitting the photon pairs with a PBS.

In the filter arm, two motorized wave plates (QWP and HWP) are used to remotely control the measurement basis for the trigger photons. The main purpose to use motorized mounts was to enable a remote operation of the source from the ion lab, and to avoid a frequent removal of the protective lids covering the whole set-up. These lids are required due to a very delicate alignment and stray-light sensitivity.

To send the photons to the ion-trap set-up, a non-polarization-maintaining single-mode fiber was installed. Special care was taken to guarantee a stable mounting over the 16 m distance between both fiber ends, by protecting it with a rigidly mounted thick and flexible plastic tube. This tube additionally provided protection against sudden temperature fluctuations. To minimize the effect of temperature drifts, the fiber was guided the furthest possible away from any outlet of both labs' air-conditioning system. A long-term measurement in [68] with a similar fiber showed that such a configuration provides an output-polarization stability with residual drifts below 0.4 % over the time of one hour. Birefringence in the fiber is neutralized by using a manual polarization controller on the ion-trap table. The neutrality is checked by sending a probe beam from the source (see Section 2.2) with horizontal or diagonal polarization and monitoring the polarization right in front of the ion-trap with a second set-up comprising a flippable HWP and PBS, and a fiber-coupled avalanche photodiode (not present in Figure 3.2). A polarimeter (Thorlabs, PAX5710) was used to check the principle functioning of the neutralization, but could not be employed for periodic checks during the measurements due to a very limited space around the ion-trap chamber.

A QWP and a HWP are used to adjust the optical pumping beam at 854 nm for the ion such that the ion's fluorescence is reduced to the background level when exciting it with 397 nm, 866 nm, and 850 nm light. In this procedure, the laser power of the pumping beam is reduced to operate below saturation, making the level of suppression of the fluorescence light a good measure for the efficiency of the optical pumping process. Measurements in Section 4.4.4 show that this strategy typically leads to pumping efficiencies above 99 %.

⁵The photon sent to the ion is entangled with the trigger photon detected in the filter arm.

Measurements in the R - L basis

The R - L polarization basis ($|R\rangle$ right-circular, $|L\rangle$ left-circular) is defined as

$$|R\rangle = \frac{1}{\sqrt{2}}(|H\rangle - i|V\rangle) \quad (3.2)$$

$$|L\rangle = \frac{1}{\sqrt{2}}(|H\rangle + i|V\rangle) \quad (3.3)$$

and the entangled state (2.5) of the photon pairs is accordingly

$$|\Psi^-\rangle = \frac{1}{\sqrt{2}}(|RL\rangle - |LR\rangle) . \quad (3.4)$$

For a measurement of single-photon absorptions in the R - L basis, the magnetic field \mathbf{B} is set along the direction of the incident photons ($\mathbf{k}_{854} \parallel \mathbf{B}$) and the ion is prepared in the $m = \{-3/2, -5/2\}$ Zeeman sub-levels of the $D_{5/2}$ state by optical pumping with σ^- polarized light (Figure 3.4 b)). In the following it will be assumed that the magnetic field orientation is such that an incident $|R\rangle$ photon will drive a σ^+ transition in the ion, thereby leading to a maximum absorption probability.

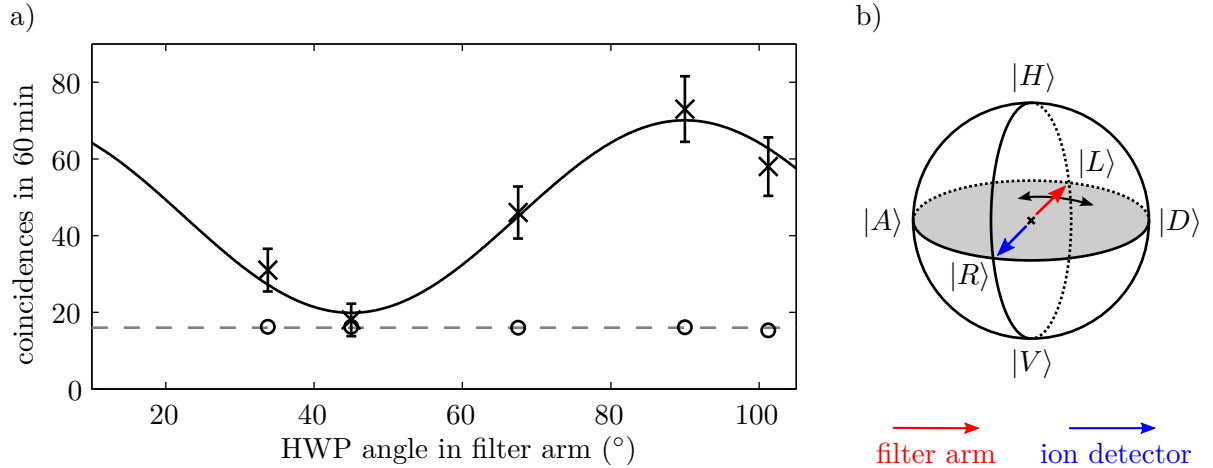


Figure 3.6.: a) Measured coincidences in the R - L basis for different angles of the HWP in the filter arm of the source. The black curve is a sinusoidal fit with a fixed period and offset angle since these values are well known from an independent calibration. The visibility is 56(6)% (87(11)%) before (after) background subtraction. Circles indicate the background for each point and the gray dashed line is the overall mean background being at 16.0(2) coincidences. b) Corresponding Poincaré representation of the detected polarization by the ion and in the filter arm. The black arrow indicates the rotation of the HWP.

The wave plates in the filter arm are set for the detection of circularly polarized trigger photons. With the individual photons having completely random polarizations, the rotation of the HWP in that arm then selects the polarization of the correlated partner photons in the other output mode of the BS that is coupled to the ion. It should be emphasized that the polarization of the photons sent to the ion is neither changed nor filtered in this measurement.

Figure 3.6 shows the measured dependence of the number of observable coincidences when rotating the HWP. A maximum of around 1.0(1) coincidence min^{-1} (73 coincidences with 15 background events in 60 min) and a minimum within the background level is observable, for orthogonal and same polarizations, respectively. This reflects the perfect anti-correlation of the photon polarizations as given by (3.4). The background for all measurements is approximately the same, showing no dependence on the settings for the HWP. This is a nice way of seeing that the ion is not experiencing any change in the state of photons that are incident and that the overall absorption rate is constant. Remaining small deviations of the backgrounds in the different measurements arise due to an overall slow drift in the alignment of the SHG unit in the pump laser of the source (Section 2.2). This influences the rate of produced photon pairs. To minimize the effect, the measurements were taken in two sweeps of half an hour per point on two consecutive days.

Measurements in the H - V and D - A bases

In terms of the H - V polarization basis (see Section 2.1), the D - A polarization basis ($|D\rangle$ diagonal, $|A\rangle$ anti-diagonal) is in the following defined as

$$|D\rangle = \frac{1}{\sqrt{2}}(|H\rangle + |V\rangle) \quad (3.5)$$

$$|A\rangle = \frac{1}{\sqrt{2}}(|H\rangle - |V\rangle) \quad (3.6)$$

with the resulting biphoton state (2.5)

$$|\Psi^-\rangle = \frac{1}{\sqrt{2}}(|DA\rangle - |AD\rangle) . \quad (3.7)$$

For measurements of correlations in the H - V basis, optical pumping into the outer Zeeman sub-levels $m = \{-5/2, +5/2\}$ is applied as illustrated in Figure 3.4 c). Therefore, the magnetic field is rotated by 90° (pointing now upwards in Figure 3.2) and the optical pumping beam is set to the vertical polarization, corresponding to π polarized light at the ion. The SPDC photons propagate with $\mathbf{k}_{854} \perp \mathbf{B}$ and can only be absorbed if they are $|H\rangle$ polarized. Owing to the angular dependence of the absorption probability on a dipole transition with respect to the main magnetic-field axis⁶, this specific configuration results in exactly one half of the maximum absorption probability compared to the measurements in the R - L basis. This effect is compensated by doubling the acquisition time per point. In the filter arm the wave plates are set to detect in the H - V basis.

To make the ion sensitive for the D - A basis, the same procedure could be used, with the main magnetic field tilted by 45° around the wave vector of the incident 854 nm photons and a corresponding tilt of the pumping beam polarization. But due to a strongly deviating geometry of both coils for the horizontal and vertical magnetic field, the application of such a rotated quantization field was considered to be not reasonably controllable. Therefore, the fiber polarization controllers are used to cause the effective basis rotation by 45° , which is controlled via the test beams that are used for the neutralization. This procedure does not require to place an additional wave plate in front of the ion trap and is equivalent to a rotation of the main magnetic field axis as proposed before. Again, the wave plates in the filter arm are set accordingly to measure in the tilted linear basis.

⁶For details see Appendix A.2.

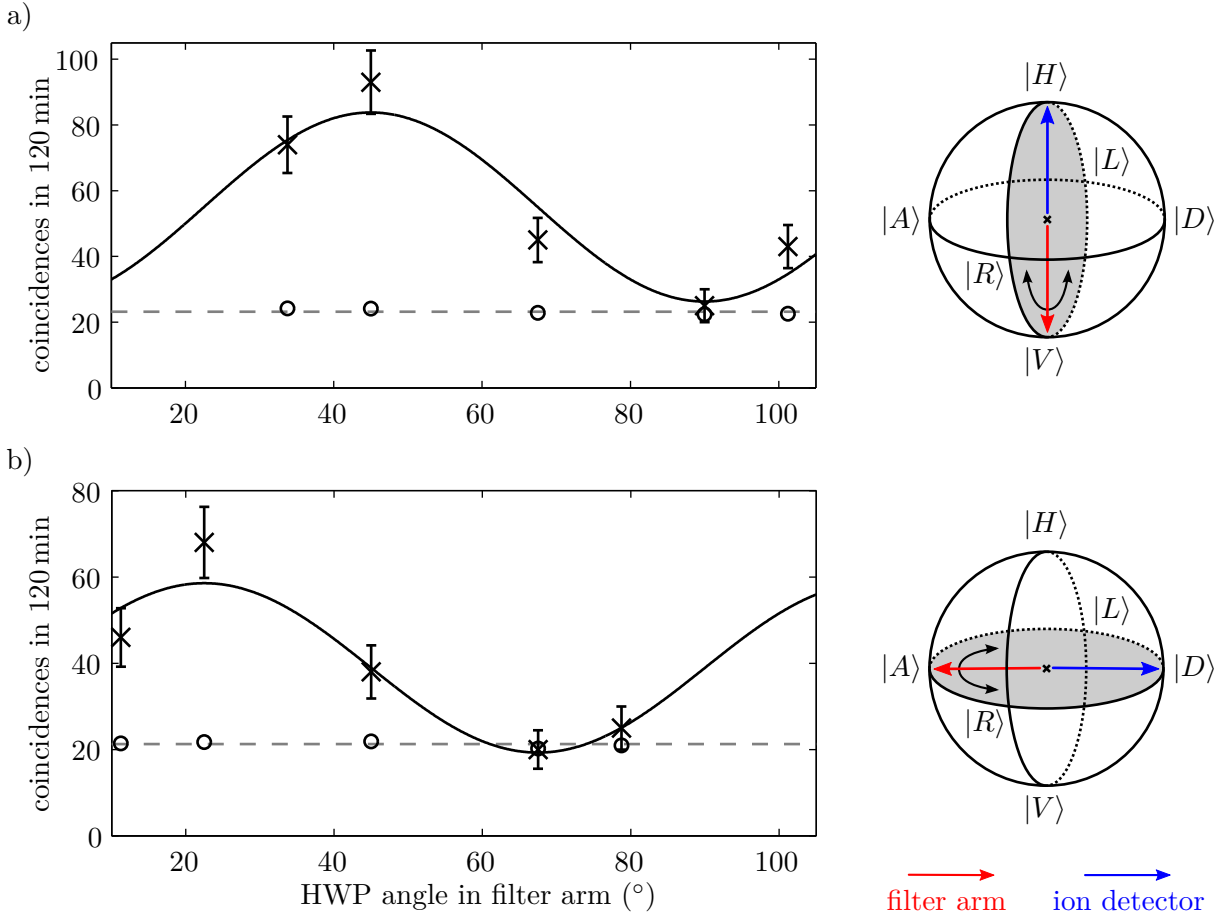


Figure 3.7.: a) Measured dependence of coincidences in the H - V basis, similar to the one shown in Figure 3.6. The fit reveals a visibility of 52(11) % (90(24) %) before (after) background subtraction, the mean background is at 23.2(3) coincidences. b) The same measurements in the D - A basis. The fringe visibility is 50(9) % before background subtraction and compatible with 100 % after subtraction of the mean background of 21.2(3) coincidences.

Figure 3.7 shows the results of the measurements in the two linear bases. The total acquisition time is two hours per point and the measurements were again taken in several sweeps to minimize an influence by drifts of the source brightness.

In the H - V basis a maximum rate of 0.57(8) coincidences min^{-1} (92 with 24 background in 120 min) is observed, which is consistent with the expected reduction by a factor of 1/2 compared to the measurements in the R - L basis. The minimum point is again well within the background level, corresponding to a full suppression of correlated absorptions when the detected trigger photons are measured in the polarization state $|H\rangle$, thereby projecting their partners to $|V\rangle$ which is not absorbed by the ion.

The same sinusoidal dependence on the HWP angle is observable when measuring in the D - A basis, again with a full suppression of the number of observed coincidences to the background

level. Here, the maximum measured rate has slightly dropped to $0.38(7)$ coincidences min^{-1} (67 with 21 background in 120 min), which is within two standard deviations still compatible with the rate expected from the measurements in the R - L basis. However, these measurements suffered from a decreasing power of the blue pump laser in the source, which is manifested in an overall reduced background.

3.1.6. Photon entanglement detection by a single ion: Quantum tomography

The measurements from the previous section demonstrate how a single ion is operated as a polarization selective single-photon detector in the three principal polarization bases spanning the Poincaré sphere. The observation of the correlation fringes in the three orthogonal bases is a manifestation of the strong non-classicality of the polarization correlation that the photon pairs share. The results of these measurements show that the interaction of the ion with the heralded single-photon source cannot be described by simply the post-selection of successful absorption events. In contrast, each detected trigger photon leads to a projection of its partner photon into a well defined polarization state right at the moment of the individual absorption events.

It is therefore possible to perform a full tomographic reconstruction of the quantum mechanical two-photon state, using another purely quantum mechanical system, a single ion. This is quantum state tomography, both at the single-photon and single-particle limit. With the set-up it is only possible to measure a single polarization state at once, both at the ion and in the filter arm. This requires a total of 16 independent measurements with different detection-basis combinations to fully determine the 4×4 density matrix of the biphoton state. The basis combinations are chosen following the procedure explained in [122] and an overview of all relevant measurements is given in Table 3.1.

In the previous section we have seen that the measurements with the ion in the linear bases intrinsically suffer from a decreased absorption probability, which is compensated by doubling the acquisition time. However, this changes the background in those measurements which makes it not feasible to evaluate numbers of measured coincidences in different bases for the reconstruction including this background. For the tomographic reconstruction therefore the net number of coincidences N_c is evaluated by subtracting the individual backgrounds⁷.

A maximum likelihood method similar to the one explained in [122] is used to reconstruct the density matrix ρ of the biphoton state from the correlation measurements. But the method described there is most suitable for experiments with a large number of events, allowing one to describe the statistics of the detection process with a Gaussian probability distribution. This limiting case cannot be applied for the present low numbers of measured events; instead, a likelihood function based on a Poissonian probability distribution for the description of the coincidence statistics is used for the reconstruction. Another effect of low statistics in the present experiments is a significant influence of the background to the error of the net coincidences. To account for this influence, the individually measured backgrounds are included in the likelihood function as an individual offset for the measurements in each basis combination. More details about the likelihood function are found in the Appendix A.3. Figure 3.8 shows

⁷It is assumed that within the finite acquisition time always an integer number of net coincidences is measured, therefore the background is rounded to integers before subtraction from the central correlation peak.

3. Experiments with single ions and single photons

pol. basis		pumping beam		geometry	filter arm		coincidences	
ion	filter arm	QWP	HWP	$\angle(\mathbf{B}, \mathbf{k}_{\text{ph}})$	QWP	HWP	N_c	N_{bg}
$ R\rangle$	$ R\rangle$	45°	–	\parallel	45°	45°	2	16
$ R\rangle$	$ L\rangle$	45°	–	\parallel	45°	90°	57	16
$ R\rangle$	$ V\rangle$	45°	–	\parallel	0°	45°	27	15
$ R\rangle$	$ D\rangle$	45°	–	\parallel	45°	67.5°	30	16
$ L\rangle$	$ R\rangle$	-45°	–	\parallel	45°	45°	46	14
$ L\rangle$	$ L\rangle$	-45°	–	\parallel	45°	90°	0	13
$ L\rangle$	$ V\rangle$	-45°	–	\parallel	0°	45°	15	14
$ L\rangle$	$ D\rangle$	-45°	–	\parallel	45°	67.5°	32	17
$ H\rangle$	$ R\rangle$	0°	45°	\perp	45°	45°	20	24
$ H\rangle$	$ L\rangle$	0°	45°	\perp	45°	90°	21	24
$ H\rangle$	$ V\rangle$	0°	45°	\perp	0°	45°	69	24
$ H\rangle$	$ D\rangle$	0°	45°	\perp	45°	67.5°	16	21
$ D\rangle$	$ R\rangle$	0°	45°	\perp	45°	45°	16	22
$ D\rangle$	$ L\rangle$	0°	45°	\perp	45°	90°	20	23
$ D\rangle$	$ H\rangle$	0°	45°	\perp	0°	90°	21	20
$ D\rangle$	$ D\rangle$	0°	45°	\perp	45°	67.5°	0	20

Table 3.1.: Overview of all 16 measured basis combinations with the corresponding settings on the ion and in the filter arm. Given is the number of net coincidences N_c and the individually determined background N_{bg} . \mathbf{k}_{ph} is the wave vector of the absorbed photons. Note that for the measurements with the ion sensitive to $|D\rangle$, the photon polarization is rotated by 45° as explained for the corresponding fringe measurements. The total acquisition time per point for the measurements with the ion in the circular bases is 1 h and in the linear bases 2 h.

a graphical representation of the reconstructed density matrix ρ of the biphoton state. Real and imaginary part are found to be

$$\text{Re}(\rho) = \begin{pmatrix} 0.009(14) & -0.021(34) & 0.002(40) & 0.007(14) \\ -0.021(34) & 0.476(59) & -0.455(27) & -0.114(46) \\ 0.002(40) & -0.455(27) & 0.479(57) & 0.099(51) \\ 0.007(14) & -0.114(46) & 0.099(51) & 0.037(23) \end{pmatrix}$$

$$\text{Im}(\rho) = \begin{pmatrix} 0 & 0.0002(278) & 0.0021(290) & -0.0064(108) \\ -0.0002(278) & 0 & -0.0369(549) & 0.0549(266) \\ -0.0021(290) & 0.0369(549) & 0 & -0.0526(286) \\ 0.0064(108) & -0.0549(266) & 0.0526(286) & 0 \end{pmatrix}.$$

Following the description in [123], the statistical errors are estimated with a Monte Carlo method by repeating the reconstruction routine for 150 data sets of coincidences with separate backgrounds that are simulated assuming Poissonian noise around the measured values.

The overlap fidelity of the reconstructed ρ with the maximally entangled singlet state $|\Psi^-\rangle$ of the photon pairs is $F = \langle \Psi^- | \rho | \Psi^- \rangle = 93(4)\%$. Given the very low statistics and overall complexity of the experiment, this is in good agreement with the earlier determined fidelity of

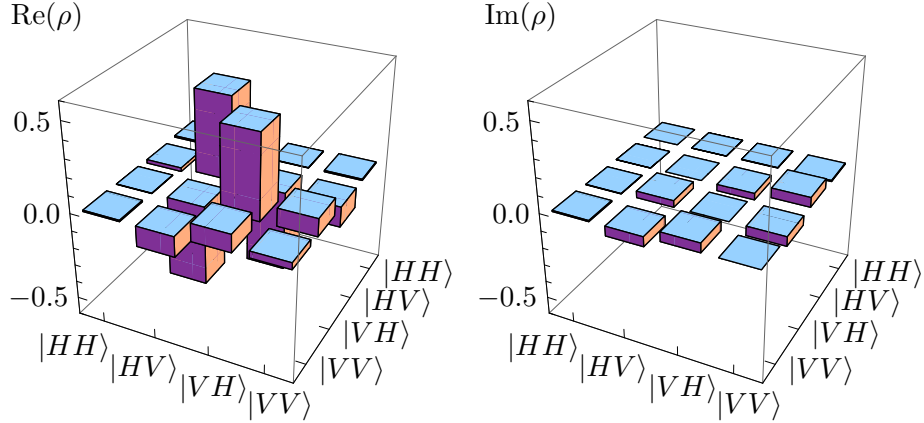


Figure 3.8.: Real and imaginary parts of the reconstructed density matrix ρ of the biphoton state, represented in the H - V basis.

the photon state ($F = 97.6(1.1)\%$) as reported in [101]. The fidelity only quantifies the overlap with an expected state and provides no reliable measure for the actual degree of entanglement that is contained in the reconstructed state. To better characterize this quantity, the so-called *entanglement of formation* is calculated which is defined as the minimum average entanglement of an ensemble of pure states that is represented by ρ [124]. The outcome for this measure is $89(8)\%$, being close to the derived overlap fidelity, which further confirms the reliability of the experimental scheme that is used for the characterization of the photon state. The observation of this strong manifestation of the non-classical polarization correlation of the photon pairs in the absorption process is an essential pre-requisite for experiments aiming at the entanglement of distant absorbers by a quantum state transfer from absorbed entangled SPDC photons.

3.1.7. Efficiency considerations

Using a BS in the source to split the photon pairs not only enables working with polarization-entangled states of photons, it also completely changes the nature of background events in the measurements and has a significant impact on the efficiency of the overall correlation process. Let us assume that the spatial output mode of the beam-splitting device that is coupled to the filter arm is called *signal mode* and the one that is coupled to the ion is called *idler mode*. When splitting the photon pairs with a PBS, the state describing a pair in the two modes is

$$|\psi\rangle_{\text{PBS}} = |H\rangle_i |V\rangle_s, \quad (3.8)$$

corresponding to the situation that all generated resonant pairs can produce a coincidence, if both detectors are set to the respective polarizations (perfect detectors and negligible photon loss is assumed). When sending the photon pairs through a BS, they are only split in 50% of all cases, giving rise to the Bell $|\Psi^-\rangle$ state

$$|\Psi^-\rangle = \frac{1}{\sqrt{2}}(|H\rangle_i |V\rangle_s - |V\rangle_i |H\rangle_s). \quad (3.9)$$

Since both detection arms are only sensitive to one polarization state at a time in the experiment, the maximum probability to detect a coincidence is 25% compared to the situation

when the photons are split with a PBS. In the remaining 50% of the cases when the pairs are not split at the BS, both photons are either sent to the signal mode or to the idler mode, with equal probability. As a consequence, the individual rates of detection events in both output modes are always exactly 50% of the rate of produced resonant photon pairs, independent on the polarization state that the detection in each mode is set to.

To extract these probabilities and other important efficiencies from the measured data and compare them with the values from the experiments employing a PBS to split the photon pairs, detection-event traces of measurements with maximum coincidence rates from both experiments were analyzed. For the measurements with the BS this is 1 hour of data in the *R-L* basis (Figure 3.6) and for the measurements with the PBS half an hour of data for the case with maximum absorption probability (Section 3.1.4). In the pulsed interaction scheme that was used in both experiments (Section 3.1.2), the PMT detectors monitoring the ion fluorescence are periodically gated off. This provides the required time stamp for a detailed analysis of the recorded detection traces, allowing the extraction of various rates and efficiencies as will be shown in the following.

Trigger photons

The APD in the filter arm of the source is not gated on or off, but the photons reaching the detector are sequentially blocked by the chopper (see Section 2.2). This makes it possible to extract the trigger-photon rate in part III of the sequence and the background rate due to detector dark counts and stray light in parts I and II. For the experiments with the BS, the background corrected average rate of detected trigger photons is found to be $R_{\text{BS}}^{\text{tr}} = 353(1) \text{ s}^{-1}$, the background rate is at $50(1) \text{ s}^{-1}$. For the earlier experiment with the PBS these values are $R_{\text{PBS}}^{\text{tr}} = 783(3) \text{ s}^{-1}$ trigger photons (background corrected) and a background level of $44(2) \text{ s}^{-1}$. The ratio of both trigger rates thereby is $\frac{R_{\text{BS}}^{\text{tr}}}{R_{\text{PBS}}^{\text{tr}}} = 0.451(2)$ which is close to but below the expected value of 0.5. As it will be seen in the following, this notable discrepancy is most likely caused by a different coupling of the output mode from the SPDC crystal that is sent to the filter arm.

Photon absorptions

An analysis of the fluorescence traces recorded with the PMTs reveals the probability for the ion to be properly initialized in the $D_{5/2}$ level in each period of the sequence. This probability is found to be 99.9% for the experiments with the BS and 99.7% for the measurements with the PBS. The practically unity efficiency for both cases confirms that stray light from the locking beam in the source that might be coupled to the ion during the preparation phase (II) is well suppressed.

Another important parameter is the rate of single-photon absorptions by the ion. The quantum-jump scheme that is used for the absorption detection suffers from a significant background due to spontaneous decay from the $D_{5/2}$ level (see Section 3.1.1). This spontaneous decay rate might differ from the literature value due to collisions with background gas in different vacuum conditions and the presence of stray light. It is therefore determined in a separate measurement by randomly pumping the ion to the $D_{5/2}$ level with an attenuated laser beam at 850 nm and analyzing the statistics of the lengths of the observed dark periods in

the ion's fluorescence⁸. For the experiments with the BS, the decay rate is determined at $1/\tau = 0.87(4) \text{ s}^{-1}$, which is consistent with the literature value given in [125]. Together with the total rate of observed jumps by the ion, this leads to a measured SPDC-photon absorption rate of $R_{\text{BS}}^{\text{abs.}} = 0.78(5) \text{ s}^{-1}$. With the total probability of 94.1% that a photon absorption causes a quantum jump of the ion (see Section 3.1.1), this corresponds then to an extrapolated absorption rate of $0.83(5) \text{ s}^{-1}$.

For the experiments with the PBS, a similar measurement for the background has been done as reported in [68], resulting in a measured absorption rate of $R_{\text{PBS}}^{\text{abs.}} = 1.55(5) \text{ s}^{-1}$. The ratio between the rates from both experiments $\frac{R_{\text{BS}}^{\text{abs.}}}{R_{\text{PBS}}^{\text{abs.}}} = 0.50(4)$ is in perfect agreement with the expected value of 0.5, as explained at the beginning of this section. This is a good benchmark for the reproducibility of the single-photon coupling, both from the SPDC crystal into the optical fiber and from the fiber output to a single ion.

The measured rate of absorptions by the ion together with the rate of produced photon pairs allows one to get a rough estimate of the single-photon absorption probability. Assuming the total coupling, transmission, and detection efficiency of the trigger photons in the filter arm to be around 7% as estimated in [68], the expected rate of produced pairs after the BS based on the rate of measured trigger photons is $R_{\text{BS}}^{\text{pairs}} \approx 5 \times 10^3 \text{ s}^{-1}$. With 54% fiber coupling efficiency of the photons that are coupled to the ion, this leads to a total absorption probability on the order of $P_{\text{abs.}} \approx 3 \times 10^{-4}$. An independent and more precise measurement of the absorption probability after setting up the experiment in the new lab will be discussed in Section 3.3.

Coincidences

The measured maximal (background corrected) coincidence rate when splitting the photon pairs with a BS is $R_{\text{BS}}^{\text{c}} = 0.95(14) \text{ min}^{-1}$, whereas it was $R_{\text{PBS}}^{\text{c}} = 5.23(44) \text{ min}^{-1}$ for the earlier experiments with the PBS. The ratio between both rates amounts to $\frac{R_{\text{BS}}^{\text{c}}}{R_{\text{PBS}}^{\text{c}}} = 0.18(3)$ which is significantly lower than the expected ratio of 0.25 for the ideal case. Taking the reduced trigger-photon rate (as discussed previously) in the measurements with the BS into account, this ratio should be around 0.23 which is at least within two standard deviations of the derived value. The same applies for an evaluation of the correlation probability⁹. In the earlier experiments it was found to be $P_{\text{PBS}}^{\text{c}} = 7.0(7) \%$ and in the more recent measurements it is derived to $P_{\text{BS}}^{\text{c}} = 2.6(4) \%$, resulting in a ratio of $\frac{P_{\text{BS}}^{\text{c}}}{P_{\text{PBS}}^{\text{c}}} = 0.37(7)$. This is close to the expected value of 0.45 when correcting for the lower trigger-photon rate.

The fact that the photon absorption rate $R_{\text{BS}}^{\text{abs.}}$ is perfectly consistent with the earlier results suggests that this notable reduction in the correlation rate together with the reduced rate of trigger photons is caused by a sub-optimal spatial mode overlap of SPDC photons that are coupled to the filter arm and photons that are coupled to the ion.

Background

The background in the correlation measurements is proportional to the product of the individual event rates in both channels. In the following it will be summarized how these independent

⁸This method will be explained in more detail in Section 3.3

⁹The probability to detect a trigger photon in the filter arm if the ion absorbed its partner photon.

detection rates decompose into different sources of background when splitting the photon pairs with the BS.

In the filter arm there are three main contributions. The extracted numbers for signal and background rates in the filter arm correspond to a contribution of 12% to the total rate of detected clicks caused by detector dark counts and stray light. Following the considerations from the beginning of this section, the remaining 88% divide into one half (44%) which is caused by photon pairs that are not split by the BS and that are therefore not leading to any coincidences, and another half (44%) which is caused by single photons where the pair was split.

At the ion there are the corresponding three contributions. The contribution due to spontaneous decay from the $D_{5/2}$ level is, due to a very low absorption probability and low photon-production rates, on the order of 53%, thereby being responsible for more than one half of the observable background in the $g^{(2)}$ function. The remaining equal contributions from split and unsplit photon pairs are 23.5%, respectively.

The only way to compensate for this dominant background at the ion is to increase the brightness of the source such that spontaneous decay events become negligible. In the filter arm this would also lead to a negligible contribution by the detector dark counts. But even then, there remains an intrinsic contribution to the background of 50% in both the ion and the filter arm, which is caused by unsplit photon pairs. This contribution may be eliminated by a different design of the source, where the photon pairs are generated inside of a polarization Sagnac interferometer as demonstrated in [126]. Such a configuration makes it possible to split the photon pairs with a PBS while maintaining their polarization entanglement. The possibility that a photon pair is not split is thereby efficiently suppressed. For the same pair production rate this type of source would however cause exactly the same background level in the evaluated $g^{(2)}$ function as the current set-up (for the same bin size and total acquisition time). The difference is that it would increase the rate of net coincidences by a factor of two, thereby leading to a maximal possible gain of 2 in the overall signal to background ratio.

3.2. Detection efficiency of single emitted 393 nm photon

All experiments done so far with the down-conversion source made use of a quantum-jump scheme (see Section 3.1.1) to detect single-photon absorption events. In terms of detection probability, this scheme is highly efficient but it does not allow a state transfer of the photon polarization onto the electronic state of the ion. Transfer schemes like the one presented in Section 2.3 require the detection of a single heralding photon at 393 nm.

Preliminary estimates for the detection efficiency of these single photons in [68] were based on the overall scaling factor that is obtained when fitting an excitation spectrum that is measured with 397 nm and 866 nm (see for example Section 5.2.1) with the corresponding 8-level Bloch equation system. Those measurements obtained an overall detection efficiency on the order of 1% for fluorescence photons at 397 nm. But a huge number of different fit parameters makes this result rather speculative. Additionally, it is not clear to what extent those results are applicable to the detection efficiency at 393 nm, since fluorescence light at that wavelength has not been measured yet and eventual differences of the losses in the used optical components are unknown.

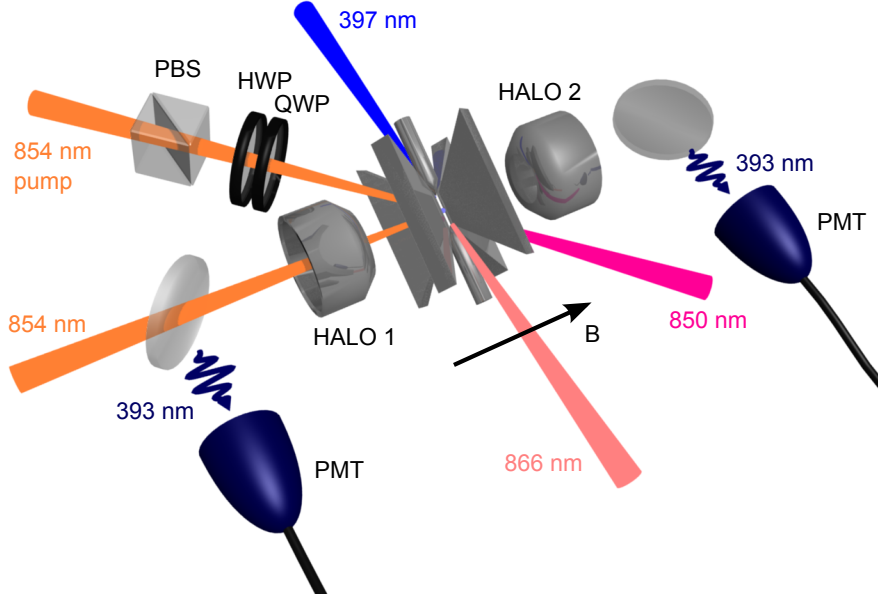


Figure 3.9.: Experimental set-up that is used to measure the combined collection and detection efficiency of single emitted photons at 393 nm. For details see text.

In the following, a photon source generating single 393 nm photons with a pulsed laser sequence is used to characterize the unknown detection efficiency in one of the two ion traps, the Bright Trap (BT). This approach might not be the simplest strategy to deduce the unknown parameter but due to the lack of a 393 nm laser on the set-up it certainly provides the cleanest method to optimize the alignment of the collection optics at that specific wavelength. Section 3.2.1 will explain the set-up and laser sequence, Section 3.2.2 will give a quick characterization of the single-photon source, and Section 3.2.3 will summarize the obtained results.

3.2.1. Experimental scheme

Figure 3.9 shows the experimental set-up that is used to characterize the detection efficiency of single Raman scattered 393 nm photons in the BT. The ion is addressed by various laser beams for optical pumping and photon generation as it will be explained in a moment. The generated photons are collected with both HALOs and coupled to a 2 m long multimode fiber (BFH22-200) on each side. Both fibers are connected to two individual PMTs and the single photon clicks are stored with the TCSPC unit that was also used for the other experiments from this chapter. The position of HALO 1 is optimized for efficient single-mode coupling at 854 nm which results in a bigger distance from the trap center compared to a configuration for optimal coupling at 393 nm or 397 nm. The telescope that is used to match the outgoing UV photons to the multimode fiber is usually optimized to compensate for this effect and to achieve best collection efficiencies at 397 nm for normal fluorescence detection. But owing to the bigger distance from the trap center the resulting NA of the HALO is reduced, leading to slightly lower collection efficiencies. To compensate for the difference in the effective focal length of the whole imaging set-up at 393 nm, a stack of two lenses ($f = -100$ mm, $f = 200$ mm) is additionally

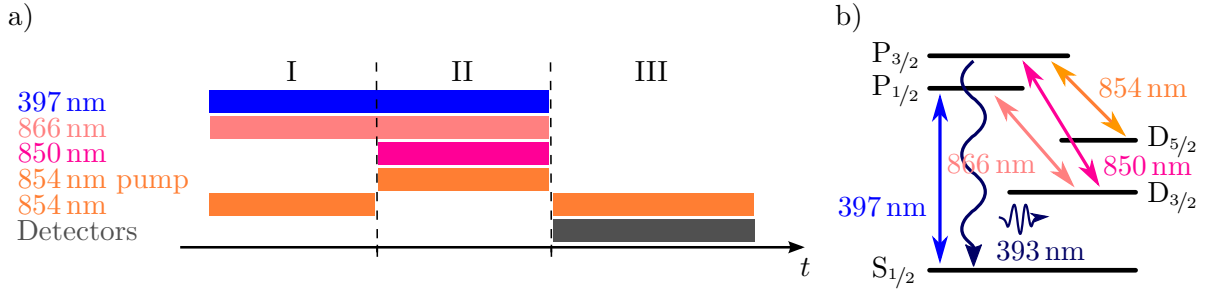


Figure 3.10.: a) Laser sequence for single-photon generation at 393 nm. The 854 nm pumping laser is optional and allows the preparation of a single Zeeman sub-level of the $D_{5/2}$ manifold. Details are explained in the text. b) Level scheme for $^{40}\text{Ca}^+$ with all relevant transitions.

introduced on a magnetic flip mount. This enables an easy switching between good collection efficiencies at the two different UV wavelengths. The position of HALO 2 is optimized for efficient fluorescence detection at 397 nm. Here a similar lens stack ($f = -75$ mm, $f = 100$ mm) is introduced to maximize the collection efficiency at 393 nm.

Figure 3.10 displays the laser sequence that is used to generate single photons at 393 nm. Part I consists of Doppler cooling as for the sequence for single-photon absorption from the last section. A linearly polarized laser beam at 854 nm that is sent through HALO 1 is used to empty remaining population in the $D_{5/2}$ state from the preceding sequence cycle. In part II, the ion is pumped to $D_{5/2}$ with laser light at 850 nm. Compared to the sequence for single-photon absorption this happens now via a three-photon resonance (397 nm, 866 nm, and 850 nm), achieving a preparation of the ion in a statistical mixture of all Zeeman sub-levels in the metastable state with more than 99% probability within $10 \mu\text{s}$. For some experiments an optical pumping beam at 854 nm is used to prepare the ion in the single $m = -5/2$ sub-level of the $D_{5/2}$ state. This is achieved by sending the pumping beam under an angle of 45° with respect to the main magnetic field axis and setting an elliptical polarization which results in a superposition of π and σ^- light at the position of the ion. In part III, only the 854 nm beam through HALO 1 is switched on, generating a single Raman-scattered photon at 393 nm. The generation probability $p_{\text{gen}} = 99.3\%$ is given by the relative branching fractions from $P_{3/2}$ to $S_{1/2}$ and $D_{3/2}$ [110]. As already demonstrated in [69], the power of incident laser light for this spontaneous Raman decay is used to tune the temporal length of the generated single-photon wave packet. For the efficiency measurements discussed in the following only short photons with $1/e$ times of $\tau < 500$ ns were used. At the same time, both detectors are gated on to receive the emitted photons. To calibrate the state preparation efficiency the detectors are usually kept open over the whole sequence, thereby monitoring the full dynamics of the ion fluorescence during the different sequence parts. The sequence repetition rate is typically ranging from 10 kHz to 200 kHz, depending on the required state preparation and the length of the generated photons.

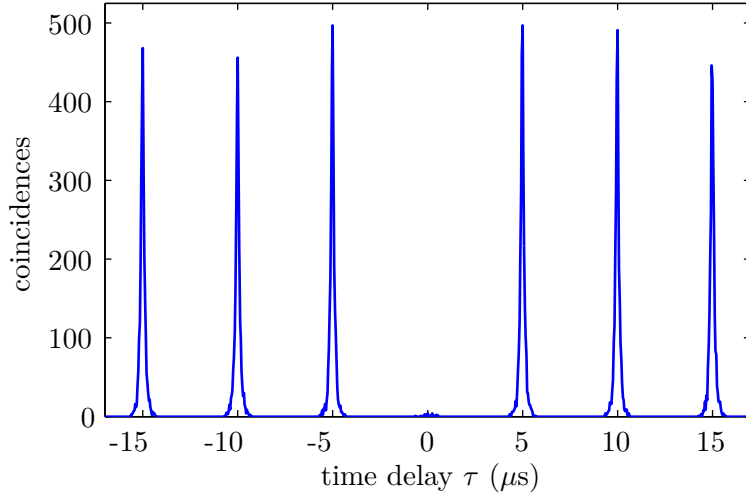


Figure 3.11.: Second order correlation function $g^{(2)}$ (not normalized) of generated 393 nm photons for a bin size of 40 ns. The data correspond to a total acquisition time of 10 min with a sequence repetition rate of 206 kHz.

3.2.2. Characterization of single-photon source

To employ a single-photon source for calibration purposes, it is of fundamental importance to ensure that multi-photon emission is efficiently suppressed. In the scheme that is used here, such multi-photon emissions might happen if the lasers from part II of the sequence are not fully switched off during the photon generation in part III. To suppress effects due to delays in the switching times of the used AOMs, an additional security delay of $1 \mu\text{s}$ is introduced between part II and part III of the sequence.

Figure 3.11 shows a measured second order correlation function $g^{(2)}$ of the generated single photons. The coincidence measurement is done by simply correlating the clicks recorded with both PMTs. Due to the symmetric configuration of the HALOs along the B-field axis, this is equivalent to collecting the photons from just one side and splitting them with a BS as it is done in a conventional Hanbury Brown and Twiss set-up [127]. The peak at $\tau = 0$ is strongly suppressed, indicating a dominant single-photon character of the source. An analysis of the ratio of the total number of events in this central peak and the mean number of events in the side peaks gives a two-photon to single-photon generation probability of the source of $0.38(7) \%$ without background subtraction¹⁰. Hence multi-photon emissions are clearly negligible and the scheme provides an excellent tool to measure the detection efficiency of single generated photons.

The second important parameter that has to be controlled is the average population p_{prep} in the $D_{5/2}$ state after state preparation in the sequence. For negligible multi-photon emissions p_{prep} directly corresponds to the expectation value for the number of emitted photons $\langle n \rangle$ in a single sequence repetition. The population is determined by measuring the pumping rate to

¹⁰A correct treatment of the background would require the knowledge of the overall detection efficiency which is the parameter that is going to be determined by using the single-photon source. The disregard of a possible background contribution makes the derived two-photon probability an upper bound.

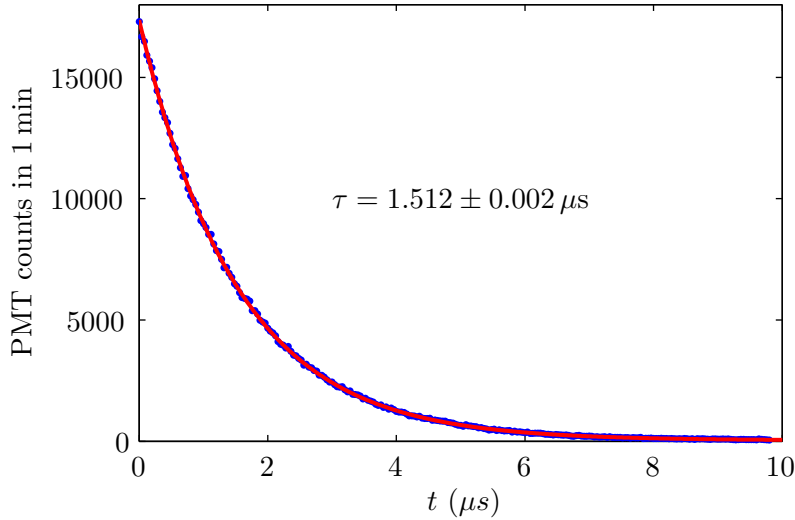


Figure 3.12.: Decay of combined 397 nm and 393 nm fluorescence during part II of the single-photon sequence caused by transfer of population to the $D_{5/2}$ state. The data are displayed with 40 ns bin size for a sequence repetition rate of 70 kHz. The red curve is an exponential fit to determine the decay constant.

$D_{5/2}$ via the observable decay of fluorescence during part II of the sequence. Figure 3.12 shows such a fluorescence decay which is obtained by correlating photon detections with the sequence trigger when using only HALO 2 for the photon collection. The exponential fit corresponds to a population-transfer rate to $D_{5/2}$ of $0.661(1) \mu\text{s}^{-1}$. Together with the effective length of the state-preparation phase determined from the same data set this results in an expected population in the metastable state before photon generation of $p_{\text{prep}} = 99.85(1) \%$.

3.2.3. Measurement of detection efficiencies

The detection efficiency η is finally obtained by evaluating the background corrected total number of detected photons N_{ph} in part III of the sequence for a fixed number of sequence repetitions N_{rep}

$$\eta = \frac{N_{\text{ph}}}{N_{\text{rep}} p_{\text{prep}} p_{\text{gen}}} . \quad (3.10)$$

When preparing the ion for photon generation in a random mixture of all Zeeman sub-levels in the $D_{5/2}$ state, the single photons are generated with random polarization on the dipole transition, making their overall angular distribution isotropic. For the configuration depicted in Figure 3.9 and when using only HALO 2 for the photon collection, we find an overall detection efficiency of single 393 nm photons of $\eta_{\text{HALO2}} = 0.799(4) \%$ for a total of 4.2×10^6 sequence repetitions at a rate of 70.05 kHz. Applying the same experimental procedure for the case of photon collection with only HALO 1 leads to a detection efficiency of $\eta_{\text{HALO1}} = 0.508(4) \%$, which is notably reduced due to the different position of HALO 1 for optimal coupling at 854 nm. When using both HALOs at the same time for photon collection we therefore expect an overall single-photon detection efficiency of $\eta = 1.307(6) \%$. The contributions by the two

HALOs to this total detection efficiency are

$$\frac{\eta_{\text{HALO1}}}{\eta} = 38.9(2) \% \quad (3.11)$$

$$\frac{\eta_{\text{HALO2}}}{\eta} = 61.1(2) \% . \quad (3.12)$$

The geometry of the state-transfer scheme that is explained in Section 2.3 is such that only σ -polarized photons are detected as herald for a successful transfer event. To measure the detection efficiency of photons in this particular polarization state the ion is prepared in $|D_{5/2}, -5/2\rangle$. From this state the only possible excitation channel at 854 nm goes to $|P_{3/2}, -3/2\rangle$ which has only one possible decay channel to $|S_{1/2}, -1/2\rangle$ via the emission of a single σ^+ -polarized 393 nm photon. The total detection efficiency for these single σ -polarized photons when combining the detection events from both HALOs is found to be

$$\eta_{\sigma} = 1.584(7) \%$$

(after 2.9×10^6 sequence repetitions at a rate of 9.75 kHz). Due to the preferential directionality of the emitted σ -photons along the axis of observation (see Appendix A.2) this detection efficiency is significantly higher than η for an isotropic emission. A reference measurement with exactly the same experimental parameters but without the pumping beam (thereby generating σ - and π -polarized photons) yields a total detection efficiency of $\eta = 1.263(7) \%$ which has a small but significant deviation from the total efficiency derived from the previous individual measurements. The ratio between both detection efficiencies is $\frac{\eta}{\eta_{\sigma}} = 0.797(6)$.

With the NA of 0.4 of the HALOs and the dipole emission pattern as given in Appendix A.2, each HALO is expected to collect 6.01 % of the total emitted σ -photons and 0.51 % of all emitted π -photons. Assuming that without the optical pumping beam the ion is prepared in a perfect mixture of all sub-levels in the $D_{5/2}$ manifold, the single-photon source produces a σ -photon with $\frac{2}{3}$ probability and a π -photon with the probability of $\frac{1}{3}$ (see Appendix A.1 for a list of Clebsch-Gordan coefficients). This leads to a theoretical ratio between the detection efficiencies for the two measured cases of $\frac{\eta}{\eta_{\sigma}} = 0.695$, about 13 % smaller than the measured ratio.

Errors in the optical pumping are negligible, the preparation efficiency of the ion in the $|D_{5/2}, -5/2\rangle$ level is typically around 99 %. One possible explanation for the observed discrepancy of the measured ratio to the theoretical value is a tilt of the main magnetic field with respect to the optical axis of photon collection. But this tilt would have to be around 27° to explain the experimental ratio, which is absolutely impossible since the geometric configuration of the B-field coils is precise down to a few degrees. Magnetic stray fields by the surrounding electronics are always carefully compensated. A more likely explanation is that the ion was not generating photons in a fully isotropic way for the measurements of η . A higher generation probability of σ -photons would then lead to an increased detection probability as observed. The imbalance of emitted photon polarizations is directly related to a non-equilibrium between the prepared populations of all Zeeman sub-levels in the $D_{5/2}$ manifold before photon generation. From numerical simulations we know that these populations are significantly influenced by the polarization and Rabi frequencies of all lasers that are involved in the three-photon resonance condition that is used for the preparation of the ion in part II of the sequence.

This delicate and complex dependence of the angular distribution of generated photons on the precise laser parameters for the preparation of the ion is also the most probable explanation for the observed discrepancy between the two individually determined values for η .

Since the obtained results for η do apparently not correspond to a fully isotropic photon generation, the total detection efficiency with both HALOs for the perfect isotropic case is deduced from η_σ by using the theoretical ratio of $\frac{\eta}{\eta_\sigma}$:

$$\eta = 1.101(5) \% .$$

With (3.12), the efficiency when collecting the isotropically emitted photons only with HALO 2 is then

$$\eta_{\text{HALO2}} = 0.673(4) \% . \quad (3.13)$$

The quantum efficiency of the PMTs is specified with 28%. For the collection with HALO 2 this gives an estimate for the combined collection and fiber-coupling efficiency of the photons of $\sim 2.4\%$. The solid angle that is covered by a single HALO is 4.17%, leaving a reasonable value of 57% for the fiber coupling and transmission efficiency through all optical components from the HALO to the detector.

The characterization of single-photon detection efficiencies was not the only purpose to implement a single-photon source at 393 nm. As demonstrated, the preparation of the ion in an outermost Zeeman sub-level of the $D_{5/2}$ state enables the efficient generation of single photons in a single polarization and frequency state, which makes this source an interesting tool for quantum networks. Further measurements were done to verify those unique photon properties and to obtain a detailed characterization of the single-photon source. The results are published in [128]. A detailed description and further experiments demonstrating the direct interaction of two distant ions in separate vacuum chambers via the exchange of single 393 nm photons will be available in [129].

3.3. Absorption probability of single 854 nm laser photons in both ion traps

The experiments presented in Section 3.1 gave a rough estimate for the single-photon absorption probability, being on the order of 3×10^{-4} . Many assumptions about coupling and transmission efficiencies of different optical components went into this preliminary value, which makes it hard to estimate its uncertainty. Therefore, the absorption probability of 854 nm photons coming from a calibrated laser beam was determined after setting up the experiment in the new lab. The measurements serve to check the quality of the newly established alignment after starting again from zero with the set-up and they deliver a more reliable value for the single-photon absorption probability than previous estimates.

The experimental procedure at the ion is rather simple and has already been used in earlier experiments with SPDC photons to determine the photon absorption rate [68]. The ion is laser cooled with light at 397 nm and 866 nm and its fluorescence is monitored with a PMT which detects the photons that are collected with a single HALO. A strongly attenuated laser beam at 850 nm is utilized to randomly pump the ion to the $D_{5/2}$ state. The power is typically adjusted such that the ion spends half of the time in this metastable state, emitting no fluorescence

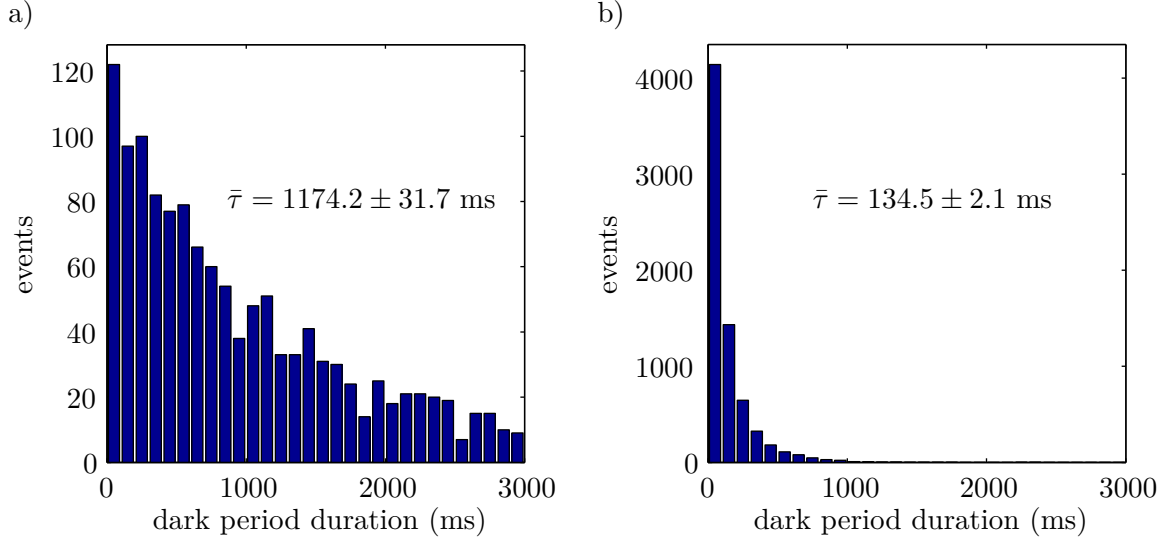


Figure 3.13.: Histogram of measured dark periods of the ion fluorescence in the DT. For the evaluation of the mean dark period duration $\bar{\tau}$, a bin size of 1 ms is used. a) Background measurement without incident photons, corresponding to a total of 1365 events in 30 min of acquisition time. b) Measurement with incident 854 nm photon stream, resulting in 7042 events in 30 min.

photons. An analysis of the lengths of dark periods in the recorded fluorescence trace is then used to determine the mean lifetime τ of the metastable state. This measurement is done once without sending 854 nm photons to the ion to determine the background decay rate $1/\tau_{\text{bg}}$ of the metastable state due to its natural lifetime τ_{nat} and other eventually present background events¹¹. The measurement is repeated with single photons at 854 nm that are coupled to the ion in a single mode through the second HALO. Photon absorptions lead to a precipitate decay from $D_{5/2}$ by excitation to $P_{3/2}$ with subsequent decay to either $S_{1/2}$ or $D_{3/2}$, as already discussed for the quantum-jump absorption scheme from Section 3.1.1. Therefore, an increased decay rate $1/\tau_{854}$ is observable when analyzing again the dark-period lengths of the ion fluorescence. Figure 3.13 shows an example for the change in the statistics of the dark period lengths for both cases as recorded in the Dark Trap (DT).

The photon absorption rate r_{abs} is then calculated as the difference between the two measured rates and by taking the probability of 5.9% [110] into account that spontaneous decay from $P_{3/2}$ might happen back to $D_{5/2}$, making those absorptions invisible:

$$r_{\text{abs}} = \frac{1}{0.941} \cdot \left(\frac{1}{\tau_{\text{bg}}} - \frac{1}{\tau_{854}} \right). \quad (3.14)$$

Highly attenuated fiber-coupled laser light at 854 nm is used to simulate single photons that are coming from the down-conversion source. This is of course no quantum light source with single-photon character in the first place, but due to the ability of the ion to only absorb a

¹¹These are usually stray light from the nearby 854 nm laser system and collisions with background gas in the vacuum chamber.

single photon at a time, it is valid to talk about single-photon absorptions in this context. A fiber coupled APD (Laser Components, COUNT-10C-FC) with a measured detection efficiency of 24.0(5.7) % at 854 nm is employed to set and calibrate the photon rate in the single-mode fiber.

Each ion trap is coupled with a separate short (2 m) single-mode fiber, which is then simply connected to the fiber with the reference laser. The fiber-to-fiber coupling efficiency is measured with a stronger laser beam and a power meter (Thorlabs, PM130D). Applying a magnetic field along the optical axis of the linearly polarized incident photons ensures that every photon can be absorbed if the ion is pumped to random sub-levels of the $D_{5/2}$ manifold. This method apparently suffers from the same uncertainty about the precise distribution of population among all of the sub-levels in $D_{5/2}$ as the experiments discussed in Section 3.2.3. However, the relative uncertainty of the APD detection efficiency of $\sim 24\%$ is expected to cause a much bigger error than a possible imbalance in the occupation of the prepared sub-levels.

Figure 3.13 shows the result for the DT when sending in a photon stream which leads to a detected rate (background corrected) of 3940 s^{-1} on the APD, corresponding to a photon rate out of the fiber of $r_{\text{ph}} = 1.65(39) \times 10^4\text{ s}^{-1}$. The background rate for the decay from the $D_{5/2}$ level is measured as $1/\tau_{\text{bg}} = 0.85(2)\text{ s}^{-1}$, being fully compatible with the literature value of 0.856 s^{-1} [125] for the natural decay rate $1/\tau_{\text{nat}}$. Together with the decay rate observed when the laser photons are sent to the ion, this results in a single-photon absorption rate of $r_{\text{abs}} = 7.0(1)\text{ s}^{-1}$. With r_{ph} and by taking the fiber-to-fiber coupling efficiency of 94.5 % into account, this leads to the absorption probability of σ -polarized 854 nm photons in the DT of

$$P_{\text{abs}}^{\text{DT}} = 4.5(1.1) \times 10^{-4} .$$

Applying the same experimental method to a single ion confined in the BT results in the corresponding single-photon absorption probability of

$$P_{\text{abs}}^{\text{BT}} = 6.3(1.5) \times 10^{-4} .$$

The higher efficiency in the BT might be explainable by a much bigger effort in coupling the output mode of the fiber to the ion, including several weeks of optimization. But given the high uncertainty of both derived efficiencies, the difference is not considered to be significant. Since the $D_{5/2}$ level was not prepared in any specific Zeeman sub-level in these measurements, the results have to be considered as approximate average efficiencies.

An independent measurement was done to estimate the mode-matching efficiency p_{mm} of single 854 nm photons emitted by the ion to the single-mode fiber. To this end a laser sequence identical to the one depicted in Figure 3.10 from the previous section is employed. The only difference is that no optical pumping beam is used in part II of the sequence and that an APD detector connected to the single-mode fiber that is coupled to one HALO is gated on in part II instead of part III. This way, the single emitted 854 nm photon that is generated during each state preparation of the 393 nm single-photon source is detected. Again, the relative uncertainty of the APD efficiency is considered to be much bigger than a possible imbalance between the three possible polarizations of emitted 854 nm photons, caused by sub-optimal parameters of the three different laser excitations that are required for the photon generation. Measurements in both traps yield an overall coupling efficiency of $p_{\text{mm}} = 2.1(5)\%$ of the

optical fiber mode with the emission (absorption) characteristic of the ion. The use of a single-mode fiber has the effect that no π -polarized photons are collected when coupling along the quantization axis. With the assumption that the ion produces arbitrary photon polarizations with equal probability, the obtained number has to be multiplied with a factor of $\frac{3}{2}$ to correct for the portion of generated but undetectable π photons. The mode overlap only for σ -photons is therefore

$$p_{\text{mm}}^{\sigma} = 3.2(8) \% . \quad (3.15)$$

Together with the previously determined absorption probabilities this provides an estimate for the transition probability of the ion for an incident photon with perfect mode overlap of $\sim 1.7\%$. The oscillator strength of the $D_{5/2}$ - $P_{3/2}$ transition is about 6% [65], leaving a remaining transition probability of $\sim 28\%$ which has to be understood as the effective Clebsch-Gordan coefficient for excitation with σ polarized photons out of the unknown (unbalanced) distribution of population in the Zeeman sub-levels of $D_{5/2}$.

Having both ions efficiently coupled to a single optical mode at 854 nm allowed us to perform a so far unique experiment with free-space coupled single atomic emitters and absorbers. In this experiment a single ion in the BT was used to generate single 854 nm photons in a pulsed laser sequence which were then coupled to a single ion in the DT. Using the quantum-jump absorption-detection scheme from Section 3.1.1 for this absorber ion made it possible to observe coincidences between single-photon emission events in one ion trap and absorption events in the second ion trap. In other words, it is the demonstration of a heralded direct exchange of single photons between two distant single ions. The results are published in [130], a detailed description of the experimental procedure and further measurements with an ion-based single-photon source at 854 nm will follow in [129].

3.4. Summary

This chapter documented a series of experiments that was done to study and quantify the interaction of a single trapped ion with single photons.

A heralded single-photon source based on spontaneous parametric down conversion was used to observe the heralded absorption of single photons by a single ion. Most importantly, the absorbed photons were entangled with their heralding partner, enabling the projection of the absorbed photons into a certain polarization state, depending on the chosen polarization for the detection of the partner photon. By making the photon absorption polarization selective with an appropriate preparation of the ion, this quantum mechanical projection phenomenon could be verified by observing herald-absorption coincidences in the three principal polarization bases. The measurements were furthermore extended to reconstruct the full entangled biphoton state emitted by the photon source by using the single ion as a polarization analyzer at the single-photon level. The measurements represent the successful operation of a complex hybrid quantum system employing fundamental quantum-mechanical phenomena such as two-photon entanglement and quantum jumps by an atomic system. The results are published in [131].

A single trapped ion was used to implement a single-photon source that generates photons at 393 nm with high purity. The calibrated source provided a powerful tool to precisely characterize the detection efficiency of a single Raman scattered 393 nm photon that is generated in entanglement-transfer schemes as the one explained in Section 2.3. The measurements showed

that detection efficiencies as high as 1.6% can be achieved when looking at σ polarized photons on the quantization axis. For the measurement of arbitrary polarizations an overall detection efficiency of 1.1% was derived when collecting photons with both HALOs, and an efficiency of 0.7% is to be expected when using a single optimally positioned HALO. The numbers are in good agreement with the individual coupling and transmission efficiencies of all employed optical components and the specified quantum efficiency of the detectors.

Another set of experiments was done to estimate the single-photon absorption probability at 854nm with an attenuated laser beam. The results showed an overall absorption probability of 5×10^{-4} in the dark trap and 6×10^{-4} in the bright trap. Owing to the general problem to precisely calibrate a stream of laser photons by the use of a commercial detector, the uncertainties of these numbers are rather high. But still, the results provide a much better and precise quantitative insight into the interaction process than obtained by preceding estimates.

The efficiency measurements for the single-photon detection at 393nm and the single photon absorption at 854nm are both in good agreement with preliminary estimates from earlier times. They furthermore prove that the overall alignment in the experimental set-up is after the rebuilding phase (due to the move) now in a shape which provides a good starting point to address heralded state-transfer schemes from photons to ions.

4. Setup of a laser system for coherent manipulations at 729 nm

As essential tool for coherent control of the ions' electronic and motional state, a laser system at 729 nm has been set up for excitation on the $S_{1/2}$ - $D_{5/2}$ transition. In the experiment, the main tasks for a laser on this narrow-linewidth optical transition are

- state discrimination by electron shelving
- qubit rotations on single ions
- preparation of coherent superpositions in the $D_{5/2}$ level
- temperature measurements of the ion motion
- sideband cooling to the motional ground state
- quantum-logic operations with multiple ions.

To have full flexibility, it should be possible to reliably address the multitude of all optical transitions between the $S_{1/2}$ and $D_{5/2}$ level (Section 1.2.3). Typically, a laser linewidth on the order of 1 kHz or lower is desirable for basic coherent manipulations, lasting not longer than $\sim 150 \mu\text{s}$. In addition, long-term stability over several hours and high laser intensities for fast excitation on the dipole-forbidden transition are further requirements.

In the past 10 years, the fast technical progress in the field of tunable diode lasers and the availability of high-finesse optical cavities made of ultra-low-expansion glass (ULE), have led to the development of a robust method to achieve the required stability in table-top experiments [132, 133, 134]. This approach is nothing else than the well established Pound-Drever-Hall laser frequency stabilization [135], pushed to its limits by the use of ultra-stable narrow-bandwidth reference cavities and a very fast feedback loop to the laser-diode current. In this chapter, the details of the construction of such a laser system will be explained, and experimental results characterizing its performance will be presented.

Section 4.1 summarizes the theoretical background for laser frequency stabilization to optical resonators. The subsequent section (4.2) is about the experimental implementation of the stabilization and the set-up involved to send the laser to both ion traps. In Section 4.3, details about the set-up of the high-finesse ULE cavity used for the laser stabilization will be discussed, including the temperature stabilization of the system and measurements of the main cavity characteristics. The last section (4.4) of this chapter explains the experimental procedure that has been established to do basic experiments with single ions, and that is used to characterize the performance and stability of the system.

4.1. Theory

4.1.1. Optical resonators

The performance of the laser stabilization will strongly depend on the optical properties of the reference oscillator. In the following, the theoretical background of importance for the relevant properties of the high-finesse cavity that is used as reference will be summarized. A detailed treatment of optical resonators is found in [136, 137].

Suppose, a sinusoidal electrical field E_{inc} with frequency ω is incident on a mirror M_1 that is forming an optical resonator together with a second mirror M_2 at the distance L . The steady state circulating field right behind the first mirror is then given by

$$E_{\text{circ}} = it_1 E_{\text{inc}} + \underbrace{r_1 r_2 \exp\left(-\alpha 2L - i\omega \frac{2L}{c}\right)}_{g_{\text{rt}}(\omega)} E_{\text{circ}} , \quad (4.1)$$

with t_1 being the transmission coefficient for M_1 and $g_{\text{rt}}(\omega)$ being the net round-trip loss of the cavity. Losses occur due to finite mirror reflectivities (r_1, r_2), absorption in the medium between the two mirrors (absorption coefficient α) and a phase mismatch between the incident and circulating light fields depending on the round-trip time of the light $t_{\text{round}} = \frac{2L}{c}$. The transmitted and reflected signals are described as

$$E_{\text{trans}} = it_2 \exp\left(-\alpha L - i\omega \frac{L}{c}\right) E_{\text{circ}} \quad (4.2)$$

with t_2 as the transmission coefficient for M_2 , and

$$E_{\text{refl}} = r_1 E_{\text{inc}} + it_1 r_2 \exp\left(-\alpha 2L - i\omega \frac{2L}{c}\right) E_{\text{circ}} . \quad (4.3)$$

Assuming identical reflection and transmission coefficients for both mirrors ($r_1 = r_2 = r$, $t_1 = t_2 = t$, $r^2 + t^2 = 1$) and negligible absorption losses ($\alpha = 0$), the cavity reflection coefficient is

$$F(\omega) = \frac{E_{\text{refl}}}{E_{\text{inc}}} = \frac{r \left(1 - \exp\left(-i\omega \frac{2L}{c}\right)\right)}{1 - r^2 \exp\left(-i\omega \frac{2L}{c}\right)} . \quad (4.4)$$

The ratio between the transmitted intensity I_{trans} and input intensity I_{inc} of the cavity can be calculated as

$$\frac{I_{\text{trans}}}{I_{\text{inc}}} = \left| \frac{E_{\text{trans}}}{E_{\text{inc}}} \right|^2 = \frac{t^4}{t^4 + 4r^2 \sin^2\left(\omega \frac{L}{c}\right)} . \quad (4.5)$$

The transmission given by this equation shows resonances for the cases that the round-trip phase shift $\omega \frac{2L}{c}$ equals an integer multiple of 2π , which is given at the frequencies

$$\nu_q = \frac{\omega_q}{2\pi} = q \cdot \frac{c}{2L} , \quad q = \text{integer} . \quad (4.6)$$

The frequency spacing between these axial cavity modes is called Free Spectral Range (FSR) and is given by

$$FSR = \Delta\nu_{\text{ax}} = \frac{c}{2L} . \quad (4.7)$$

Using Equation (4.5), the FWHM of the resonance peaks is calculated as

$$\Delta\nu_{\text{cav}} = \frac{c}{L\pi} \arcsin\left(\frac{1-r^2}{2r}\right) \stackrel{r^2 \approx 1}{\approx} \frac{1-r^2}{\pi r} \Delta\nu_{\text{ax}} . \quad (4.8)$$

The ratio between the axial cavity-mode spacing $\Delta\nu_{\text{ax}}$ and the mode linewidth $\Delta\nu_{\text{cav}}$ is called the finesse \mathcal{F} :

$$\mathcal{F} = \frac{\Delta\nu_{\text{ax}}}{\Delta\nu_{\text{cav}}} \approx \frac{\pi r}{1-r^2} . \quad (4.9)$$

The finesse is a measure for the frequency resolution of the optical resonator, and for negligible absorptive losses it only depends on the reflectivity coefficients of the mirrors. It is therefore closely related to the decay time τ_{cav} of the cavity field that can be measured if the input field is suddenly switched off [138].

$$\mathcal{F} = \frac{\pi c}{L} \tau_{\text{cav}} \quad (4.10)$$

A physical interpretation of $\mathcal{F}/2\pi$ is the number of roundtrips that a photon survives inside of the resonator before it decays out of it. When used as a frequency reference, a narrow linewidth $\Delta\nu_{\text{cav}}$ of the optical cavity is essential. From Equations (4.7) and (4.9) it follows that this can be achieved with highly reflecting mirrors and a big cavity length L .

So far, the optical radiation inside of the cavity has been treated as a plane wave, ignoring any possible transverse spatial variation of the wavefront. But due to diffraction depending on the position (x, y) relative to the optical axis z of the resonator, plane waves are not representing stationary fields in an open resonator. Eigenfunctions of the system can be found by solving the paraxial wave equation [136] and are called Hermite polynomial solutions. In general, these mode functions are referred to as transverse electro magnetic modes TEM_{nm} with n and m being the transverse mode numbers. The normalized field pattern for the lowest order solution TEM_{00} is given by [139]

$$u(r, z) = \frac{\omega_0}{\omega(z)} \exp\left[-i\left\{k(z-z_0) - \arctan\left(\frac{\lambda(z-z_0)}{\pi\omega_0^2}\right)\right\}\right] \exp\left[-r^2\left(\frac{1}{\omega(z)^2} + i\frac{k}{2R(z)}\right)\right] , \quad (4.11)$$

representing a mode with a purely Gaussian transversal intensity profile with the beam waist

$$\omega(z) = \omega_0 \sqrt{1 + \left(\frac{\lambda(z-z_0)}{\pi\omega_0^2}\right)^2} \quad (4.12)$$

and the radius of curvature of the wave front

$$R(z) = (z-z_0) \left(1 + \left(\frac{\pi\omega_0^2}{\lambda(z-z_0)}\right)^2\right) , \quad (4.13)$$

with $\omega(z_0) = \omega_0$ and $R(z_0) = \infty$. To represent a stable solution for an optical resonator with two mirrors at the distance L with the radii of curvature R_1 and R_2 , the wavefront curvature of the Gaussian mode obviously has to match the curvatures of the mirrors and the beam

parameters ω_0 , z_1 and z_2 have to be determined by solving the following equation system:

$$\begin{aligned} R(z_0 + z_1) &= -R_1 \\ R(z_0 + z_2) &= +R_2 \\ L &= z_2 - z_1 . \end{aligned} \tag{4.14}$$

For a half-symmetric cavity consisting of a planar mirror ($R_1 = \infty$) and a concave mirror ($R_2 = R$) at a distance L , this leads to a waist ω_0 which is located at the position of the planar mirror:

$$\begin{aligned} z_1 &= z_0 := 0 \\ z_2 &= L \\ \omega(z_1) = \omega_0 &= \left(\frac{L\lambda}{\pi} \sqrt{\frac{R-L}{L}} \right)^{\frac{1}{2}} . \end{aligned} \tag{4.15}$$

To efficiently couple an external beam to the cavity, these conditions have to be perfectly matched, which is the so-called mode matching.

To calculate the parameters of optical elements that are required to achieve the mode-matching condition, a Gaussian beam is usually described by the complex beam parameter $q(z) = z + i\frac{\pi\omega_0^2}{\lambda}$. This has the advantage that the transformation of a beam q_{in} by the transmission through optical elements can be easily described by the ray-transfer-matrix formalism [139, 136] with the propagation law

$$q_{\text{out}}(M, q_{\text{in}}) = \frac{Aq_{\text{in}} + B}{Cq_{\text{in}} + D} . \tag{4.16}$$

$M = \begin{pmatrix} A & B \\ C & D \end{pmatrix}$ is the transfer matrix, describing the properties of the optics. The mode-matching condition to a cavity mode q_{cav} is then found by solving the equation

$$q_{\text{cav}} \stackrel{!}{=} q_{\text{out}}(M, q_{\text{in}}) \tag{4.17}$$

for the optical parameters that are contained in M .

4.1.2. Laser stabilization

When stabilizing the frequency of a laser, its spectrum has to be compared to some stable spectral reference or frequency discriminator. This could be for example an atomic sample, a second stable laser or an optical cavity. The latter provides the highest flexibility as a reference, since an adjustment of the cavity design makes it possible to fit its properties to the exactly needed requirements for the stabilization. This is in particular necessary for an active linewidth reduction of a tunable laser via a very fast feedback loop by the comparison with a narrow-band reference.

A very powerful technique to stabilize tunable lasers to optical resonators has been developed by Drever and Hall [135], which adopted an older technology originally invented by Pound for

the microwave regime. The principle of this so-called Pound-Drever-Hall stabilization is to measure the phase shift of a laser beam that is reflected by an optical resonator. In contrast to the intensity dependence of the reflection (which is symmetric around resonance), the accumulated phase exhibits a monotonic dependence on the detuning with a strong variation close to resonance. Most importantly, it permits the measurement of the sign of the frequency difference between laser and cavity mode. Generating a feedback signal from the measured phase shift thereby allows one to stabilize the laser to the center of a cavity resonance.

To perform the phase measurement, a phase-modulated laser beam with a modulation frequency ω_{mod} much higher than the bandwidth of the cavity resonance is usually sent to the optical resonator.

$$E_{\text{inc}} = E_0 e^{i(\omega t + \beta \sin(\omega_{\text{mod}} t))} \stackrel{\beta < 1}{\approx} E_0 \left[e^{i\omega t} + \frac{\beta}{2} \left(e^{i(\omega + \omega_{\text{mod}})t} - e^{i(\omega - \omega_{\text{mod}})t} \right) \right] \quad (4.18)$$

ω is the unmodulated carrier frequency of the laser. For a small modulation depth ($\beta < 1$), the phase modulation causes first order spectral sidebands of the incident light at the frequencies $\omega \pm \omega_{\text{mod}}$. When the laser is now tuned close to the resonance frequency ω_{cav} of the cavity, only a portion of the carrier will be coupled to the resonator, with its reflection undergoing a frequency dependent phase shift (see Equation (4.4)). At the same time the sidebands are fully reflected, as their frequencies are outside the cavity transmission range. The interference of the carrier reflection with the sidebands acting as a reference oscillator, leads to a beat signal carrying the important phase information which is then measured with a fast photodiode. The signal is finally extracted by mixing the intensity beat with the local oscillator running at ω_{mod} down to DC and isolating it from the other frequency components with a low-pass filter¹. Doing the calculation [140], the resulting error signal is given by

$$\epsilon(\omega) = -2\sqrt{P_c P_s} \text{Im}\{F(\omega)F^*(\omega + \omega_{\text{mod}}) - F^*(\omega)F(\omega - \omega_{\text{mod}})\}, \quad (4.19)$$

with P_c and P_s being the power of the incident carrier and sideband frequency components and $F(\omega)$ the cavity reflection coefficient as given by (4.4). It is then fed to a fast servo amplifier (PID), which transforms the error signal to give a feedback to the laser frequency, keeping it on the cavity resonance.

Given this explanation, the resulting stabilization set-up simply seems to be a frequency discriminator, which corrects for a frequency detuning between the laser and the cavity mode and which is limited by the response function of the measured phase shift on the detuning. However, in practice it turns out that the stabilization is capable of an effective linewidth reduction of the laser by several orders of magnitude below the spectral linewidth of the reference-cavity mode. This effect can be understood when considering the explained locking mechanism as a phase lock, which keeps the laser in phase with the light that is circulating in the cavity. Especially for small bandwidths of the cavity mode and therefore long cavity-field decay times, the out-coupled field contributing to the carrier reflection will not follow fast phase fluctuations that the laser may undergo. Via the phase-sensitive feedback loop, the laser is therefore phase locked to a short-time stable phase reference, generated by the stored laser light in the cavity. This leads then to a drastic reduction of the laser linewidth, which is far below the frequency resolution of the reference cavity.

¹To compensate phase shifts due to the different signal propagation delays of the photodiode and the local oscillator, usually an overall phase shift is applied before mixing both signals.

4.2. 729 nm laser

The laser that is used in the experiment is a commercial grating-stabilized diode laser that is amplified with a tapered amplifier (Toptica, TA Pro). Around 400 mW of laser power at 729.1467 nm are available on the main output, after the amplifier and an optical isolator.

In this type of diode laser, a diffraction grating is set up in the *Littrow* configuration, feeding back the 1st diffraction order to the laser diode and building an external cavity together with the rear facet of the diode [141]. The 0th diffraction order is then available as the output of the laser resonator. The diffraction grating can be tilted with a piezo actuator, enabling control of the wavelength that is fed back to the laser diode over its whole gain profile, thus providing a big tuning range of the system. Due to the rather high finesse of this external cavity compared to the resonator built by the diode itself, the spectral linewidth of the free running laser is effectively reduced to typically a few 100 kHz for the commercial system that is used. The tunability additionally offers the possibility for a stabilization of the laser wavelength on longer timescales, limited by the finite speed of the piezo actuator. To achieve a further reduction of the spectral linewidth, a fast feedback with an appropriate error signal onto the laser-diode current has to be applied, as it will be explained in the following section.

During the thesis two different generations of laser systems were operated. The older system (Toptica, DL 100 + TA) had quite some trouble to run at the precise wavelength needed to be on resonance with the transition in the ion. The required point of operation was just in a very narrow window between two mode jumps. By tuning the diode temperature and current it was only possible to center the range of normal operation between these two mode jumps. Changes of the lab temperature then often caused the laser to go to multi-mode operation, which had a failure of the lock as consequence. After moving the experiment to the new lab, the laser (including the diode) got replaced by the newest generation of the same model. Nevertheless, the new laser diode shows exactly the same feature as the older one, having only a very narrow range of single-mode operation around the required wavelength. Thanks to a much better temperature stabilization of both, the laser and the laboratory air conditioning, drifts of the mode of operation do not happen anymore, and the laser usually stays locked during the whole day.

4.2.1. Set-up for frequency stabilization

Figure 4.1 gives an overview over the main components building the locking chain. Before passing through the tapered amplifier, 2.7 mW of laser power are coupled out to a probe beam which is used for the frequency stabilization.

A little portion of light is split off and sent through a low-finesse optical cavity of the same type as the ones that are used for the transfer lock for all the other lasers in the experiment [66, 91]. While measuring the transmission signal with a photodiode, the cavity length is permanently scanned to monitor the laser mode structure on an oscilloscope. This set-up has no function for the lock and is only necessary to verify the single-mode operation of the laser, when locking it. In principle this could be done with the ULE cavity itself by measuring the transmission while scanning the laser frequency. But due to the very high finesse and the huge free spectral range (Section 4.3), almost no light is coupled to the cavity when scanning the laser over its resonances, even for scan speeds in the range of 1 Hz. Another small fraction of

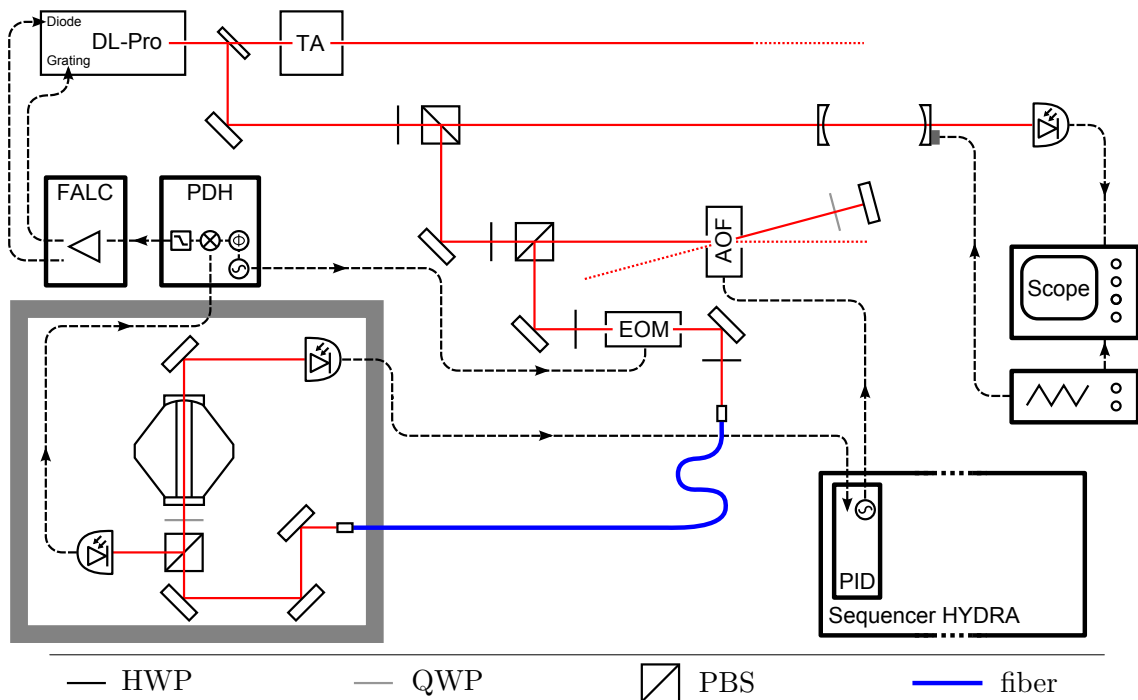


Figure 4.1.: Schematic representation of the experimental set-up to lock the 729 nm laser to the high-finesse cavity. Lenses and other components not contributing to the basic function of the lock are omitted in the drawing. Abbreviations and acronyms are explained in the text.

the beam is sent to a wavemeter (not displayed), to identify the right cavity mode.

The remaining part of the beam (2 mW) is used for the lock. It first passes through an acousto-optic frequency shifter² (AOF, Brimrose TEF-270-100-729) in double-pass configuration, enabling the control of the amplitude and frequency of light that is sent to the cavity. It is running at 288 MHz and thereby shifting the laser frequency by +576 MHz. This frequency shift is necessary to bridge the frequency difference between the electronic transition of the calcium ion and the closest resonance of the cavity (see Figure 4.4).

The beam is then phase-modulated with an electro-optic modulator (EOM) made of LiNbO_3 , which is running at 20 MHz. The RF signal is supplied by the local oscillator of the Pound-Drever-Hall (PDH) module (Toptica, PDD 110) from the laser locking electronics. To achieve a good modulation depth, the RF signal is first amplified with a commercial RF amplifier (Minicircuits, ZHL-1-2W-S) and second with a home-built transformer. The EOM set-up has been adapted from an earlier version of the laser set-up, running at a different wavelength and with a different locking scheme. Details can be found in [142].

A polarization-maintaining single-mode fiber (PM630-HP) is used to send the laser light to the box containing the ULE-cavity set-up (Section 4.3). To minimize phase noise of the light that is sent to the cavity and to keep the signal paths short for the feedback loop, the cavity set-up should be placed as close as possible to the laser. At the same time it should

²Throughout this chapter, acousto-optic modulators that are optimized for efficient frequency shifting will be referred to as AOF and modulators optimized for fast amplitude switching will be referred to as AOM.

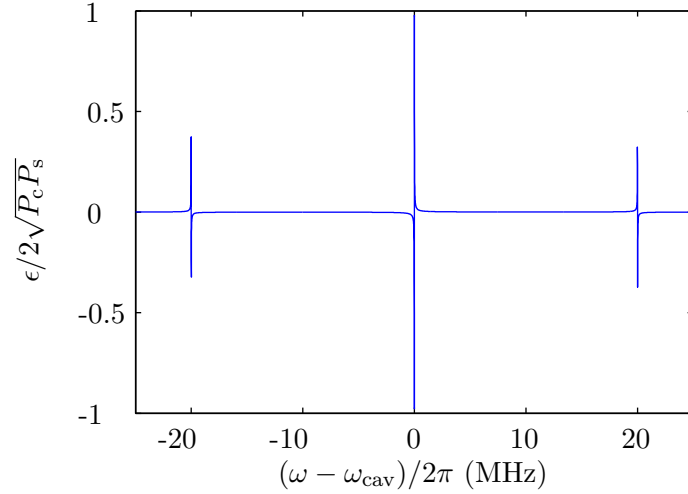


Figure 4.2.: Error signal calculated with (4.19) for the experimentally determined cavity parameters ($\Delta\nu_{\text{cav}} \approx 4$ kHz, Section 4.3.3) and a modulation frequency $\frac{\omega_{\text{mod}}}{2\pi} = 20$ MHz.

be well isolated from the rest of the laboratory environment, to keep it safe from acoustic and mechanic vibrations and temperature drifts. In our laboratory this compromise results in a fiber length of 7 m and a signal-cable length of 5 m.

Inside the box, the 729 nm light is coupled to the cavity and two fast photodiodes are used to measure the reflection and transmission signal. The signal from the photodiode looking at the reflection (NewFocus, 1801-FS, 125 MHz) is fed back to the PDH module, which contains the reference oscillator, a phase shifter, a frequency mixer and a low-pass filter to generate the error signal for the lock (see Section 4.1.2 and Figure 4.2). The signal from the photodiode in transmission (ICFO design, 100 MHz) is sent to the pulse sequencer *HYDRA* (Section 1.3.3), which is giving a feedback to the locking-beam intensity via the AOF, to keep the transmitted power constant³. To keep heating effects of the mirror coatings of the cavity as low as possible, the lock has been optimized for the lowest possible power of the incident beam, yielding still the required robustness for daily lab operation. When locked, the system operates with $14.5 \mu\text{W}$ of laser light incident on the vacuum chamber containing the high-finesse cavity, achieving a transmitted power of $5.5 \mu\text{W}$, which can be seen with bare eye. Given the very narrow linewidth of the cavity of ~ 4 kHz (details in Section 4.3), the transmission of 38% is remarkable and a good benchmark for the performance of the lock. It was found to be constant even after several months of operation.

To close the feedback loop for the frequency stabilization, the error signal coming from the PDH module is fed into a commercial high-speed control amplifier (Toptica, FALC 110). The amplifier has a low-speed integrating part which is used to compensate for slow frequency drifts via a feedback onto the piezo actuator that is tilting the grating from the external laser resonator. A second – high-speed – circuit branch is used to give a feedback onto the laser-diode current and thereby leading to an effective reduction of the laser linewidth. This fast

³ Since the error signal for the frequency lock is to first order independent on the laser power [140], the two feedback loops don't interfere and the lock with both loops activated stays stable during the whole day.

amplifier branch is divided into four variable filtering stages allowing a flexible adjustment of the overall transfer function over the whole bandwidth ranging from DC to ~ 10 MHz [143]. As already mentioned before, the narrow linewidth of the ULE cavity provides a sensitive tool for optimization of the lock parameters, by simply maximizing the cavity transmission when the laser is locked. The final positions for the dip switches on the module for the best locking performance are as follows (see [143] for details): XSLI 10 (deactivated), SLI 9, FLI 7, FLD 7. Figure 4.3 displays a measurement of the resulting transfer function of the fast feedback part of the amplifier.

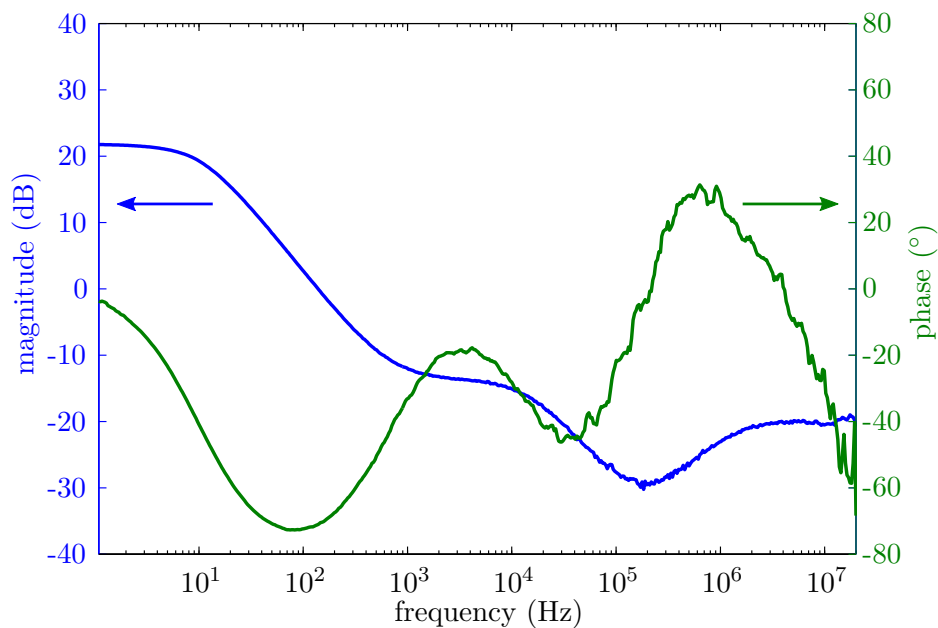


Figure 4.3.: Measured transfer function of the high-speed amplifier FALC 110 with the settings that are used to lock the laser to the ULE cavity. The measurement was done with the network-analyzer mode of a DigiLock module (Toptica) from another laser system in the experiment.

Additional care had to be taken when adjusting the side-band modulation amplitude. Theoretically, the highest performance of the lock is expected for a rather high modulation depth ($\beta = 1.08$) [140], leading to a significant portion of power in the spectral sidebands. However, for this situation the system sometimes locks to a sideband rather than to the carrier, leading to a shift of the laser wavelength by the modulation frequency of 20 MHz which is hard to see by simply looking at the wavemeter reading. Changing the other feedback parameters had no influence, therefore the modulation amplitude has been reduced such that the effect did not happen anymore.

4.2.2. AOM set-up to ion

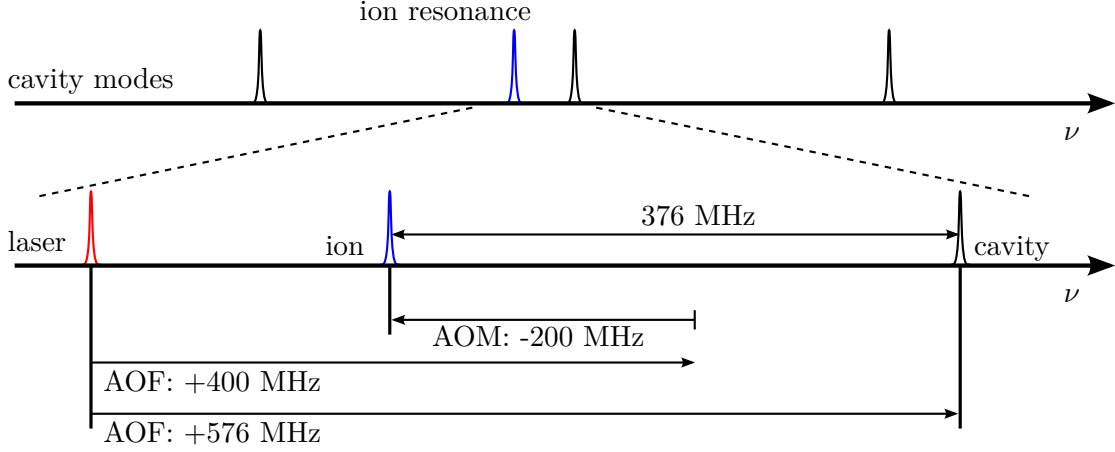


Figure 4.4.: Schematic drawing of the relative position of the resonances of the high-finesse cavity at its zero expansion temperature and the optical transition in the ion. Given the free spectral range of the cavity of ~ 2 GHz, we were really lucky that the ion resonance is within a distance of the next cavity resonance, that can be easily bridged with standard AOMs.

Figure 4.4 illustrates the relative positions of the ion resonance, the closest cavity modes, and the laser frequency. In principle it would be possible to operate the laser on resonance with the closest cavity mode. Since the absolute distance to the $S_{1/2}$ - $D_{5/2}$ transition frequency is only about 376 MHz, the laser could be easily shifted with a single AOM. But because of a completely unknown zero-expansion temperature of the ULE cavity (Section 4.3) at the time when setting up the system, an AOF controlling the frequency and amplitude of light that is sent to the cavity guaranteed a much higher flexibility. In addition it is required for the intensity stabilization of the locking beam (see last section) and in future experiments it will be used for an automatized compensation of slow drifts of the cavity resonance.

When sending the laser beam to the ion, the precise control of frequency, phase, and amplitude of the light is required. For future experiments that require the entanglement of several ions in a string in a trap, it should additionally be possible to easily generate bichromatic laser pulses [144]. In the present set-up, the most robust way to achieve those requirements is to use a configuration consisting of two cascaded AOMs (see Figure 4.5).

One AOF per trap (Brimrose, TEF-200-50-729) is set up in double-pass configuration on the laser table. It is mainly used to set the frequency of the laser beams⁴. The output is sent through a fiber (PM780-HP, selected for 729 nm) to the ion-trap set-up. A small fraction of the fiber output is split off with a coated glass plate and monitored with a photodiode. The signal is used to give a feedback onto the AOF amplitude via the experiment control *HYDRA*, which ensures that the laser intensity at the ion traps is always kept constant. A second AOM (Brimrose, TEM-200-50-729) is positioned right in front of one of the viewports of each vacuum

⁴The AOFs are set up with the +1st order, center frequency: 200 MHz.

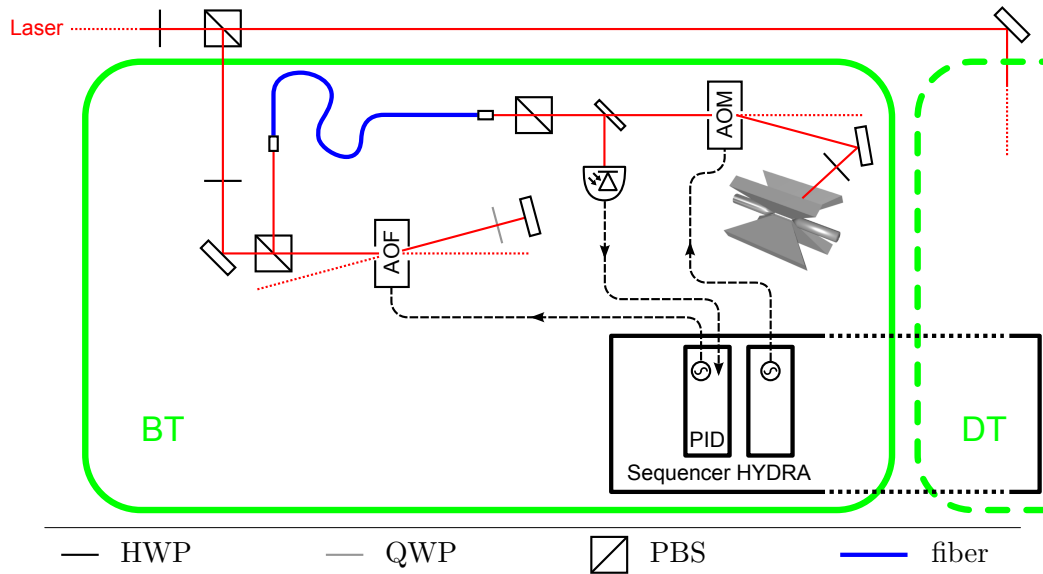


Figure 4.5.: Schematic drawing of the AOM set-up for the control of 729 nm light that is sent to the ion. The solid and dashed green box indicate that an identical assembly is used for both ion traps of the experiment, the bright trap (BT) and dark trap (DT).

chamber⁵. It is used for setting and switching of amplitudes and phases of the 729 nm beam. Since it is set up in single passage, it also offers the option to generate a bichromatic light field by the supply with a bichromatic RF signal. A HWP is used to control the linear polarization of light that is sent to the ion. Since the beam is oriented under a 45° angle with respect to the magnetic field direction (see Figure 4.14), it is possible to excite all electronic transitions on the $S_{1/2}$ - $D_{5/2}$ manifold (see Section 4.4).

The available space in front of the vacuum chambers is very limited. To achieve fast switching times and a good diffraction efficiency of the AOMs, a focal-spot size within the crystal of around $55 \mu\text{m}$ has to be reached (resulting rise time: $\sim 11 \text{ ns}$). At the same time the smallest possible spot size at the ion position is required for fast coherent manipulations. Due to the limited space the working distance of the last lens focusing the beam onto the ion must be bigger than 280 mm. Figure 4.6 shows the final arrangement of off-the-shelf lenses to achieve the required performance. The fiber out-coupler that is used (Schäfter + Kirchhoff, 60FC-4-M15-37), generates a collimated Gaussian beam with a $1/e^2$ diameter of 2.71 mm. The spot size after focusing the beam with a lens of focal length $f = 150 \text{ mm}$ into the AOM is around $51 \mu\text{m}$, leading to the required switching performance while keeping the losses on a moderate level (70% diffraction efficiency). A lens with $f = 200 \text{ mm}$ collimates the beam to a diameter of 3.61 mm which is then focused to a spot size of $77 \mu\text{m}$ at the position of the trap center.

⁵The AOMs are set up with the -1st order, center frequency: 200 MHz

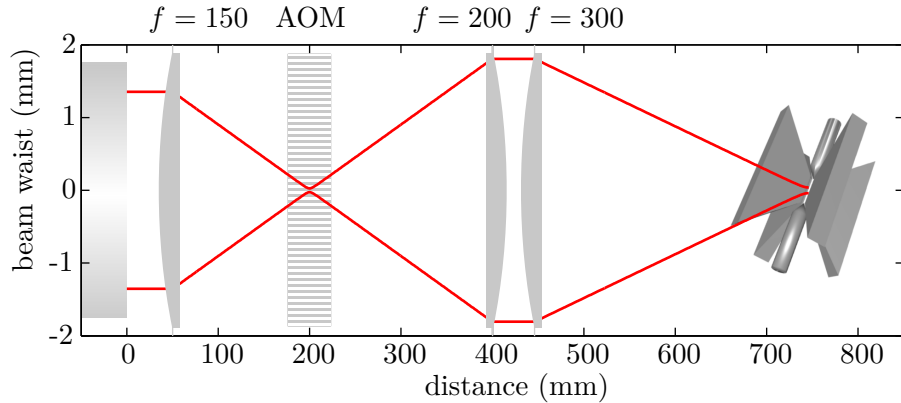


Figure 4.6.: Illustration of the beam-diameter propagation from the output of the fiber coupler (left) through the AOM to the center of the ion trap (right). Three lenses at the given focal lengths (in mm) are used. The displayed components are not to scale.

4.3. High-finesse ULE cavity

The high-finesse optical cavity that is used to stabilize the laser is a vertically midplane mounted model [133] bought from Advanced Thin Films, with a length of 77.5 mm. The design of the cavity spacer is optimized to reduce length changes of the cavity caused by mechanical vibrations, especially in the vertical direction. To minimize the effects of thermal expansion of the cavity spacer, it is made of ultra-low-expansion glass (ULE) from Corning, having a zero crossing of its coefficient of thermal expansion at a certain temperature T_z ⁶. In other works [133, 134] this cavity model has been successfully used to achieve sub-Hertz laser line widths with reasonable drift rates below 1 kHz per day.

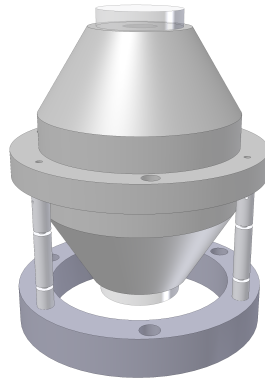


Figure 4.7.: Drawing of high-finesse ULE cavity resting on three teflon bars that are fixed in a stainless-steel ring. The laser beam is coupled-in from below.

During this thesis, a simpler version of the set-ups that have been used in the already mentioned works was implemented, to achieve a laser stability which is sufficient to perform the main tasks for the experiment (see beginning of this chapter). The cavity rests on three

⁶According to the specifications of the purchased cavity $T_z = 26^\circ\text{C} \dots 33^\circ\text{C}$.

50 mm long teflon bars with a diameter of 5 mm (Figure 4.7). To provide transportation stability for the move of the experiment, the bars are screwed to the cavity and their other end is tightly fixed in a ring made of stainless steel. This ring is then attached to the bottom flange of the vacuum chamber containing the cavity. Each bar has two intersections with a reduced diameter of 2 mm, to damp the heat flow and mechanical stress coming from the stainless-steel flange caused by temperature drifts.



Figure 4.8.: Picture of the vacuum chamber containing the high-finesse cavity. The whole set-up is resting on a passive vibration-damping platform and is surrounded by a temperature-stabilized aluminum box.

Figure 4.8 shows a picture of the set-up surrounding the high-finesse cavity. Compared to the cavity size, a rather big vacuum chamber made of stainless steel (304L) with a volume of 2.94 L is used to thermally and acoustically isolate the cavity from the environment. Due to its rather bad thermal conductivity⁷, stainless steel provides a good passive thermal isolation, and is easier to manufacture compared to chambers made of aluminum. The oversize was chosen to keep the possibility to include a temperature stabilization with heat shields inside of the vacuum chamber in a future version of the set-up, but the current measurements show, that

⁷ $\lambda_{\text{St. Steel}}/\lambda_{\text{Al}} \approx 7\%$

the stability is by far sufficient for the planned experiments. The vacuum chamber is kept at a pressure of 4.5×10^{-10} mbar (without bakeout) with a 20 L ion pump (Gamma Vacuum, 25S).

The system is floating on a passive vibration-damping platform (Minus K, 100BM-4), which offers a better damping performance than the optical air-tables in the lab. In addition, it makes it possible to place the set-up in a protected corner, independent from the other experiments. The total weight of the assembly on top of the platform is close to its maximum load of 48 kg, therefore the number of components is reduced to a minimum.

To operate the cavity close to its zero-expansion temperature T_z , a twofold temperature stabilization is required as it will be explained in Section 4.3.1. The laser beam is coupled to the cavity from below, details about the mode matching will be explained in Section 4.3.2. In Section 4.3.3, measurements of the main cavity properties will be presented.

4.3.1. Temperature stabilization

Several other groups working with the same model of the high-finesse cavity have experienced that T_z is significantly lower than room temperature. They had to deal with this problem by the aid of sophisticated temperature-stabilization schemes as for example in [134]. The problem was caused by a mistake in the mixture of the components in the ULE glass forming the cavity spacer. Our cavity came from a different batch and was specified to have a T_z significantly above room temperature, which would allow a temperature stabilization only by heating.

In a first version, the vacuum-chamber temperature was stabilized with four heater mats (RS, 245-540) which are directly attached to the outside of the chamber walls. Two NTC temperature sensors (EPCOS B57703M0103G040) are placed at opposite positions on the vacuum-chamber wall (see Figure 4.9) and a home-built temperature controller (ICFO design) evaluates the average temperature between both sensors and regulates the heater mat current. First measurements of the cavity resonance for different temperatures of the vacuum chamber (see Section 4.4.3) revealed a value of the zero-expansion temperature of $T_z \approx 21^\circ\text{C}$, being exactly at the laboratory temperature. This makes it impossible to stabilize the chamber with a circuit that is only able to either heat or cool. One common approach is to use peltier elements that are directly attached to the vacuum-chamber walls, but such a system usually has a decreased stability if it is regulating to a temperature that is close to the temperature of the surrounding heat bath. Furthermore, to achieve a short reaction time for the regulation, a chamber made of aluminum would be much more suitable for that approach.

To avoid opening the vacuum chamber to implement an in-vacuum stabilization, the whole set-up is placed inside a 1 cm thick aluminum box which is cooled with two peltier elements (Multicomp, HPE-127-10-08). Figure 4.9 gives an overview of all relevant components for the stabilization. A commercial high-current temperature controller (Wavelength electronics, PTC5000) that is supplied with a 12 V current source (Mean Well, SP-100-12) is used to stabilize the box temperature at its coldest point to 15°C . The controller drives a probe current of $100\ \mu\text{A}$ through an NTC sensor (Betatherm, 30K6A309I) which is placed in the copper spacer between one of the peltier elements and the box wall. To reduce the total resistance for a maximized tuning range of the controller current, both peltier elements are operated in parallel. Each peltier element is thermally contacted to a heatsink which is dimensioned such, that no fan is required to dissipate the absorbed heat. The outside of the aluminum

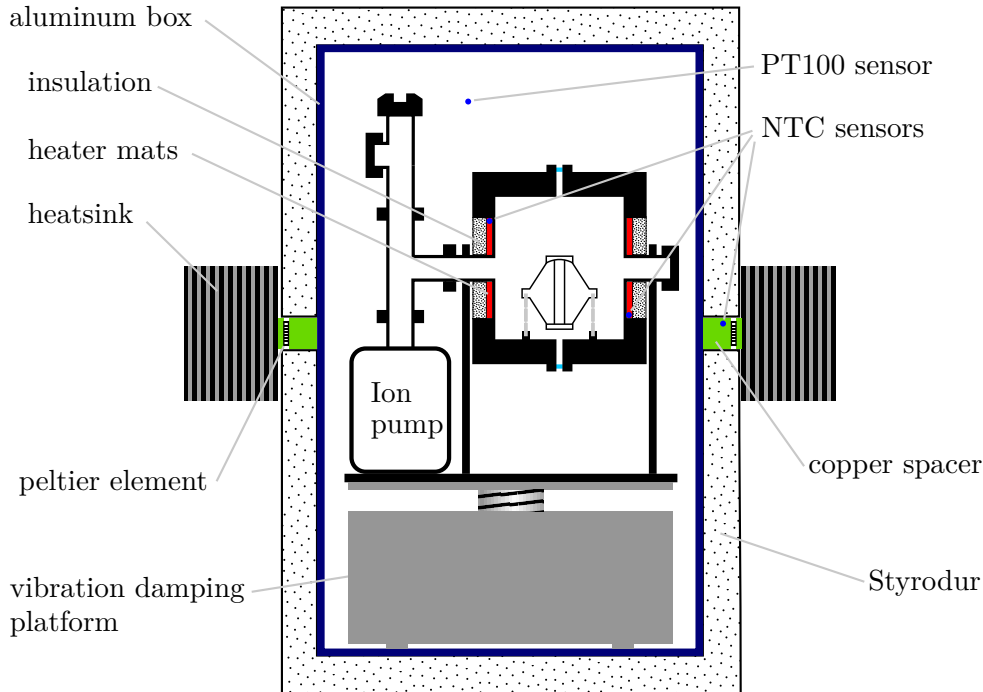


Figure 4.9.: Schematic cut through the box containing the high-finesse cavity set-up. Two individual control loops are used to stabilize the vacuum-chamber temperature. A heating circuit directly attached to the chamber and a cooling circuit which cools the surrounding air via the box walls.

box is thermally isolated with 5 cm of *Styrodur*. The heating circuit described in the previous paragraph is then used to stabilize the chamber temperature to T_z . For monitoring, one PT100 sensor is hanging freely in the air inside of the box and an additional sensor is placed outside, in the close proximity to measure the laboratory temperature. The vacuum-chamber temperature is monitored with the two NTC sensors that are also used for the stabilization.

Figure 4.10 shows a long-term temperature measurement of the system. The temperature drifts around their mean value are not following a pure normal distribution. To get a good measure for the temperature stability, the interval ΔT centered at the arithmetic mean of each measurement and containing 95 % of all data points has been numerically determined. Within the 15 days of measurement, the instabilities are as follows:

$$\begin{aligned}\Delta T_{\text{Lab}} &= 336 \text{ mK} \\ \Delta T_{\text{Box}} &= 76 \text{ mK} \\ \Delta T_{\text{Chamber}} &= 0.6 \text{ mK} .\end{aligned}$$

The air temperature inside of the box is at $18.34(2)^\circ\text{C}$, more or less centered between the 15°C of the peltier coolers and the $22.2643(2)^\circ\text{C}$ of the cavity chamber. The temperature fluctuations from the laboratory air are reduced to a level of 23 % by the thermal insulation and stabilization of the box. They are then further reduced to a level of 0.2 % by the insulation of the vacuum chamber itself and the stabilization via the heating circuit.

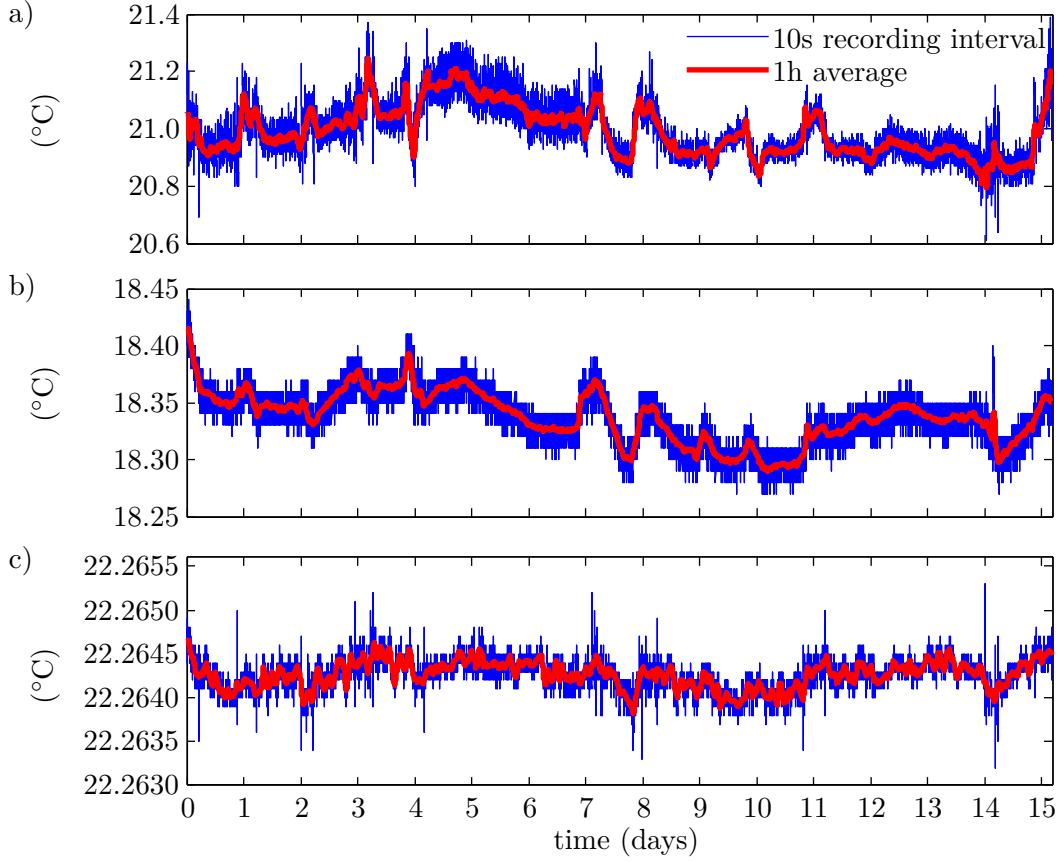


Figure 4.10.: Long-term temperature measurement of a) the laboratory, b) the air inside of the box, and c) the vacuum chamber. Sharp spikes to higher and lower temperature in c) are caused by electronic noise in the measurement circuit that are induced by switching on and off power supplies in the lab.

The crosstalk of the laboratory temperature fluctuations to the chamber-temperature drifts is further evaluated by calculating the correlation coefficients (see Appendix A.4) between the different systems. The speed v_{th} , at which a temperature change is propagating from one thermal reservoir to a second thermal reservoir that is separated by a rigid body, can be derived from the heat equation [145] and is given by

$$v_{\text{th}} = \sqrt{\frac{2\omega\lambda}{\rho c}} .$$

λ is the heat conductivity, c the specific heat capacity, and ρ the density of the isolating material. ω is the angular frequency of a periodic temperature change. When analyzing the crosstalk of the systems, a maximum of correlation between two different temperature measurements is expected after a certain time delay Δt , assuming that temperature drifts occur mainly with a fixed frequency. Figure 4.11 shows the variation of the correlation coefficient calculated with the three measurements as a function of an applied delay Δt between the data sets. To remove noise, a moving-average filter has been applied to the data with an

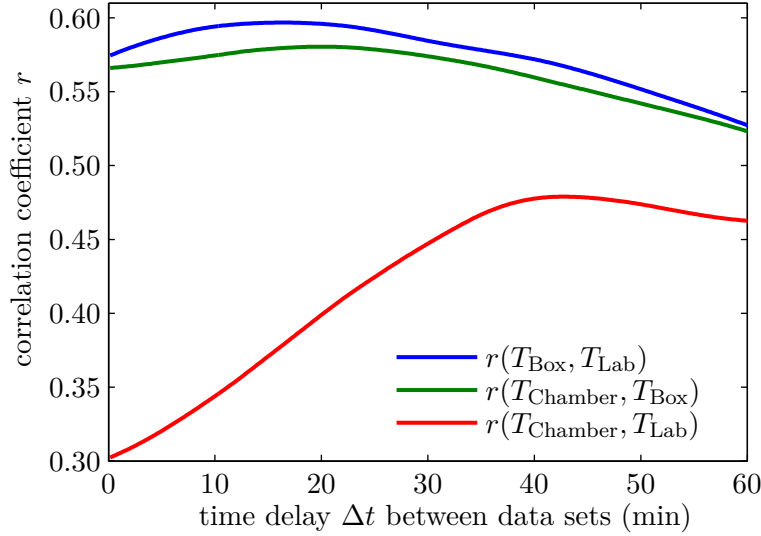


Figure 4.11.: Correlation coefficients r calculated for the three temperature measurements from Figure 4.10 as a function of an applied delay Δt between the datasets.

averaging interval of one hour (red lines in Figure 4.10). From the positions of the maxima, the typical time constants Δt for the coupling of the different systems are derived. The heat flow from the laboratory to the inside of the box has a delay of $\Delta t \approx 16$ min and a maximum correlation coefficient of $r \approx 0.6$, indicating a remaining strong correlation. The crosstalk from the temperature of the box to the vacuum chamber is slightly reduced ($r \approx 0.58$) and happens on a timescale of $\Delta t \approx 20$ min. When looking at the correlation from the laboratory to the chamber temperature, a value of $r \approx 0.48$ indicates that crosstalk is still a dominant source for variations, but given the sub-milikelvin stability it is clearly negligible and might only have importance for higher temperature drifts of the lab AC. The response time of the vacuum-chamber temperature to external drifts of the lab temperature is $\Delta t \approx 43$ min, a bit higher than the sum of the two other involved processes. The measurements furthermore indicate, that temperature drifts of the electronic components used for the internal setpoint of the heating circuit, which have direct contact to the laboratory temperature, can be ruled out as a source for instability, since they would cause a correlation on a much shorter timescale.

4.3.2. Mode matching

The high-finesse cavity is a half-symmetric resonator, consisting of a planar and a concave mirror with a radius of curvature of $R = 50$ cm and a mirror distance of $L = 77.5$ mm. The cavity is non-confocal ($L \neq R/2$) which leads to non-degenerate cavity modes TEM_{nm} .

For higher values of n and m the modes have bigger transverse sizes on the cavity mirrors, making them more susceptible to imperfections in the mirror substrates and thereby leading to a reduction of the cavity finesse. In addition, higher order modes have complex transverse structures which are difficult to match with an external beam that is coupled to the cavity. Therefore the TEM_{00} mode is used to couple the laser to the resonator.

For convenience, the laser beam is coupled-in through the planar mirror of the cavity, co-

inciding with the position of the beam waist ω_0 of the Gaussian mode (Section 4.1.1). With the given cavity parameters and Equation (4.15) this results in a $1/e^2$ diameter of the intensity distribution of the incident beam of

$$2\omega_0 = 410 \mu\text{m} .$$

The output of the fiber that sends the laser beam to the cavity set-up is collimated with a fiber coupler (Schäfter+Kirchhoff, 60FC-4-M8-10) to a beam diameter of $1450 \mu\text{m}$. To keep the set-up simple, mode matching should be achieved by the use of a single lens. Solving the mode-matching equation (4.17) for the given beam parameters, this leads to a required lens with a focal length of $f = 666 \text{ mm}$ which is not available from stock.

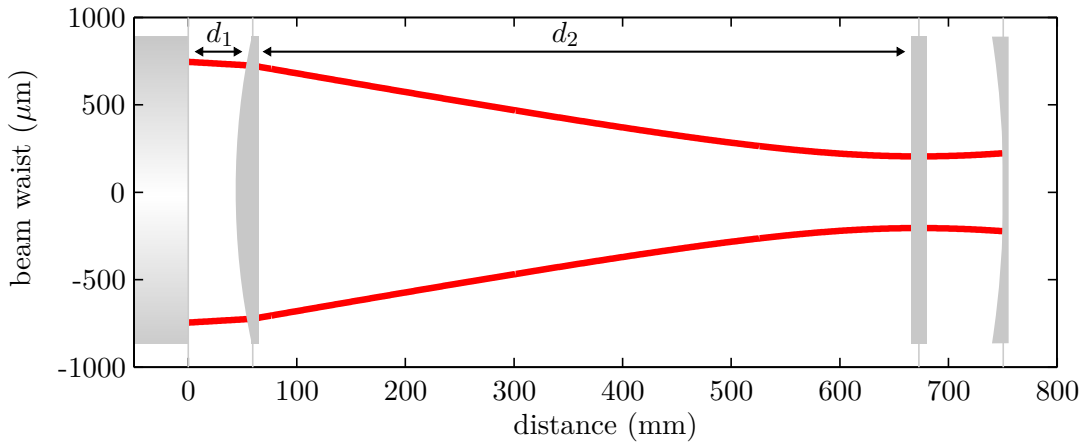


Figure 4.12.: Mode matching from the fiber coupler output (left) to the TEM_{00} of the high-finesse cavity (right). The sketched optics are not to scale. The shown beam propagation is calculated based on the measured parameters of the fiber-coupler output mode. Perfect mode-matching is achieved with a single lens by adjusting the distances d_1 and d_2 to the mode-matching condition.

To overcome this problem, the fiber-coupler lens has been adjusted to generate a slightly convergent beam. This then allows perfect mode matching with a single plano-convex lens with a fixed focal length f only by an adjustment of the two distances between fiber coupler and lens (d_1), and lens and planar cavity mirror (d_2). Before, the properties of the Gaussian beam coming out of the coupler had been determined by measuring the beam waist with a CCD camera at various distances and fitting the resulting dependence with the theoretical relation (4.12). Figure 4.12 displays the resulting beam propagation for a lens with focal length $f = 1000 \text{ mm}$ and the distances $d_1 = 6 \text{ cm}$ and $d_2 = 61 \text{ cm}$.

Coupling a laser to a high-finesse optical cavity is a non-trivial task. The higher the finesse, the bigger is the ratio between FSR and cavity linewidth (Section 4.1.1), and the narrower the cavity linewidth, the more time it takes for a cavity field to build-up. A big FSR requires a wide frequency scan of the laser to monitor the full spectrum of coupled modes, which usually results in a fast sweep over the cavity linewidth. To deal with these difficulties, a rather high laser power of a few $100 \mu\text{W}$ and a slow scan speed of the laser frequency around 10 Hz

was used to optimize the coupling of the beam to the cavity. The cavity transmission was simultaneously monitored with a rather slow but sensitive photodiode (Thorlabs, DET110) and a CCD camera to identify the different TEM_{nm} modes via their transverse intensity profiles. By an optimization of the in-coupling alignment and the distances d_1 and d_2 , a strong suppression of all higher order modes except for the TEM_{00} mode was achieved. This made the CCD camera obsolete and together with the slow photodiode it got replaced by a fast photodiode which is used for the intensity stabilization of the locking beam (Section 4.2.1).

Due to changes in the set-up and the move of the experiment, the coupling to the cavity was done at least four times from scratch. Interestingly, the optimal configuration for the position of the in-coupling beam was always found to be slightly off-center on the in-coupling mirror (around 1 mm). The same applied for the position of the transmission beam. Since the cavity is half-symmetric, this could be caused by a off-centered curvature of the concave mirror, or even a slight tilt of the mirror on the spacer. However, as it will be shown in the following section, the overall performance of the cavity is not affected at all by this manufacturing error.

4.3.3. Spectral properties

The most important property of the cavity when used as a frequency reference is its spectral linewidth $\Delta\nu_{\text{cav}}$. In absence of a reference frequency with a smaller signal bandwidth that could be used to probe the width of the cavity resonance, the common approach is to measure the field-decay time τ_{cav} of the cavity in a so-called ring-down measurement. τ_{cav} is directly related to the cavity finesse \mathcal{F} (Equation 4.10), which together with the FSR (Equation 4.9) leads to the well known dependence of the cavity resonance linewidth

$$\Delta\nu_{\text{cav}} = \frac{1}{2\pi\tau_{\text{cav}}} . \quad (4.20)$$

In the experiment, τ_{cav} is measured by first locking the laser to the cavity⁸ and then switching the locking beam off with the AOM while monitoring the transmission signal with the installed photodiode (Section 4.2.1). Figure 4.13 shows the obtained decay of the transmission signal from the cavity, the red curve is an exponential fit to the data. The photodiode signal for times smaller than zero corresponds to a spectral power of the cavity transmission of $9.4 \mu\text{W}$ (locking-beam power $24 \mu\text{W}$). Doing ten ring-down measurements and taking the mean decay time results in

$$\tau_{\text{cav}} = 39.45(5) \mu\text{s} .$$

The photodiode bandwidth (100 MHz) and the AOM fall time (25 ns) are negligible compared to that long decay time and are not modeled by the fit. With (4.20), this cavity decay corresponds to a spectral linewidth of

$$\Delta\nu_{\text{cav}} = 4.034(5) \text{ kHz} .$$

The free spectral range is determined by locking the laser to the four neighboring higher and lower lying axial modes and measuring the respective frequencies of the laser with a wavemeter (HighFinesse, WS7):

$$FSR = 1.935(3) \text{ GHz}$$

⁸In this measurement the intensity stabilization via the transmission was switched off.

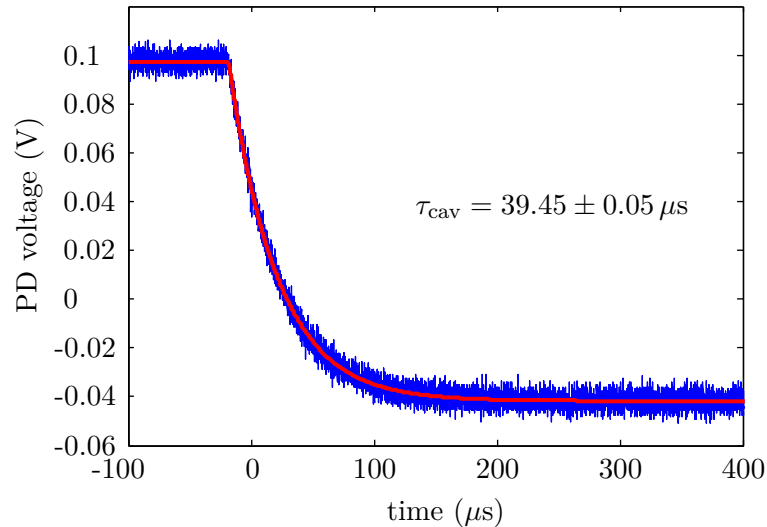


Figure 4.13.: Cavity ring-down measurement with a fast photodiode (PD). The red curve shows an exponential fit to the data. From ten individual ring-down measurements a cavity-field decay time of $\tau = 39.45 \pm 0.05 \mu\text{s}$ is derived.

Together with the cavity linewidth this leads to a finesse of

$$\mathcal{F} = 4.79(1) \times 10^5$$

which is at the upper end of the manufacturer’s specifications. Compared to other cavities of the same model that are used in other experiments, our cavity has an exceptionally high finesse. This is one of the reasons why the vacuum chamber was not opened to implement an internal temperature stabilization after finding T_z to be around room temperature. A single dust particle sucked into the cavity spacer through the venting holes could decrease the performance drastically.

4.4. Experiments

To characterize the absolute stability of the laser system, a second reference is required with at least a comparable or higher stability. Since at the time of the thesis no other laser with a comparable stability was available in the experiment, the best reference were of course the ions themselves. However, efficiently interrogating the dipole-forbidden transition with well controlled excitation parameters requires a pulsed experimental procedure, employing several other laser beams [86].

Figure 4.14 shows the geometry of the different laser beams that are used to interrogate and manipulate trapped ions on the $S_{1/2}$ - $D_{5/2}$ transition. The 729 nm laser is sent to the trap center under an angle of 45° with respect to the applied magnetic field \mathbf{B} . With the proper linear polarization that is set with a HWP, this enables the excitation of all possible transitions on the $S_{1/2}$ - $D_{5/2}$ manifold (see Section 1.2.3). Furthermore, an optical pumping beam at 397 nm is required to initialize the ion in a single Zeeman sub-level of the $S_{1/2}$ ground state (see Figure

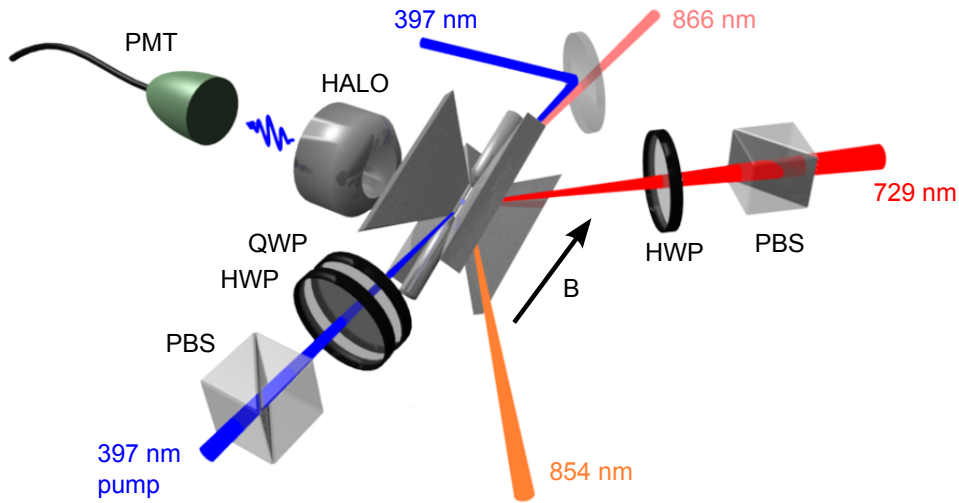


Figure 4.14.: Experimental set-up that is used to excite the ion on the $S_{1/2}$ - $D_{5/2}$ transition at 729 nm. Blue fluorescence photons are collected with one HALO and detected by a PMT. A magnetic field \mathbf{B} is applied on axis with the blue optical pumping beam, perpendicular to the direction of photon collection.

4.15 b)). In addition to the Doppler-cooling beams at 397 nm and 866 nm, a repumping beam at 854 nm is needed to release the population from the metastable $D_{5/2}$ state after the excitation with 729 nm light. The ion's fluorescence at 397 nm is collected with a HALO and detected with a PMT (after coupling the fluorescence to a multimode fiber). The whole experiment is controlled with the pulse sequencer *HYDRA* (Section 1.3.3), which switches the laser beams via AOMs and discriminates the quantum state of the ion via the recorded PMT signal in real-time.

Section 4.4.1 will explain some details about the laser sequence. In the following Section 4.4.2, the results of spectroscopy on the quadrupole transition will be presented and the main experimental parameters are determined. Being able to do spectroscopy, Section 4.4.3 will deal with measurements to determine the zero-expansion temperature T_z of the cavity and further measurements that characterize the stability of the laser system. Another important task of the laser is to do state discrimination in the $S_{1/2}$ ground state with the electron-shelving technique. An experimental example will be given in Section 4.4.4.

4.4.1. Sequence

A typical timing for the laser sequence that is used in the following experiments of this chapter is sketched in Figure 4.15 a).

Part I consists of Doppler cooling for $100 \mu\text{s}$, more details about an analysis of the involved dynamics can be found in Chapter 5. In part II, the blue cooling laser is switched off and a σ^- polarized laser beam on axis with the magnetic field optically pumps the ion within $5 \mu\text{s}$ to the $|S_{1/2}, -1/2\rangle$ level, initializing the system in a pure quantum state ($> 99.4\%$ pumping

4. Setup of a laser system for coherent manipulations at 729 nm

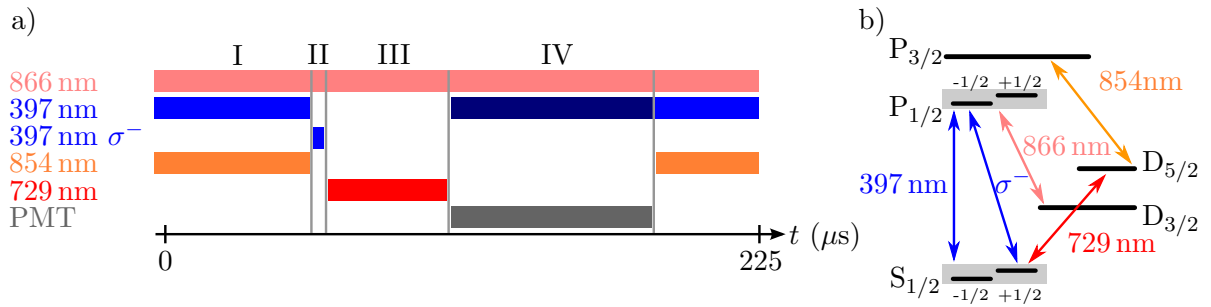


Figure 4.15.: a) Typical timing of the laser sequence that is used for 729 nm spectroscopy. Details are given in the text. Depending on the experiment, the 729 pulse in part III varies in length or gets replaced by a sequence of several pulses. b) Level scheme for $^{40}\text{Ca}^+$ with all relevant transitions.

efficiency⁹). What follows in part III is a single pulse at 729 nm which excites the ion to the Zeeman manifold of the $D_{5/2}$ state. Depending on the measurement, the power and length of the pulse are varied and for experiments involving more sophisticated quantum states (as in Chapter 6), part III gets replaced by a sequence of pulses at different frequencies. In the detection phase (part IV), the blue cooling laser is switched to an amplitude which yields a higher scattering rate of blue photons than it is required for good Doppler cooling. If the ion got transferred to the $D_{5/2}$ state, it will remain dark during that period. If it is still in the $S_{1/2}$ state, it will scatter photons. At the same time, a counter from *HYDRA* is activated and is counting the photon clicks recorded with the PMT during a time interval of $100 \mu\text{s}$. In each repetition of the sequence, the accumulated counts are compared with a threshold value to discriminate if the ion was either projected to the $S_{1/2}$ or $D_{5/2}$ state. The result of this comparison (0 for $S_{1/2}$ and 1 for $D_{5/2}$) is then stored in a second counter (see Figure 4.16 for more details). By repeating this experiment many times this allows a reconstruction of the amount of population that is transferred during part III to the $D_{5/2}$ state¹⁰. Finally, the amplitude of the blue cooling laser is set back for Doppler cooling and a laser beam at 854 nm is switched on to remove any remaining population from the metastable $D_{5/2}$ state, thereby initializing the ion again for Doppler cooling. Typical repetition rates of the sequence are around 4.5 kHz, depending on the length of the 729 pulses.

⁹The pumping efficiency is measured in CW with a non-saturating pumping beam via the extinction of fluorescence while rotating the polarization from linear to circular.

¹⁰The Bayesian probability is used to calculate the $D_{5/2}$ population from the finite number of samples. See A.5 for details.

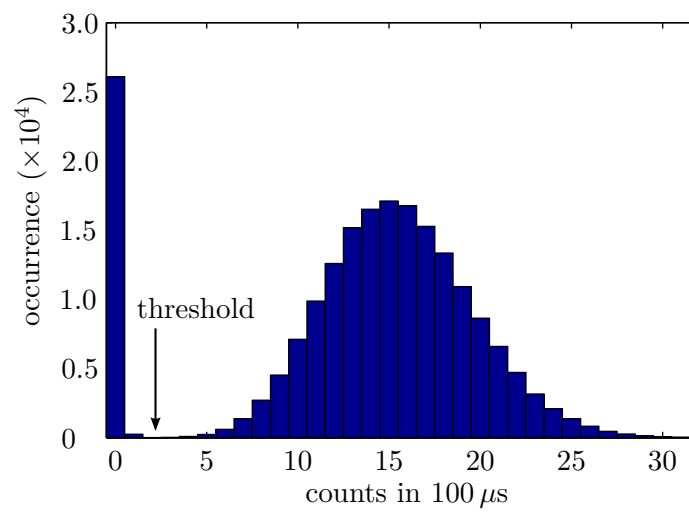


Figure 4.16.: Measured histogram of 397 nm fluorescence photons during the detection phase of the sequence. The displayed data correspond to an acquisition time in part IV of the sequence of $100 \mu\text{s}$ with a continuous countrate of $1.55 \cdot 10^5 \text{ s}^{-1}$ for the ion being in the $S_{1/2}$ state and 100 s^{-1} for the ion being in $D_{5/2}$. The optimal threshold to distinguish between the two states in a single measurement is at 2.

4. Setup of a laser system for coherent manipulations at 729 nm

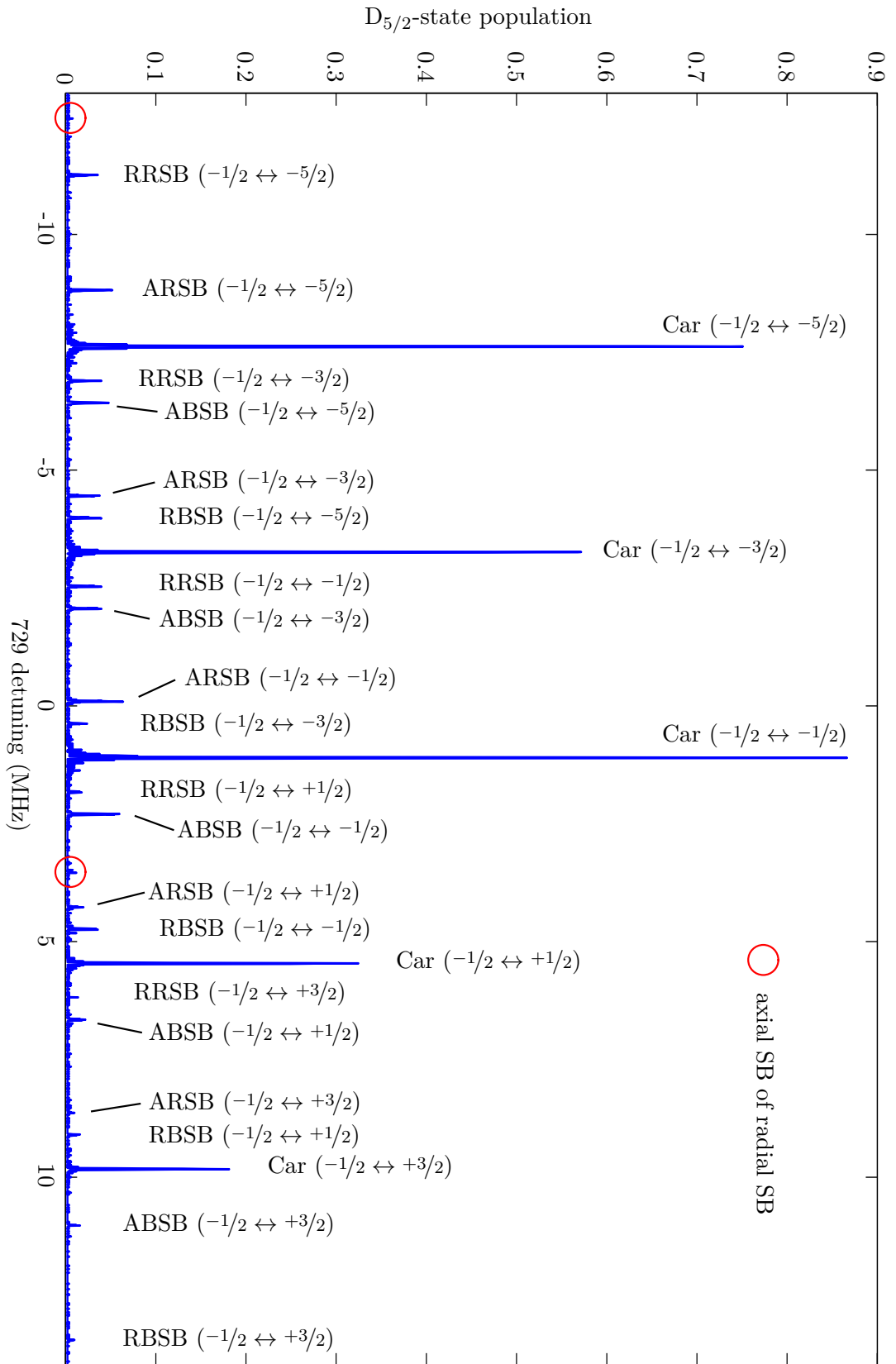


Figure 4.17: 729 spectroscopy with 32 μ s pulse length and 206 μ W power. Each data point represents 500 sequence repetitions. For details about the line identifications see text.

4.4.2. Spectroscopy

The most basic experiment on the $S_{1/2}$ - $D_{5/2}$ transition is to do spectroscopy. This is usually done every day once in the morning, to determine the different transition frequencies and check the operation of the whole experiment.

Figure 4.17 shows such an overview spectrum recorded in the BT. The 729 pulse length was $32 \mu\text{s}$ which is equivalent to a Fourier-limited bandwidth of the laser pulse of $\sim 5 \text{ kHz}$. The step size for the scan was chosen accordingly. All five carrier transitions (labeled as Car) that exist for the initial $|S_{1/2}, -1/2\rangle$ state are observable with different coupling strengths, corresponding to their Clebsch-Gordan coefficient and the geometry of the laser radiation with respect to the magnetic field orientation (see Chapter 1.2.3 and Figure 1.4). The magnetic quantum numbers of initial and final state for each carrier are given in the notation ($m_S \leftrightarrow m_D$).

The remaining lines are mostly axial and radial motional sidebands of the ion in the trapping potential, labeled as RBSB and RRSB for Radial Blue and Red SideBands and ABSB and ARSB for Axial Blue and Red SideBands. Again, the magnetic quantum numbers for the corresponding carrier transitions are given in brackets. Apart from two second order sidebands (indicated by red circles) which are due to a coupling of the axial and radial motion, only first order motional sidebands are observable and transitions starting from the $|S_{1/2}, +1/2\rangle$ level are completely suppressed due to the optical pumping at the beginning of each sequence repetition.

The spectrum contains important information about the main experimental parameters. The distance between the carrier transitions and the axial sidebands is the axial trap frequency ω_z . An evaluation of the two line positions for the $(-1/2 \leftrightarrow -5/2)$ carrier via a fit leads to

$$\omega_z/2\pi = 1.195(1) \text{ MHz}$$

for an endtip voltage of 400 V. Evaluating the position of the observable radial sideband of the same carrier yields a radial trap frequency

$$\omega_r/2\pi = 3.638(1) \text{ MHz}$$

for a trap RF drive frequency of 26.135 MHz and a power of 9 W. With Equation (1.7) this corresponds to a pure radial trap frequency (for 0 V endtips) of $\omega_{r0}/2\pi = 3.735(1) \text{ MHz}$.

The Zeeman-split positions of the $D_{5/2}$ levels (with respect to the center of the transition) in presence of a magnetic field B are given by

$$\nu_m = g m \frac{\mu_B}{h} B = m B 1.68 \frac{\text{MHz}}{\text{G}} \quad (4.21)$$

with $g = 6/5$ as g -factor for $D_{5/2}$ and m as magnetic quantum number. Extracting the distance $\nu_{+3/2} - \nu_{-5/2}$ of the outermost two carriers from the spectrum ($\Delta m = +3/2 - -5/2 = 4$) with a fit, this leads to a magnetic field of $2.59649(7) \text{ G}$. The relative error of 3×10^{-5} of this value shows what a precise tool the spectroscopy provides to measure magnetic fields at the position of the ion. Unfortunately, a strong magnetic-field influence is exactly what is not wanted in quantum-information experiments with high fidelities. Usually transitions with a weak magnetic-field dependence are desired, lowering the sensitivity of the coherence of a created superposition state to magnetic-field fluctuations. A precise way to characterize this magnetic-field noise is therefore to probe it with a superposition of quantum states which is directly affected by the

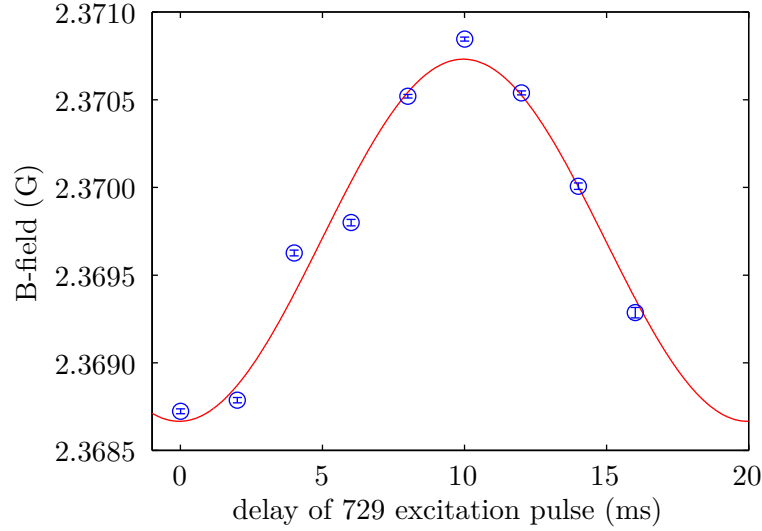


Figure 4.18.: Measurement of 50 Hz B-field oscillations. For each data point the B-field is derived via a measurement of the $(-1/2 \leftrightarrow -1/2)$ and $(-1/2 \leftrightarrow +3/2)$ carrier positions. The laser sequence is triggered to the 50 Hz power-line frequency and the relative delay of the 729 pulse is varied. The red curve is a sinusoidal fit to the data, revealing a peak-to-peak amplitude of 2.1(1) mG.

B-field induced phase fluctuations. One example for this approach will be given in Section 6.3, a more detailed analysis will follow in [146].

At the time of the thesis, the main source of magnetic field noise was the 50 Hz power-line frequency, emitted by all kinds of electronics in the proximity of the trap apparatus. By triggering the spectroscopy sequence to this frequency, the magnetic-field oscillation is directly measured when varying the relative delay between the 729 nm pulse and the power-line phase, as the transition is always probed at fixed B-field values within the 20 ms oscillation period. Figure 4.18 displays the result of such a measurement. To determine the magnetic field, the $(-1/2 \leftrightarrow -1/2)$ and $(-1/2 \leftrightarrow +3/2)$ carrier positions are measured. Due to $\Delta m = 2$ of the magnetic quantum numbers, the sensitivity is reduced by a factor of 1/2 compared to the previous measurement. But still, the plot shows that the errors of the individual measurements are negligible compared to the induced oscillation of the B-field. The peak-to-peak amplitude of the oscillation deduced by a sinusoidal fit is $\Delta B = 2.1(1)$ mG, the highest value that has been measured so far in the experiment. This can be explained by a suboptimal arrangement of power supplies in the shelf above the vacuum chamber. In later experiments the B-field oscillation has been reduced by more than a factor of 1/2 (see Section 6.3) thanks to a reallocation of the electronics and most importantly of the individual line cords.

The electronic transitions that are affected most by these B-field oscillations are $(\pm 1/2 \leftrightarrow \mp 3/2)$ which have an effective B-field coupling of $\Delta\nu = 2.8 \cdot 1.4 \frac{\text{MHz}}{\text{G}} \cdot \Delta B$, resulting in an effective broadening of the transition frequency of $\Delta\nu \approx 6$ kHz, for the above determined B-field amplitude and if the excitation pulse is not triggered to the power-line. Compared to that, in a similar experiment the most insensitive transitions $(\pm 1/2 \leftrightarrow \pm 1/2)$ would only be broadened by $\Delta\nu \approx 1$ kHz, making them much more suitable for fast electron shelving (Section 4.4.4) and

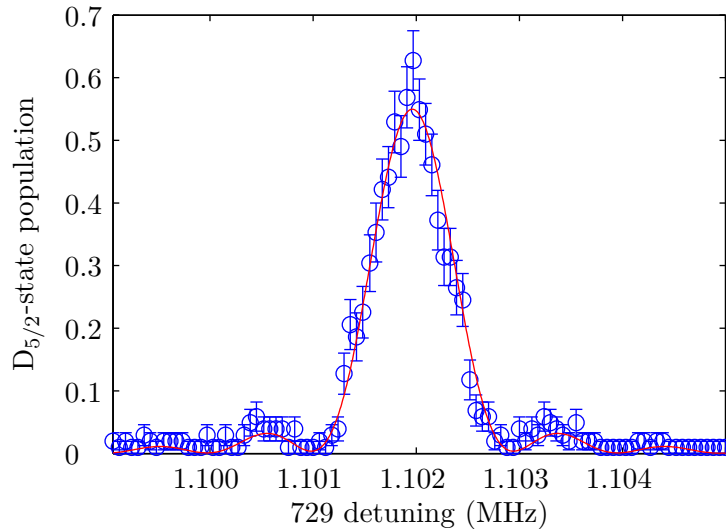


Figure 4.19.: Spectroscopy on the $(-1/2 \leftrightarrow -1/2)$ transition with a power-line triggered sequence with 100 repetitions per point. A 729 pulse length of 1 ms was used with a power of 130 nW, to suppress Rabi sidebands (on resonance, this power corresponds to a $\sim 0.54\pi$ -pulse). The red curve is a fitted numerical convolution of a Gaussian incoherently broadened line (assuming white frequency noise) and the spectrum for the coherent interaction of a two-level system with a laser pulse of finite length. From the Gaussian contribution we obtain a FWHM of the broadened transition of $\Delta\nu = 181(48)$ Hz. For further details see text.

coherent manipulations (Chapter 6).

Apart from characterizing the parameters of the ion trap and the magnetic field, the spectroscopy is also used to characterize the spectral linewidth of the 729 laser. Due to the sub-Hertz linewidth of the atomic transition, it serves as an excellent reference, provided that magnetic field fluctuations are sufficiently suppressed. Figure 4.19 shows a recorded spectrum of the $(-1/2 \leftrightarrow -1/2)$ carrier with a Fourier-limited pulse width of 159 Hz, corresponding to the pulse length of 1 ms which was used. To minimize magnetic-field noise, the sequence was again triggered to the power-line. The fit reveals a broadened transition linewidth of around 200 Hz. This linewidth contains both, the effective laser linewidth and broadening effects due to remaining magnetic field fluctuations that are not phase synchronous to the power-line frequency. Therefore, this value can be taken as a first estimate¹¹ of the spectral linewidth and short-term stability of the laser within the time of ~ 1 min that it takes to scan the central peak in Figure 4.19.

Figure 4.20 shows a spectrum recorded in the second ion trap (DT) of the experiment. Due to a sub-optimal positioning of compensation electrodes in that trap, it is impossible to achieve good micro-motion compensation for the ion on axis of the incident 729 beam. As a result, the spectrum exhibits micro-motion sidebands. Apparently the micro motion is so strong, that

¹¹A Ramsey experiment discussed in Section 6.2.2 demonstrates, that the actual laser linewidth is almost one order of magnitude smaller than estimated from the spectrum. As a consequence, the here observed broadening can almost fully be attributed to magnetic-field noise.

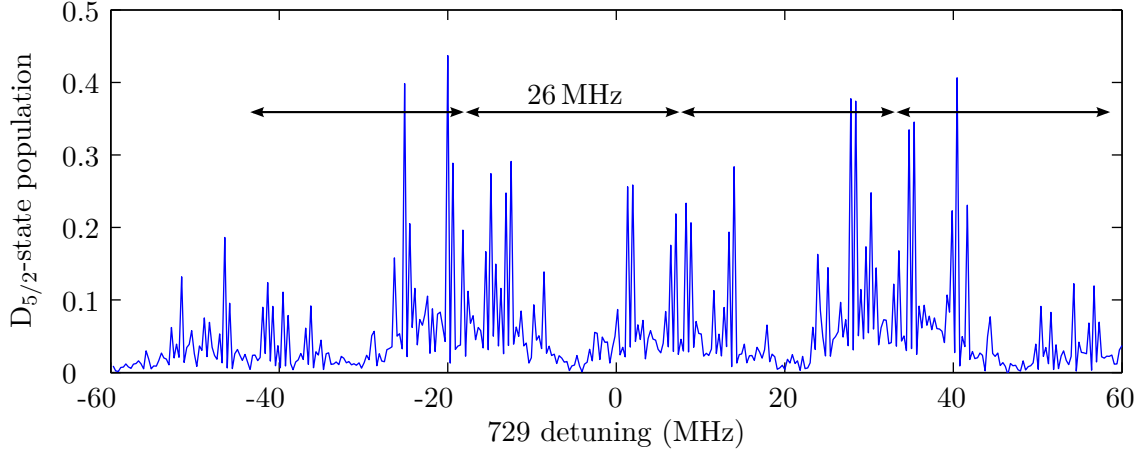


Figure 4.20.: 729 spectrum of single ion trapped in the DT, without optical pumping. Strong sidebands at the trap radio frequency of 26 MHz due to micro motion of the ion are visible, making the spectrum appear multiple times.

the maximum coupling strength is shifted to the first order sidebands, letting the unperturbed spectrum centered around 8 MHz appear rather weak. Apart from doing spectroscopy, all other measurements involving the 729 laser in this thesis were done in the BT, where a much better micro-motion compensation is possible.

4.4.3. Stability of the laser

Even though all transitions between the $S_{1/2}$ and $D_{5/2}$ levels are to a lesser or greater extent affected by magnetic field instabilities, the center of the transition serves as an excellent reference to characterize the long-term stability of the laser.

The main limitation for the long-term stability of the absolute B-field at the trap center is given by the stability of the current supply for the coils that are generating the field. Measurements have shown a stability of $100 \mu\text{A}$, resulting in a long-term stability of the applied magnetic field of $\sim 0.1 \text{ mG}$. In addition, the magnetic field might be occasionally influenced by the operation of machines from the mechanical workshop which is situated right below the laboratory.

To be insensitive to long-term drifts of the B-field, always two lines from the spectrum have to be measured. This makes it then possible to determine the actual B-field in each measurement which is taken into account for a calculation of the unperturbed atomic transition frequency.

Aging of cavity spacer (long-term stability)

It is known that the ULE glass of the cavity spacer constantly undergoes a very slow crystallization process [147]. This phenomenon which is generally referred to as material aging leads to a compression of the spacer and hence a reduction of the cavity length.

Figure 4.21 shows the measurement of this linear drift of the laser frequency caused by the slow deformation of the cavity spacer. For each data point the position ν_1 of the $(+1/2 \leftrightarrow +1/2)$

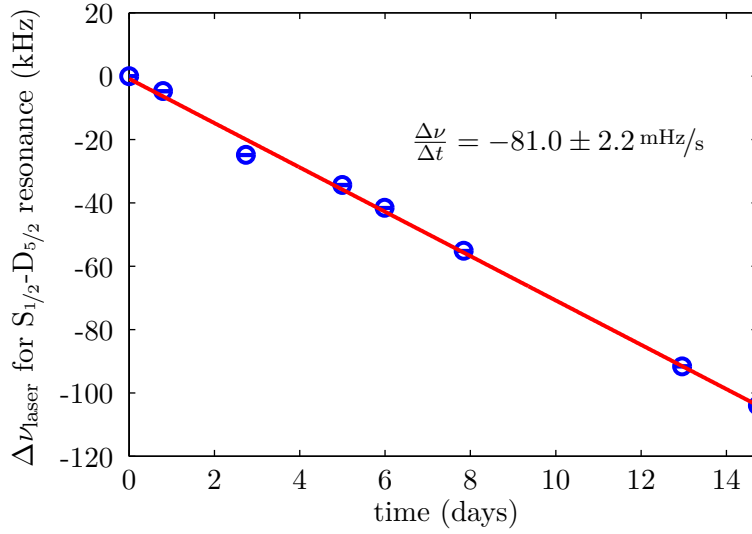


Figure 4.21.: Drift between cavity resonance and ion resonance on the $S_{1/2}$ - $D_{5/2}$ transition (blue circles). The deviations from the linear model (red line) are most likely due to thermal fluctuations of the cavity. The drift is caused by a slow deformation of the cavity spacer due to aging of the ULE material.

and ν_2 of the ($+1/2 \leftrightarrow +5/2$) carrier is measured. With respect to the unperturbed center ν_0 of the whole spectrum, the positions of these two lines for a given magnetic field B are

$$\begin{aligned}\nu_1 &= \nu_0 - \frac{1}{2} \cdot 2 \cdot \frac{\mu_B}{h} B + \frac{1}{2} \cdot \frac{6}{5} \cdot \frac{\mu_B}{h} B \\ \nu_2 &= \nu_0 - \frac{1}{2} \cdot 2 \cdot \frac{\mu_B}{h} B + \frac{5}{2} \cdot \frac{6}{5} \cdot \frac{\mu_B}{h} B\end{aligned}$$

which allows us to calculate ν_0 as

$$\nu_0 = \frac{5\nu_1 + \nu_2}{6}.$$

The observed drift of the applied detuning of the laser to keep it on resonance with the atomic transition is caused by a drift of the cavity resonance to the opposite direction with a rate of 81(2) mHz/s. From Equations (4.6) and (4.7) it follows that the relation between a change of the cavity resonance $\Delta\nu_0$ and the cavity length ΔL is given by

$$\Delta L = -L \frac{\Delta\nu_0}{\nu_0}. \quad (4.22)$$

The resonance drift can thus be attributed to a slow compression of the cavity spacer with a rate of $\sim -1.3 \times 10^{-12}$ m/day.

Zero-expansion point

The thermal expansion of a rigid body is usually described by the coefficient of thermal expansion (CTE) α , describing a linear dependence of the length change ΔL on a temperature change ΔT . However, this relation is only a first order approximation and a better description

is obtained by adding a second (quadratic) order with a coefficient β which accounts for a temperature dependence of α [145]. The resulting expansion law in the case of the high-finesse cavity is then

$$\frac{\Delta L}{L_z} = \alpha(T - T_z) + \beta(T - T_z)^2 \stackrel{(4.22)}{=} -\frac{\Delta\nu}{\nu_z} \quad (4.23)$$

with L_z being the cavity length with the corresponding resonance ν_z at the temperature T_z .

The cavity spacer is made from ULE which exhibits a very low thermal expansion in general. Additionally, in a certain temperature range the linear coefficient α in (4.23) is negligible, leaving only the quadratic dependence which gives rise to a minimum of the relative length change at the temperature T_z . In the minimum of the resulting parabola, the thermal expansion can be approximated by a linear CTE of 0, which is why this point of operation T_z is called zero-expansion point. Due to the dependence of the cavity resonance in (4.23), T_z can be determined by measuring the AOM detuning that has to be applied to the locked laser to excite the atomic transition for different temperatures of the cavity.

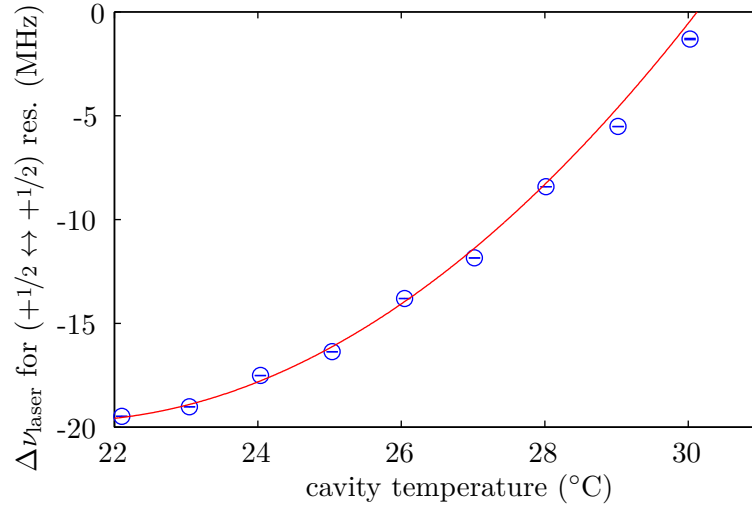


Figure 4.22.: Preliminary measurement of T_z of the high-finesse cavity. The data points are the AOM detunings of the 729 laser to be resonant with the $|S_{1/2}, +1/2\rangle - |D_{5/2}, +1/2\rangle$ transition for different temperatures of the cavity. The red curve is a parabolic fit with its minimum at $T_z = 21.2(3)^\circ\text{C}$.

Figure 4.22 shows a preliminary measurement of T_z that was done with a temperature stabilization of the cavity chamber employing only the heating circuit (see Section 4.3.1), which is why temperatures lower or close to the laboratory temperature of 21°C could not be set. The measurement was susceptible to magnetic field drifts (only a single line from the spectrum was measured) and the data points are not corrected for the constant linear drift due to aging of the cavity¹². These two effects lead to a notable deviation of the data points from the theoretical curve, but the quadratic dependence of the cavity resonance on the temperature is still clearly observable.

¹²After setting a new temperature, the system was typically given one day to come to rest, leading to a significant contribution of the drift due to cavity aging over the few weeks lasting period of measurements.

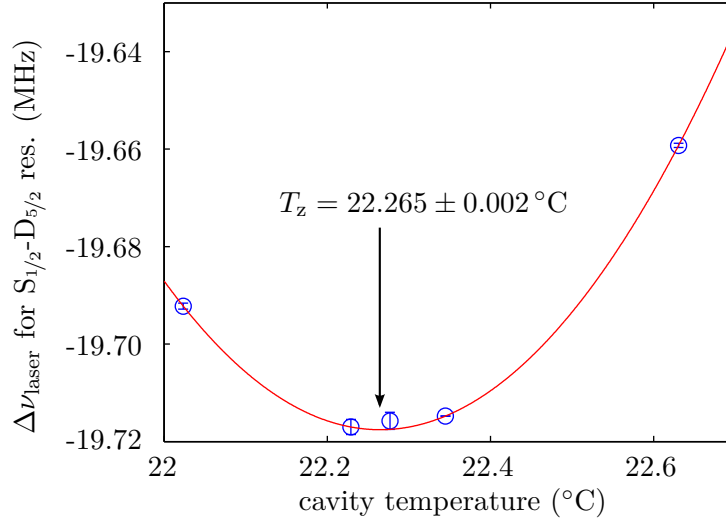


Figure 4.23.: Precise measurement of T_z . The data points are the AOM detunings of the 729 laser to be on resonance with the center of the $S_{1/2}$ - $D_{5/2}$ transition. The red curve is a parabolic fit.

After adding the cooling circuit to the temperature stabilization (Section 4.3.1), the measurements for T_z were repeated. In analogy to the measurements for the linear cavity drift from the previous section, this time the center of the $S_{1/2}$ - $D_{5/2}$ transition is determined via the positions of the $(+1/2 \leftrightarrow +1/2)$ and $(+1/2 \leftrightarrow +5/2)$ carriers, avoiding drifts due to magnetic field instabilities. Additionally, the previously determined linear drift rate is used to correct the recorded resonance values depending on their measurement time with respect to the first data point. Figure 4.23 shows the result. A parabolic fit reveals a value for the zero-expansion temperature of the cavity

$$T_z = 22.265(2)^\circ\text{C} ,$$

which is significantly above the preliminary result and emphasizes the influence of the magnetic field instabilities and the linear drift due to aging on the measurement. Again, the displayed data points are the detunings of the laser to keep it on resonance with the ion which corresponds to a shift of the cavity resonance to the opposite direction, leading to a maximum ν_z at T_z , as given by Equation (4.23). Rewriting this relation in terms of the laser detuning as it is measured (and assuming $\alpha = 0$) reads

$$\frac{\Delta\nu_{\text{Laser}}}{\nu_z} = \beta(T - T_z)^2 . \quad (4.24)$$

With an independent measurement of ν_z ¹³ with the wavemeter and the determined parameters of the fit in Figure 4.23, the quadratic temperature dependence of the cavity-resonance frequency is determined to

$$\beta = 1.06(1) \times 10^{-9} \text{K}^{-2} .$$

¹³ $\nu_z = 411.04251(6)$ THz

Remaining frequency drifts (intermediate-term stability)

After the zero-expansion temperature is found and the temperature stabilization is carefully adjusted accordingly, the question arises what laser drifts remain during the daily operation of the system. To characterize this time regime on the order of a few hours, the laser frequency was probed with a similar procedure as for the long-term drift, but in short time intervals over a whole working day.

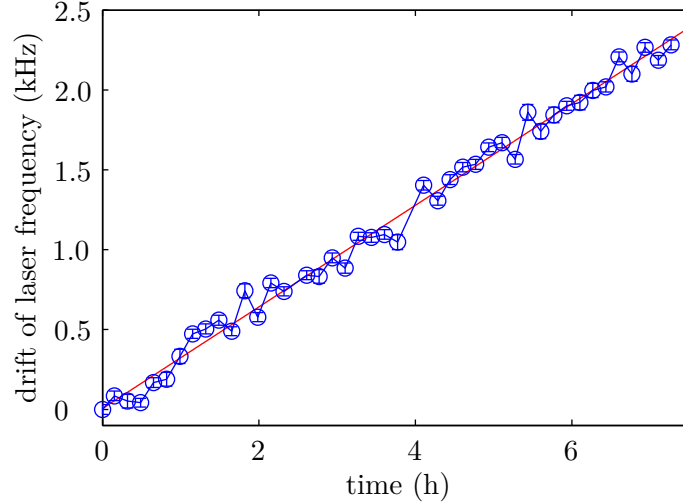


Figure 4.24.: Drift of laser frequency over one working day. The same measurement as for the drift due to ULE aging was done, but this time using the $(-1/2 \leftrightarrow -1/2)$ and $(-1/2 \leftrightarrow -5/2)$ carriers and repeating the measurement every ~ 10 min for a total time of 7 hours. The red curve is a linear fit revealing a drift rate of $88(1)$ mHz/s due to material aging.

The observed drift in Figure 4.24 has a linear component which is slightly higher than the result obtained in the long-term measurement discussed before. This could be caused by a temperature difference of 12 mK between both measurements, but daily variations of the drift rate on the order of 10 mHz/s are also reported in [134], where no temperature changes were present, i.e. without a clearly identified cause.

To get a measure for the remaining frequency fluctuations around the linear drift, the FWHM of the fluctuation amplitudes is evaluated in Figure 4.25 a). The resulting frequency spread of the laser is $184(41)$ Hz, which is surprisingly high given the sub-mK stability of the temperature stabilization and the fact that the cavity is operated at a temperature within the uncertainty of the determined value for T_z . Assuming a worst-case scenario that the set temperature is 10 mK away from the true zero-expansion temperature and using β from the last section, the observed fluctuations would correspond to a cavity-temperature drift on the order of 21 mK. This value is significantly higher than the stability inferred from the temperature sensors (Section 4.3.1) and the scenario is therefore rather unlikely. Another possible explanation could be thermal noise in the mirror coatings. But experiments reported in [133] with a similar reference cavity have reported a thermal noise limited fractional stability of 1×10^{-15} for the time scale of our measurements, leading only to a contribution in the sub-Hertz region. Also frequency drifts

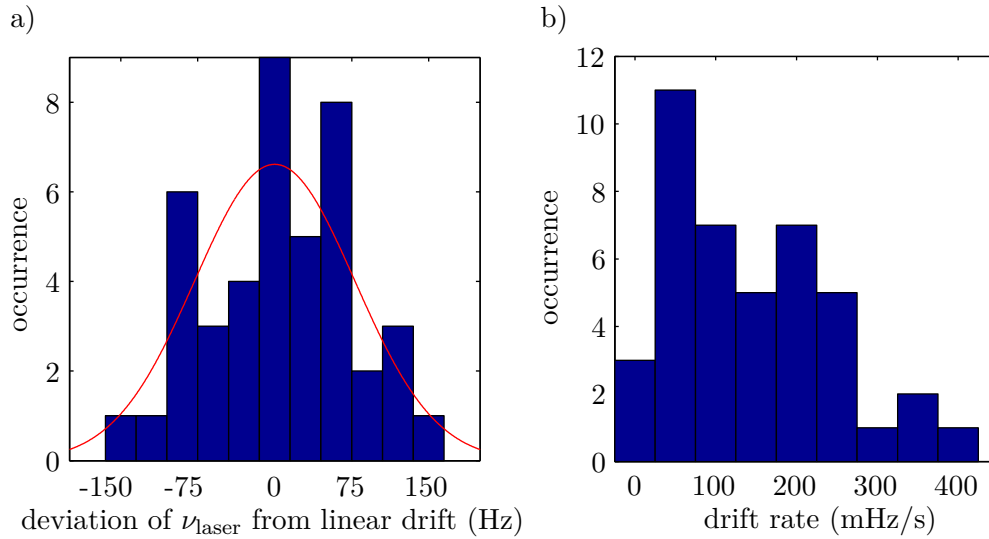


Figure 4.25.: a) Histogram of deviations of the individual frequency measurements from the determined linear drift in Figure 4.24. The red curve is a Gaussian fit, estimating the FWHM of the fluctuation amplitudes to 184(41) Hz. b) Histogram of drift rates under the assumption of a linear drift between subsequent measurements.

of the reference clock of the pulse sequencer *HYDRA* controlling the AOMs can be ruled out as they are expected to result in drifts of the laser frequency which are below 1 mHz per day. What remains as possible cause are mechanical instabilities. Since the teflon rods that support the cavity are fixed in a stainless-steel ring ($\text{CTE}_{\text{Steel}} \approx 10^3 \text{CTE}_{\text{ULE}}$), it could be possible that mechanical stress caused by temperature drifts of this ring is transferred to the cavity spacer, resulting in a shift of its resonance frequency.

Figure 4.25 b) finally shows a histogram of the different drift rates calculated from residual deviations from the linear drift. Interpolating the frequency fluctuations between subsequent measurements with a linear dependence leads to drift rates which are mainly below a value of 300 mHz/s. Since the performed and future experiments only require a coherence time of the laser on the order of at most one millisecond, these drifts have no impact at all for the performance of the system.

In the next generation of the experiment control, the slow linear drift of a few kHz per day will be automatically compensated by a feed-forward to the AOM of the locking beam. This will then provide a long-term stability limited only by the discussed fluctuations on the order of ~ 200 Hz. If at some point in the future a higher stability is required, the easiest approach will certainly be to improve the temperature stabilization of the box by adding more peltier elements. This would result in a more homogeneous distribution of the cooling power over the whole box surface. Less temperature fluctuations of the box air will then lead to a higher stability of the bottom-flange temperature and will reduce the observed instabilities.

4.4.4. Electron shelving

As already mentioned at the beginning of this chapter, one of the main applications of the 729 laser in the experiment is to measure the quantum state of the ion by electron shelving. The idea behind this technique is to transfer the population of one of the two $S_{1/2}$ ground states to the $D_{5/2}$ state where it is hidden from the cooling laser which is subsequently switched on to discriminate between S and D (as explained in Section 4.4.1). Some kind of electron shelving is already utilized when doing spectroscopy (Section 4.4.2), even though there it is not used to discriminate between the two ground states. It is rather used to probe the transfer efficiency from one well known ground state to the different sub-levels of the $D_{5/2}$ manifold.

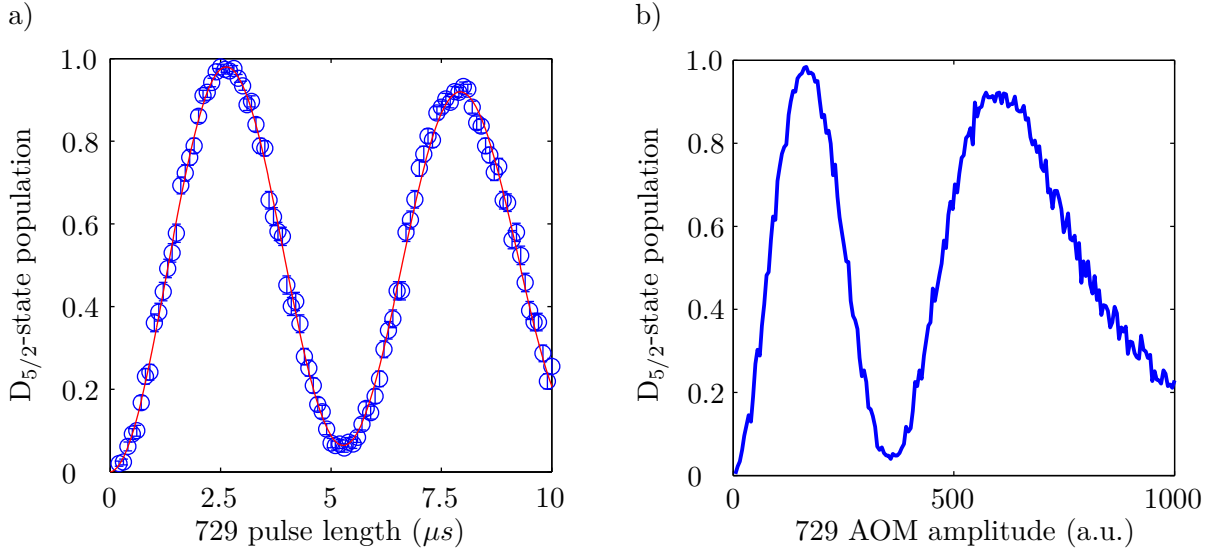


Figure 4.26.: a) Pulse-length scan on $(-1/2 \leftrightarrow -5/2)$ carrier for a 729 power of 63.3 mW. The red curve is a sinusoidal fit with a damped amplitude to account for a damping of the Rabi oscillation. The derived length for a π -pulse is 2.65 μs , achieving a $D_{5/2}$ population of 97.9(5)%. b) Amplitude scan of 729 AOM for a fixed pulse length of 10 μs . In the first maximum, a $D_{5/2}$ population of 98.4(6)% is reached.

To achieve a good transfer efficiency of population to $D_{5/2}$, the parameters of the 729 shelving pulse have to be adjusted properly. Since a high ion temperature causes a strong damping of Rabi oscillations [86] and thereby reduces the transfer efficiency significantly, good Doppler-cooling is another prerequisite for fast electron shelving (details in Chapter 5). To determine the optimal length for a shelving pulse, usually a pulse-length scan is done on a strong carrier transition with a fixed power (Figure 4.26 a)). The length for a π -pulse is then inferred from the measured Rabi frequency. With the set-up on the BT Rabi frequencies up to $\Omega/2\pi = 300$ kHz are possible when exciting the $\Delta m = 0$ transitions. Sometimes it is required to have a shelving pulse with a certain Fourier-limited bandwidth, in this case the pulse length is kept fixed and the power of the 729 laser is scanned (Figure 4.26 b)). The resulting dependence is a convolution of the atomic population dynamics with the nonlinear diffraction dependence of the AOM that is used to scan the power. The position of the first maximum is then taken as the required power to achieve a π -pulse with the given pulse length.

When optically pumping the initial population to one Zeeman sub-level of the ground state, the typically achieved populations in the $D_{5/2}$ state with a single electron-shelving pulse are on the order of 98 % (see Figure 4.26). This population includes already imperfections of the initial optical pumping. The optical pumping efficiency is 99.44(7) %, determined by a comparison of the population in $D_{5/2}$ when doing a shelving pulse on the $(-1/2 \leftrightarrow -1/2)$ and $(+1/2 \leftrightarrow +1/2)$ transition. This leads to a pure shelving efficiency slightly below 99 %. The main reason for this non-unity transfer efficiency is due to the damping of the Rabi oscillations, caused by the fact that the ion is not in the motional ground state of the trap potential. Great improvement is expected when the ion is further ground-state cooled by side-band cooling. However, this typically takes several milliseconds and thereby leads to a significant reduction of the repetition rate of experiments. The optical pumping efficiency could be further improved by the use of frequency-selective pumping, using the 729 nm laser and a quenching laser at 854 nm to selectively empty remaining population in one of the two ground-state sub-levels [111]. This would be (just like side-band cooling) rather slow compared to the time of only $5 \mu\text{s}$ for the conventional pumping pulse.

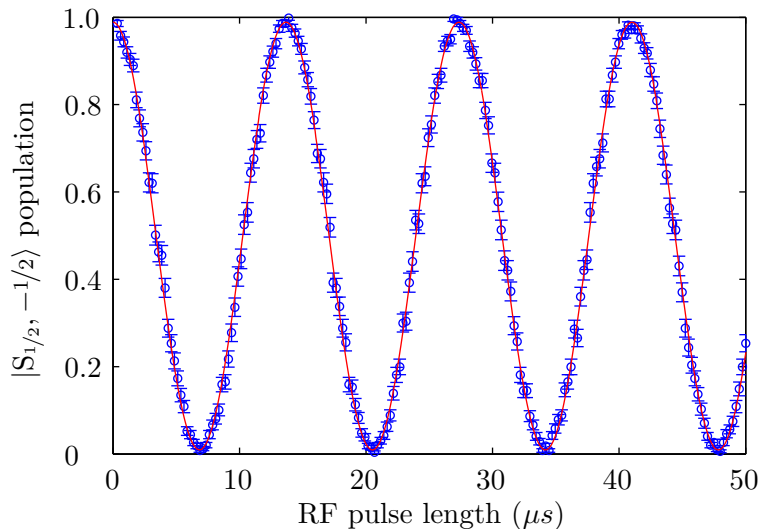


Figure 4.27.: Rabi oscillations between both Zeeman sub-levels of the $S_{1/2}$ ground state. The spin flips are driven via a direct radio-frequency (RF) excitation at the Zeeman-splitting frequency of 7.273 MHz. The $|S_{1/2}, -1/2\rangle$ population is measured via electron shelving to the $|D_{5/2}, -5/2\rangle$ level. The red curve is a sinusoidal fit, corresponding to a Rabi frequency of $\Omega/2\pi = 73.15(2)$ kHz.

Figure 4.27 shows a first physical application of the 729 laser in our experiment to discriminate the quantum state of an ion in the $S_{1/2}$ ground state. For the experiment, the ion is optically pumped to the $|S_{1/2}, -1/2\rangle$ level. After this initialization, a radio-frequency (RF) field emitted from a coil outside the vacuum chamber¹⁴ is coherently driving the spin-flip transition between both Zeeman sub-levels of the ground state with variable length. The population remaining in the initial state is finally probed via electron shelving. For each RF-pulse length,

¹⁴A detailed documentation of the set-up for the RF excitation and further experiments will be available in [129, 146].

the experiment is repeated 500 times with a repetition rate of the sequence of ~ 3.6 kHz, making it possible to visualize the RF-driven coherent dynamics within the ground state.

For the implementation of entanglement-transfer schemes based on the state mapping of photon polarizations onto the ground state of an ion (see Section 2.3), state detection with 729 and qubit rotations with the RF radiation are the key tools to analyze the quantum state after photon absorption in arbitrary detection bases.

4.5. Summary

This chapter documented the setup and characterization of an ultra-stable laser system for coherent manipulations on the optical quadrupole transition in $^{40}\text{Ca}^+$ at 729 nm. The set-up allows a controlled and completely independent excitation of single ions with 729 nm light in both ion traps of the experiment. The characterization of the system was done in the BT.

The high-finesse ULE cavity that is used to stabilize the laser is operated at its determined zero-expansion temperature of $T_z = 22.265^\circ\text{C}$. Long-term measurements revealed a linear drift rate of the laser system around 80 mHz/s, this is compatible with the rate caused by material aging as it is observed by other groups with comparable cavities. Residual frequency fluctuations were found to remain within a bandwidth of 200 Hz around this slow linear drift.

A cavity linewidth of $\Delta\nu_{\text{cav}} = 4$ kHz was determined in a ring-down measurement, a first estimate of the resulting laser linewidth by doing spectroscopy on an atomic transition delivered a value of $\Delta\nu_{\text{laser}} < 181$ Hz. However, more sophisticated measurements employing Ramsey interferometry that will follow in Section 6.2.2 will show that the short-term stability of the laser is expected to be even below $\Delta\nu_{\text{laser}} = 32$ Hz.

As a first application, the laser system was used to do pulsed spectroscopy on the quadrupole transition. This made it possible to determine trap frequencies and magnetic-field fluctuations at the position of a trapped ion. Maximal B-field fluctuations with a peak-to-peak amplitude of 2.1 mG were found, synchronous to the 50 Hz frequency of the power line.

The measurement of Rabi oscillations demonstrated a pure electron-shelving efficiency on the order of 99 %, the efficiency for state initialization in one of the two sub-levels of the atomic ground state was found to be above 99 % as well. The electron shelving technique was further employed to visualize RF induced Rabi oscillations between both Zeeman sub-levels of the ground state.

To conclude, the spectral linewidth and stability of the laser were found to be significantly better than the initially sighted objectives when planning the set-up. This makes it a versatile and sustainable tool for future implementations of different kinds of coherent manipulations in the experiment. After moving the experiment and finally getting the whole system running, the laser was extensively used to characterize and optimize the Doppler-cooling process (Chapter 5) and to demonstrate first basic coherent manipulations (Chapter 6).

5. Ion cooling dynamics

Good Doppler cooling is an essential prerequisite to carrying out high-fidelity coherent manipulations on single ions when no other cooling mechanism is used. Ground-state cooling via the excitation on a red motional sideband is usually implemented in a second step after Doppler cooling. Due to its typically much lower cooling rate it is also here desirable to reach a rather low motional state already before starting with the sideband cooling. Ground-state cooling is only of interest for quantum-logic operations using the collective motional state of several ions as a logic bus, as proposed in [148, 144], but it was not a necessary requirement for the experiments of this thesis. The main interest here was to achieve good electron shelving efficiencies and coherent manipulations with the 729 nm laser after short cooling time.

To optimize the cooling performance, the ion temperature was measured for various settings of the two cooling lasers at 397 nm and 866 nm. Section 5.1 will provide a theoretical framework for the cooling mechanism which gives a better insight into the cooling process than the purely classical treatment presented in the beginning in Section 1.2.2. In addition, the method employed for the temperature measurement will be explained. In Section 5.2, experimental results including a numerical analysis are presented which were used to find the optimal cooling parameters for the Bright Trap.

5.1. Theoretical background

5.1.1. Laser cooling of a trapped multilevel ion

The description of the Doppler-cooling process given in Section 1.2.2 was based on the assumption of a free or weakly bound two-level atom. When laser cooling $^{40}\text{Ca}^+$ on the $S_{1/2}$ - $P_{1/2}$ transition with a repumper tuned to the $P_{1/2}$ - $D_{3/2}$ transition, the employed levels have more similarity with a Λ -type three-level system which comprises 8 magnetic sub-levels in total. As pointed out in [149], such a system is challenging if not impossible to treat in an analytical way and is better addressed with a quantum statistical approach using numerical methods based on a master-equation description. The dynamics of the density matrix ρ containing all internal and motional degrees of freedom of the atom are described by the master equation [150]

$$\frac{d\rho}{dt} = \frac{1}{i\hbar} [H, \rho] + \mathcal{L}\rho \quad (5.1)$$

where H is a Hamiltonian similar to (1.8) but for the 8-level configuration and \mathcal{L} is the Liouville operator describing the damping of the system due to spontaneous decay. As already discussed in Section 1.2.1, the interaction part of H is usually treated in the rotating-wave approximation and is further simplified by assuming the Lamb-Dicke regime (1.12).

In this limiting case and when considering the motion only in one dimension, the cooling dynamics of a single ion are dominated by three different types of photon-scattering processes.

Processes leading to loss of motional quanta ($|g, n\rangle \rightarrow |e, n-1\rangle \rightarrow |g, n-1\rangle$, $|g, n\rangle \rightarrow |e, n\rangle \rightarrow |g, n-1\rangle$), processes leading to a gain of motional quanta ($|g, n\rangle \rightarrow |e, n+1\rangle \rightarrow |g, n+1\rangle$, $|g, n\rangle \rightarrow |e, n\rangle \rightarrow |g, n+1\rangle$), and processes that leave the motional state unchanged ($|g, n\rangle \rightarrow |e, n\rangle \rightarrow |g, n\rangle$, $|g, n\rangle \rightarrow |e, n-1\rangle \rightarrow |g, n\rangle$, $|g, n\rangle \rightarrow |e, n+1\rangle \rightarrow |g, n\rangle$). Effective cooling of the ion's motion is achieved when the cooling transitions happen at a higher rate (nA_-) than the heating transitions ($(n+1)A_+$) [88]. Indeed, the dynamics derived from (5.1) for a motional state $|n\rangle$ are fully described by the two rate coefficients A_+ and A_-

$$\frac{d}{dt}p(n) = (n+1)A_-p(n+1) - [(n+1)A_+ + nA_-]p(n) + nA_+p(n-1) \quad (5.2)$$

with $p(n) = \langle n|\rho|n\rangle$. Below saturation, both coefficients are determined as

$$A_+ = \Gamma\eta^2 \left(\frac{\xi}{\cos^2\phi} P(\Delta) + P(\Delta - \omega_T) \right) \quad (5.3)$$

$$A_- = \Gamma\eta^2 \left(\frac{\xi}{\cos^2\phi} P(\Delta) + P(\Delta + \omega_T) \right), \quad (5.4)$$

where $P(\Delta)$ is the excitation probability for a certain detuning Δ of the laser from the atomic resonance. As already defined in Section 1.2.1, Γ is the natural decay rate on the $S_{1/2}$ - $P_{1/2}$ transition, η is the Lamb-Dicke parameter as defined in (1.10), ξ is accounting for the directionality of the dipole emission pattern, ϕ is the angle between the cooling laser beam and the oscillation direction of the ion, and ω_T is the trap frequency.

The time dependence of the average occupation of the vibrational mode $\langle n \rangle$ is described by

$$\frac{d}{dt}\langle n \rangle = - \underbrace{(A_- - A_+)}_W \langle n \rangle + A_+ \quad (5.5)$$

with the solution

$$\langle n(t) \rangle = \langle n(0) \rangle e^{-Wt} + \langle n(\infty) \rangle (1 - e^{-Wt}) \quad (5.6)$$

for $A_- > A_+$. W is the cooling rate and

$$\langle n(\infty) \rangle = \frac{A_+}{A_- - A_+} \quad (5.7)$$

is the minimum (steady state) occupation of the vibrational mode which can be optimally achieved for long cooling times.

5.1.2. Temperature measurements with the 729 nm laser

The very narrow effective linewidth of the optical quadrupole transition when exciting it with the narrow-band 729 nm laser allows for an operation in the so-called resolved-sideband regime ($\Gamma_{\text{eff}} \ll \omega_T$). In this regime, the dynamics for excitation on the carrier and sideband transitions can be measured individually, making it possible to derive the ion temperature due to the strong dependence of the observable dynamics on the motional state. As explained in [86], there exist several different methods to determine the ion's temperature by an analysis of the coupling on the carrier and sideband transitions. For the characterization of mean vibrational quantum numbers $\langle n \rangle$ which are significantly above the ground state, two methods have proven to give reasonable results.

Rabi oscillations on the carrier transition

In Section 1.2.1 the matrix element (1.11) describing the coupling strength on the carrier was found to be independent on the Lamb-Dicke parameter ($\Omega_{n,n} \approx \Omega$) up to the first order in η . Extending the expansion to the second order in η leads to the expression

$$\Omega_{n,n} \approx \Omega \left(1 - \eta^2 \left(n + \frac{1}{2} \right) \right) \quad (5.8)$$

which shows a dependence of the Rabi frequency on the motional state n also on the carrier. For the existence of only one vibrational mode this would lead to discrete frequency components which result in a damping of the observable Rabi oscillations, characteristic for the average occupation number $\langle n \rangle$ of vibrational states. However, the trapping potential is three-dimensional and there exists one axial vibration mode at a lower frequency and two radial vibration modes at a higher frequency. For the typical frequencies in our experimental set-up (see Section 4.4.2) this leads to a ratio of the squared Lamb-Dicke parameter for the axial and radial modes of $\eta_{\text{ax}}^2/\eta_{\text{rad}}^2 \approx 3$. With the axial vibration mode having a dominant contribution to the dynamics, it is therefore feasible to get a good guess for $\langle n \rangle$ on the axial mode by fitting the observed Rabi oscillations of the population in D on the carrier with

$$P_{\text{D}}(t) = \sum_{n=0}^{\infty} p_n \sin^2 \left(\frac{\Omega_{n,n} t}{2} \right) \quad (5.9)$$

where $p_n = \frac{\langle n \rangle^n}{(\langle n \rangle + 1)^{n+1}}$ is the occupation of the state $|n\rangle$ for a thermal distribution with expectation value $\langle n \rangle$ [85]. $\Omega_{n,n}$ is usually not approximated as in (5.8) but calculated in its full form as given by (1.11) to reduce errors for higher $\langle n \rangle$.

This method works out nice in our experiments but due to the fact that the optical pumping efficiency for the initialization in a single Zeeman sub-level of the ground state and the bare Rabi frequency Ω have to be taken into account as well, the errors are usually rather big. Better results are only expected for long pulse-length scans lasting more than hundred micro seconds to measure a higher number of oscillation periods. But due to the strong magnetic-field noise in the experiment (see Section 6.3.2), pulse-length scans of that length are significantly affected by decoherence. This results in an additional damping of the Rabi oscillations which cannot be distinguished from the damping due to the thermal distribution of vibrational states. For the current status of the experiment this method is therefore expected to give inaccurate results for the absolute values of $\langle n \rangle$ but it provides a good tool to optimize the cooling parameters in an empirical way.

Ratio of coupling strengths on red sideband and carrier

Better results are achieved with a comparison of the coupling strength on the first red axial sideband and the carrier. For very small pulse areas, (5.9) can be approximated by the parabolic form

$$P_{\text{D}}(t) \approx \sum_{n=0}^{\infty} p_n \frac{\Omega_{n,n}^2 t^2}{4} . \quad (5.10)$$

The ratio of the excitation strength from the red sideband and the carrier can then be used to estimate $\langle n \rangle$ by comparing it with the expected ratio for a thermal distribution

$$\frac{P_{\text{D,rsb}}}{P_{\text{D,car}}} \approx \frac{\sum_{n=1}^{\infty} p_n \Omega_{n-1,n}^2}{\sum_{n=0}^{\infty} p_n \Omega_{n,n}^2} = \frac{\sum_{n=1}^{\infty} p_n \frac{(n-1)!}{n!} \eta^2 (L_n^1(\eta^2))^2}{\sum_{n=0}^{\infty} p_n (L_n^0(\eta^2))^2}. \quad (5.11)$$

In contrast to (5.9), the ratio in (5.11) is independent of Ω , contributions due to the radial vibration modes, and the optical pumping efficiency. As for the previous method, the Rabi frequencies are calculated in their full form including the Laguerre polynomials to reduce errors for higher $\langle n \rangle$. To assure the validity of the approximation made in (5.10), the intensity and length of the 729 pulse is usually adjusted such that a pulse area of $\Omega_{n,n} \cdot t = \frac{\pi}{5}$ is reached on the carrier. Due to the consequently low excitation probabilities, the coupling on each transition is probed 10^5 times to get sufficient statistics.

5.2. Optimization of Doppler cooling

As already pointed out in [86], the performance of Doppler cooling strongly depends on the parameters of the cooling lasers. Slight deviations from the optimum settings can have a huge influence on the ion temperature. This is especially the case when the ion is cooled in a pulsed sequence on a timescale which is on the order of the inverse of the cooling rate. Then not only a shift of the Doppler limit but also changes in the cooling rate caused by changes of the detunings and powers of the cooling lasers influence the effectively reached $\langle n \rangle$ of the ion in the trap.

Using temperature measurements with the 729 nm laser as described in the previous section, the cooling parameters were optimized to reach low temperatures on the axial vibration mode within a cooling time of $100 \mu\text{s}$. The so-found parameters were then used in every-day operation to guarantee reproducible conditions for electron shelving (Section 4.4.4) and coherent manipulations (Chapter 6).

5.2.1. Calibration of the cooling-laser parameters with spectroscopy

The frequency offsets of the cooling lasers (397 nm and 866 nm) are calibrated every day in the morning after locking the overall laser system. The calibration is done with spectroscopy on the $P_{1/2}$ - $D_{3/2}$ transition and by fitting the result with a solution for the corresponding 8-level Bloch-equation system as described in [151, 66, 109].

Figure 5.1 shows such a spectrum, recorded with 866 nm and 397 nm beams incident on the main magnetic field axis (90° resp. to the HALO axis) and with linear polarization. The cleanest resonance spectra for this configuration¹ are obtained for $9 \mu\text{W}$ power at 397 nm and $18 \mu\text{W}$ power at 866 nm. The fitted model reveals that this corresponds to Rabi frequencies of $\Omega_{397}/2\pi = 26.5 \text{ MHz}$ and $\Omega_{866}/2\pi = 11.8 \text{ MHz}$. The detuning of the 397 nm laser from resonance is determined to $\Delta_{397} = -18.6 \text{ MHz}$.

¹Both beams are collimated with 60FC-4-M12 (Schäfter u. Kirchhoff) couplers and focused with a $f = 500 \text{ mm}$ plano-convex lens.

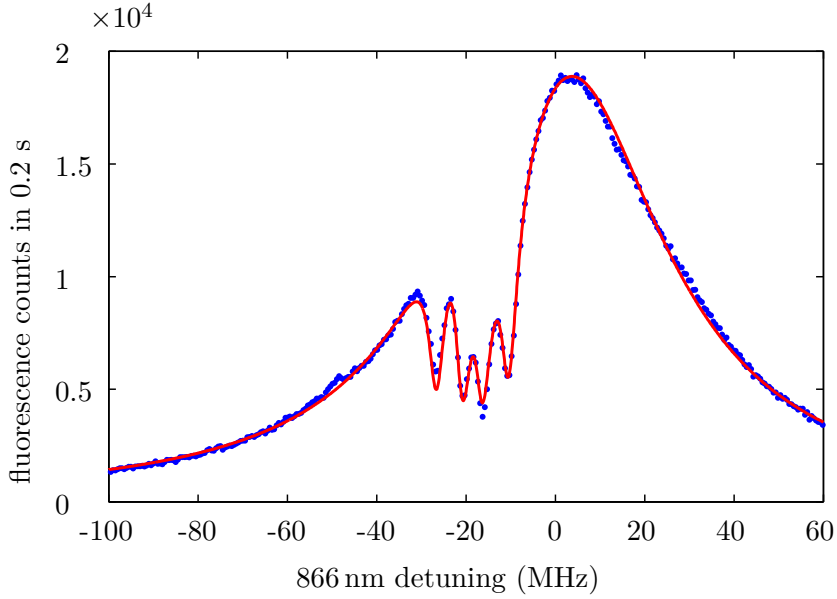


Figure 5.1.: 866 nm spectroscopy that is used for calibration. The red curve is a fit based on the 8-level Bloch equations. The obtained AOM detuning for the 866 nm resonance is used to calibrate the x -axis.

5.2.2. Measurement of cooling rate and cooling limit

The Doppler-cooling dynamics are measured by a temperature measurement² with the 729 laser with the second method described in Section 5.1.2. Different lengths of the Doppler cooling time are applied in a sequence as described in Section 4.4.1. The transition that is suited best for that purpose is between $|S_{1/2}, -1/2\rangle$ and $|D_{5/2}, -5/2\rangle$ as it sits on the low-frequency end of the spectrum and its carrier and red sidebands are well separated from all other spectroscopic lines. Due to an unknown geometry factor in the Lamb-Dicke parameter for the radial vibration modes (see (1.10)), in the following only the axial mode is going to be used for the temperature measurements. The resulting evolution of $\langle n \rangle$ is then fitted with the expected functional dependence as given by (5.6).

Figure 5.2 shows such a measurement for the laser parameters $\Delta_{866} = 0$ MHz, $\Delta_{397} = -18$ MHz, $\Omega_{866}/2\pi = 11.1$ MHz, and $\Omega_{397}/2\pi = 17.7$ MHz. The Rabi frequencies correspond to laser powers of $4 \mu\text{W}$ at 397 nm and $16 \mu\text{W}$ at 866 nm. These settings are the optimum values to achieve the lowest possible $\langle n \rangle$ within a Doppler-cooling time of $100 \mu\text{s}$. They were found in an empirical way by monitoring Rabi oscillations on the carrier for different cooling-laser settings. During the optimization process it was found that the cooling performance is mainly influenced by the power and detuning of the 397 nm laser and rather unaffected by changes of the parameters for the repumper. The fit in Figure 5.2 corresponds to a cooling rate of $30(8) \text{ ms}^{-1}$ and a steady state mean vibrational quantum number of $\langle n \rangle = 16(2)$. In the daily lab operation when Doppler cooling with the above parameters for $100 \mu\text{s}$, measurements of

²All temperature measurements and experiments with coherent manipulations discussed in this thesis were done with an axial trap frequency of $\omega_z/2\pi = 1.195$ MHz as determined in Section 4.4.2.

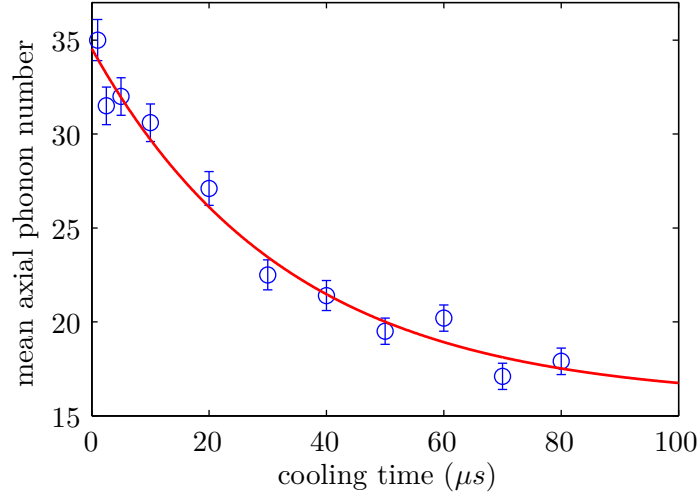


Figure 5.2.: Decay of $\langle n \rangle$ with increasing Doppler-cooling time. The red curve is a fit of the theoretical model from Section 5.1, for more details see text.

$\langle n \rangle$ are usually yielding values between 14 and 16.

5.2.3. Dependence of cooling performance on 397 nm laser detuning

Of particular interest is the dependence of the cooling dynamics on the detuning of the 397 nm laser. In Section 5.1.1 it has been shown that the main characteristics of the cooling process are determined by the rate parameters A_+ and A_- which can be calculated for arbitrary detunings Δ of the cooling laser once the shape of the excitation probability $P(\Delta)$ is known. However, this description is assumed to be valid only in the Lamb-Dicke regime and below saturation. Even for low motional states as $n = 15$, the Lamb-Dicke criterion from (1.12) is not well fulfilled ($\eta^2(2n + 1) \approx 0.7$) and the optimal cooling parameters from the last section lead to a saturation parameter of $s = 2\Omega^2/\Gamma^2 \approx 1.4$. It is therefore of interest to see how good the obtained results from a real experimental situation are still explainable with this intuitive and simple theoretical description.

$P(\Delta)$ can be either calculated if all laser parameters are known or it can be directly measured by fluorescence spectroscopy with a frequency scan of the 397 nm laser for a fixed 866 nm laser detuning. Figure 5.3 shows both, the simulation of the spectrum for a known $P(\Delta)$ and its direct measurement. The good agreement between both curves shows that up to a scaling factor ϵ between population and detection rate, the directly measured spectrum perfectly agrees with the theoretical distribution of excitation probabilities $P(\Delta)$.

From (5.3) and (5.4) it follows that the cooling rate W is for sufficiently small trap frequencies ω_T approximately proportional to the slope of $P(\Delta)$. In the vicinity of the observable dark resonances the agreement between theory and measurement is therefore rather surprising since here the Doppler-cooling process is expected to be significantly disturbed by the steep changes of slope in $P(\Delta)$. Bad Doppler cooling or even heating leads to an increased motional spread of the ion position inside the trapping potential and strong Doppler shifts for the absorption of photons, causing a drop in the measured fluorescence signal. Apparently, this effect is negligible

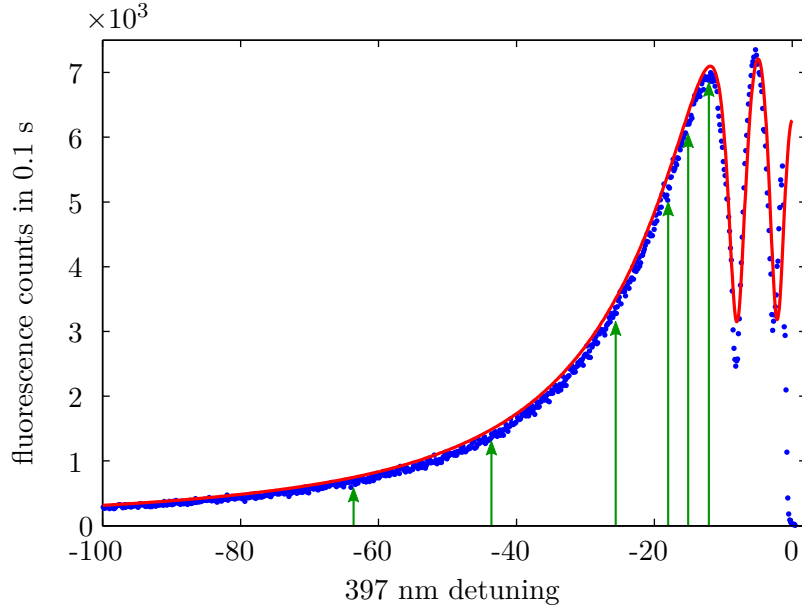


Figure 5.3.: 397 nm spectroscopy with the repumper at 866 nm on resonance and laser powers of $4 \mu\text{W}$ for the blue and $16 \mu\text{W}$ for the red beam. Close to resonance of the 397 the ion starts heating and the fluorescence signal drops. The red curve is a simulation of the expected spectrum for the used laser parameters with the calibration obtained by the previously shown 866 nm spectrum. The green arrows indicate the 397 detunings for which the cooling dynamics were investigated in detail.

in the displayed measurement.

Even for an unknown scaling factor ϵ , the measured spectrum serves to derive the expected minimum $\langle n \rangle$ for arbitrary detunings Δ since in (5.7) any pre-factor of $P(\Delta)$ drops out. In contrast, the cooling rate is not obtainable in a quantitative way but at least the approximate (for small ω_T) detuning for its maximum value is traceable by evaluating the slope of the measured spectrum with numerical methods. In the following, $P(\Delta)$ obtained from the simulation is used to predict the cooling rates and steady state temperatures for different detunings Δ .

Figure 5.4 shows the calculated dynamics of the cooling process as a function of the 397 nm laser detuning. The blue points are experimental values determined in a measurement as discussed in the previous section. Even though none of the approximations for the model are satisfyingly fulfilled in the experiment, there is a clear correlation between the experimental data and the theoretical curves observable. The rather big error bars indicate that the statistics for the temperature measurements are still not sufficiently good and that better agreement might be observed by further increasing the number of repetitions. An influence by higher order motional sidebands due to non-negligible coupling strengths (Lamb-Dicke criterion not safely fulfilled) might explain the observed remaining deviations from the theory. But given its simplicity, the model still serves to provide a useful interpretation of the measured dynamics and yields a good guess of the expected cooling performance for arbitrary detunings.

The simulation predicts that the minimal value of $\langle n \rangle \approx 9.5$ is reached for a detuning of $\Delta_{397} = -20 \text{ MHz}$, which is very close to the expected Doppler-cooling limit for a free particle

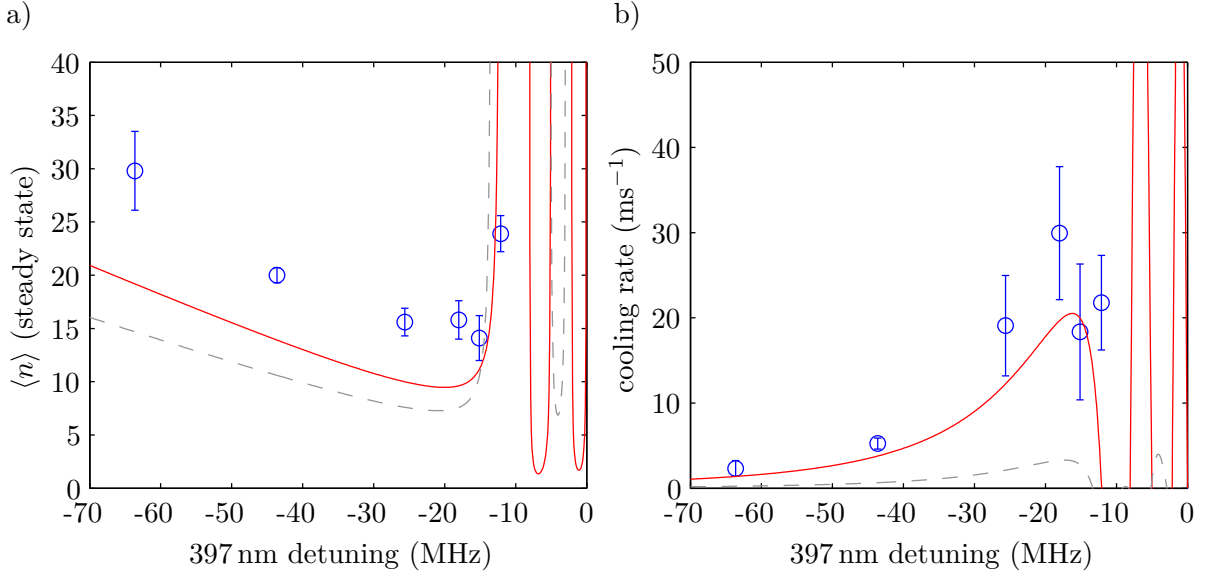


Figure 5.4.: a) Cooling limit for the mean axial photon number as a function of the cooling laser detuning. The red curve is a calculation based on the model from Section 5.1.1 with $P(\Delta)$ as calculated for Figure 5.3. The gray dashed line is the corresponding simulation for the radial sidebands. Blue points are experimental data for the detunings -63.6 MHz, -43.6 MHz, -25.6 MHz, -18 MHz, -15.1 MHz, and -12.1 MHz. b) The corresponding simulated and measured cooling rates.

as obtained with Equation (1.23). The model further predicts that the maximal cooling rate of 20.5 ms^{-1} will be reached for a detuning of $\Delta_{397} = -16 \text{ MHz}$. Interestingly, the optimum cooling parameters that were independently determined before are just in the center between both optimum cases, representing the best compromise between cooling rate and minimal $\langle n \rangle$.

As already extensively theoretically studied in several publications like for example [152, 149], the simulation and experimental data from this chapter show that the cooling process in a multi-level system significantly differs from the situation for a simple two-level atom. Most importantly, the presence of dark resonances in the spectrum strongly alters the cooling process in their close surrounding. As a consequence, the general rule of thumb that the best cooling performance below saturation is reached for $\Delta = \Gamma/2$ is not applicable anymore. But as observable in Figure 5.4 a), the strong resonance dependence close to the dark states opens up the possibility for a greatly enhanced cooling efficiency on the axial mode which results in temperatures significantly below the Doppler limit that are reachable at very high rates. Unfortunately, for the current ratio of the trap frequencies and the chosen magnetic field, good cooling of the axial mode on the slope of a dark resonance always coincides with strong heating of the radial modes, which makes such an enhanced Doppler-cooling scheme impossible. Further simulations have shown that an increase of the B-field from 2.61 G to 3.57 G should solve the problem by essentially overlapping the positions of the sharp local minimum of $\langle n \rangle$ for the radial modes (dashed curve in Figure 5.4 a)) and the first sharp minimum of $\langle n \rangle$ for the axial mode (red curve), when coming from negative frequencies. This may be investigated in future experiments.

6. Coherent manipulations on the $S_{1/2}$ - $D_{5/2}$ transition

The creation of customized coherent superpositions between two Zeeman sub-levels of the $D_{5/2}$ state is one key technology to study the polarization-state mapping of photons onto the electronic state of an ion (see Section 2.3). After the absorption of one photon of an entangled photon pair, rotations of the quantum state of the ion by coherent manipulations with subsequent electron shelving are another essential tool to fully characterize the state with the techniques of quantum tomography [153] and to characterize the entanglement-transfer fidelity.

In the current chapter, experiments with the 729 nm laser are presented that demonstrate the capability of the set-up to do the required coherent manipulations. Having the ability to create coherent superpositions, Ramsey experiments were performed that further characterize the stability of the laser system and the dephasing of the atomic state, caused by magnetic-field noise.

Section 6.1 summarizes the basic theoretical formalism that is required to describe the interaction of the atomic state with the laser. It will be used throughout the chapter. In Section 6.2, Ramsey experiments employing a superposition state between $S_{1/2}$ and $D_{5/2}$ are discussed. In Section 6.3, experiments with coherent manipulations involving two $D_{5/2}$ levels are presented, illustrating the dynamics of the atomic state in the atom-laser interaction. The section finishes with the creation and characterization of a coherent superposition within the $D_{5/2}$ state.

6.1. Theory

For coherent manipulations of the ion with the 729 nm laser, usually a carrier transition between a single Zeeman sub-level of the $S_{1/2}$ state and a single Zeeman sub-level of the $D_{5/2}$ state is driven on resonance. In the following it will be assumed that off-resonant coupling to transitions between other sub-levels of the two states and their motional sidebands is negligible¹. The observable physics is therefore governed by the interaction of an atomic two-level system with a monochromatic light field, as it is described in standard quantum-mechanics textbooks. Residual neglected off-resonant couplings will lead to lower contrast values of the resulting dynamics compared to what is predicted with this approximation.

An arbitrary quantum state of a two-level system consisting of the two eigenstates $|g\rangle$ and $|e\rangle$ is written as

$$|\psi\rangle = c_1|g\rangle + c_2|e\rangle, \quad (6.1)$$

¹In an experiment this is achieved by choosing the Rabi frequency $\Omega \ll \omega_T$, with ω_T being the smallest trap frequency.

with the complex probability amplitudes c_1 and c_2 . Following the derivation from Section 1.2.1, the Hamiltonian describing the interaction of this two-level atom (with transition frequency ω) with a near-resonant monochromatic light field ω_L is (1.13)

$$H = -\hbar \frac{\Omega}{2} \left(e^{i(\phi-\Delta t)} |e\rangle\langle g| + e^{-i(\phi-\Delta t)} |g\rangle\langle e| \right) \quad (6.2)$$

with the Rabi frequency Ω describing the strength of the interaction and ϕ being the phase of the laser with respect to the atomic quadrupole moment. $\Delta = \omega_L - \omega$ is the detuning of the laser from the atomic transition frequency. The operator describing the corresponding unitary transformation of an initial state $|\psi(0)\rangle$ due to the interaction for a time t to the final state $|\psi(t)\rangle = R(\Omega t, \phi)|\psi(0)\rangle$ is derived as [154]

$$R(\Omega t, \phi) = \cos\left(\frac{\Omega t}{2}\right) (|g\rangle\langle g| + |e\rangle\langle e|) + i \sin\left(\frac{\Omega t}{2}\right) (e^{i\phi} |e\rangle\langle g| + e^{-i\phi} |g\rangle\langle e|) . \quad (6.3)$$

Here the resonance condition $\Delta = 0$ has been assumed.

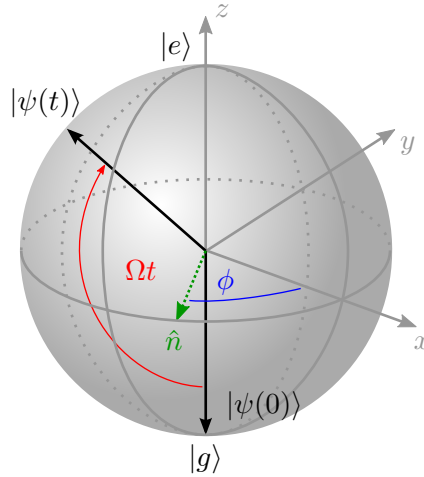


Figure 6.1.: Bloch-sphere representation of the rotation of a state vector $|\psi\rangle$ by the interaction with a resonant light field for the time t with the Rabi frequency Ω and the relative phase ϕ .

When visualizing the action of this unitary operation on a quantum state represented on the Bloch sphere, the result is a rotation of the state vector by the angle Ωt around an axis \hat{n} , lying in the equatorial plane [155] (see Figure 6.1). The angle ϕ of \hat{n} with respect to the x -axis² of the coordinate system is then just the phase difference between the light-field oscillation and the atomic-state evolution.

Ω is mainly controlled by the laser power and detuning, ϕ is changed via a phase shift of the AOM frequency, switching the laser beam. Another contribution to ϕ can emerge when the interaction is switched off for a while. In the absence of laser radiation, the atomic-state phase evolves with $e^{i\omega t}$, corresponding to the non-perturbed time evolution of its energy eigenstates. For the case of $\omega \neq \omega_L$, this causes, after a waiting time t , a phase mismatch $e^{-i\Delta t}$ between

²Any other axis in the equatorial plane could be chosen as reference.

the atomic state and the laser, leading to different final states when applying the same laser pulse after different waiting times. This effect is used, for example, in a Ramsey experiment.

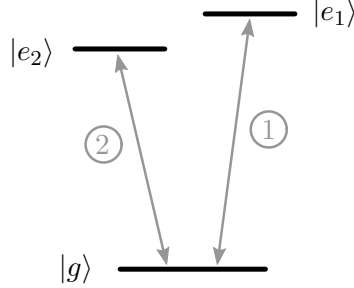


Figure 6.2.: Level scheme with one ground state $|g\rangle$ that is coupled to the excited states $|e_1\rangle$ and $|e_2\rangle$ via the transitions 1 and 2.

Let us assume now that instead of a single excited state, two excited states $|e_1\rangle$ and $|e_2\rangle$ at different transition frequencies are present (Figure 6.2). It is further assumed that only one transition is addressed at a time, allowing a description of the resulting dynamics by two independent two-level systems with the common initial state $|g\rangle$. It is convenient to describe the state of the overall wave function

$$|\psi\rangle = b_1|g\rangle + b_2|e_1\rangle + b_3|e_2\rangle \quad (6.4)$$

as a vector $\begin{pmatrix} b_1 \\ b_2 \\ b_3 \end{pmatrix}$ in the basis spanned by the three eigenstates of the system $\{|g\rangle, |e_1\rangle, |e_2\rangle\}$.

Writing the unitary operators $R_1(\Omega t, \phi)$ and $R_2(\Omega t, \phi)$, describing the interaction of the atom with laser light on the transitions 1 and 2 in the same basis, leads to the representation

$$R_1(\Omega t, \phi) = \begin{pmatrix} \cos\left(\frac{\Omega t}{2}\right) & ie^{-i\phi} \sin\left(\frac{\Omega t}{2}\right) & 0 \\ ie^{i\phi} \sin\left(\frac{\Omega t}{2}\right) & \cos\left(\frac{\Omega t}{2}\right) & 0 \\ 0 & 0 & 1 \end{pmatrix} \quad (6.5)$$

and

$$R_2(\Omega t, \phi) = \begin{pmatrix} \cos\left(\frac{\Omega t}{2}\right) & 0 & ie^{-i\phi} \sin\left(\frac{\Omega t}{2}\right) \\ 0 & 1 & 0 \\ ie^{i\phi} \sin\left(\frac{\Omega t}{2}\right) & 0 & \cos\left(\frac{\Omega t}{2}\right) \end{pmatrix}, \quad (6.6)$$

always assuming that the laser is tuned in resonance with the respective transition. The interaction with n subsequent pulses resonant with either transition is then described by the product

$$R_{\text{eff.}} = \prod_{i=1}^n R_{\beta_i}(\Omega_i t_i, \phi_i), \quad \beta = \{1, 2\} \quad (6.7)$$

of the individual rotation matrices, applied to the initial state $|\psi(0)\rangle$. The population in one of the eigenstates $|\psi_{\text{eig.}}\rangle$ of the system after the interaction is calculated as

$$p_{|\psi_{\text{eig.}}\rangle} = |\langle\psi_{\text{eig.}}|R_{\text{eff.}}|\psi(0)\rangle|^2. \quad (6.8)$$

6.2. Coherent superposition between $S_{1/2}$ and $D_{5/2}$

A very powerful technique employing coherent superposition states has been developed by Ramsey, achieving a highly increased precision in NMR-spectroscopy experiments [156]. The principle of these Ramsey experiments is as follows. After initializing an atom in a single energy eigenstate, a certain coherent excitation applied at time 0 is used to create a coherent superposition between two atomic levels. After the waiting time t_{wait} , the superposition is rotated back to the initial eigenstate by applying an identical pulse but with phase $\phi = \pi$ with respect to the first one. As mentioned in the previous section, a frequency mismatch between the exciting radiation and the atomic transition causes a phase mismatch of the second pulse in this experiment. This leads to a measurable transfer of population to the second eigenstate of the system. Since the accumulated phase is proportional to t_{wait} , very high sensitivity to small frequency changes is achieved for long waiting times. Being phase sensitive, the technique is moreover the ultimate tool to characterize decoherence, of both the atomic system and the exciting radiation.

Section 6.2.1 will demonstrate a basic Ramsey experiment on the $S_{1/2}$ - $D_{5/2}$ transition, which reveals further information about the medium-term frequency stability of the experiment. In Section 6.2.2, a Ramsey experiment is used to estimate the coherence time of the ion-laser interaction, giving an upper bound for the spectral linewidth of the laser.

6.2.1. Ramsey signal

Figure 6.3 illustrates the laser sequence that is used to generate and probe a coherent superposition between the $|S_{1/2}, -1/2\rangle := |g\rangle$ and $|D_{5/2}, -1/2\rangle := |e\rangle$ level. It is embedded in the overall laser sequence for excitation with 729 nm light that is explained in Section 4.4.1.

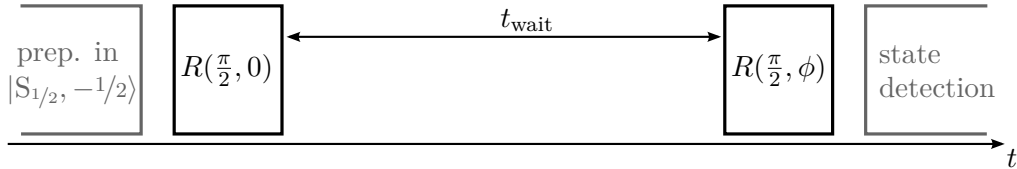


Figure 6.3.: Laser sequence for a Ramsey experiment. First, the ion is initialized in a single Zeeman sub-level of the ground state by optical pumping. Then, a 729 nm pulse is applied to create a coherent superposition and after a waiting time t_{wait} , a second pulse is used to rotate the superposition back to an energy eigenstate. $R(\theta, \phi)$ represents a laser pulse with the pulse area $\Omega t_\theta = \theta$ and phase ϕ , see Equation (6.3). Finally, the state of the ion is determined by measuring the $D_{5/2}$ population. For details about the initialization and state detection (in gray) see Section 4.4.1.

The length and intensity of the pulses are set for a pulse area of $\theta = \frac{\pi}{2}$, generating the symmetric coherent superposition

$$|\psi\rangle = \frac{1}{\sqrt{2}}(|g\rangle + i|e\rangle) \quad (6.9)$$

after the first pulse, when starting from the initial state $|g\rangle$. With the second pulse, the coherent superposition is then rotated to $|g\rangle$ or $|e\rangle$ by scanning the phase ϕ with respect to the

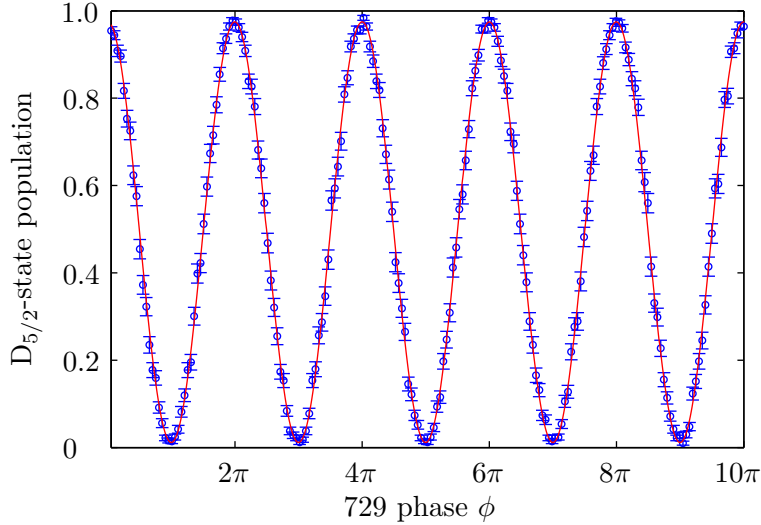


Figure 6.4.: Ramsey interference signal on the $|S_{1/2}, -1/2\rangle$ - $|D_{5/2}, -1/2\rangle$ transition when scanning the phase ϕ of the second Ramsey pulse. Each point represents 500 sequence repetitions. The timing parameters were $t_{\pi/2} = 0.885 \mu\text{s}$ and $t_{\text{wait}} = 0.5 \mu\text{s}$. The red curve is a sinusoidal fit, revealing a fringe visibility of $97.7(2)\%$.

first laser pulse. This is strictly speaking a Ramsey experiment with a phase scan instead of a frequency scan. When measuring the population in D, an interference signal oscillating with ϕ as

$$p_{|e\rangle} = \frac{1}{2} (1 + \cos(\phi - \Delta t_{\text{wait}})) \quad (6.10)$$

is expected by using the theoretical description from the previous section. The additional phase Δt_{wait} accounts for a frequency difference Δ between laser and atomic transition during the waiting time t_{wait} .

Figure 6.4 shows such a phase scan, corresponding obviously to the dependence given by (6.10). The phase offset is around zero, owing to the very short waiting time. When increasing t_{wait} , a linear dependence of the offset phase is expected if $\Delta \neq 0$. As shown in Figure 6.5 a), a significant deviation from the linear behavior is observable. A mean deviation of $\Delta = 176(12)$ Hz of the laser frequency from the atomic resonance is extracted with a fit. Figure 6.5 b) shows a slow drift of the detunings $\Delta = \omega_L - \omega$ as derived from the measured phase offsets for increasing recording times of the measurements. This drift is responsible for the non-linear dependence of the accumulated phase on the waiting time t_{wait} observed in Figure 6.5 a), because it took up to 2 min to take a single data point.

In these experiments, the frequency of the 729 nm laser was determined by spectroscopy and then set with a precision of 100 Hz. The used transition has the smallest magnetic field dependence (560 Hz/mG), for the current long-term stability of the B-field of 0.1 mG this could cause a drift of the atomic resonance on the order of 60 Hz within a few minutes, compatible with the measured data. But the observed drift could be just as well explained with a laser drift owing to cavity aging or remaining temperature instabilities of the reference cavity (Section 4.4.3). Nevertheless, the drift on the minute timescale appears to be rather smooth, making it

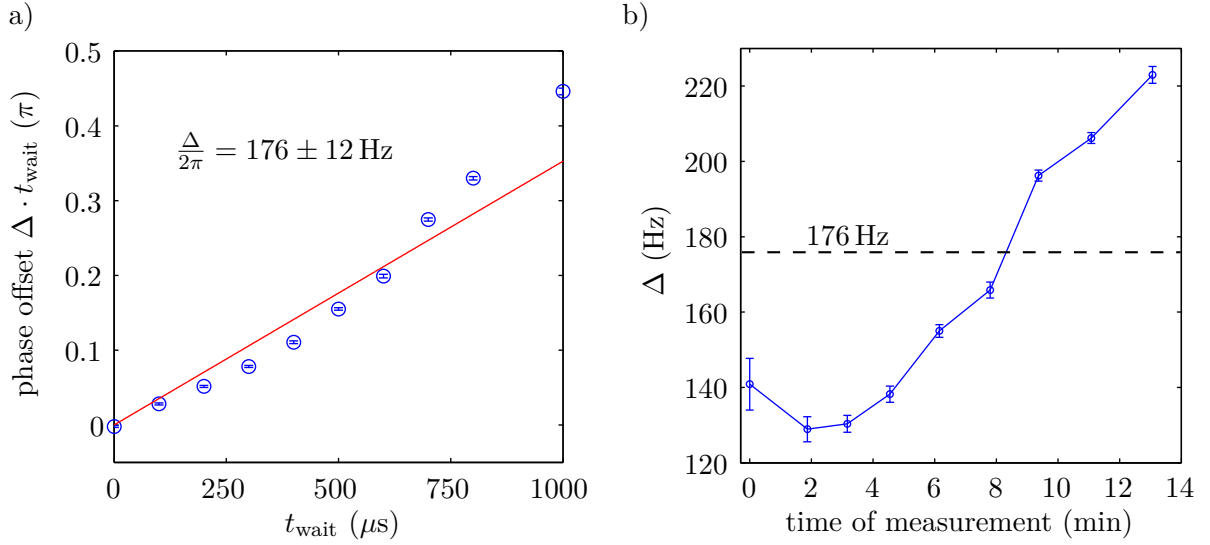


Figure 6.5.: a) Ramsey-fringe phase offset for different waiting times caused by a small detuning of the laser from the atomic resonance. The red line is a linear fit yielding a constant detuning, the deviations of the data points from the fit indicate an additional drift of the laser-atom detuning. b) Drift of laser detuning Δ derived from measured phase offset, plotted versus the relative time of measurement. The first data point in Figure a) is omitted since it has a huge uncertainty due to a very small t_{wait} .

feasible to effectively compensate it in the future with a slow feed-forward to the laser frequency as proposed in Section 4.4.3.

6.2.2. Measurement of laser linewidth

When calculating (6.10) it has been assumed that the state right before the second Ramsey pulse ($t = t_{\text{wait}}$) is the same as the state (6.9) right after the preparation with the first pulse ($t = 0$). However, magnetic-field fluctuations and fast changes of the laser frequency lead to an effective phase uncertainty of the prepared state at $t = t_{\text{wait}}$. It is therefore better to assume

$$|\psi(t_{\text{wait}})\rangle = c_g|g\rangle + c_e|e\rangle \quad (6.11)$$

with the complex probability amplitudes c_g and c_e which might vary from shot to shot. The observable effects when measuring an ensemble of such identically prepared states are better described in the density-matrix representation

$$\rho(t_{\text{wait}}) = \begin{pmatrix} \rho_{gg} & \rho_{ge} \\ \rho_{eg} & \rho_{ee} \end{pmatrix} \quad (6.12)$$

with $\rho_{ge} = \langle c_g c_e^* \rangle$ being the ensemble average of the respective coefficient products. Applying the unitary operation $R(\frac{\pi}{2}, \phi)$ with the second Ramsey pulse to the ensemble and assuming an on-average resonant excitation ($\langle \Delta \rangle = 0$) results in the dependence of the measured $D_{5/2}$ population

$$\langle p_{|e\rangle} \rangle = \rho_{ee} = \frac{1}{2} + |\rho_{ge}| \cos(\phi + \phi_{\text{dec.}}) \quad (6.13)$$

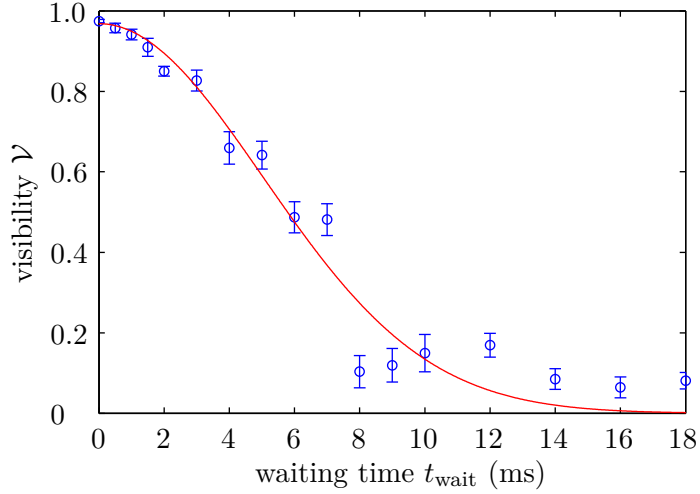


Figure 6.6.: Visibility of Ramsey signal for different waiting times. The red curve is a Gaussian fit, corresponding to a $1/e$ decay time of 7.1(4) ms.

with the additional phase $\phi_{\text{dec.}}$ owing to the argument of ρ_{ge} . $\phi_{\text{dec.}}$ is interpreted as the ensemble average of the phase fluctuations, for a symmetric distribution function of possible phases it is therefore set to zero. Assuming Gaussian white noise for the frequency fluctuations³ in our experimental situation it is derived [157, 158] that

$$\rho_{ge} \propto \exp\left(-\frac{t_{\text{wait}}^2}{2\tau^2}\right). \quad (6.14)$$

The decay constant τ is a measure for the timescale at which the system decoheres, it is related to the Root-Mean-Square (RMS) amplitude of the frequency fluctuations Δ_{RMS} by

$$\Delta_{\text{RMS}} = \frac{1}{\tau}. \quad (6.15)$$

In a Ramsey measurement as demonstrated in the previous section, the off-diagonal density-matrix element $|\rho_{ge}|$ from (6.13) is directly obtained from the visibility \mathcal{V} of a phase scan (Figure 6.4) with $|\rho_{ge}| = \mathcal{V}/2$.

To get an estimate for the spectral linewidth of the 729 laser, the Ramsey experiment on the $|S_{1/2}, -1/2\rangle$ - $|D_{5/2}, -1/2\rangle$ transition from Section 6.2.1 has been repeated, but this time triggering the sequence to the 50 Hz power-line frequency. This minimizes decoherence effects caused by the periodic B-field oscillation as measured in Section 4.4.2. Figure 6.6 shows the resulting decay of the Ramsey fringe contrast for increasing waiting times. From the measurement, an RMS amplitude of the frequency fluctuations of

$$\Delta_{\text{RMS}} = (2\pi) \cdot 32(2) \text{ Hz}$$

is derived. Supposing that the observed decay of coherence is dominated by frequency fluctuations of the laser, this value gives an upper bound for its short-term stability and thereby spectral linewidth.

³Frequency fluctuations $\Delta(t)$ cause phase fluctuations $\phi(t) = \int_0^t \Delta(t') dt'$.

Figure 6.6 further shows, that even for very short waiting times, the obtained Ramsey-fringe visibility is not reaching unity. The shortest waiting time measured was $t_{\text{wait}} = 500$ ns with a laser-pulse length of $t_{\frac{\pi}{2}} = 898$ ns and a resulting visibility of 97.5(4) %. On this time scale, decoherence caused by frequency fluctuations is expected to be negligible. But the resulting rather high Rabi frequencies of almost 300 kHz might result in non-negligible off-resonant coupling to neighboring carrier transitions or motional sidebands, thereby reducing the contrast. Imperfections of the $\frac{\pi}{2}$ -pulse timings might be further responsible for the limited visibility. Even though the pulse lengths are usually carefully determined by measuring Rabi oscillations (Section 4.4.4), the maximal slope of the population transfer at the end of a $\frac{\pi}{2}$ -pulse makes those pulses most vulnerable to timing imperfections. An additional source of error is the limited fidelity of coherent manipulations owing to the vibrational state of the ion after Doppler cooling and the resulting excitation at many different Rabi frequencies (Section 5.1.2). The observed visibility would correspond to a single $\frac{\pi}{2}$ -pulse fidelity of 98.7(2) %, compatible with the measured efficiency of single π -pulses for electron shelving in Section 4.4.4.

6.3. Coherent superposition in the $D_{5/2}$ state

As already mentioned in Section 2.3, the creation of coherent superpositions within the $D_{5/2}$ state is essential for several possible entanglement-transfer schemes, employing the state mapping of polarization-entangled photon pairs at 854 nm onto the electronic ground state of an ion. In the following, it will be demonstrated that the experimental set-up is capable of creating such coherent superpositions, opening up the possibility for experiments aiming at the quantum-state transfer from single photons to single ions.

Section 6.3.1 presents a measurement which extends the Ramsey experiments from the last section by employing a second sub-level of the $D_{5/2}$ state. This makes it possible to investigate the dynamics of the probability amplitude of an atomic state, when interacting with a resonant coherent light field. Section 6.3.2 demonstrates the generation of a coherent superposition in the $D_{5/2}$ state and a measurement of its coherence time. The result is used to obtain an estimate for the expected coherence times of arbitrary superposition states in the experiment.

6.3.1. Coherent dynamics involving an auxiliary $D_{5/2}$ level

When calculating the dynamics of a Rabi oscillation with the Rabi frequency Ω in a two-level system, the periodicity of the wave function returning to its initial state is $\Omega t = 4\pi$, owing to the factor of $\frac{1}{2}$ in the Hamiltonian (6.2) describing the interaction⁴. However, when looking only at the populations, a 2π -periodicity is observed since only the squared absolute values of the probability amplitudes are accessible in a measurement. The 4π -period can nevertheless be measured when before driving Rabi oscillations between $|g\rangle$ and $|e\rangle$, $|g\rangle$ is put in a coherent superposition with an auxiliary level $|e_{\text{aux}}\rangle$. After the interaction, this coherent superposition is rotated back to one of the two eigenstates ($|g\rangle, |e_{\text{aux}}\rangle$), resulting in a final state which depends on the sign and value of the probability amplitude that the state $|g\rangle$ acquired during the interaction that coherently excited it to $|e\rangle$.

⁴The 4π -periodicity of the interaction is a key ingredient for quantum logic operations using ion strings as proposed by Cirac and Zoller [148].

In the experiment, the $D_{5/2}$ levels with $m = -1/2$ and $m = +1/2$ are used as $|e\rangle$ and $|e_{\text{aux}}\rangle$, respectively, the ground-state level $|S_{1/2}, -1/2\rangle$ is chosen as $|g\rangle$ (see Figure 6.7). The transition between $|g\rangle$ and $|e_{\text{aux}}\rangle$ will be referred to as transition 1 and the transition between $|g\rangle$ and $|e\rangle$ will be labeled as transition 2.

A first measurement to determine the Rabi frequency on transition 2 is depicted in Figure 6.8. The theoretical dependence of the measured $D_{5/2}$ population on the 729 pulse length t_θ is given by

$$p_{D_{5/2}} = \sin^2\left(\frac{\Omega t_\theta}{2}\right) = \frac{1}{2}(1 - \cos(\Omega t_\theta)) \quad (6.16)$$

with Ω being the Rabi frequency. The fitted model takes an additional damping of the amplitude into account, which is caused by the thermal distribution of different Rabi frequencies when the ion's motion is only Doppler cooled. The effective Rabi frequency is determined to $\Omega/2\pi = 203.9(2)$ kHz, corresponding to a 2π -period of the measured oscillation of $4.904(5)$ μs .

The experiment is then repeated, but this time creating first a coherent superposition between $|g\rangle$ and $|e_{\text{aux}}\rangle$. The laser sequence is depicted in Figure 6.9 a). A $\frac{\pi}{2}$ -pulse ($t_{\frac{\pi}{2}} = 2.7$ μs)

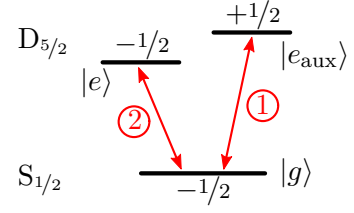


Figure 6.7.: Atomic levels that are used for the demonstration of coherent manipulations on the $S_{1/2}$ - $D_{5/2}$ transition. The magnetic quantum numbers are indicated above and below the respective sub-levels.

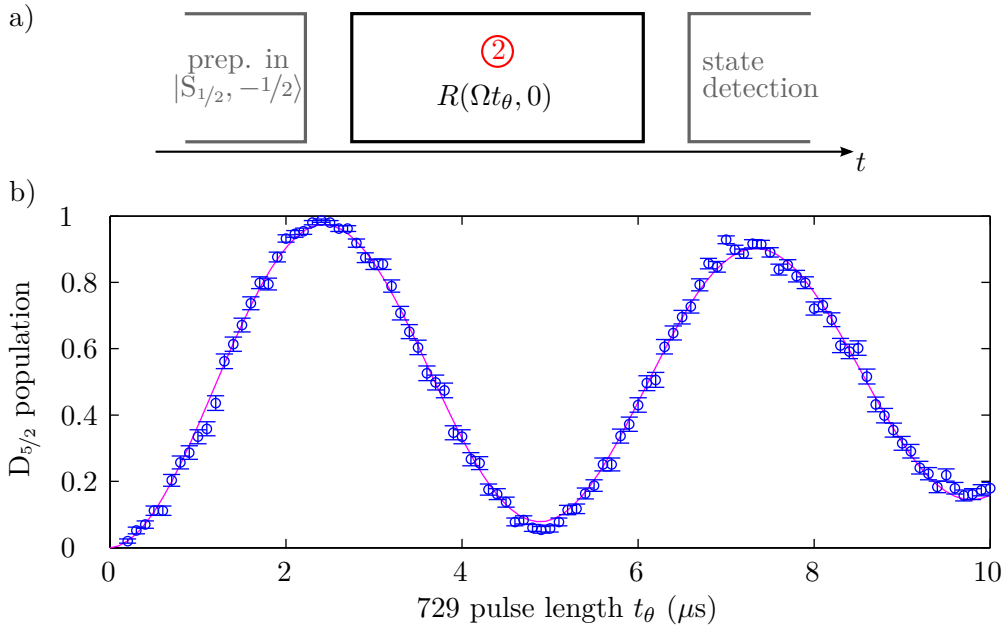


Figure 6.8.: Rabi oscillation on the $|S_{1/2}, -1/2\rangle$ - $|D_{5/2}, -1/2\rangle$ transition. a) Part III of the overall laser sequence (Section 4.4.1) consists of a single pulse of 729 nm light with fixed Rabi frequency Ω and variable length t_θ . b) Measured $D_{5/2}$ population as a function of the 729 pulse length. The magenta curve is a fit revealing a Rabi frequency of $\Omega/2\pi = 203.9(2)$ kHz.

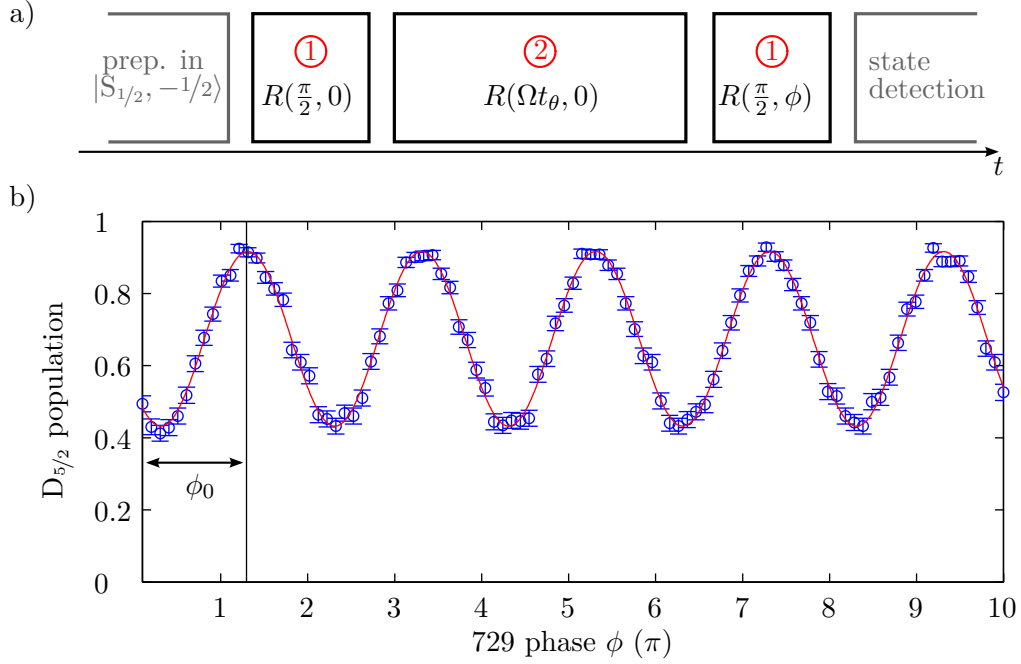


Figure 6.9.: a) Laser sequence to probe the dynamics of the ground state $|g\rangle$ when it is coherently coupled to $|e\rangle$ on transition 2. For details see text. b) Measurement of $D_{5/2}$ population as a function of the phase ϕ of the final $\frac{\pi}{2}$ -pulse. The data correspond to a pulse area for the excitation on transition 2 of $\Omega t_\theta = 0.65 \pi$, each point represents 500 sequence repetitions. The red curve is a sinusoidal fit, revealing the constant phase offset ϕ_0 present in all experiments.

on transition 1 rotates the state vector to the equatorial plane of the Bloch sphere (see Figure 6.12), thereby creating a symmetric coherent superposition and defining the phase $\phi = 0$. Subsequently, the laser is tuned to transition 2, driving Rabi oscillations between $|g\rangle$ and $|e\rangle$ for a certain time t_θ , just as in the previous experiment. $20 \mu\text{s}$ after the first laser pulse, a second rotation with a similar $\frac{\pi}{2}$ -pulse as the first one is applied to the coherent superposition between $|g\rangle$ and $|e_{\text{aux}}\rangle$. In the subsequent state detection the overall population remaining in $D_{5/2}$ is measured, being the sum of the populations in $|e_{\text{aux}}\rangle$ and $|e\rangle$.

The experiment control *HYDRA* is designed for phase-preserving frequency switching. In the sequence, the laser frequency is always tuned for a fixed time to transition 2, leading to a fixed phase offset ϕ_0 between the atomic superposition state on transition 1 and the laser after tuning it back for the last $\frac{\pi}{2}$ -pulse. To determine this phase offset, the phase ϕ of the last $\frac{\pi}{2}$ -pulse is scanned, resulting in an oscillation of the measured $D_{5/2}$ population as a function of ϕ (see Figure 6.9). By taking this phase offset into account, this measurement method then allows the extraction of the final $D_{5/2}$ population for arbitrary phases $\phi' = \phi - \phi_0$ of the second $\frac{\pi}{2}$ -rotation from the data.

Using the formalism from Section 6.1, the dynamics of the measured $D_{5/2}$ population for arbitrary pulse lengths t_θ on transition 2 and arbitrary phases ϕ' of the final rotation on

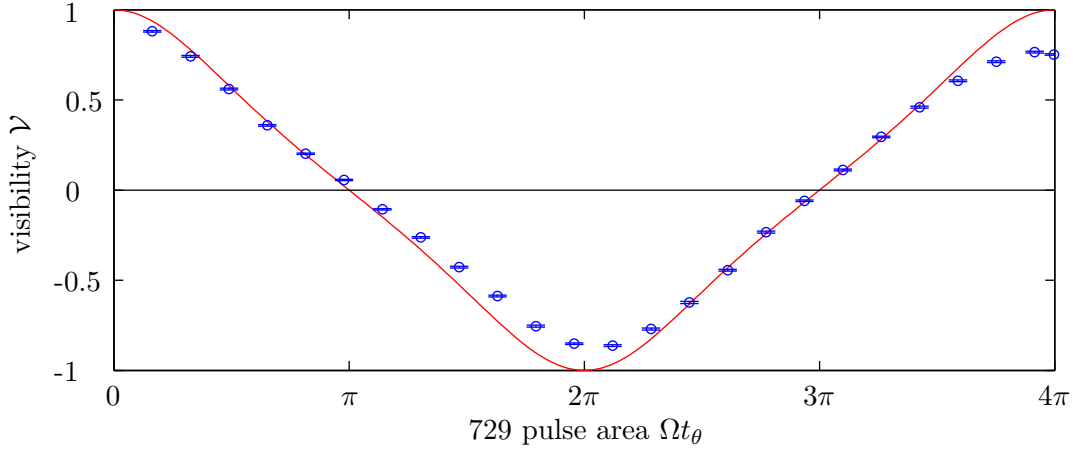


Figure 6.10.: Evolution of interference-fringe visibility for different pulse areas Ωt_θ for the excitation on transition 2. The red curve shows the theoretical dependence as given by (6.18).

transition 1 is derived as

$$p_{D_{5/2}} = \frac{1}{2} \left[1 + \frac{1}{2} \sin^2 \left(\frac{\Omega t_\theta}{2} \right) + \cos \left(\frac{\Omega t_\theta}{2} \right) \cos(\phi') \right]. \quad (6.17)$$

The fit of the data as displayed in Figure 6.9 has the general functional dependence $p_{D_{5/2}} = O(1 + \mathcal{V} \cos(\phi'))$ where O is the offset and \mathcal{V} the visibility of the observable sinusoidal interference signal. Comparing this with (6.17), leads to a dependence for \mathcal{V} of

$$\mathcal{V} = \frac{\cos \left(\frac{\Omega t_\theta}{2} \right)}{1 + \frac{1}{2} \sin^2 \left(\frac{\Omega t_\theta}{2} \right)}. \quad (6.18)$$

Note that this definition allows negative values for the visibility, corresponding to an inversion of the measured interference signal.

Figure 6.10 shows the measured dependence of \mathcal{V} on the pulse area Ωt_θ that is applied on transition 2 between $|g\rangle$ and $|e\rangle$. The measured data is in good agreement with the theoretical evolution as given by (6.18), exhibiting a 4π -periodicity in terms of Ωt_θ . The evolution of the probability amplitude c_g of the ground state $|g\rangle$ when being coherently coupled to $|e\rangle$ is described by $c_g(t_\theta) = \cos(\Omega t_\theta/2)$, thereby experiencing a change of sign for $\Omega t_\theta = (2n + 1)\pi$ (n integer). This change of sign is directly related to a change of sign of \mathcal{V} which makes the 4π -periodicity in the evolution of c_g observable in this measurement. This process will be further discussed in a moment with examples.

Figure 6.11 shows the measured evolution of the $D_{5/2}$ population as a function of the pulse area Ωt_θ for excitation on transition 2 and of the effective phase ϕ' of the final $\frac{\pi}{2}$ -rotation on transition 1. The experimental data agree very well with the theoretical dependence described by Equation (6.17). Only for increasing pulse areas a loss of contrast is observable; as in the measurement of Rabi oscillations this can be attributed to the finite temperature of the ion when its motion is only Doppler cooled.

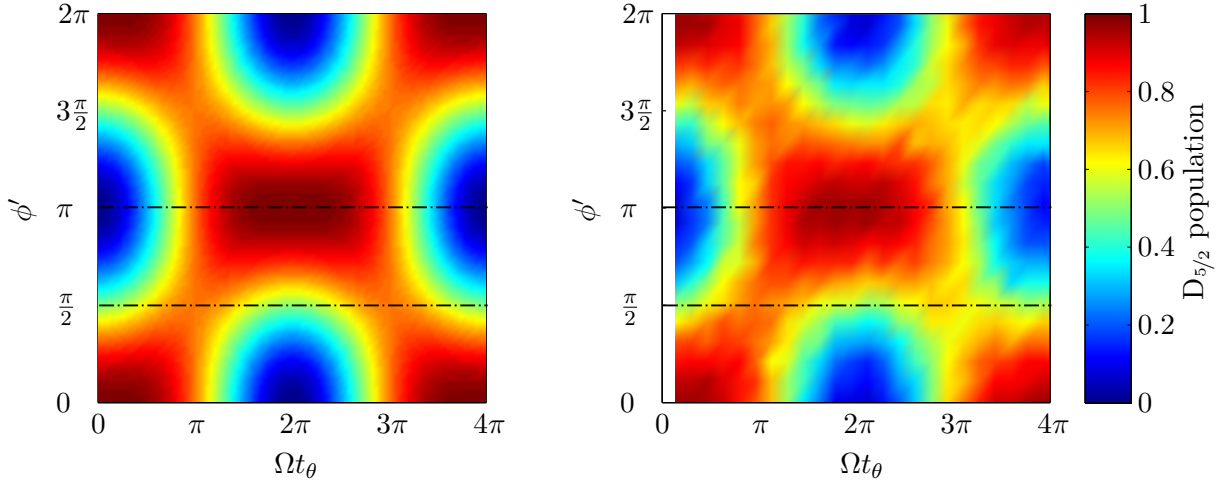


Figure 6.11.: Theoretical (left) and measured (right) evolution of the $D_{5/2}$ -state population as a function of the pulse area Ωt_θ of the central laser pulse and of the phase ϕ' of the final $\frac{\pi}{2}$ -rotation. The cuts indicate two sets of data that are analyzed in more detail in the following.

To get a better understanding of the dynamics of the atomic state in the experiment, the following two paragraphs will provide a more detailed look at the evolution of the $D_{5/2}$ population for two specific phases ϕ' of the final $\frac{\pi}{2}$ -rotation (indicated in Figure 6.11).

For $\phi' = \pi$, the population evolves as

$$p_{D_{5/2}} = \underbrace{\frac{1}{4} \left[1 - \cos \left(\frac{\Omega t}{2} \right) \right]^2}_{p_{|e_{\text{aux}}\rangle}} + \underbrace{\frac{1}{2} \sin^2 \left(\frac{\Omega t}{2} \right)}_{p_{|e\rangle}}, \quad (6.19)$$

exhibiting a 4π -period for the contribution of the population in the auxiliary state $|e_{\text{aux}}\rangle$ and a 2π -period for the population in $|e\rangle$, as expected for Rabi oscillations. Figure 6.12 b) shows the corresponding experimental data, featuring nicely the 4π -periodicity of the overall dynamics. In part a) of the figure, the evolution of the state vector on the Bloch sphere is illustrated for the case of a 2π -pulse on transition 2. During the excitation on transition 2, population gets coherently transferred from $|g\rangle$ to $|e\rangle$, resulting in a rotation of the state vector in the subsystem $\{|g\rangle, |e\rangle\}$ by the angle Ωt_θ . This changes the probability amplitude of $|g\rangle$ and thereby results in a rotation of the state vector in the subsystem $\{|g\rangle, |e_{\text{aux}}\rangle\}$ by $\Omega t_\theta/2$. For $\Omega t_\theta = 2\pi$, the superposition state in $\{|g\rangle, |e_{\text{aux}}\rangle\}$ therefore experiences a phase shift of π . This results then in a full transfer of all population to $|e_{\text{aux}}\rangle$ when applying a $-\frac{\pi}{2}$ -rotation at the end. Without the acquired phase-shift of π in the subsystem $\{|g\rangle, |e_{\text{aux}}\rangle\}$ (e.g. $\Omega t_\theta = 4\pi$), the final pulse rotates all population back to $|g\rangle$. It is now just straight forward to reconstruct the state evolution in both subsystems for arbitrary values of Ωt_θ .

As one can see in Figure 6.11, the 4π -periodicity of the evolution of the $D_{5/2}$ population holds for all phases ϕ' of the final $\frac{\pi}{2}$ -rotation except for values of $\phi' = (2n + 1)\frac{\pi}{2}$ (n integer).

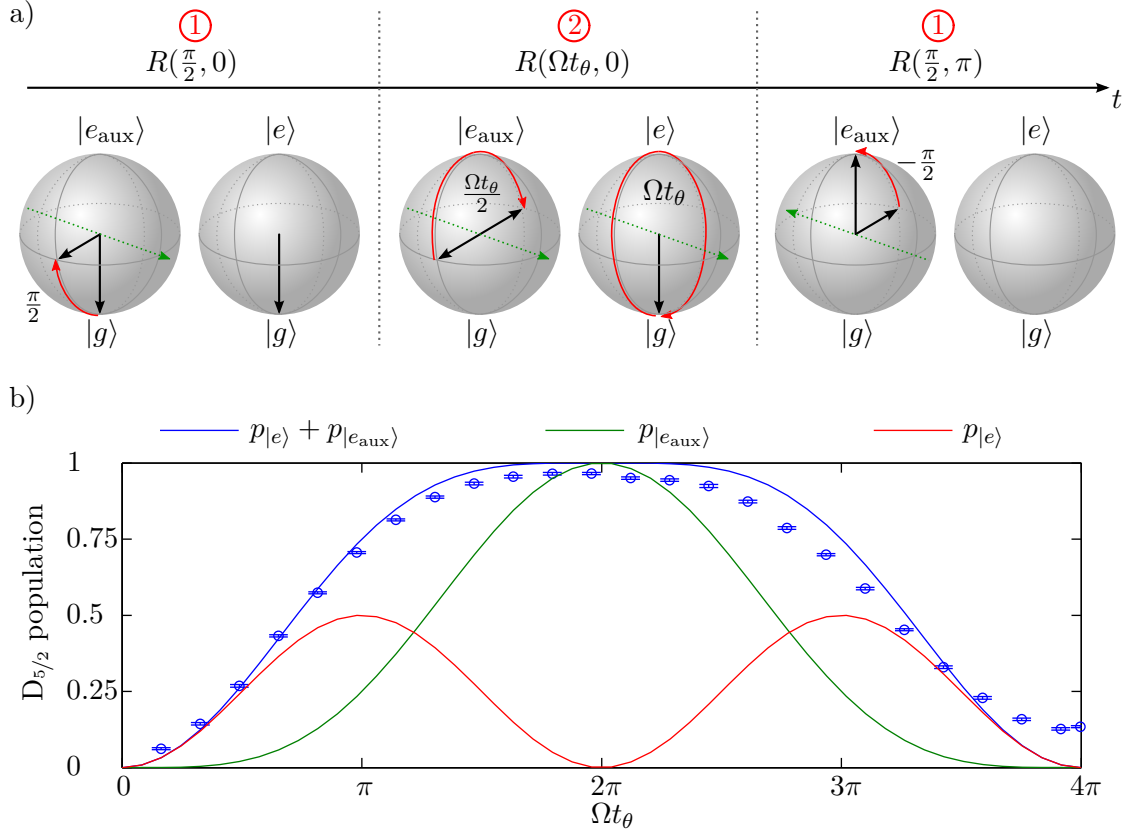


Figure 6.12.: Evolution of the $D_{5/2}$ population as a function of the pulse area Ωt_θ on transition 2 and for a final $\frac{\pi}{2}$ -rotation on transition 1 with the effective phase $\phi' = \pi$. a) Bloch-sphere representation of the evolution of the state vector in the two subsystems $\{|g\rangle, |e\rangle\}$ and $\{|g\rangle, |e_{\text{aux}}\rangle\}$ for $\Omega t_\theta = 2\pi$. During the interaction, population is coherently transferred between both subsystems; in this representation it is assumed that the Bloch spheres are normalized at any time. b) Experimental data and theoretical evolution of the populations as given by Equation (6.19).

For $\phi' = \frac{\pi}{2}$, the change in the population is described by

$$p_{D_{5/2}} = \underbrace{\frac{1}{4} \left[1 + \cos^2 \left(\frac{\Omega t}{2} \right) \right]}_{p_{|e_{\text{aux}}\rangle}} + \underbrace{\frac{1}{2} \sin^2 \left(\frac{\Omega t}{2} \right)}_{p_{|e\rangle}}, \quad (6.20)$$

having a period of 2π for the individual contributions from both excited states $|e\rangle$ and $|e_{\text{aux}}\rangle$. Figure 6.13 shows the corresponding data and again an illustration of the state evolution in the two subsystems on the Bloch sphere for $\Omega t_\theta = 2\pi$. The important point is that the last rotation in $\{|g\rangle, |e_{\text{aux}}\rangle\}$ happens now around an axis which is parallel to the state vector, thus having no influence at all. Therefore the populations remain equally distributed between $|g\rangle$ and $|e_{\text{aux}}\rangle$, just as right after the preparation of the coherent superposition with the first rotation. With the given illustration it is easy to see that for arbitrary pulse areas Ωt_θ , the final $\frac{\pi}{2}$ -rotation on transition 1 will always rotate the state vector in $\{|g\rangle, |e_{\text{aux}}\rangle\}$ to the equatorial plane of the

6. Coherent manipulations on the $S_{1/2}$ - $D_{5/2}$ transition

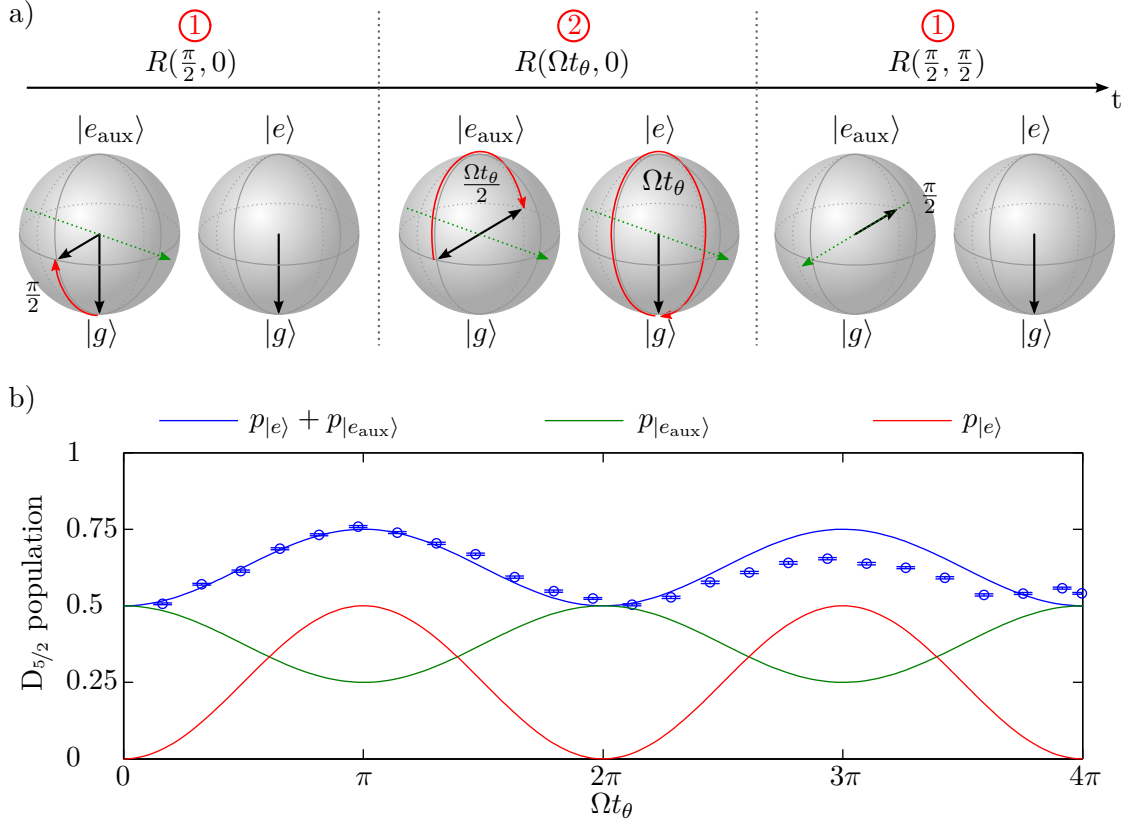


Figure 6.13.: Evolution of the $D_{5/2}$ population as in Figure 6.12 but for a final $\frac{\pi}{2}$ -rotation on transition 1 with the effective phase $\phi' = \frac{\pi}{2}$. a) Bloch-sphere representation of the evolution of the state vector for $\Omega t_\theta = 2\pi$, similar to Figure 6.12. b) Experimental data and theoretical evolution of the populations as given by Equation (6.20).

Bloch sphere. Consequently, it only permits a maximal population transfer of 50% from the subsystem $\{|g\rangle, |e_{\text{aux}}\rangle\}$ back to $|g\rangle$. This can only compensate the population oscillation on transition 2 by a factor of 1/2 which is why the Rabi oscillation between $|g\rangle$ and $|e\rangle$ is still observable in the total $D_{5/2}$ population.

The experiments from this section demonstrate fundamental (textbook) quantum-mechanical phenomena in an atomic two-level system that is coupled to a coherent light field. Especially, they illustrate how a phase shift of π in a superposition state is easily produced by a 2π -pulse from one of the superposition states to an auxiliary level. The overall agreement between the experimental data and the theory demonstrates a considerable degree of control of coherent manipulations on the optical quadrupole transition. This is elementary for the preparation of coherent superpositions for photon absorption and for unitary operations on qubit states enabling their measurement in different bases.

6.3.2. Generation of coherent superposition in $D_{5/2}$

The creation of a coherent superposition between two levels from the $D_{5/2}$ state can be achieved by creating in a first step a superposition state between $|S_{1/2}, -1/2\rangle$ and one of the $D_{5/2}$ levels. In a second step, the remaining population from the ground state is then coherently transferred to the second $D_{5/2}$ level.

As a proof of principle that it is possible to generate such coherent superpositions with the set-up, a symmetric coherent superposition between $|D_{5/2}, -1/2\rangle$ and $|D_{5/2}, +1/2\rangle$ has been created and subsequently analyzed. In this experiment, the same levels as in the previous section are used, as a reminder the scheme is depicted on the right. The pulse sequence is sketched in Figure 6.15. Obviously, the sequence is a modification of the sequence that has been introduced in the previous section by splitting the central pulse on transition 2 into two individual pulses of fixed pulse area π and separated by the waiting time t_{wait} .

More specifically, first a $\frac{\pi}{2}$ -pulse on transition 1 with length $t_1 = 2.7 \mu\text{s}$ is used to create a symmetric coherent superposition between $|S_{1/2}, -1/2\rangle$ and $|D_{5/2}, +1/2\rangle$. Then, the remaining population in $|S_{1/2}, -1/2\rangle$ is coherently transferred to $|D_{5/2}, -1/2\rangle$ (transition 2) with a π -pulse of length $t_2 = 2.56 \mu\text{s}$ ⁵. After the time t_{wait} , the superposition in D is transferred back to a superposition between S and D by applying a second π -pulse on transition 2. Finally, the coherence of the state is probed by scanning the phase ϕ of a $\frac{\pi}{2}$ -pulse on transition 1.

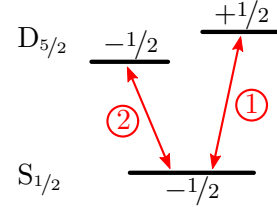


Figure 6.14.: Atomic levels and transitions that are used for the generation of a coherent superposition within the $D_{5/2}$ state. The magnetic quantum numbers are indicated above and below the respective sub-levels.

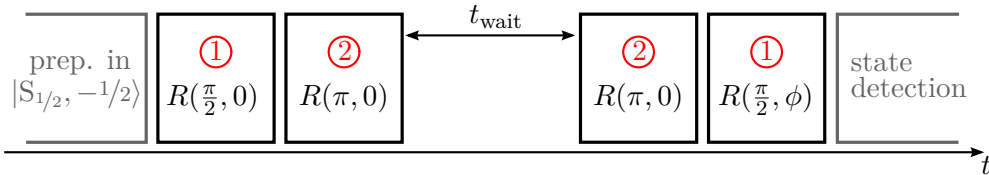


Figure 6.15.: Pulse sequence to generate and probe a coherent superposition in the $D_{5/2}$ state between the sub-levels with $m = -1/2$ and $m = +1/2$. The corresponding level scheme is shown in Figure 6.14.

Figure 6.16 shows the resulting oscillation of the $D_{5/2}$ population as a function of ϕ . The observation of such an interference signal proves that the phase information of the superposition in the $D_{5/2}$ level persists for the time t_{wait} . However, the visibility of about 87% is significantly lower than the maximum visibility of the Ramsey fringes from Section 6.2.2. The dependence of the contrast on the time for which the superposition is kept in $D_{5/2}$ is rather flat for small values of t_{wait} ($\leq 100 \mu\text{s}$) as it can be seen in Figure 6.17. It is therefore unlikely that the low fringe contrast is mainly influenced by phase-noise induced decoherence. Systematic errors in the individual pulses of the sequence are much more probable to be the main reason for the discrepancy. An offset of the center line of the fringes in Figure 6.16 substantiates the suspicion

⁵The different duration is due to the difference in transition strength and polarization coupling.

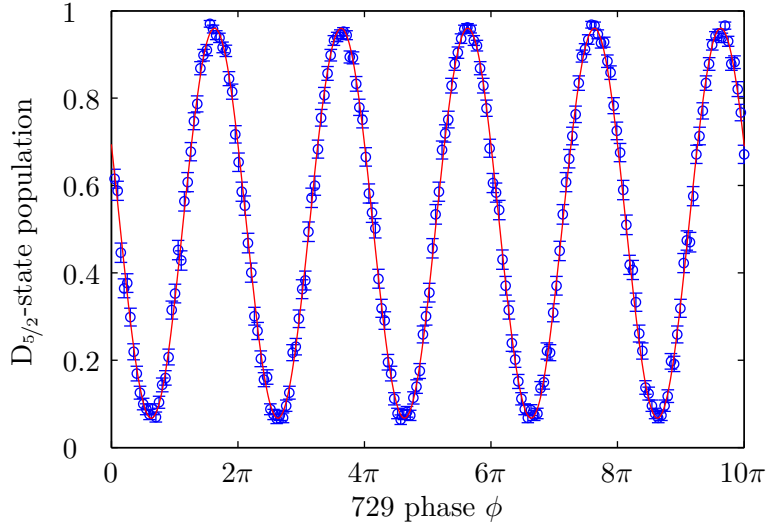


Figure 6.16.: Interference signal when scanning the phase of the last $\frac{\pi}{2}$ -pulse after the transfer and retrieval of a coherent superposition to and from the $D_{5/2}$ state for a waiting time of $t_{\text{wait}} = 1 \mu\text{s}$. The red curve is a sinusoidal fit corresponding to a visibility of 86.9(3)%. Furthermore, the fit reveals a center line of the observed interference signal of 0.514(1) ($D_{5/2}$ population), significantly higher than the expected value of 0.5.

of systematic errors. The error is most likely caused by a synchronization problem between the AOM that switches the frequency and the AOM that switches the amplitude of the 729 nm laser. To create the coherent superposition in the shortest possible time of $5.45 \mu\text{s}$, the delay between the frequency- and amplitude-switching for the first π - and second $\frac{\pi}{2}$ -pulse was set to 25 ns. A delay between both AOMs due to a slow response time of the frequency switching would then lead to an effective increase of the pulse area of the first $\frac{\pi}{2}$ -pulse at the cost of a corresponding decrease of pulse length of the second $\frac{\pi}{2}$ -pulse. This would then cause a shift of the center line of the fringes to higher values for the population. The pulse lengths of the π -pulses would change correspondingly but the impact for the experiment would be negligible due to the small temporal derivative of the population change. For future experiments which rely on high-fidelity state preparation, the delay between both AOMs has to be carefully characterized and compensated⁶.

In the experiment, the same two laser pulses are used to create and to subsequently retrieve and probe the coherent superposition. Assuming that the impact of the possible timing imperfections onto the fidelity of both processes is identical, an estimate for the purity of the created superposition state is obtained by $\sqrt{\mathcal{V}} \approx 93\%$, where \mathcal{V} is the visibility of the measured interference signal.

Figure 6.17 shows the dependence of the fringe visibility on the time that the superposition is kept in the $D_{5/2}$ level. As in Section 6.2.2, the observed decay is used to classify the decoherence of the superposition state. But this time the sequence is not triggered to the power line, giving

⁶While writing the thesis, my coworkers have in fact identified a delay of ~ 150 ns of the frequency-switching AOM to be the main reason for the decreased visibility. The problem got solved by delaying the amplitude-switching AOM accordingly.

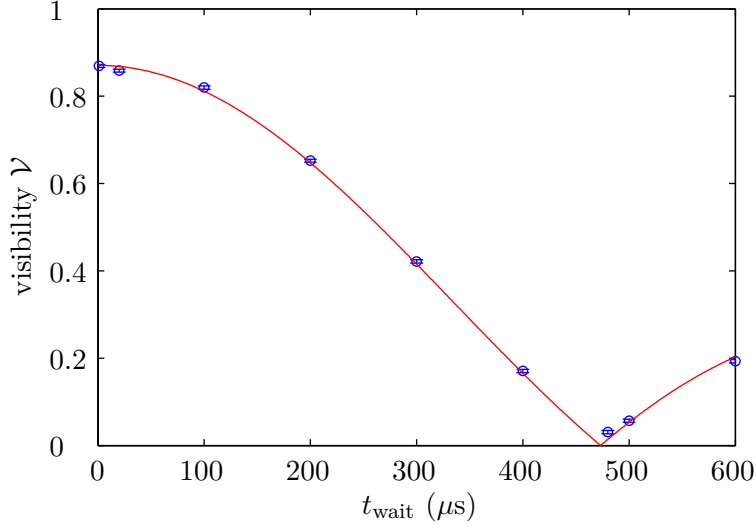


Figure 6.17.: Decay of the visibility of the interference signal depending on the storage time t_{wait} of the coherent superposition. The red curve is a fit by the product of a Gaussian and a zero order Bessel function as given by (A.17). From the fit an RMS amplitude of uncorrelated B-field noise of 0.09(1) mG is obtained and the peak-to-peak amplitude of periodic B-field fluctuations is found to be 0.963(6) mG.

rise to a more complicated dependence of the visibility as explained in more detail in Appendix A.6. From the fit, an effective coherence time of the superposition of

$$T_2^* = 279(9) \mu\text{s}$$

is obtained. In the absence of the presently strong periodic B-field noise, the Gaussian noise contribution will remain as the main limiting process. For that case, the dephasing time $\tau_G = 1.5(2)$ ms from the fit can be taken as a lower bound for the expected effective coherence time of the state (Details in Appendix A.6). An active magnetic-field noise compensation which is currently under construction is therefore expected to yield coherence times significantly above 1 ms.

6.3.3. Outlook

The two levels for the demonstration of a coherent superposition were selected to have good coupling to the laser (fast creation) and small coupling to the magnetic field (slow dephasing) of the final superposition state ($g \cdot \Delta m = 1.2$). But in the current set-up, the used procedure can be applied to create any superposition between $D_{5/2}$ levels that are accessible⁷ from $|S_{1/2}, -1/2\rangle$ (see Figure 6.18), especially the superposition between the levels $|D_{5/2}, -3/2\rangle$ and $|D_{5/2}, +3/2\rangle$ that is required for the scheme discussed in Section 2.3. It is also straightforward to create asymmetric superposition states by replacing the first $\frac{\pi}{2}$ -pulse by a pulse with the corresponding

⁷The limitation arises due to the maximal allowed change of $\Delta m = 2$ on the optical quadrupole transition for a single excitation pulse.

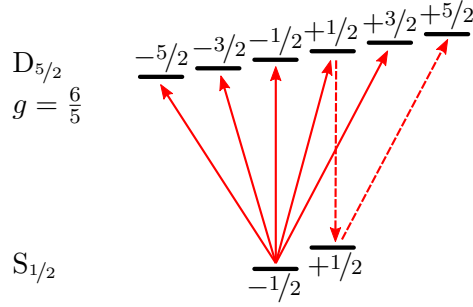


Figure 6.18.: Level scheme for the 729 nm transition in $^{40}\text{Ca}^+$. The magnetic quantum numbers are indicated below and above the respective Zeeman sub-levels. The straight red arrows indicate the $D_{5/2}$ levels that can be used for coherent superpositions when using only two laser pulses. The dashed red arrows indicate two additional π -pulses that are necessary to create a coherent superposition between the outermost Zeeman levels of the $D_{5/2}$ manifold. A direct RF excitation that transfers population between the $S_{1/2}$ sub-levels may alternatively be used. For details see text.

pulse area. To create a coherent superposition between the outermost $D_{5/2}$ levels by using only the 729 laser, two additional π -pulses are necessary as indicated in Figure 6.18.

Direct RF excitation for the creation of coherent superpositions

The more laser pulses are needed to create a superposition, the slower gets the overall experimental sequence and the lower gets the purity of the superposition state. When the ion's motion is only Doppler cooled, the efficiency of a single π -pulse is limited to slightly below 99% (see Section 4.4.4). Assuming a similar efficiency for a single optimal $\frac{\pi}{2}$ -pulse, the maximum purity of a coherent superposition created in $\{|D_{5/2, -5/2}\rangle, |D_{5/2, +5/2}\rangle\}$ by a four-pulse sequence would be limited to around 96%.

A completely different approach is to create first a coherent superposition within the two Zeeman sub-levels of the ground state, with the aid of a radio-frequency (RF) $\frac{\pi}{2}$ -pulse, which is then simply transferred to the outermost $D_{5/2}$ levels with two independent π -pulses of the 729 nm laser. This scheme also serves to create arbitrary superpositions in $D_{5/2}$. As it has been shown in Section 4.4.4, $\frac{\pi}{2}$ -pulse lengths with a direct RF excitation of around $3.4 \mu\text{s}$ are realistic which is quite close to the pulse lengths that are typically used with the laser. Hence this approach is clearly compatible in speed with schemes that only employ pulses from the laser. Additionally, the RF excitation is rather insensitive to the ion's motion due to a very small Lamb-Dicke factor, enabling high-fidelity state manipulations even without sideband cooling. Nevertheless, the purity of the final superposition state will still be limited by the two π -pulses with the laser to something around 98%, which is already better than with the scheme employing only the excitation with optical frequencies.

One drawback when starting to work with the RF excitation toward the end of the thesis was a strong pickup noise on all installed photodiodes in the laboratory. Since the RF excitation was at that time still at a preliminary stage, it was not fully investigated to which extent this noise affected the intensity-stabilization loops especially of the 729 nm laser system. In principle this could result in an additional source of decoherence during the preparation of

coherent superpositions.

Coherence times for arbitrary superpositions in $D_{5/2}$

Even though there is a clear limitation in the quality of the created superposition when using only Doppler cooling, the main limitation at the moment is the effective coherence time of the superposition. For an experiment where single photons are absorbed by the ion, this coherence time limits the maximum available exposure time of the ion to the photon stream before the superposition has to be reinitialized. Further Ramsey experiments on the $S_{1/2}$ - $D_{5/2}$ transition with superposition states that have different magnetic-field dependencies have shown that the measured decoherence rate is proportional to the overall B-field sensitivity $g' = g \cdot \Delta m$ of the superposition⁸. The determined coherence time in this section ($T_2^* \approx 280 \mu\text{s}$ for $g' = 1.2$) can therefore be extrapolated to the expected coherence time of any other superposition in $D_{5/2}$. The entanglement-transfer scheme presented in Section 2.3 requires a coherent superposition between the $m = -3/2$ and $m = +3/2$ levels. The effective sensitivity to the B-field is $g' = 3.6$, which leads to an expected dephasing time of $T_2^* \approx 93 \mu\text{s}$. Even shorter maximal exposure times of an ion for state transfer by single-photon absorption are expected for a scheme using the superposition between the outermost Zeeman sub-levels. Here, the effective B-field sensitivity is $g' = 6$, corresponding to an expected value of $T_2^* \approx 56 \mu\text{s}$.

Duty cycles in state-transfer experiments

In experiments aiming at the state transfer from photons to a single ion, the ion will be sequentially prepared in a coherent superposition in $D_{5/2}$, waiting for an absorption and subsequent detection of the heralding photon (see Section 2.3). This waiting time will be maximally limited by the coherence time T_2^* of the superposition state as characterized in this chapter⁹. After the superposition has dephased, it has to be reinitialized in the ground-state with a laser pulse at 854 nm. This is typically achieved in less than $1 \mu\text{s}$. Since the overall success probability for photon absorption and detection of the herald is very low (Sections 3.2 and 3.3), nothing will happen for most of the time which is why the Doppler cooling can be reduced to a minimum of about $10 \mu\text{s}$. The experiments from this section further suggest that a time of $15 \mu\text{s}$ is a realistic value for the creation of an arbitrary coherent superposition in $D_{5/2}$ (including optical pumping for the initialization in $|S_{1/2}, -1/2\rangle$). The state detection plus state rotations for measurements in different bases will only be executed conditioned on the detection of the herald; their impact on the overall sequence length is therefore negligible. Summing up all of these timings, we end up with a minimum time of $T_{\text{init}} = 26 \mu\text{s}$ that it takes to reinitialize the coherent superposition. We define the duty cycle in a state-transfer experiment as the total fraction of time P_{duty} that the ion is able to absorb a photon in a coherent manner:

$$P_{\text{duty}} = \frac{T_2^*}{T_{\text{init}} + T_2^*} . \quad (6.21)$$

⁸For a negligible influence of the laser and no other sources of decoherence, this is of course expected.

⁹Note that for state-transfer experiments aiming at high fidelities, the waiting time should be kept significantly below T_2^* since this time scale would already correspond to a reduction of the coherence in the superposition to $1/e \approx 37\%$.

For the single-photon absorption experiments from Section 3.1 this duty cycle was 85 %, given by the ratio of slits in the chopper of the photon-pair source. Especially when fighting with overall low efficiencies for the absorption and detection processes, the duty cycle should ideally approach 100 %. With the above estimated coherence times for superpositions between $\{|D_{5/2}, -3/2\rangle, |D_{5/2}, +3/2\rangle\}$ and $\{|D_{5/2}, -5/2\rangle, |D_{5/2}, +5/2\rangle\}$ we expect duty cycles of 78 % and 68 %, respectively. However, these experiments would not yield high fidelities in the mapping process since the superposition would experience a significant amount of decoherence for a waiting time of T_2^* . Reducing the waiting time by a factor of 0.2 and thereby staying in the almost flat region for the loss of coherence in Figure 6.17 would result in duty cycles of only 42 % and 30 % for the two discussed scenarios. These numbers nicely illustrate how essential it will be to achieve a fast initialization of the coherent superposition in the $D_{5/2}$ state. At the same time, an improvement of the B-field stability by an active servo loop will be indispensable to reach duty cycles above 90 %.

7. Conclusions

7.1. Summary

This thesis has been carried out on a highly versatile experimental set-up, designed to study basic principles for quantum-networking operations with single trapped ions and single photons. As a special component, the set-up includes an entangled photon-pair source which extends the range of possible experiments to studies of hybrid network scenarios and fundamental quantum-optics experiments with a heralded single-photon source. The work was started as a second generation PhD student (the only one), right after the completion of the overall experimental set-up and the realization of first experiments. The main objective of the thesis was to advance the experimental set-up to a level which would allow the coherent transfer of a photonic qubit (originating from the entangled photon-pair source) to a qubit encoded in the electronic levels of a single $^{40}\text{Ca}^+$ ion.

The main achievements of the thesis are threefold. First, the existing experimental set-up was used to demonstrate a fundamental quantum-optics experiment, being the controlled interaction of single entangled photons from the photon-pair source with a single trapped ion. These measurements represent the most sophisticated type of experiment that was possible with the collective hybrid set-up in its old configuration. Then, after dismantling the whole experiment, relocating it, and re-building it in a new lab, the main focus of the work was the completion of the ion-trap apparatus by the implementation of coherent manipulations. This was the last missing principal component in the overall system to enable the study of different quantum-network scenarios. Furthermore, the single-photon coupling efficiencies from optical fibers to single ions and from single ions to detectors in the set-up were optimized and characterized in detail.

The experiments for the interaction of entangled photons from the photon-pair source with a single ion (Section 3.1) made use of the time correlation of the photon pairs to herald the absorption process as demonstrated in earlier experiments with the set-up. The results are published in [131]. As a major extension, the ion was prepared as a polarization-selective absorber in the three principal polarization bases, revealing that the polarization entanglement of the photon pairs is manifested in the measured absorption-herald correlations. This fulfills a necessary requirement for transferring the photonic entanglement to the ion. The measurements were extended to perform a full tomography of the quantum state of the photon pairs by using a single trapped ion as a polarization analyzer at the single-photon level. The reconstructed density matrix shows an excellent agreement with the known Bell singlet state of the photon pairs. The measurements represent for the first time the controlled interaction of *entangled* photons from an SPDC photon-pair source with a single ion and demonstrate a new level of control in this kind of hybrid quantum-optics experiment. They are an important step of the overall experimental set-up toward implementing entanglement-transfer schemes from photon pairs to distant absorbers, necessary for quantum-network studies.

After the relocation of the whole experiment, a single trapped ion was used to implement a single-photon source, generating photons at 393 nm (Section 3.2). A characterization of the source showed negligible multi-photon emissions, making it a highly precise tool to measure the detection efficiency of single emitted 393 nm photons. This is an important experimental quantity as these photons are produced as single heralds in state-transfer schemes from a single photon to a single ion (Section 2.3). When taking advantage of the directionality of circularly polarized photons on a dipole transition as they are generated in the presented state-transfer scheme, we found a maximum detection efficiency with the set-up of 1.6 %. The corresponding detection efficiency for arbitrary polarized photons is 1.1 %. The characterization of the detection efficiencies formed part of a general demonstration of a single-photon source which produced tunable photons with a single frequency in a pure polarization state, another important tool for the study of quantum network schemes. These aspects of the experiments will be discussed in another PhD thesis. The results are published in [128].

While featuring high detection efficiencies in the UV, the set-up offers at the same time high coupling efficiencies from single photons to a single ion in the IR at 854 nm. The absorption efficiency of these photons was measured with a calibrated stream of laser photons and a quantum-jump scheme for absorption detection as utilized in the interaction experiments with the photon-pair source. For linearly polarized photons incident on the main magnetic-field axis, we found an overall coupling and absorption probability of 5×10^{-4} in one ion trap and 6×10^{-4} in the second ion trap. These values are in good agreement with the independently determined coupling efficiency of 3 % and the estimated transition probability for the atom.

In the context of single-photon single-ion interaction we have performed two experiments demonstrating the controlled heralded interaction of two distantly trapped ions by the exchange of single photons at 393 nm and 854 nm. The results of the latter are published in [130]. Both experiments were not subject of this work and will be documented in another PhD thesis.

To provide the ability for coherent manipulations of the electronic state of single ions in both ion traps, the thesis documented the setup of an ultra-stable narrow-bandwidth laser system at 729 nm (Chapter 4). The spectral linewidth was found to be below 32 Hz, theoretically allowing for successive coherent manipulations over the time scale of at least 5 ms. The long-term stability is only limited by a constant slow drift of the reference cavity caused by material aging. Basic experiments such as pulsed spectroscopy on the optical quadrupole transition, and the discrimination between both Zeeman sub-levels of the atomic ground-state by electron shelving (with around 99 % efficiency), have demonstrated the controlled operation and usability of the system.

After optimizing the Doppler-cooling process by the aid of temperature measurements with the narrow-bandwidth laser (Chapter 5), the system was used to demonstrate basic coherent manipulations in an atomic two-level system (Chapter 6). Employing a third atomic level as auxiliary state further allowed the illustration of the dynamics of the probability amplitude of an atomic state when being coherently coupled with a resonant light field. The agreement with the given simple theoretical description further proved the potential of the installed laser system to carry out arbitrary rotations of electronic superposition states. This is, together with electron shelving, the essential requisite for state discrimination in different measurement bases as it is required for the tomographic reconstruction of atomic qubit states, one key technology when studying principle quantum-network scenarios.

Finally, coherent manipulations were utilized to show the general preparation and charac-

terization of a coherent superposition within the metastable $D_{5/2}$ state. The coherence of the superposition state was found to be significantly affected by magnetic-field noise at the position of the ion. Hence, the initialization of coherent superpositions in very short times was identified as a crucial requirement to reach high duty cycles in an experiment for the state mapping from a single photon to an ion. The performed measurements showed that total preparation times of a superposition in less than $15 \mu\text{s}$ are possible with the set-up. The maximal possible duty cycle for an experiment aiming at the state-transfer from a photon to a single ion as presented in Section 2.3 is thereby expected to be around 40 % with the present level of magnetic-field noise.

7.2. Outlook

The derived efficiencies allow one to estimate the success probability of arbitrary state-transfer schemes with the set-up. In particular, for the scheme discussed in this thesis (Section 2.3) it is now possible to derive a realistic estimate about the overall efficiency. Let us assume that the goal is to have a minimum rate of successful transfers of 1 min^{-1} . The measurements with the heralded single-photon source have shown that this is at the edge of what is possible to obtain sufficient statistics over a measurement time of a few weeks. The total success probability of a state transfer from an 854 nm photon to an ion is calculated as follows: 3 % coupling efficiency from the fiber output to the ion, 2.4 % absorption probability given by the oscillator strength (6 %) and the squared Clebsch-Gordan coefficient for the transition (40 %) (Appendix A.1), 93.5 % branching fraction from $P_{3/2}$ to $S_{1/2}$, 33 % emission probability for a σ -polarized heralding photon at 393 nm (Appendix A.1), and 1.6 % detection probability of the herald, resulting in an overall success probability of 3.6×10^{-6} . Taking in addition the previously discussed duty cycle of 40 % into account, this corresponds to a minimum required rate of around 1.2×10^4 fiber-coupled photons per second. When aiming at the entanglement transfer from a photon-pair to a photon-ion pair with the available photon-pair source, the splitting probability of a photon pair in the source (50 %), the combined coupling and detection probability of photons in the filter arm (7 %), and the fiber-coupling efficiency of photons to the ion (54 %) have to be taken additionally into account. The required rate of produced photon-pairs in the source that are within the spectral bandwidth of the atomic transition amounts then to $6.2 \times 10^5 \text{ s}^{-1}$ which is almost two orders of magnitude above the currently estimated brightness of the source ($\sim 10^4$ resonant pairs/s after the crystal). To tackle this problem the photon-pair source got recently equipped with a longer down-conversion crystal featuring an optical wave guide. Even though this technology is still at an early stage and the available devices are challenging to operate, successfully working systems in other groups have shown that the required gain of brightness by at least two orders of magnitude should be possible with our device.

Concerning the ion-trap apparatus, the biggest challenge for the near future will be to efficiently suppress magnetic-field noise in the traps. The best performance would certainly be achieved by enclosing the whole set-up with a mu-metal shielding. But given the size of the double-trap system this approach would be highly costly and impractical. At the moment, the pursued strategy is to implement an active magnetic-field stabilization. Since the current set-up does not permit to place a magnetic-field sensor in the close proximity of the ions, a set of well positioned sensors outside of the vacuum chambers has to be used to deduce the

field at the position of each ion. This will certainly be a big effort, but preliminary tests have shown that it should be possible to reduce the present field fluctuations by at least one order of magnitude. This would result in the corresponding gain of one order of magnitude in the dephasing time for coherent superpositions, thereby enabling state-transfer experiments with duty cycles above 80%.

But even without an improvement of the magnetic-field stability, the results in this thesis have shown that the state transfer from photons to a single ion is in principle possible with the available tools. In fact, while writing this thesis report, my co-workers have already succeeded in measuring the transfer and storage of arbitrary polarization states of laser photons in the electronic ground state of a single ion. The scheme that they used is only a slight modification of the one that was discussed in Section 2.3. These measurements demonstrate for the first time the *heralded* transfer of a photonic qubit to a single atom and are of fundamental interest for future quantum-network implementations. It is now only a matter of time to extend the measurements to the single-photon regime and to demonstrate the long proposed transfer of entanglement from a photon pair to an ion-photon pair with the set-up.



Figure 7.1.: Picture of combined experimental set-up (ion traps + photon source) at its last day at ICFO (03/09/2010). Three optical tables and four heavy wooden boxes are missing on the picture.



Figure 7.2.: Picture of trap table at the first day of the rebuilding phase in Saarbrücken (09/09/2010), trying a new sustainable ultra-stable mounting option for breadboards. A picture of the table after finishing the reconstruction is given in Figure 1.6.

A. Appendix

A.1. List of Clebsch-Gordan coefficients

The following tables list the Clebsch-Gordan coefficients $\Lambda_{m,m'}$ for the $S_{1/2}$ - $D_{5/2}$, $D_{5/2}$ - $P_{3/2}$, and $P_{3/2}$ - $S_{1/2}$ transitions.

m	$\pm 1/2$	$\pm 1/2$	$\pm 1/2$	$\pm 1/2$	$\pm 1/2$
m'	$\pm 5/2$	$\pm 3/2$	$\pm 1/2$	$\mp 1/2$	$\mp 3/2$
$\Lambda_{m,m'}$	1	$\sqrt{\frac{4}{5}}$	$\sqrt{\frac{3}{5}}$	$\sqrt{\frac{2}{5}}$	$\sqrt{\frac{1}{5}}$

Table A.1.: Clebsch-Gordan coefficients $\Lambda_{m,m'}$ for the quadrupole-allowed $S_{1/2}$ - $D_{5/2}$ transition. m and m' indicate the magnetic quantum numbers of the Zeeman sub-levels of $S_{1/2}$ and $D_{5/2}$, respectively. The values are taken from [82].

m	$\pm 5/2$	$\pm 3/2$	$\pm 3/2$	$\pm 1/2$	$\pm 1/2$	$\pm 1/2$
m'	$\pm 3/2$	$\pm 3/2$	$\pm 1/2$	$\pm 3/2$	$\pm 1/2$	$\mp 1/2$
$\Lambda_{m,m'}$	$\sqrt{\frac{10}{15}}$	$-\sqrt{\frac{4}{15}}$	$\sqrt{\frac{6}{15}}$	$\sqrt{\frac{1}{15}}$	$-\sqrt{\frac{6}{15}}$	$\sqrt{\frac{3}{15}}$

Table A.2.: Clebsch-Gordan coefficients $\Lambda_{m,m'}$ for the dipole-allowed $D_{5/2}$ - $P_{3/2}$ transition. m and m' indicate the magnetic quantum numbers of the Zeeman sub-levels of $D_{5/2}$ and $P_{3/2}$, respectively. The values are taken from [159].

m	$\pm 3/2$	$\pm 1/2$	$\pm 1/2$
m'	$\pm 1/2$	$\pm 1/2$	$\mp 1/2$
$\Lambda_{m,m'}$	1	$\sqrt{\frac{2}{3}}$	$\sqrt{\frac{1}{3}}$

Table A.3.: Clebsch-Gordan coefficients $\Lambda_{m,m'}$ for the dipole-allowed $P_{3/2}$ - $S_{1/2}$ transition. m and m' indicate the magnetic quantum numbers of the Zeeman sub-levels of $P_{3/2}$ and $S_{1/2}$, respectively. The values are taken from [159].

A.2. Dipole emission and absorption characteristic

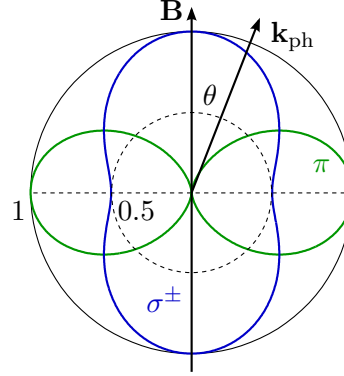


Figure A.1.: Angular dependence of photon emission on an electronic dipole transition. Plotted is the relative probability per time unit as a dependence of the angle θ between the main magnetic field \mathbf{B} and the wave vector \mathbf{k}_{ph} of the emitted photon. The emission characteristic obeys full rotational symmetry around the B-field axis. The same picture is valid for the case of photon absorption.

The angular dependence of the relative probability for photon emission or absorption on an electronic dipole transition has a characteristic shape, depending on the photon polarization. Figure A.1 illustrates this emission (absorption) characteristic for the three possible photon polarizations π and σ^\pm (in the reference frame of the atom). The emission (absorption) probability per time unit of a π -polarized photon into (from) the solid angle Ω is characterized by

$$dR_\pi \propto \sin^2(\theta) d\Omega , \quad (\text{A.1})$$

the characteristic for σ^\pm -polarized photons obeys the proportionality

$$dR_\sigma \propto \frac{1}{2}(1 + \cos^2(\theta)) d\Omega . \quad (\text{A.2})$$

The sum over all three contributions leads to an isotropic distribution. A detailed description is found, for example, in [160].

For the measurements described in Section 3.1.5, only photons exciting σ transitions ($\Delta m = \pm 1$) are of interest. When changing from a configuration with $\mathbf{k}_{\text{ph}} \parallel \mathbf{B}$ to $\mathbf{k}_{\text{ph}} \perp \mathbf{B}$, a reduction of the absorption probability per time unit by a factor of 1/2 is expected.

A.3. Likelihood function for the tomographic reconstruction

The tomographic measurements from Section 3.1.6 are suffering from very low statistics and a rather high background. The reconstruction of the density matrix via a maximum-likelihood estimate as proposed in [122] is therefore better achieved with a different likelihood function than the one given in the paper, which is only valid for the limiting case of high counting statistics with negligible backgrounds.

The general idea of the maximum likelihood approach for the reconstruction is to maximize the probability $P(n_1, \dots, n_{16})$, that a guessed density matrix ρ_g produces the set of measured data $\{n_1, \dots, n_{16}\}$. The number of events that is expected in a certain measurement is

$$n_{\nu,g} = \mathcal{N} \langle \psi_\nu | \rho_g | \psi_\nu \rangle \quad (\text{A.3})$$

where \mathcal{N} is a known scaling factor and $|\psi_\nu\rangle$ is a four component vector, defining the measurement-basis combination for both components of the two-qubit state. In our experiments, the measurement outcomes n_ν caused by a certain two-photon state are in principle the net coincidences, after background subtraction. But since the subtraction of the backgrounds $n_{\text{bg},\nu}$ has a significant influence on the uncertainty of the derived value n_ν , it is better to take the measured backgrounds into account and to describe the expected total number of coincidences in a certain measurement as

$$N_{\nu,g} = \mathcal{N} \langle \psi_\nu | \rho_g | \psi_\nu \rangle + n_{\text{bg},\nu} . \quad (\text{A.4})$$

Assuming Poissonian counting statistics, the overall probability that ρ_g produces the measured set of total coincidences $\{N_1, \dots, N_{16}\}$ with $N_\nu = n_\nu + n_{\text{bg},\nu}$ is

$$P(N_1, \dots, N_{16}) \propto \prod_{\nu=1}^{16} \frac{N_{\nu,g}^{N_\nu} e^{-N_{\nu,g}}}{N_\nu!} , \quad (\text{A.5})$$

neglecting a normalization constant. Numerically searching for the maximum of this function with the *Mathematica* function `FindMaximum` is rather slow which is inconvenient, especially for the error analysis. An almost twenty-fold improvement in speed is achieved when searching for the maximum of the logarithm of (A.5). Therefore, the likelihood function

$$\mathcal{L}(\rho_g) = \sum_{\nu=1}^{16} \ln(\mathcal{N} \langle \psi_\nu | \rho_g | \psi_\nu \rangle + n_{\text{bg},\nu}) \cdot N_\nu - (\mathcal{N} \langle \psi_\nu | \rho_g | \psi_\nu \rangle + n_{\text{bg},\nu}) - \ln(N_\nu!) \quad (\text{A.6})$$

is used for the reconstruction of ρ in the experiments discussed in Section 3.1.6. Further details about the analytical structure of ρ_g and the general method are found in [122].

A.4. Correlation coefficient

The correlation coefficient (also called product-moment coefficient of correlation) is a measure for the resemblance of a correlation between two variables X and Y to a linear dependence. It is defined as [161]

$$r(X, Y) = \frac{\sum (x_i - \bar{x})(y_i - \bar{y})}{\sqrt{\sum (x_i - \bar{x})^2} \sqrt{\sum (y_i - \bar{y})^2}} \quad (\text{A.7})$$

with \bar{x} and \bar{y} being the arithmetic mean of both data sets. The possible values for r are ranging from $r = 0$ for a complete absence of linear correlation to $|r| = 1$ for a perfect linear dependence.

A.5. Measurement of $D_{5/2}$ population

In the experiments involving the 729 nm laser, a certain $D_{5/2}$ population is usually probed by repeating the preparation with the same laser pulses and subsequent state detection n times and counting the number k of successful transfers. The following gives a summary of how the parameters n and k are connected to the expectation value of the probability p for excitation to $D_{5/2}$.

The probability to measure k transfers is described by the binomial distribution

$$\rho(k|p) = \binom{n}{k} p^k (1-p)^{n-k}, \quad (\text{A.8})$$

under the condition that the probability p is a well known parameter. What is required to deduce p from a set of n measurements, is the continuous probability density $\rho(p|k)$ that describes the probability of a value p under the condition that n measurements have been performed with k successful transfers. With the Bayesian probability theory, this distribution can be calculated as [161]

$$\rho(p|k) = \frac{\rho(k|p)\rho(p)}{N} \quad (\text{A.9})$$

with $\rho(p)$ being the unconditioned (prior) probability distribution, and N being a normalization constant. Under the assumption that $\rho(p)$ is a uniform distribution (no measurement has been performed yet), the expectation value of p and its uncertainty are derived as

$$\bar{p} = \frac{k+1}{n+2} \quad (\text{A.10})$$

and

$$s_{\bar{p}} = \sqrt{\frac{(n-k+1)(k+1)}{(3+n)(2+n)^2}}. \quad (\text{A.11})$$

A detailed discussion and derivation will be given in [146].

A.6. Decoherence in the presence of periodic magnetic-field noise

The presence of periodic magnetic-field fluctuations in a Ramsey experiment strongly alters the Gaussian dependence of the decoherence on the waiting time between the two Ramsey pulses as given in Section 6.2.2. This effect has been observed and used in several sophisticated experiments to probe and characterize the noise properties in an ion-trap experiment, as described in [162, 163]. To explain the effects in the experiment presented in Section 6.3.2, it is sufficient to assume a periodic B-field fluctuation with a single frequency component at the power-line frequency of 50 Hz. In the following, the derivation of the functional dependence will be briefly sketched, a more detailed derivation and analysis of measurements characterizing the exact B-field noise in our experiment will be given in a future thesis.

While a completely uncorrelated noise source is described by a Gaussian density function, the probability density function $\rho(B)$ of a sinusoidal B-field modulation as $B(t) = B_1 \sin(\omega t) + B_0$ has a pronounced bimodal shape [164] with maxima at the minimum and maximum B-field amplitudes $B_{\min} = B_0 - B_1$ and $B_{\max} = B_0 + B_1$:

$$\rho_{\text{sine}}(B) = \frac{1}{\pi} \frac{1}{\sqrt{B_1^2 - (B - B_0)^2}} . \quad (\text{A.12})$$

For a Ramsey experiment that is performed at random times with respect to the phase of the periodic B-field noise, this means that B_{\min} and B_{\max} are more likely to be observed. With (A.12), the probability density for the accumulated phase α after the waiting time t_{wait} is derived to

$$\rho_{\alpha, \text{sine}}(t_{\text{wait}}) = \frac{1}{\pi t_{\text{wait}}} \frac{1}{\sqrt{\alpha_1^2 - \left(\frac{\alpha}{t_{\text{wait}}}\right)^2}} \quad (\text{A.13})$$

with $\alpha_1 = 2\pi g \Delta m \frac{\mu_B}{h} B_1$. The phase offset arising due to B_0 in (A.12) has been set to 0. In absence of phase noise, the excited-state population after a Ramsey experiment with the second pulse having the phase ϕ is given by $p_D = \frac{1}{2}(1 + \cos(\phi))$. In the presence of phase noise with a certain probability density distribution $\rho_{\alpha}(t_{\text{wait}})$, p_D is obtained as

$$p_D(t_{\text{wait}}) = \int_{-\infty}^{+\infty} \frac{1}{2}(1 + \cos(\phi + \alpha))\rho_{\alpha}(t_{\text{wait}})d\alpha \quad (\text{A.14})$$

$$= \frac{1}{2} + \frac{\cos(\phi)}{2} \underbrace{\int_{-\infty}^{+\infty} \cos(\alpha)\rho_{\alpha}(t_{\text{wait}})d\alpha}_{:=\mathcal{V}(t_{\text{wait}})} - \frac{\sin(\phi)}{2} \underbrace{\int_{-\infty}^{+\infty} \sin(\alpha)\rho_{\alpha}(t_{\text{wait}})d\alpha}_{=0} , \quad (\text{A.15})$$

where the $\sin(\phi)$ term is set to 0 because it has been assumed that $\rho_{\alpha}(t_{\text{wait}})$ is a symmetric distribution. For a periodic phase fluctuation with $\rho_{\alpha}(t_{\text{wait}})$ as given by (A.13), the visibility contained in (A.15) is calculated as

$$\mathcal{V}(t_{\text{wait}}) = J_0(\alpha_1 t_{\text{wait}}) , \quad (\text{A.16})$$

where J_0 is the 0th order Bessel function of the first kind.

In the presence of an additional uncorrelated noise component in the form of Gaussian white noise as explained in Section 6.2.2, the resulting $\rho_\alpha^*(t_{\text{wait}})$ is the convolution of the probability density distributions of the individual noise processes. As the visibility in (A.15) is then the integral over the convoluted probability density distribution for the phase, the resulting dependence of the visibility is just the product of the individual dependencies:

$$\mathcal{V}^*(t_{\text{wait}}) = V_0 \exp\left(-\frac{t_{\text{wait}}^2}{\tau_G^2}\right) J_0\left(1.752 \cdot \frac{t_{\text{wait}}}{\tau_S}\right). \quad (\text{A.17})$$

V_0 accounts for a non-unity contrast for $t_{\text{wait}} = 0$ caused by experimental imperfections, τ_G and τ_S will be explained in a moment. In the literature, the coherence time of a system which is affected by Gaussian phase noise is usually specified by the $1/e$ decay time of the fringe visibility in a Ramsey experiment [158]. τ_G is therefore a measure for the expected coherence time of the system in absence of the single-frequency periodic noise. In analogy, we define τ_S as the time at which the amplitude of the Bessel-function component in the visibility is decreased to a value of $1/e$ ($J_0(1.752) \approx 1/e$). In an experiment which happens at random times with respect to the periodic noise component, we define a net coherence time T_2^* as the inverse of the overall decoherence rate which is obtained by summing the two individual decoherence rates $\frac{1}{\tau_G}$ and $\frac{1}{\tau_S}$:

$$T_2^* = \frac{1}{\frac{1}{\tau_G} + \frac{1}{\tau_S}}. \quad (\text{A.18})$$

Owing to the completely different nature of both involved decoherence processes, this parameter should be rather considered as a practical approximate measure for the experimentally relevant coherence time than for the coherence of the atomic state.

Bibliography

- [1] D. Deutsch. Quantum theory, the church-turing principle and the universal quantum computer. *Proc. R. Soc. Lond. A*, 400:97–117, 1985.
- [2] D. Deutsch. Quantum computational networks. *Proc. R. Soc. Lond. A*, 425:73–90, 1989.
- [3] W. Neuhauser, M. Hohenstatt, P. E. Toschek, and H. Dehmelt. Localized visible $ba+$ mono-ion oscillator. *Phys. Rev. A*, 22(3):1137–1140, Sep 1980.
- [4] M. Brune, F. Schmidt-Kaler, A. Maali, J. Dreyer, E. Hagley, J. M. Raimond, and S. Haroche. Quantum rabi oscillation: A direct test of field quantization in a cavity. *Phys. Rev. Lett.*, 76(11):1800–1803, Mar 1996.
- [5] L. Grover. A fast quantum mechanical algorithm for database search. *Proc. 28th Annual ACM Symposium on the Theory of Computing*, page 212, 1996.
- [6] *Algorithms for Quantum Computation: Discrete Logarithms and Factoring*, 35th Annual Symposium on Foundations of Computer Science. IEEE Computer Society Press, 1994.
- [7] T. Sleator and H. Weinfurter. Realizable universal quantum logic gates. *Phys. Rev. Lett.*, 74:4087–4090, May 1995.
- [8] S. M. Barnett. *Quantum Information*. Oxford master series in atomic, optical, and laser physics. Oxford University Press, 2009.
- [9] P. Schindler, D. Nigg, T. Monz, J. T. Barreiro, E. Martinez, S. X. Wang, S. Quint, M. F. Brandl, V. Nebendahl, C. F. Roos, M. Chwalla, M. Hennrich, and R. Blatt. A quantum information processor with trapped ions. *arXiv*, (1308.3096), 2013.
- [10] H.-J. Briegel, T. Calarco, D. Jaksch, J. I. Cirac, and P. Zoller. Quantum computing with neutral atoms. *Journal of Modern Optics*, 200.
- [11] J. I. Cirac and P. Zoller. A scalable quantum computer with ions in an array of microtraps. *Nature*, 404:579–581, 200.
- [12] B. E. Kane. A silicon-based nuclear spin quantum computer. *Nature*, 393:133–137, 1998.
- [13] L. M. K. Vandersypen, M. Steffen, G. Breyta, C. S. Yannoni, M. H. Sherwood, and I. L. Chuang. Experimental realization of shor’s factoring algorithm using nuclear magnetic resonance. *Nature*, 414:883–887, 2001.
- [14] Y. Makhlin, G. Schön, and A. Shnirman. Quantum-state engineering with josephson-junction devices. *Rev. Mod. Phys.*, 73(2):357–400, May 2001.

- [15] R. Hanson, L. P. Kouwenhoven, J. R. Petta, S. Tarucha, and L. M. K. Vandersypen. Spins in few-electron quantum dots. *Reviews of Modern Physics*, 79(4):1217, 2007.
- [16] E. Knill, R. Laflamme, and G. J. Milburn. A scheme for efficient quantum computation with linear optics. *Nature*, 409:46–52, 2001.
- [17] D. Leibfried, B. DeMarco, V. Meyer, D. Lucas, M. Barrett, J. Britton, W. M. Itano, B. Jelenkovic, C. Langer, T. Rosenband, and D. Wineland. Experimental demonstration of a robust high-fidelity geometric two ion-qubit phase gate. *Nature*, 422:412–415, 2003.
- [18] J. Benhelm, G. Kirchmair, C. F. Roos, and R. Blatt. Towards fault-tolerant quantum computing with trapped ions. *Nature Physics*, 4:463–466, 2008.
- [19] R. Blatt and D. Wineland. Entangled states of trapped atomic ions. *Nature*, 453, June 2008.
- [20] J.J. Bollinger, D.J. Heizen, W.M. Itano, S.L. Gilbert, and D.J. Wineland. A 303-mhz frequency standard based on trapped be+ ions. *IEEE Transactions on Instrumentation and Measurement*, 40(2):126–128, Apr 1991.
- [21] C. Langer, R. Ozeri, J. D. Jost, J. Chiaverini, B. DeMarco, A. Ben-Kish, R. B. Blakestad, J. Britton, D. B. Hume, W. M. Itano, D. Leibfried, R. Reichle, T. Rosenband, T. Schaetz, P. O. Schmidt, and D. J. Wineland. Long-lived qubit memory using atomic ions. *Phys. Rev. Lett.*, 95:060502, Aug 2005.
- [22] S. Gulde, M. Riebe, G. Lancaster, C. Becher, J. Eschner, H. Häffner, F. Schmidt-Kaler, I. L. Chuang, and R. Blatt. Implementation of the deutsch-jozscha algorithm on an ion-trap quantum computer. *Nature*, 421:48–50, 2003.
- [23] M. Barrett, J. Chiaverini, T. Schaetz, J. Britton, W. M. Itano, J. D. Jost, E. Knill, C. Langer, D. Leibfried, R. Ozeri, and D. J. Wineland. Deterministic quantum teleportation of atomic qubits. *Nature*, 429:737–739, 2004.
- [24] M. Riebe, H. Häffner, C. F. Roos, W. Hänsel, J. Benhelm, G. Lancaster, T. Körber, C. Becher, F. Schmidt-Kaler, D.F.V. James, and R. Blatt. Deterministic quantum teleportation with atoms. *Nature*, 429:734–737, 2004.
- [25] J. Chiaverini, D. Leibfried, T. Schaetz, M. Barrett, E. B. Blakestad, J. Britton, W. M. Itano, J. D. Jost, E. Knill, C. Langer, R. Ozeri, and D. J. Wineland. Realization of quantum error correction. *Nature*, 432:602–605, 2004.
- [26] P. Schindler, J. T. Barreiro, T. Monz, V. Nebendahl, D. Nigg, M. Chwalla, M. Hennrich, and R. Blatt. Experimental repetitive quantum error correction. *Science*, 332:1059, 2011.
- [27] D. Hanneke, J. P. Home, J. D. Jost, J. M. Amini, D. Leibfried, and D. J. Wineland. Realization of a programmable two-qubit quantum processor. *Nature Physics*, 6:13–16, 2009.

-
- [28] J. Chiaverini, J. Britton, D. Leibfried, E. Knill, M. D. Barrett, R. B. Blakestad, W. M. Itano, J. D. Jost, C. Langer, R. Ozeri, T. Schaetz, and D. J. Wineland. Implementation of the semiclassical quantum fourier transform in a scalable system. *Science*, 308(5724):997–1000, 2005.
- [29] R. Blatt and C. Roos. Quantum simulations with trapped ions. *Nature Physics*, 8:277–284, 2012.
- [30] N. Gisin, G. Ribordy, W. Tittel, and H. Zbinden. Quantum cryptography. *Rev. Mod. Phys.*, 74:145–195, Mar 2002.
- [31] C. H. Bennett, G. Brassard, C. Crépeau, R. Jozsa, A. Peres, and W. K. Wootters. Teleporting an unknown quantum state via dual classical and einstein-podolsky-rosen channels. *Phys. Rev. Lett.*, 70(13):1895–1899, Mar 1993.
- [32] H.-J. Briegel, W. Dür, J. I. Cirac, and P. Zoller. Quantum repeaters: The role of imperfect local operations in quantum communication. *Phys. Rev. Lett.*, 81(26):5932–5935, Dec 1998.
- [33] I. Marcikic, H. de Riedmatten, W. Tittel, H. Zbinden, and N. Gisin. Long-distance teleportation of qubits at telecommunication wavelengths. *Nature*, 421(6922):509–513, 2003.
- [34] X.-S. Ma, T. Herbst, T. Scheidl, D. Wang, S. Kropatschek, W. Naylor, B. Wittmann, A. Mech, J. Kofler, E. Anisimova, V. Makarov, T. Jennewein, R. Ursin, and A. Zeilinger. Quantum teleportation over 143 kilometres using active feed-forward. *Nature*, 489:269–273, 2012.
- [35] H. J. Kimble. The quantum internet. *Nature*, 453, June 2008.
- [36] D. L. Moehring, M. J. Madsen, K. C. Younge, Jr. R. N. Kohn, P. Maunz, L.-M. Duan, C. Monroe, and B. B. Blinov. Quantum networking with photons and trapped atoms (invited). *J. Opt. Soc. Am. B*, 24(2):300–315, 2007.
- [37] L.-M. Duan and H. J. Kimble. Efficient engineering of multiatom entanglement through single-photon detections. *Phys. Rev. Lett.*, 90(25):253601, Jun 2003.
- [38] C. Simon and W. T. M. Irvine. Robust long-distance entanglement and a loophole-free bell test with ions and photons. *Phys. Rev. Lett.*, 91(11):110405, Sep 2003.
- [39] X.-L. Feng, Z.-M. Zhang, X.-D. Li, S.-Q. Gong, and Z.-Z. Xu. Entangling distant atoms by interference of polarized photons. *Phys. Rev. Lett.*, 90:217902, May 2003.
- [40] C. Cabrillo, J. I. Cirac, P. García-Fernández, and P. Zoller. Creation of entangled states of distant atoms by interference. *Phys. Rev. A*, 59(2):1025–1033, Feb 1999.
- [41] S. Lloyd, M. S. Shahriar, J. H. Shapiro, and P. R. Hemmer. Long distance, unconditional teleportation of atomic states via complete bell state measurements. *Phys. Rev. Lett.*, 87(16):167903, Sep 2001.

- [42] A. D. Boozer, A. Boca, R. Miller, T. E. Northup, and H. J. Kimble. Reversible state transfer between light and a single trapped atom. *Physical Review Letters*, 98(19):193601, 2007.
- [43] T. Wilk, S. C. Webster, A. Kuhn, and G. Rempe. Single-atom single-photon quantum interface. *Science*, 317(5837):488–490, 2007.
- [44] A. Stute, B. Casabone, P. Schindler, T. Monz, P. O. Schmidt, B. Brandstätter, T. E. Northup, and R. Blatt. Tunable ion-photon entanglement in an optical cavity. *Nature*, 485:482–485, 2012.
- [45] N. Schlosser, G. Reymond, I. Protsenko, and P. Grangier. Sub-poissonian loading of single atoms in a microscopic dipole trap. *Nature*, 411:1024–1027, 2001.
- [46] S. Gerber, D. Rotter, M. Hennrich, R. Blatt, F. Rohde, C. Schuck, M. Almdendros, R. Gehr, F. Dubin, and J. Eschner. Quantum interference from remotely trapped ions. *New Journal of Physics*, 11(1):013032 (13pp), 2009.
- [47] M. Khoon Tey, Z. Chen, S. A. Aljunid, B. Chng, F. Huber, G. Maslennikov, and C. Kurtziefer. Strong interaction between light and a single trapped atom without the need for a cavity. *Nature Physics*, page 1096, October 2008.
- [48] G. Shu, M. R. Dietrich, N. Kurz, and B. B. Blinov. Trapped ion imaging with a high numerical aperture spherical mirror. *Journal of Physics B: Atomic, Molecular and Optical Physics*, 42(15):154005, 2009.
- [49] R. Maiwald, A. Golla, M. Fischer, M. Bader, S. Heugel, B. Chalopin, M. Sondermann, and G. Leuchs. Collecting more than half the fluorescence photons from a single ion. *Phys. Rev. A*, 86:043431, Oct 2012.
- [50] A. P. VanDevender, Y. Colombe, J. Amini, D. Leibfried, and D. J. Wineland. Efficient fiber optic detection of trapped ion fluorescence. *Phys. Rev. Lett.*, 105(2):023001, Jul 2010.
- [51] H. Takahashi, A. Wilson, A. Riley-Watson, F. Orucevic, N. Seymour-Smith, M. Keller, and W. Lange. An integrated fiber trap for single-ion photonics. *New Journal of Physics*, 15(5):053011, 2013.
- [52] R. Gehr, J. Volz, G. Dubois, T. Steinmetz, Y. Colombe, B. L. Lev, R. Long, J. Estève, and J. Reichel. Cavity-based single atom preparation and high-fidelity hyperfine state readout. *Phys. Rev. Lett.*, 104:203602, May 2010.
- [53] M. Steiner, H. M. Meyer, C. Deutsch, J. Reichel, and M. Köhl. Single ion coupled to an optical fiber cavity. *Phys. Rev. Lett.*, 110:043003, Jan 2013.
- [54] E. Vetsch, D. Reitz, G. Sagué, R. Schmidt, S. T. Dawkins, and A. Rauschenbeutel. Optical interface created by laser-cooled atoms trapped in the evanescent field surrounding an optical nanofiber. *Phys. Rev. Lett.*, 104:203603, May 2010.

-
- [55] B. B. Blinov, D. L. Moehring, L.-M. Duan, and C. Monroe. Observation of entanglement between a single trapped atom and a single photon. *Nature*, 428:153–157, 2004.
- [56] D. L. Moehring, P. Maunz, S. Olmschenk, K. C. Younge, D. N. Matsukevich, L.-M. Duan, and C. Monroe. Entanglement of single-atom quantum bits at a distance. *Nature*, 449:68–71, 2007.
- [57] J. Hofmann, M. Krug, N. Ortegel, L. Gérard, M. Weber, W. Rosenfeld, and H. Weinfurter. Heralded entanglement between widely separated atoms. *Science*, 337(6090):72–75, 2012.
- [58] L. Slodička, G. Hétet, N. Röck, P. Schindler, M. Hennrich, and R. Blatt. Atom-atom entanglement by single-photon detection. *Phys. Rev. Lett.*, 110:083603, Feb 2013.
- [59] S. Ritter, C. Nölleke, C. Hahn, A. Reiserer, A. Neuzner, M. Uphoff, M. Mücke, E. Figueroa, J. Bochmann, and G. Rempe. An elementary quantum network of single atoms in optical cavities. *Nature*, 484:195–200, 2012.
- [60] S. Olmschenk, D. N. Matsukevich, P. Maunz, D. Hayes, L.-M. Duan, and C. Monroe. Quantum teleportation between distant matter qubits. *Science*, 23, 2009.
- [61] C. Nölleke, A. Neuzner, A. Reiserer, C. Hahn, G. Rempe, and S. Ritter. Efficient teleportation between remote single-atom quantum memories. *Phys. Rev. Lett.*, 110:140403, Apr 2013.
- [62] R. Ikuta, Y. Kusaka, T. Kitano, H. Kato, Y. Yamamoto, M. Koashi, and N. Imoto. Wide-band quantum interface for visible-to-telecommunication wavelength conversion. *Nature Communications*, 2:537, 2011.
- [63] S. Zaske, A. Lenhard, C. A. Keßler, J. Kettler, C. Hepp, C. Arend, R. Albrecht, W.-M. Schulz, M. Jetter, P. Michler, and C. Becher. Visible-to-telecom quantum frequency conversion of light from a single quantum emitter. *Phys. Rev. Lett.*, 109:147404, Oct 2012.
- [64] S. Tanzilli, W. Tittel, M. Halder, O. Alibart, P. Baldi, N. Gisin, and H. Zbinden. A photonic quantum information interface. *Nature*, 437:116–120, 2005.
- [65] C. Schuck. *Interfacing single ions and single photons for quantum networks*. PhD thesis, ICFO - The Institute of Photonic Sciences, 2009.
- [66] F. Rohde. *Remote ion traps for quantum networking: Two-photon interference and correlations*. PhD thesis, ICFO - The Institute of Photonic Sciences, 2009.
- [67] M. Almendros. *Towards Long-Distance Quantum Communication*. PhD thesis, ICFO - The Institute of Photonic Sciences, 2009.
- [68] N. Piro. *Controlled absorption of heralded single photons by a single atom: Towards entanglement distribution in quantum networks*. PhD thesis, ICFO - The Institute of Photonic Sciences, 2010.

- [69] M. Almendros, J. Huwer, N. Piro, F. Rohde, C. Schuck, M. Hennrich, F. Dubin, and J. Eschner. Bandwidth-tunable single-photon source in an ion-trap quantum network. *Phys. Rev. Lett.*, 103(21):213601, 2009.
- [70] F. Rohde, J. Huwer, N. Piro, M. Almendros, C. Schuck, F. Dubin, and J. Eschner. Polarization-correlated photon pairs from a single ion. *J. Opt. Soc. Am. B*, 27(6):A81–A87, 2010.
- [71] C. Schuck, F. Rohde, N. Piro, M. Almendros, J. Huwer, M. W. Mitchell, M. Hennrich, A. Haase, F. Dubin, and J. Eschner. Resonant interaction of a single atom with single photons from a down-conversion source. *Phys. Rev. A*, 81(1):011802, Jan 2010.
- [72] N. Piro, F. Rohde, C. Schuck, M. Almendros, J. Huwer, S. Ghosh, A. Haase, M. Hennrich, F. Dubin, and J. Eschner. Heralded single-photon absorption by a single atom. *Nature Physics*, 7:17–20, 2011.
- [73] T. W. Hänsch and A. L. Schawlow. Cooling of gases by laser radiation. *Optics Communications*, 13:68–69, 1975.
- [74] D. J. Wineland and H. G. Dehmelt. *Bull. Am. Phys. Soc.*, 20:637, 1975.
- [75] W. Paul. Electromagnetic traps for charged and neutral particles. *Rev. Mod. Phys.*, 62(3):531–540, Jul 1990.
- [76] W. Neuhauser, M. Hohenstatt, P. Toschek, and H. Dehmelt. Optical-sideband cooling of visible atom cloud confined in parabolic well. *Phys. Rev. Lett.*, 41(4):233–236, Jul 1978.
- [77] D. J. Wineland, R. E. Drullinger, and F. L. Walls. Radiation-pressure cooling of bound resonant absorbers. *Phys. Rev. Lett.*, 40(25):1639–1642, Jun 1978.
- [78] T. Rosenband, D. B. Hume, P. O. Schmidt, C. W. Chou, A. Brusch, L. Lorini, W. H. Oskay, R. E. Drullinger, T. M. Fortier, J. E. Stalnaker, S. A. Diddams, W. C. Swann, N. R. Newbury, W. M. Itano, D. J. Wineland, and J. C. Bergquist. Frequency ratio of al^+ and hg^+ single-ion optical clocks; metrology at the 17th decimal place. *Science*, 319:1808, 2008.
- [79] C. Monroe, D. M. Meekhof, B. E. King, W. M. Itano, and D. J. Wineland. Demonstration of a fundamental quantum logic gate. *Phys. Rev. Lett.*, 75(25):4714–4717, Dec 1995.
- [80] F. Schmidt-Kaler, H. Häffner, M. Riebe, S. Gulde, G. Lancaster, T. Deuschle, C. Becher, C. F. Roos, J. Eschner, and R. Blatt. Realization of the Cirac-Zoller controlled-not quantum gate. *Nature*, 422:408–411, 2003.
- [81] P. K. Ghosh. *Ion Traps*. Oxford University Press, 1995.
- [82] S. Gulde. *Experimental Realization of Quantum Gates and the Deutsch-Jozscha Algorithm with Trapped $^{40}Ca^+$ Ions*. PhD thesis, Universität Innsbruck, 2003.
- [83] J. Jin and D. A. Church. Precision lifetimes for the $ca^+ 4 p^2 P$ levels: Experiment challenges theory at the 1% level. *Phys. Rev. Lett.*, 70:3213–3216, May 1993.

-
- [84] P. A. Barton, C. J. S. Donald, D. M. Lucas, D. A. Stevens, A. M. Steane, and D. N. Stacey. Measurement of the lifetime of the $3d\ ^2d_{5/2}$ state in $^{40}\text{Ca}^+$. *Phys. Rev. A*, 62(3):032503, Aug 2000.
- [85] D. Leibfried, R. Blatt, C. Monroe, and D. Wineland. Quantum dynamics of single trapped ions. *Rev. Mod. Phys.*, 75(1):281–324, Mar 2003.
- [86] C. F. Roos. *Controlling the quantum state of trapped ions*. PhD thesis, Universität Innsbruck, 2000.
- [87] D. J. Wineland and Wayne M. Itano. Laser cooling of atoms. *Phys. Rev. A*, 20:1521–1540, Oct 1979.
- [88] S. Stenholm. The semiclassical theory of laser cooling. *Rev. Mod. Phys.*, 58:699–739, Jul 1986.
- [89] C. J. Foot. *Atomic Physics*. Oxford University Press, 2005.
- [90] D.F.V. James. Quantum dynamics of cold trapped ions with application to quantum computation. *Applied Physics B*, 66:181, 1998.
- [91] F. Rohde, M. Almendros, C. Schuck, J. Huwer, M. Hennrich, and J. Eschner. A diode laser stabilization scheme for $^{40}\text{Ca}^+$ single-ion spectroscopy. *Journal of Physics B: Atomic, Molecular and Optical Physics*, 43(11):115401, 2010.
- [92] J. I. Cirac, P. Zoller, H. J. Kimble, and H. Mabuchi. Quantum state transfer and entanglement distribution among distant nodes in a quantum network. *Phys. Rev. Lett.*, 78(16):3221–3224, Apr 1997.
- [93] Z. Y. Ou and L. Mandel. Violation of bell’s inequality and classical probability in a two-photon correlation experiment. *Phys. Rev. Lett.*, 61:50–53, Jul 1988.
- [94] P. G. Kwiat, K. Mattle, H. Weinfurter, A. Zeilinger, A. V. Sergienko, and Y. Shih. New high-intensity source of polarization-entangled photon pairs. *Phys. Rev. Lett.*, 75:4337–4341, Dec 1995.
- [95] C. K. Hong and L. Mandel. Experimental realization of a localized one-photon state. *Phys. Rev. Lett.*, 56:58–60, 1986.
- [96] R. Raussendorf and H. J. Briegel. A one-way quantum computer. *Phys. Rev. Lett.*, 86:5188–5191, May 2001.
- [97] J. L. O’Brien, G. J. Pryde, A. G. White, T. C. Ralph, and D. Branning. Demonstration of an all-optical quantum controlled-not gate. *Nature*, 426:264–267, 2003.
- [98] P. Walther, K. J. Resch, T. Rudolph, E. Schenck, H. Weinfurter, V. Vedral, M. Aspelmeyer, and A. Zeilinger. Experimental one-way quantum computing. *Nature*, 434:169–176, 2005.
- [99] J. L. O’Brien. Optical quantum computing. *Science*, 318(5856):1567–1570, 2007.

- [100] R. Prevedel, P. Walther, F. Tiefenbacher, P. Böhi, R. Kaltenbaek, T. Jennewein, and A. Zeilinger. High-speed linear optics quantum computing using active feed-forward. *Nature*, 445:65–69, 2007.
- [101] A. Haase, N. Piro, J. Eschner, and M. Mitchell. Tunable narrowband entangled photon pair source for resonant single-photon single-atom interaction. *Optics Letters*, 34:55, 2009.
- [102] N. Piro, A. Haase, M. W. Mitchell, and J. Eschner. An entangled photon source for resonant single-photon-single-atom interaction. *J. Phys. B*, 42:114002, 2009.
- [103] S. Tanzilli, H. de Riedmatten, H. Tittel, H. Zbinden, P. Baldi, M. De Micheli, D. B. Ostrowsky, and N. Gisin. Highly efficient photon-pair source using periodically poled lithium niobate waveguide. *Electronics Letters*, 37(1):26–28, 2001.
- [104] B. E. A. Saleh and M. C. Teich. *Fundamentals of Photonics*. Wiley, 2007.
- [105] N. Sangouard, C. Simon, H. de Riedmatten, and N. Gisin. Quantum repeaters based on atomic ensembles and linear optics. *Rev. Mod. Phys.*, 83:33–80, Mar 2011.
- [106] M. Gündoğan, P. M. Ledingham, A. Almasi, M. Cristiani, and H. de Riedmatten. Quantum storage of a photonic polarization qubit in a solid. *Phys. Rev. Lett.*, 108:190504, May 2012.
- [107] L.-M. Duan, M. D. Lukin, J. I. Cirac, and P. Zoller. Long-distance quantum communication with atomic ensembles and linear optics. *Nature*, 414:413–418, 2001.
- [108] P. Müller et al. in preparation.
- [109] P. Müller. *in preparation*. PhD thesis, Universität des Saarlandes.
- [110] R. Gerritsma, G. Kirchmair, F. Zähringer, J. Benhelm, R. Blatt, and C. F. Roos. Precision measurement of the branching fractions of the $4p \ ^2P_{3/2}$ decay of ca ii. *Eur. Phys. J. D*, 50:13–19, 2008.
- [111] H. Häffner, C.F. Roos, and R. Blatt. Quantum computing with trapped ions. *Physics Reports*, 469(4):155 – 203, 2008.
- [112] B. Darquie, M. P. A. Jones, J. Dingjan, J. Beugnon, S. Bergamini, Y. Sortais, G. Messin, A. Browaeys, and P. Grangier. Controlled single-photon emission from a single trapped two-level atom. *Science*, 309(5733):454–456, 2005.
- [113] J. McKeever, A. Boca, A. D. Boozer, R. Miller, J. R. Buck, A. Kuzmich, and H. J. Kimble. Deterministic generation of single photons from one atom trapped in a cavity. *Science*, 303(5666):1992–1994, 2004.
- [114] T. Legero, T. Wilk, M. Hennrich, G. Rempe, and A. Kuhn. Quantum beat of two single photons. *Phys. Rev. Lett.*, 93(7):070503, Aug 2004.
- [115] M. Keller, B. Lange, K. Hayasaka, W. Lange, and H. Walther. Continuous generation of single photons with controlled waveform in an ion-trap cavity system. *Nature*, 431: 1075–1078, 2004.

-
- [116] H. G. Barros, A. Stute, T. E. Northup, C. Russo, P. O. Schmidt, and R. Blatt. Deterministic single-photon source from a single ion. *New Journal of Physics*, 11(10):103004, 2009.
- [117] B. Lounis and W. E. Moerner. Single photons on demand from a single molecule at room temperature. *Nature*, 407:491–493, 200.
- [118] C. Santori, D. Fattal, J. Vuckovic, G. S. Solomon, and Y. Yamamoto. Indistinguishable photons from a single-photon device. *Nature*, 419:594–597, 2002.
- [119] B. Blauensteiner, I. Herbauts, S. Bettelli, A. Poppe, and H. Hübner. Photon bunching in parametric down-conversion with continuous-wave excitation. *Phys. Rev. A*, 79:063846, Jun 2009.
- [120] W. Nagourney, J. Sandberg, and H. Dehmelt. Shelved optical electron amplifier: Observation of quantum jumps. *Phys. Rev. Lett.*, 56(26):2797–2799, Jun 1986.
- [121] S. Friberg, C. K. Hong, and L. Mandel. Measurement of time delays in the parametric production of photon pairs. *Phys. Rev. Lett.*, 54:2011–2013, May 1985.
- [122] D. F. V. James, P. G. Kwiat, W. J. Munro, and A. G. White. Measurement of qubits. *Phys. Rev. A*, 64(5):052312, Oct 2001.
- [123] J. B. Altepeter, D. F. V. James, and P. G. Kwiat. *Qubit Quantum State Tomography*, volume 649 of *Lecture Notes in Physics*, chapter 4, pages 113–145. Springer, 2004.
- [124] W. K. Wootters. Entanglement of formation of an arbitrary state of two qubits. *Phys. Rev. Lett.*, 80:2245–2248, Mar 1998.
- [125] A. Kreuter, C. Becher, G. P. T. Lancaster, A. B. Mundt, C. Russo, H. Häffner, C. Roos, W. Hänsel, F. Schmidt-Kaler, R. Blatt, and M. S. Safronova. Experimental and theoretical study of the $3d^2d$ -level lifetimes of $^{40}\text{Ca}^+$. *Phys. Rev. A*, 71:032504, Mar 2005.
- [126] T. Kim, M. Fiorentino, and F. N. C. Wong. Phase-stable source of polarization-entangled photons using a polarization sagnac interferometer. *Phys. Rev. A*, 73:012316, Jan 2006.
- [127] R. Hanbury Brown and R. Q. Twiss. Correlation between photons in two coherent beams of light. *Nature*, 177:27–29, 1956.
- [128] C. Kurz, J. Huwer, M. Schug, P. Müller, and J. Eschner. A high-rate source for single photons in a pure quantum state. *New Journal of Physics*, 15(5):055005, 2013.
- [129] M. Schug. *in preparation*. PhD thesis, Universität des Saarlandes.
- [130] M. Schug, J. Huwer, C. Kurz, P. Müller, and J. Eschner. Heralded photonic interaction between distant single ions. *Phys. Rev. Lett.*, 110:213603, May 2013.
- [131] J. Huwer, J. Ghosh, N. Piro, M. Schug, F. Dubin, and J. Eschner. Photon entanglement detection by a single atom. *New Journal of Physics*, 15(2):025033, 2013.

- [132] M. Notcutt, L.-S. Ma, J. Ye, and J. L. Hall. Simple and compact 1-hz laser system via an improved mounting configuration of a reference cavity. *Opt. Lett.*, 30(14):1815–1817, 2005.
- [133] A. D. Ludlow, X. Huang, M. Notcutt, T. Zanon-Willette, S. M. Foreman, M. M. Boyd, S. Blatt, and J. Ye. Compact, thermal-noise-limited optical cavity for diode laser stabilization at 1×10^{-15} . *Opt. Lett.*, 32(6):641, 2007.
- [134] J. Alnis, A. Matveev, N. Kolachevsky, Th. Udem, and T. W. Hänsch. Subhertz linewidth diode lasers by stabilization to vibrationally and thermally compensated ultralow-expansion glass fabry-pérot cavities. *Physical Review A*, 77:053809, 2008.
- [135] R. W. P. Drever, John L. Hall, F. V. Kowalski, J. Hough, G. M. Ford, A. J. Munley, and H. Ward. Laser phase and frequency stabilization using an optical resonator. *Applied Physics B*, 31:97–105, 1983.
- [136] A. E. Siegman. *Lasers*. University Science Books, 1986.
- [137] W. Demtröder. *Laser Spectroscopy, Volume 1, Basic Principles*. Springer-Verlag, 2008.
- [138] D. Z. Anderson, J. C. Frisch, and C. S. Masser. Mirror reflectometer based on optical cavity decay time. *Applied Optics*, 23:1238–1245, 1984.
- [139] H. Kogelnik and T. LI. Laser beams and resonators. *Applied Optics*, 5:1550–1567, 1966.
- [140] E. D. Black. An introduction to pound-drever-hall laser frequency stabilization. *American Journal of Physics*, 69(1):79–87, January 2000.
- [141] L. Ricci, M. Weidemüller, T. Esslinger, A. Hemmerich, C. Zimmermann, V. Vuletić, W. König, and T. W. Hänsch. A compact grating-stabilized diode laser system for atomic physics. *Optics Communications*, 117:541–549, 1995.
- [142] M. Alloing. Frequency stabilization of a 732 nm diode laser. Master’s thesis, ICFO - The Institute of Photonic Sciences, 2008.
- [143] Toptica Potonics AG. *Sys DC 110, Diode Laser Supply Electronics*.
- [144] A. Sørensen and K. Mølmer. Quantum computation with ions in thermal motion. *Phys. Rev. Lett.*, 82(9):1971–1974, Mar 1999.
- [145] W. Demtröder. *Experimentalphysik 1*. Springer, 2008.
- [146] C. Kurz. *in preparation*. PhD thesis, Universität des Saarlandes.
- [147] U. Sterr, T. Legero, T. Kessler, H. Schnatz, G. Grosche, O. Terra, and F. Riehle. Ul-trastable lasers - new developments and applications. In T. Ido and D. T. Reid, editors, *Time and Frequency Metrology II*, volume 7431 of *Proc. of SPIE*, 2009.
- [148] J. I. Cirac and P. Zoller. Quantum computations with cold trapped ions. *Phys. Rev. Lett.*, 74(20):4091–4094, May 1995.

-
- [149] D. Reiß, A. Lindner, and R. Blatt. Cooling of trapped multilevel ions: A numerical analysis. *Phys. Rev. A*, 54:5133–5140, Dec 1996.
- [150] C. Cohen-Tannoudji, J. Dupont-Roc, and G. Grynberg. *Atom-Photon Interactions*. Wiley-VCH, 2004.
- [151] H. Oberst. Resonance fluorescence of single barium ions. Diploma thesis, Universität Innsbruck, 1999.
- [152] I. Marzoli, J. I. Cirac, R. Blatt, and P. Zoller. Laser cooling of trapped three-level ions: Designing two-level systems for sideband cooling. *Phys. Rev. A*, 49:2771–2779, Apr 1994.
- [153] C. F. Roos, G. P. T. Lancaster, M. Riebe, H. Häffner, W. Hänsel, S. Gulde, C. Becher, J. Eschner, F. Schmidt-Kaler, and R. Blatt. Bell states of atoms with ultralong lifetimes and their tomographic state analysis. *Phys. Rev. Lett.*, 92:220402, Jun 2004.
- [154] M. O. Scully and M. S. Zubairy. *Quantum Optics*. Cambridge University Press, 1997.
- [155] M. Fox. *Quantum Optics: An Introduction*. Oxford University Press, 2006.
- [156] N. F. Ramsey. A molecular beam resonance method with separated oscillating fields. *Phys. Rev.*, 78(6):695–699, Jun 1950.
- [157] D. S. Elliott, Rajarshi Roy, and S. J. Smith. Extracavity laser band-shape and bandwidth modification. *Phys. Rev. A*, 26:12–18, Jul 1982.
- [158] K. Toyoda, H. Shiibara, S. Haze, R. Yamazaki, and S. Urabe. Experimental study of the coherence of a terahertz-separated metastable-state qubit in $^{40}\text{Ca}^+$. *Phys. Rev. A*, 79:023419, Feb 2009.
- [159] N. Sangouard, J.-D. Bancal, P. Müller, J. Ghosh, and J. Eschner. Heralded mapping of photonic entanglement into single atoms in free space: proposal for a loophole-free bell test. *New Journal of Physics*, 15:085004, 2013.
- [160] I. V. Hertel and C.-P. Schulz. *Atome, Moleküle und optische Physik*. Springer-Verlag Berlin Heidelberg, 2008.
- [161] J. Honerkamp. *Statistical Physics: An Advanced Approach with Applications*. preprint, 2000.
- [162] S. Kotler, N. Akerman, Glickman Y., A. Keselman, and R. Ozeri. Single-ion quantum lock-in amplifier. *Nature*, 473:61–65, 2011.
- [163] S. Kotler, N. Akerman, Y. Glickman, and R. Ozeri. Nonlinear single-spin spectrum analyzer. *Phys. Rev. Lett.*, 110:110503, Mar 2013.
- [164] K. Shin and J. K. Hammond. *Fundamentals of Signal Processing for Sound and Vibrational Engineers*. Wiley, 2008.

Acknowledgments

The experimental set-up that I worked with during this thesis is a complex piece of technology when being considered as a whole, filling an entire research lab. Obviously, the obtained results with such a device are not the achievement of a single person's effort, but a large number of people contributed in different ways to the success of this work.

Most importantly, I would like to thank Jürgen Eschner for giving me the opportunity to join this project and to enter this fascinating and thrilling branch of quantum optics. I highly appreciate the unlimited support that I experienced, both in physics and normal life, which I think is really exceptional.

Starting with the team at ICFO, I would like to thank Francois Dubin for getting me started in the world of ion trapping, for constant support, and especially for teaching me how to make things work quick. Also the numerous car rides between BCN and Castelldefels were quite a luxury that I don't want to miss.

I also thank Nicolas Piro for setting up the photon-pair source and finally getting the interaction with the ion running. We were just a great team of fellow sufferers in staring infinite hours at single quantum jumps while making even fun of it.

Special thanks goes to the special forces Carsten Schuck, Felix Rohde and Marc Almendros for setting up an impressive ion-trap experiment after starting from scratch, and for patiently introducing me to every little detail of the apparatus. Extra thanks go to Nico and Felix for proofreading the manuscript.

I want to thank Hannes Gothe for being such a pleasant office mate during all the years and in particular for supporting each other as the only two ICFO relicts after moving with the group to Germany.

I thank the other group members Matteo, Tristan and Mathieu for making the work in the group such a nice time, this was of particular importance during the half year period before the move, when we were essentially on our own.

As representatives of the electronic and mechanical workshop at ICFO, I want to thank José Carlos and Xavi, who always provided great solutions with their teams for any request.

I want to thank Joyee Ghosh for taking care of the photon-pair source after joining the project in a very exciting phase, and for challenging together a long period of difficult measurements while running most of the time two labs by only two people. I greatly appreciated our team play and the way we mastered the big adventure of moving the labs from Spain to Germany.

Continuing with the new team at the Saarland University I want to direct many thanks to Michael Schug and Christoph Kurz, who joined the ion team with great enthusiasm and played a major role in un-mounting the experiment at ICFO and getting things running again in Saarbrücken. In the following years, with joined efforts we managed to advance the overall set-up to an unprecedented level of control which would have been impossible without such a great team. The same thank goes to Philipp Müller who, after running the first experiments in Saarbücken, provided the necessary theoretical support for a detailed interpretation of any measured data with the ions. For the preparation of this thesis I also thank him for extensive Latex support, I'm convinced that he'll make it one day for the *grandmaster of Tex*.

I also want to thank José Brito for maintaining the international appearance of the group with his south-american spirit and for providing valuable advice about scientific Spanish.

My best wishes go to Pascal and Stefan as the next generation of PhD students on the

combined set-up, who have proven during their Diploma theses to be perfectly suitable for that job.

At last I want to thank my parents for giving me always support in all of my decisions. The biggest thank goes to my love Berta and my son Max (who just joined during the last year) for their patience, for being always there, standing by my side, and giving me fresh motivation during all of the tough phases of the thesis.